Universitat Autònoma de Barcelona

Heat transfer fluids: From fundamental aspects of graphene nanofluids at room temperature to molten salts formulations for solar-thermal conversion

María del Rocío Rodríguez-Laguna

Heat transfer fluids:

From fundamental aspects of graphene nanofluids at room temperature to molten salts formulations for solar-thermal conversion

María del Rocío Rodríguez-Laguna

Doctoral Thesis

Memòria presentada per optar al grau de Doctor per la

Universitat Autònoma de Barcelona

Director	*Codirector*	*Codirector*	*Tutor*
Prof. Dr. Pedro Gómez-Romero	Prof. Dr. Clivia M. Sotomayor Torres	Dr. Emigdio Chávez-Ángel	Prof. Dr. Josep Ros Badosa

Programa de doctorat en Ciència de Materials

Departament de Química

Facultat de Ciències

Bellaterra, juny de 2019

Thesis Abstract

Heat transfer fluids and nanofluids constitute an important element in the industry and their performance is key to the successful application in technologies that go from heat management and cooling to heat exchangers in thermal-solar energy and electricity generation. These industries demand heat transfer fluids with a wider liquid temperature range and better thermal performance than the conventional fluids. From low-temperature fluids to high-temperature molten salts, these fluids seem to benefit from the dispersion of solid nanoparticles, leading to nanofluids which frequently feature improved thermal conductivities and/or specific heats as compared with the bare fluids. However, there are some exceptions. Contradictory reports make it necessary to study these materials in greater depth than has been usual. Yet, the liquid nature of these materials poses a real challenge, both from the experimental point of view and from the conceptual framework.

The work reported in this thesis has tackled two different challenges related to heat transfer fluids and nanofluids. In the first place, a careful and systematic study of thermal, morphological, rheological, stability, acoustic and vibrational properties of graphene-based nanofluids was carried out. We observed a huge increase of up to 48% in thermal conductivity and 18% in heat capacity of graphene-N,N-dimethylacetamide (DMAc) nanofluids. A significant enhancement was also observed in graphene-N,N-dimethylformamide (DMF) nanofluids of approximately 25% and 12% for thermal conductivity and heat capacity, respectively. The blue shift of several Raman bands (max. ~ 4 cm^{-1}) with increasing graphene concentration in DMF and DMAc nanofluids suggested that graphene has the ability to affect solvent molecules at long-range, in terms of vibrational energy. In parallel, numerical simulations based on density functional theory (DFT) and molecular dynamics (MD) showed a parallel orientation of DMF towards graphene, favoring π–π stacking and contributing to the modification of the Raman spectra. Furthermore, a local order of DMF molecules around graphene was observed suggesting that both this special kind of interaction and the induced local order may contribute to the enhancement of the thermal properties of the fluid. Similar studies were also performed in graphene-N-methyl-2-pyrrolidinone nanofluids, however, no modification of the thermal conductivity or the Raman spectra was observed. All these observations together suggest that there is a correlation between the modification of the vibrational spectra and the increase in the thermal conductivity of the nanofluids.

The second line of research focused on the development and characterization of novel molten salts formulations with low-melting temperature and high thermal stability. In this regard, two novel formulations of six components based on nitrates with a melting temperature of 60-75 °C and a thermal stability up to ~ 500 °C were synthesized. Moreover, the complexity of the samples led to establish a series of experimental methods which are proposed for the melting temperature detection of these materials as an alternative to conventional calorimetry. These methods are Raman spectroscopy, three-omega technique, and optical transmission.

Resumen

Los fluidos de transferencia de calor, y en particular los nanofluidos, se pueden considerar un elemento esencial en diversos sectores industriales y su rendimiento es clave para una adecuada aplicación en tecnologías que van desde la gestión térmica y la refrigeración, a la generación de energía solar térmica y eléctrica mediante el uso de intercambiadores de calor. Estas industrias necesitan fluidos de transferencia de calor con un rango de temperatura del líquido más amplio y mejores prestaciones en la transferencia de calor que los fluidos convencionales. Todos los fluidos parecen beneficiarse de la dispersión de nanopartículas sólidas, tanto aquellos usados en aplicaciones de baja temperatura y temperatura ambiente, como aquellos que funden a más alta temperatura (p. ej. sales fundidas). La dispersión de nanopartículas conduce a la obtención de nanofluidos que con frecuencia presentan mejores conductividades térmicas y/o calores específicos en comparación con los fluidos base. Sin embargo hay algunas excepciones. En la bibliografía podemos encontrar resultados contradictorios acerca de la mejora de las propiedades térmicas en nanofluidos, lo cual hace que sea necesario un estudio de estos materiales en mayor profundidad. Por otra parte, la naturaleza líquida de estos materiales plantea un verdadero desafío, tanto desde el punto de vista experimental como en relación al marco conceptual.

El trabajo que se presenta en esta tesis ha abordado dos retos diferentes relacionados con los fluidos de transferencia de calor y los nanofluidos. En primer lugar, se llevó a cabo un estudio riguroso y sistemático de las propiedades térmicas, morfológicas, reológicas, de estabilidad, acústicas y vibracionales de nanofluidos de grafeno en disolventes orgánicos. Observamos un gran aumento de la conductividad térmica de hasta un 48% y un aumento del 18% en la capacidad calorífica de los nanofluidos de grafeno en N,N-dimetilacetamida (DMAc). También se observó una mejora significativa en los nanofluidos de grafeno en N,N-dimetilformamida (DMF) del orden del 25% y 12% para la conductividad térmica y la capacidad calorífica, respectivamente. El desplazamiento de varias bandas del espectro Raman de DMF y DMAc hacia altas frecuencias (máx. ~ 4 cm^{-1}) al aumentar la concentración de grafeno, sugirió que éste tiene la capacidad de afectar a las moléculas de disolvente a larga distancia, en términos de energía vibracional. En paralelo, las simulaciones numéricas basadas en la teoría funcional de la densidad (DFT) y dinámica molecular (MD) mostraron una orientación paralela de DMF hacia el grafeno, favoreciendo la interacción π-π y contribuyendo a la modificación de los espectros de Raman. Además, se observó un orden local de las moléculas de DMF alrededor del grafeno, lo que sugiere que tanto este tipo especial de interacción como el orden local inducido pueden contribuir a la mejora de las propiedades térmicas del fluido. También se realizaron estudios similares en nanofluidos de grafeno disperso en 1-metil-2-pirrolidona, sin embargo, no se observó ninguna modificación de la conductividad térmica o de los espectros de Raman. Todas estas observaciones juntas sugieren que existe una correlación entre la modificación de los espectros vibracionales y el aumento de la conductividad térmica de los nanofluidos.

La segunda línea de investigación se centró en el desarrollo y caracterización de nuevas formulaciones de sales fundidas con baja temperatura de fusión y alta estabilidad térmica. Con este propósito, se sintetizaron dos nuevas formulaciones de seis componentes basadas en nitratos con una temperatura de fusión de 60-75 °C y una estabilidad térmica de aprox. 500 °C. Por otro lado, la complejidad de las muestras llevó a establecer una serie de métodos experimentales que se proponen para la detección del punto de fusión de estos materiales como una alternativa a la calorimetría convencional, estas técnicas son: espectroscopia Raman, técnica 3ω y transmisión óptica.

Preface

The present PhD Thesis summarizes my work at the Novel Energy-Oriented Materials Group and Phononic and Photonic Nanostructures Group of the Catalan Institute of Nanoscience and Nanotechnology (ICN2) carried out between the years 2015 and 2019. According to the decision of the commission of the doctoral program of materials science, this thesis is presented as a collection of articles.

All articles are listed below in order of appearance in the thesis:

Article 1. M.R. Rodríguez-Laguna, A. Castro-Alvarez, M. Sledzinska, J. Maire, F. Costanzo, B. Ensing, M. Pruneda, P. Ordejón, C.M. Sotomayor Torres, P. Gómez-Romero, E. Chávez-Ángel, Mechanisms behind the enhancement of thermal properties of graphene nanofluids, Nanoscale. 10 (2018) 15402–15409. doi:10.1039/C8NR02762E.

Article 2. M.R. Rodríguez-Laguna, P. Gómez-Romero, C.M. Sotomayor Torres, E. Chavez-Angel, Modification of the Raman Spectra in Graphene-Based Nanofluids and Its Correlation with Thermal Properties, Nanomaterials. 9 (2019) 804. doi:10.3390/nano9050804.

Article 3. M.R. Rodríguez-Laguna, P. Gómez-Romero, C.M. Sotomayor Torres, M.-C. Lu, E. Chávez-Ángel, Development of low-melting point molten salts and detection of solid-to-liquid transitions by alternative techniques to DSC, Solar Energy Materials and Solar Cells, (2019). Manuscript submitted for publication: second round of peer review.

Each article is preceded by a section that contains an introduction to the topic and a summary of the results.

Table of contents

Chapter 1: Introduction

Chapter Summary

The growth of the world population has led humanity to an energy crisis. The United Nations estimated an annual growth rate of 1.1 % in 2017. In the last 100 years, the population has quadrupled due to medical advances and political stability, which has led to a decrease in mortality rates and an increase in the average human age. In turn, the global demand for energy has increased considerably. Fossil fuels are depleted and its consumption leads to environmental problems. Hence, there is an urgent need for making advances in the use of renewable sources. Solar thermal energy is one of the most promising energy technologies. However, the efficiency rate is not comparable to that of non-renewable power plants. Yet, as it will be discussed below, it could be enhanced by improving the thermo-physical properties of the heat transfer fluid using a variety of strategies. We should remark that, in addition to primary energy generation, these same strategies can also be used to solve an underlying problem of the growing energy consumption, the thermal management and cooling processes. Indeed, the relentless development of information and communication technology (ICT) during the last century has caused an increase in internal heat generation of electronic components and temperature rise. Forced liquid-cooling is an effective way to cool electronics; however, the thermo-physical properties of common fluids are not meeting the needs of the ever-advancing technology. The dispersion of nanoparticles in the fluid is one of the aforementioned strategies. In this chapter, I describe the problems related to energy and the potential solutions. Then, I expose the motivation and objectives of this thesis.

1.1 Heat transfer fluids

When we think of ‘materials’ we could envisage simple elements, more or less complex chemical compounds, elaborate molecular architectures or even the most sophisticated nanoengineered composites. But, most likely, we will think of them as solids. Yet, there is much more to liquid materials than it meets the eye. Literally, liquid materials lurk inside a great variety of our dearest technological devices serving maybe not too glamorous but very effective functions. Thus, from electrolytes in Redox Flow Batteries to Heat Transfer Fluids in heat exchangers, we have come to depend on the reliable service of flowing materials.

Heat Transfer Fluids constitute a particularly important technological subset. Fast and effective transfer of heat is key to the optimal performance of a wide variety of technologies, from heat management and cooling systems in microelectronics to heat exchangers in thermal-solar power plants for electricity generation.

In all these applications high thermal conductivity and large specific heats are desirable. Yet, liquids are characterized by low thermal conductivities as compared with solids. An effective way to overcome this problem is to disperse solid particles in the base fluid. It is well known that the dispersion of solid particles in a fluid leads to an enhancement of the thermal conductivity and the specific heat, in some cases. However, this approach presents a serious drawback related to the coagulation and precipitation of the solid, leading to clogging. The reduction of the solid particle size to nanometric dimensions leading to stable dispersions of nanoparticles in the base fluid does solve this problem. The resulting nanofluids will be described in detail below. However, some of the industries mentioned above, such as solar-thermal, not only require fluids with improved thermal conductivity and heat capacity, but require new formulations with a wider range of operating temperature, which is essential to maximize the energy conversion process. The advances made in the development of new formulations will also be described in the following pages.

But before that we will present two sections introducing some of the most relevant aspects related to the possible application of fluids and nanofluids, both for energy conversion as well as for cooling applications.

1.2 Energy problems

Currently, we are attempting to solve the severe energy crisis that we suffer due to the increase in energy demand from industrial, commercial, domestic and urban sectors. This energy crisis derives from the predictable end of the oil, gas and coal cycle, which in turn have generated a significant increment in greenhouse gases. Renewable sources are the way to go and solar-thermal energy is one of the most promising resources available.

An underlying problem of the increase in energy consumption is the management of thermal energy, especially in electronics. The rapid development of computing has led to the fabrication of denser, faster and cheaper integrated circuits (ICs), as predicted by Gordon Moore [1]. However, the miniaturization of electronic components results in higher internal heat generation and temperature rise. The cooling of the components is fundamental to achieve good efficiencies and reliability of the entire system.

1.2.1 Energy crisis

Currently, the global energy consumption is based predominantly on fossil fuels. The burning of fossil fuels for transport, generation of electricity and heat is the largest human source of greenhouse gases and contribute significantly to global warming.

In addition to the negative effect on the environment, it is worth mentioning that the reserves of conventional fossil fuels, in particular oil, are seriously depleted. The reason behind the shortage of supply is the rapidly increase in consumption of fossil fuels during the last century. As a consequence, it is necessary to reconsider the mid-term and long-term perspectives of the current energy market scheme [2]. It has never been more evident that renewable energy sources are fundamental to meet the growing demand for energy and to achieve a sustainable future for humankind. Among the available renewable energy sources, wind and solar energies are the best technologies for large-scale energy production.

Solar energy is probably the cleanest, most reliable form of sustainable power source available. Solar radiation can be directly converted into electricity by using photovoltaic cells or alternatively, its thermal energy can be harnessed by means of solar thermal collectors to produce thermal-solar electricity [2].

Solar thermal collectors can be classified according to their operation temperature range, as low-, medium-, or high-temperature collectors. Flat plate solar collectors are typically used for low-temperature applications: water heating and space heating [3]. They are limited to heating water or air up to ≈ 80 ^{o}C [2]. Among medium-temperature collectors, evacuated tube collectors are the most representative. They are based on a heat pipe inside a vacuum-sealed tube [4] connected to a copper manifold within a heat exchanger tank. They can reach temperatures of ≈ 125 ^{o}C [2] and they typically use water or a mixture of propylene glycol-water (50-50%) as HTF. High-temperature collectors require the use of reflectors to concentrate the sunlight into a smaller area to attain high temperatures. Sun's rays can be focused onto a receiver located along the focal line or the focal point of the reflector; depending on that, the system will work at a different range of temperatures. Concentrated technologies can be divided into four optical types, namely parabolic trough, linear Fresnel reflector, dish and solar power tower (see **Figure 1**). Parabolic trough and linear Fresnel technologies use line-focus geometry, whereas, dish and solar power towers use point-focus configurations. As a result, the latter achieve higher temperatures (i. e. solar power tower, T=1000 ^{o}C and dish concentrators, T >2000 ^{o}C) than linear Fresnel reflectors (≈320 ^{o}C) and parabolic-trough collectors (400 ^{o}C) [2]. These temperature values are approximate; however, they provide a general idea of the variety of heat transfer fluids needed to run these applications. The working principle of a solar-thermal power plant is further explained below.

Concentrated solar power (CSP) plants focalize sunlight onto a receiver, where the heat is collected by a heat transfer fluid. The fluid is circulated through pipes and is directed to a heat exchanger. Then, the heat is transferred to water and produces steam. The steam flows to a turbine and thermal energy is converted into mechanical that in turn drives a generator to produce electricity.

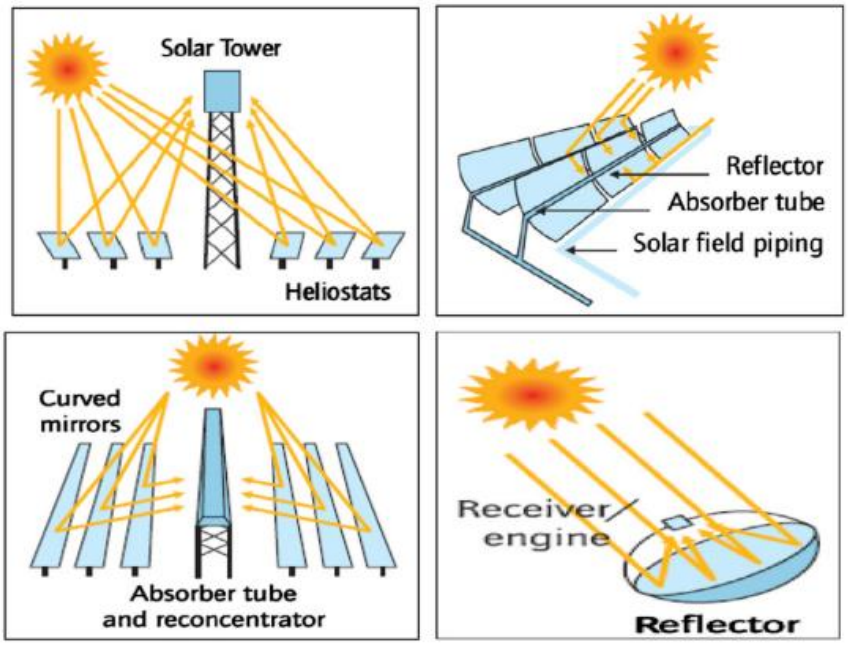

Figure 1 Currently available CSP technologies: (a) power tower (b) parabolic trough (c) linear Fresnel reflector (d) parabolic dish. Image taken from Zhang et al. 2013 [5]

The heat transfer fluid (HTF) is one of the most important components of the CSP plant, and the energy conversion efficiency of the entire system is subsidiary to the thermal performance of the fluid [6]. Heat transfer fluids can be categorized into different classes: (1) water/steam, (2) thermal oils, (3) organics, (4) molten salts and (5) liquid metals. **Figure 2** illustrates a comparison in the operating temperature range of some fluids that belong to the mentioned categories [6]. Thermal oils and organic compounds, such as the well-known eutectic mixture of biphenyl-diphenyl ether [7], work in a similar temperature range ≈ (-20)-400 ^{o}C. Their operating temperature is compatible with their use in solar parabolic trough plants. In addition, they have an advantage over water; they can work at higher temperatures without producing high pressure inside the receiver tube and piping [1]. However, thermal oils are highly expensive [8].

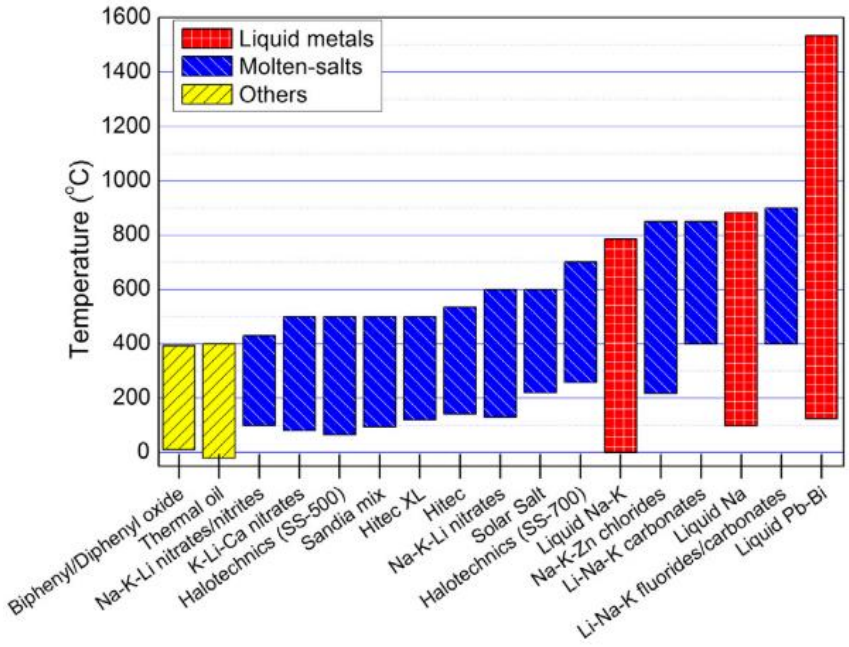

Figure 2 Operating temperature range for various heat transfer fluids [6]

Molten salts have been widely used in thermal-solar applications, not only as thermal working fluids but as thermal storage materials. They have extremely high thermal stability (more than 500 ºC) compared to that of the common fluids. This feature has placed them at the forefront in the field of solar energy materials. In addition, they have other suitable properties for the application, namely, good heat capacity, low vapor pressure, and good thermal and physical properties at elevated temperatures [9]. In fact, they have viscosity and vapor pressure values similar to those of water, at high temperatures [10]. However, these materials have relatively high melting temperature, which means that extra energy is necessary to keep the salt in the molten state to avoid pipe freezing. As a result, the cost of the entire CSP plant rises. Novel compositions are being investigated to improve the energy conversion rate and to reduce the final cost of electricity generation [11].

To achieve desirable advances in CSP technology, fluids with low melting temperature and high thermal stability are required. A fluid with a wide operational temperature range is beneficial for both energy conversion and energy storage. Thus, producing high-temperature steam in the heat exchanger will substantially increase the efficiency of the steam turbine (Carnot's theorem) and that of the overall energy conversion. And in terms of sensible energy storage, a larger temperature difference in the storage system will

result in a significantly increased specific storage capacity [12,13]. Furthermore, the improvement of thermal and physical properties of the salts, such as thermal conductivity (k), specific heat (Cp) and viscosity are fundamental for the performance and efficiency in the energy conversion process. A number of investigations have focused on the development of novel compositions with better thermal properties than the available molten salts. Other studies have tried, in a sense, to upgrade well-known compositions. They have used a variety of strategies:

a. To improve Cp and k, some have dispersed nanoparticles in the molten salt;

b. To increase the thermal stability, some researchers have i) incorporated another inorganic salt (with a different anion) to the original composition; or ii) controlled the cover gas atmosphere;

c. To lower the melting temperature, some scientists have i) used thermodynamic modeling to predict novel compositions with low melting point; ii) used experimental design and data analysis methods; iii) added extra constituents (same anion) or iv) introduced an additional constituent to form a superior multi-component salt (more than 4 components).

An overview of the literature on these strategies and further details can be found in chapter 3. In our case, we were interested on widening the operating temperature of the heat transfer material; in particular we focused our efforts on lowering the melting temperature of the salt.

1.2.2 Thermal management in electronics

The most recent advances in electronic technology have been directed towards the miniaturization of its components to achieve faster performances. These developments imply an increase in the energy consumption of the components. As a result, the heat flux generated by a microelectronic system increases considerably and the temperature control becomes a crucial challenge. If not cooled down, the reliability and performance of an electronic item will be negatively influenced [14]. Therefore, heat removal from electronic constituents has turned into a subject of significant importance due to the continuous reduction of the size of components and the increase of their power density.

Conventional cooling strategies can be classified into passive and active. Passive cooling is based on natural convection, radiation and heat conduction by means of a heat sink with very high thermal conductivity, e.g. aluminum, copper or zinc [15]. All electronic devices

include a heat sink or a heat spreader. Their efficiency depends on the election of the material and the design of the metallic part [16]. Active cooling, on the other hand, requires the supply of energy to force the cooling of the system, e.g. forced convection to maximize heat removal (e.g. fan). The rate of heat removal that active strategies offer is much larger than that provided by passive cooling methods, excluding strategies using latent heat [17]. Hence, it can deal with higher power densities. Active cooling strategies include: forced-air and -liquid cooling, direct liquid immersion and thermoelectric coolers [17–19].

Among these methods the forced-air cooling (heat-sink-fan) is the most widely used due to its simplicity compared to other active methods. However, it is an old-fashioned strategy with some limitations, that is, it is not capable to dissipate large amounts of heat at a reasonable cost and the fan can have maintenance problems (e.g. dust).

Liquid cold plates are the most commonly used solutions within liquid cooling strategies for electronics. The plates are in direct contact with the heat source and heat is transferred to the liquid that circulates through the cold plates and eventually to the heat exchanger.

Conventional coolants can be classified into dielectric and non-dielectric fluids. On one hand, the dielectric coolants are organic-based fluids, with quite low thermal conductivity but widely used in direct liquid immersion systems. On the other hand, the non-dielectric coolants are preferred for heat pipes and microfluidics due to their superior thermal properties compared to their dielectric counterparts. Normally, they are aqueous solutions and thus exhibit quite high heat capacity and low viscosity. Water, ethylene glycol, and mixtures of these two are the most popular and widely used coolants for many electronic devices [17]. However, a major problem of conventional coolants is the low heat exchange rate and the thermal conductivity, which is too small to meet the coming needs and challenges in the field. One way to overcome this barrier is by using solid particles dispersed in fluids to improve their thermal properties [20,21].

1.2.2.1 Nanofluids

Nanofluids are colloidal dispersions of nanoparticles (1–100 nm) in a base fluid, i.e. sols designed to flow. The term was first coined by Choi and Eastman [22] in 1995, from Argonne National Laboratory. The concept describes a new class of nanotechnology-based heat transfer fluids that exhibit superior thermal properties than those of the base fluids [23].

Colloidal dispersions have been known and studied for centuries. Yet, nanoscience and nanotechnology provide tools to understand and control their properties as it has never been possible before. Choi and Eastman are credited for discovering that the thermal properties of the investigated nanofluids significantly exceeded the values predicted by classical macroscopic theories and models [24]. That is the reason why the term 'nanofluid' has always been related to the thermal field, although there are many other fields in which nanofluids could play a central role, and we could take ferrofluids and magnetic properties as a particularly well-known example.

The addition of micrometer- or millimeter-sized solid particles will lead to an increased thermal conductivity of the resultant fluids, as it could be expected given the larger thermal conductivity of solids as compared to liquids. But the presence of milli- or microsized particles in a fluid poses a number of problems. One of the most serious ones is that these large particles typically do not form stable dispersions and tend to settle down and clog flow channels [23,25].

The novel concept of 'nanofluids' has been proposed as a route to surpassing the performance of heat transfer fluids currently available [23]. A very small amount of nanoparticles, when dispersed uniformly and stably in base fluids, can provide very substantial improvements in the thermal properties of the resulting fluids. Several investigations have revealed that the thermal conductivity of the fluid containing nanoparticles could be increased by more than 20% for the case of very low nanoparticles concentrations [23].

According to a recent research, nanoparticle volume fraction has a significant effect on direct solar collector efficiency [26]. The effectiveness of heat transfer enhancement has been found to be dependent on the amount of dispersed particle, material type, particle shape and so on [25]. At present, there is significant discrepancy in nanofluid thermal conductivity data in the literature. Besides this, the mechanisms for the enhancement of thermal conductivity in nanofluids have not been fully understood yet [27].

The specific heat capacity of a nanofluid is another important property that has an impact on the nanoparticle and fluid temperature changes, which affect the temperature field of the nanofluid and consequently, the heat transfer and flow status. Some research studies show that the specific heat capacities of nanofluids are different from those of the bare fluids and vary with the size and volume concentration of nanoparticles. However, in the majority of cases, there are no experimental data available for specific heat capacity [28].

1.3 Motivation and objectives

The motivation for this thesis was to develop heat transfer and thermal storage fluids with better thermo-physical properties than those of the conventional fluids used for thermal applications. The limits of conventional fluids and the needs of the cooling and solar thermal energy industries were taken into consideration to plan the general and particular goals of this thesis. However, to contribute to the general goal of developing new and improved HTFs, two specific objectives were targeted, namely,1) to unveil and understand the enhanced heat transfer phenomenon in nanofluids and 2) to study the thermal behavior of multi-component salts and the factors affecting its internal structure in the solid and molten states.

Nanofluids are an emerging new area with fundamental implications in nanoscience, therefore, many challenges, such as long-term dispersion stability remained to be solved. Also, solar thermal energy, in particular concentrated solar power (CSP) technology is in its infancy. And so far, no known fluid is thermally stable from room-temperature to the high-temperatures that power tower and dish-type stations can potentially reach.

The following list collects some of the most relevant particular goals pursued as part of the present PhD Thesis:

- To develop stable dispersions of nanoparticles in room-temperature fluids (sols).
- To develop thermally stable fluids able to operate efficiently in a wide range of temperatures, ideally from room-temperature up to 500-550 ºC.
- Sols, fluids and nanomaterials characterization: composition, long-term dispersion stability, thermo-physical properties (melting point, thermal conductivity, heat capacity, thermal stability), viscosity, nanomaterial dimensions, size distribution and nanostructure.
- To study the fundamental physics related to heat transfer mechanisms, i.e. the nature of the expected enhancement of properties in nanofluids.
- To develop novel, fast and cheap characterization techniques for liquids and high-temperature.

Chapter 2: Study on the thermal enhancement of graphene-amide nanofluids: an insight into the mechanisms at work

Chapter Summary

A number of experimental studies confirm that the dispersion of nanomaterials is effective in enhancing the thermal properties of fluids. However, the mechanisms behind this enhancement remain to be elucidated. In this chapter, the mechanisms suggested in the literature are described and discussed. In addition, we review the latest research on graphene-based nanofluids and explain some of the challenges the heat transfer and cooling industry faces with the implementation of these materials. This then leads to the description of the work done in articles 1 and 2, where we decided to prepare and study a simple system, a nanofluid made of graphene dispersed in simple organic amide solvents, in order to shed some light on the heat transfer across nanofluids. In this chapter, and related articles, surfactant-free graphene nanofluids, based on N,N-dimethylacetamide (DMAc), N,N-dimethylformamide (DMF) and N-Methyl-2-pyrrolidone (NMP) are presented. Graphene nanofluids based on DMAc and DMF showed an enhancement in thermal conductivity, specific heat, viscosity, as well as a modification of their vibrational spectra with increasing graphene concentration. The blue shift of several Raman bands with increasing graphene concentration in DMAc and DMF indicates that graphene has the ability to affect solvent molecules at long-range, in terms of vibrational energy. Density functional theory and molecular dynamics simulations showed a parallel orientation of DMF towards graphene, favoring π–π stacking. Furthermore, a local order of DMF molecules around graphene was observed suggesting that both this special kind of interaction and the induced local order may contribute to the enhancement of the fluid's thermal properties. Additionally, a correlation was found between the modification of the Raman spectra of the fluids in the presence of graphene and the improvement of heat transfer in the fluids.

2.1 A general introduction to the potential mechanisms of heat transfer in nanofluids

The outstanding improvement of the effective thermal conductivity in fluids with small volume fractions of nanoparticles captured the attention of researchers a couple of decades ago [22,29–31]. Since then, hundreds of studies on nanofluids have been carried out in relation to their preparation, thermo-physical properties and heat transfer performance. As an example, see **Figure 3** to examine the upward trend in the number of papers published related to 'nanofluids' and 'graphene' from 2009 to 2018.

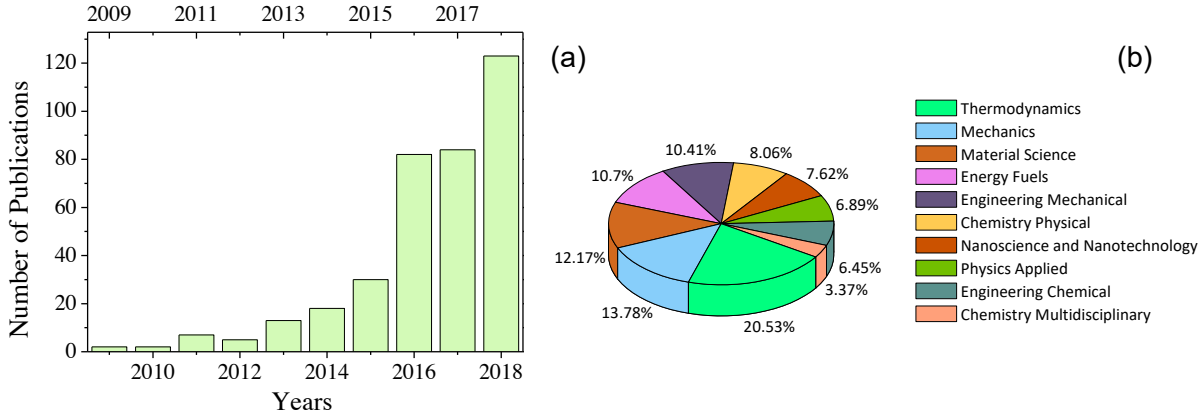

Figure 3 (a) Number of JCR articles per year, as reported by Journal of Citation Report, Web of Science (http://apps.webofknowledge.com), from 2009 and updated to 2018 retrieved via the keyword "nanofluid" and "graphene" in the topic of the paper, (b) Distribution of these publications in different fields of science, expressed as a percentage.

The vast majority of the publications on nanofluids (NFs) have been limited to i) experimental studies on the physical properties of particular nanofluids [32–37] and ii) theoretical models proposed to estimate the effective thermal conductivity of common NFs [38–40]. Few researchers have attempted to explain the mechanism behind the enhanced thermal transport in the fluid due to the presence of small concentrations of nanoparticles (NPs) [30,41,42]. The mechanisms that could explain this phenomenon are i) percolation pathway created by agglomeration of nanoparticles, ii) formation of a solid-like structure of the liquid surrounding the NP with a higher thermal conductivity than the bulk liquid, iii) modification of the interatomic interactions in the liquid, iv) increase of the thermal transfer due to Brownian motion of nanoparticles [40], v) localized convection in the liquid caused by the Brownian motion of NPs [43], vi) ballistic phonon transport in the nanomaterial, vii)

thermophoresis effect in the nanoparticles and viii) heat conduction in the liquid and in the solid-liquid interface. Four proposed potential mechanisms are illustrated in **Figure 4**.

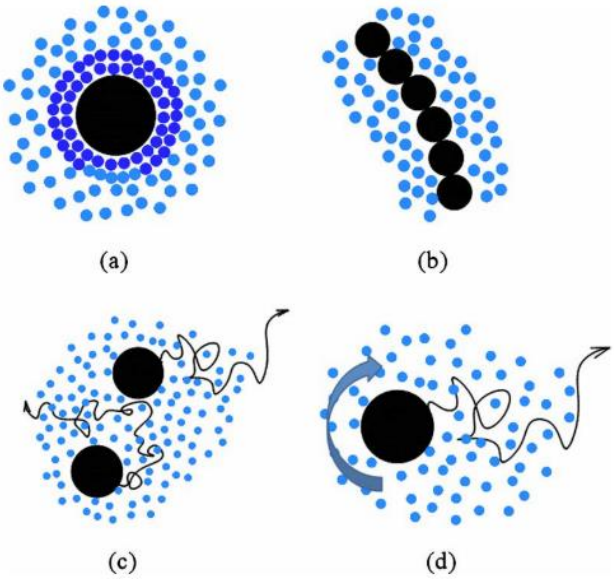

Figure 4 Schematic diagram of four heat transfer mechanisms possibly involved in the enhancement of thermal transport in nanofluids: (a) solid-like structuration, (b) particle agglomeration, (c) Enhancement of heat transfer due to Brownian motion of particles and (d) localized convection in the liquid caused by the Brownian motion. Image taken from Fan and Wang [44].

The potential mechanisms responsible for the enhancement of heat transport in nanofluids will be thoroughly explained and discussed. These mechanisms can be classified into three groups: those directly related to 1) electrostatic forces between NPs, solvent molecules or NP-liquid, 2) those that involve the motion of NPs and molecules and 3) other mechanisms.

2.1.1 Mechanisms related to electrostatic forces in the nanofluid

This group includes i) agglomeration of NPs, ii) solid-like structure of the liquid around the NP and iii) modification of the interatomic interactions in the liquid.

i) Percolation pathway created by agglomeration of nanoparticles

The aggregation of nanoparticles is a common behavior in most known nanofluids. Very few nanofluids form stable long-term dispersions. The affinity between liquid molecules and nanoparticles plays a decisive role in the final arrangement of the nanofluid. In the initial stage of the preparation of the nanofluid, nanoparticles can agglomerate to form a

more stable structure. Occasionally, this agglomeration results in the total precipitation of the nanoparticles. But nanoparticles can also agglomerate as stable-clusters with different shapes, such as in the case of chain-like structures. Some researchers claim that these chain-like structures favor the heat flow in a certain direction [30]. Others consider these clusters as special particles with a high aspect ratio [45]. Evgin et al. reported that a large aspect ratio has a positive impact on the thermal conductivity of nanomaterials [46]. To summarize, the heat conduction could be stimulated by the presence of aggregates compared to nanofluids showing no agglomeration of nanoparticles [44].

ii) Solid-like structure of solvent molecules surrounding the NP

This theory was first proposed by Choi et al. [47]. They suggested that a solid-like structure of the liquid solvent is formed around the nanoparticle, which exhibits a higher thermal conductivity than the bulk liquid. Later on, Yu and Choi [41] postulated that this organized nanolayer acts as a thermal bridge between the nanoparticle and the bulk liquid, favoring the heat transport in the interface and increasing the effective heat transfer throughout the nanofluid [41]. More recent studies propose that these ordered liquid layers can provide a more effective thermal path between solid-solid nanoparticles when there is small separation between them [29]. They suggest that adjacent ordered-nanolayers overlap and that 'heat conduction' across the nanomaterial could be the dominant mechanism.

The existence of liquid layering around NPs has been demonstrated both theoretically [48–50] and experimentally [51–53].

Molecular dynamics (MD) simulations revealed that the strength of the interaction NP-liquid determines the thickness of the solid-like liquid layering. Weak-interactions allow the formation of a single layer of liquid around the NP, while stronger interactions permit the development of several layers of ordered liquid with a lower thermal resistance [48,54]. However, numerical calculations showed that the slope of the thermal profiles of nanofluids with long- and short-distance liquid layering around the NPs, are similar [48]. These findings seem to rule out the theory of liquid layering for the explanation of the enhancement of the effective thermal conductivity in the nanofluid.

iii) Modification of the interatomic interactions in the liquid arising from interatomic potential

This hypothesis was conceived in the field of chemical physics, particularly within the sub-field of molecular dynamics (MD). Molecular dynamics studies the movement of atoms and molecules in complex systems as a response to interatomic, intermolecular or even long-range interactions. MD simulations are important tools to understand the behavior of complex atomic or molecular systems and predict their properties. To prognosticate the trajectory of atoms or molecules, the forces between particles and their potential energy are calculated using interatomic potentials. Several researchers [42,55] suggested that 'the thermal energy transfer in nanofluids improved due to increased interatomic interactions arising from interatomic potential' [42]. They claim that the interatomic interactions of the liquid molecules are modified by the presence of solid nanoparticles. Abou-Tayoun [42] studied the role of interatomic interactions in the enhancement of the thermal transport in cooper-water nanofluid, particularly the interactions water-water, water-copper and copper-copper. He concluded that the interatomic interactions played an important role on the enhancement of the thermal conductivity in nanofluids. Coulomb and Van der Waals interactions were modified in the nanofluid as compared to those in the bare fluid. These interactions directly depend on the nature of the nanoparticle and liquid, and their affinity.

2.1.2 Motion/mass transfer-related mechanisms

These heat transfer mechanisms are based exclusively on the movement of NPs and/or molecules. This group includes: iv) increase of the thermal transfer due to Brownian motion of nanoparticles, v) localized convection in the liquid caused by the Brownian motion of NPs, vi) enhancement of thermal transport due to thermophoresis effect and vii) heat conduction in the liquid and in the solid-liquid interface due to collisions of particles.

iv) The nanoparticles act as heat carriers due to Brownian motion

It is well known that in a liquid medium there is a natural diffusion of the molecules due to temperature and concentration gradients. In nanofluids, the movement of liquid molecules results in collisions between molecules and NPs which cause a random motion of the latter. This phenomenon is called 'Brownian motion'. Now, if we consider the NPs as heat carriers within the nanofluid, the Brownian motion of nanoparticles can favor the heat transport diffusion in the liquid medium. Therefore, this distribution and continuous

movement of nanoparticles in the liquid may enhance the heat transfer in the medium [40,56,57].

v) Localized convection in the liquid caused by Brownian motion of NPs

To understand this phenomenon it is necessary to take into account that nanoparticles are considerably larger than molecules. The Brownian motion of nanoparticles has an impact on the adjacent liquid molecules. The movement of nanoparticles produces a massive but localized migration of the liquid molecules which are near the nanoparticle. Prasher et al. [43] claimed that heat is effectively transferred through this induced convection

vi) Thermophoresis or Soret effect in nanoparticles

The thermophoresis effect refers to the motion of dispersed particles in a liquid produced by a temperature gradient [43,58]. It results in a perturbation of the natural Brownian motion of the NP [59]. The molecules and particles located in the hot side have higher-energy; hence, they hit the surrounding particles with a higher momentum. They are responsible for the migration of the particles to the cold side [60]. Thus, this motion phenomenon can favor the heat transport and, consequently, enhance the thermal conductivity.

vii) Heat conduction in the liquid and in the solid-liquid interface

Microscopic collisions of particles are partly responsible for the heat transfer in a material. Such particles include: nanoparticles, molecules or atoms which, as a result of the collision give rise to the propagation of phonons and/or electrons. These collisions can explain the heat transfer between solid-solid (NP-NP) and solid-liquid [43] as well as liquid-liquid [29]. Keblinski et al. showed that energy transport due to Brownian diffusion is two orders of magnitude smaller than energy transport due to conduction in the liquid [29]. Prasher et al. proposed a model to predict the thermal conductivity in nanofluids and took into consideration the conduction through particles and in the liquid-NP interface [43].

2.1.3 Other mechanisms

viii) The nature of heat transport across the nanomaterial

It has been suggested that the nature of heat transport across the nanomaterial has a significant impact on the effective thermal conductivity of the nanofluid. Keblinski et al. [29] demonstrated that phonons move ballistically across nanoparticles with sizes in the order of 10 nm, instead of diffusively. However, whether ballistic or diffusive, they claim that the temperature within the solid particle will remain constant, and will result in a similar thermal resistance in the interface. This information reduces the chances of considering the nature of heat transport across the nanomaterial as the main responsible mechanism of thermal enhancement.

ix) Modification of the thermal transport in nanofluids: non-Fourier heat conduction

Wang and Wei [61] proposed that the presence of nanoparticles modifies the heat transport in the material by shifting from the Fourier heat conduction (typical in a fluid) into the dual-phase-lagging heat conduction in the nanofluid, at the macroscale. In this model, the heat equation is decoupled in two for the liquid and particle phases, where the Fourier law is satisfied separately. The relationship between these phases is given by continuity condition of temperature and heat flux at each interface. Under these assumptions, the coupled conduction between phases gives rise to thermal waves and resonances in the nanofluid. They claim that these waves and resonances are responsible for the enhancement of the thermal conductivity.

2.2 Simulations of nanofluids systems: computational approaches

Theoretical studies on nanofluids are fundamental for the understanding of the system NP-fluid in the nano and macro scales. A number of simulations tools have been used to predict the nanofluids properties. However, many of these models oversimplify the problem by neglecting important data such as: nanoparticle agglomeration or surface chemistry of the nanoparticle.

Recently, Cardellini et al. [62] proposed a multi-scale approach for modeling systems of nanofluids. Previous authors have been using the classical Derjaguin, Landau, Verwey and Overbeek (DLVO) theory, which is applied to model aqueous dispersions and describes the force between NPs in a liquid medium and the level of aggregation. Despite

the introduction of some changes in the initial theory by some authors, it still fails to give a good description of colloidal interactions at long-distances. Cardellini et al. summarized that classical DLVO or adaptations used so far neglect …"hydration effects, solvent polarization, NP surface phenomena and the finite size of ions"… [62]. Their new model is able to predict aggregation timescale, self-assembly and the formation of nanoparticles networks in aqueous media, by molecular dynamics (MD) and stochastic dynamics (SD) simulations. They conclude that the model can predict the dispersion stability and the overall macroscopic properties [62].

2.3 Recent research on graphene-based nanofluids

The research of graphene nanofluids from 2017 to present has focused mainly on the development of suitable materials for applications related to heat dissipation [63,64] and solar-energy conversion [65–67].

Graphene in the form of nanoplatelets (GNP) [38,63,64,66] is the most common dispersed material under study, but also nanocomposites are receiving great attention, such as graphene oxide/gold or graphene-embedded Sn-SiO_2-Ag core-shell nanoparticles [65,67].

The fundamental research interest was put on the thermal performance of the nanofluids. Thermal conductivity continues to be the most relevant property to analyse [38,66–68]. Iranmanesh et al. achieved an enhancement of the thermal conductivity of 27.6% for GNP-distilled water nanofluid [66]. Similarly, Fan et al. measured an enhancement of 16 % for 0.3 g/L graphene-embedded Sn-SiO_2-Ag nanofluid at 50 ºC [67]. In comparison, our studies show an enhancement of thermal conductivity of up to 48% for 0.18 wt% graphene in N,N-dimethylacetamide at 25 ºC [49].

In this period of time, and despite the appearance of new relevant data, very few authors have attempted to give an explanation on the enhancement of thermal transport in graphene nanofluids [38,49].

2.4 Challenges of nanofluids

Physical-chemical properties of nanofluids are very important data to assess the suitability of the material for industrial applications. In order to avoid problems in the pipelines or tanks, such as clogging, wall-covering or elevated pressure in the system, the nanofluid should exhibit low viscosity, long-term dispersion stability and low vapor pressure, among other characteristics, depending on the final application. In the particular case of thermal

transport, the dispersion of nanoparticles is responsible for the enhanced thermal properties of the fluid. Hence, the type of agglomeration that leads to the precipitation of nanoparticles must be avoided to preserve the original properties of the material.

2.4.1 Long-term stability

The main challenge in the preparation of nanofluids is to culminate the process with a homogeneous and stable material. Intermolecular forces, such as Van der Waals interactions, determine the stability of the dispersion. Very often, attractive forces between nanoparticles are strong enough to cause agglomeration. This clustering may appear immediately or after some time and will also depend on the storage conditions of the material. However, as mentioned above, the properties of the material will change to a greater or lesser extent as a function of nanoparticle precipitation. There are a number of strategies to avoid agglomeration, e.g.: chemical or physical modification of the surface of the nanoparticle, addition of surfactants or careful selection of the nanoparticle and fluid, as well as trial and error experiments. Furthermore, techniques such as bath or high-energy-probe ultrasonication are often used to force nanoparticles to disperse or to redisperse after precipitation. This procedure is sometimes successful for a short time. In other cases, the effect is longer-lasting due to the breaking of agglomerates [69] or the nanomaterial during sonication, as in the case of laminar exfoliation [70]. In conclusion, ultrasonic methods can produce lighter dispersible material as well as functionalized nanoparticles on the surface. The latter may favor the interaction between NP and liquid molecules. However, in some cases, ultra-sonication can produce the degradation of the liquid molecules, as in the case of N-Methyl-2-pyrrolidone [71]. Hence, contaminants are generated and may, as a result, have an influence on the heat performance of the fluid or nanofluid.

Among the aforementioned strategies, the addition of surfactants is also a very common practice. Well-accepted dispersants for this application are sodium dodecyl sulfate (SDS) or sodium dodecyl benzoic sulfate (SDBS) [72–74], among others. They are amphiphilic organic compounds able to form micelles in polar solvents and capture/coat non-polar nanoparticles. Micelle-formation prevents agglomeration of nanoparticles. However, the addition of surfactants has several disadvantages: i) they are organic compounds and have low thermal stability: they cannot be used in high-temperature applications; ii) several studies demonstrate the negative effect of surfactants on the thermal properties of the

pure nanofluid (nanoparticle & fluid) [74] and iii) the dispersibility effect depends on pH, temperature, etc., therefore, the presence of surfactant makes the material more vulnerable to change.

Functionalization of the nanomaterial is another feasible approach [33,75]. It slightly complicates the nanofluid preparation; although, it takes into account the possible interactions solid-fluid. It can be a winner-strategy, although the dispersibility of a material in a fluid not only depends on attractive-repulsive forces but particle size and morphology, NP-NP attractive forces, temperature, etc. Chemical functionalization may present other disadvantages such as: i) contamination of the nanofluid due to remains of the reactant (higher probability in the one-step method); ii) reduction of the thermal conductivity in the nanofluid due to the presence of functional groups [76].

Different techniques have been used to study dispersion stability. These are the most commonly utilized: Dynamic light scattering (DLS), UV-visible spectroscopy, transmission electron microscopy (TEM) and 3-ω technique. However, the evaluation of the long-term stability of a dispersion at high-temperatures (>100 ºC) is still challenging.

2.4.2 Viscosity

In general, the rheological studies on nanofluids show a critical increment of the viscosity with increasing nanoparticle concentration [77,78]. This phenomenon has been attributed to the increasing interaction NP-NP, NP-agglomerate and agglomerate-agglomerate [77]. This, in turn, can increase the frictional force between layers of the liquid, and hence the viscosity. Other researchers have associated this enhancement with the tendency of the nanoparticles to agglomerate under pressure (during the rheological test). The agglomerates raise the internal shear stress and the resistance to flow in the NF, which leads to an increase in viscosity during measurement. To conclude, the viscosity of the resulting nanofluid will depend on the viscosity of the pristine fluid, the shape and size of nanoparticles, concentration, intermolecular forces and temperature. It is important to bear in mind that for example, a 50% increase in the viscosity of the nanofluid compared to the bare fluid can still be an acceptable value for certain applications.

2.5 Results: The effect of graphene on the thermal properties of the fluid. A multi-scale study

As discussed above, the dispersion of nanomaterials can exert a strong effect on the thermal properties of the fluid. In articles 1 and 2, three types of graphene-based nanofluids were investigated in detail to shed some understanding on the phenomenon behind the improvement of the thermal properties in the fluids.

The first objective of the research was to prepare very stable dispersions so as not to rely upon time as a determining factor and hence, guarantee solid results in the characterization of materials.

Graphene was selected as the additive material due to its excellent thermal conductivity (above 2000 W m^{-1} K^{-1}) [79] .The solvents, N,N-dimethylacetamide (DMAc), N,N-dimethylformamide (DMF) and N-Methyl-2-pyrrolidone (NMP) were used to prepare graphene NFs because they form highly stable graphene dispersions. Moreover, these fluids possess a higher boiling point than most coolants, e.g. water.

The nanofluids were completely characterized. Thermal and chemical-physical properties were evaluated as a function of graphene concentration, i.e. thermal conductivity, specific heat, viscosity, sound velocity and vibrational spectra, etc. In addition, density functional theory (DFT) and molecular dynamics (MD) simulations were carried out to gather information on the interaction between graphene and the solvent molecules, as well as to evaluate the role of some of the heat transfer mechanisms suggested in the literature.

2.5.1 Materials and methods

i) Graphene and nanofluids preparation

Graphene flakes with lateral sizes ~ 150-450 nm and thicknesses from 1 to 10 layers were prepared from graphite (Sigma-Aldrich, purity > 99+% and size < 20 um) by a mechanical exfoliation method, similar to that used by Hermann et al. [80]. Thus, 0.4 g of graphite were ball-milled in a 100mL stainless steel jar with zirconia beads (5- and 12-mm diameter) in a high-energy planetary ball mill (All-direction planetary ball mill 0.4L, model CIT-XBM4X-V0.4L, Columbia International) at 378 rpm for 64 hours. From the resulting material, graphene nanofluids were prepared as follows. Graphene NFs were prepared based on DMAc (ACROS Organics, 99+ %) with concentrations ranging from 0.01-0.27 wt.%, DMF (Scharlau, HPLC grade) with concentrations ranging from 0.01-0.12 wt.% and

NMP (Sigma Aldrich, 99.5%) with concentrations ranging from 0.005-0.05 wt.%. The preparation of the nanofluids consisted of direct mixing of the base fluid with graphene flakes. To suppress particle clustering and obtain stable dispersions, graphene was dispersed in the fluid using a high energy- planetary ball mill. Graphene and the solvent were mixed in a proportion of 1:31 in weight and ball milled for 1 h, employing 5- and 12-mm diameter zirconia beads and 100 mL stainless steel jars. The ball to powder weight ratio used was 16:1 and the rotating speed of the jars was 378 rpm. Soft ultrasonic vibration, 1000 W (Ovan, model ATM40-6LCD) was then applied for 1h. After this procedure, the samples were centrifuged at 6000 rpm for one hour to ensure the stability of the nanofluids (Digicen 21 centrifuge, Orto alresa).

ii) Methods

The stability of the dispersions was analyzed as a function of time using a dynamic light scattering system (ZetaSizer nano ZS, ZEN3600, Malvern Instruments, Ltd. Malvern). The photon count rate, the hydrodynamic diameter and the polydispersity index (PdI) of the nanofluids were periodically analyzed (over a period of 4 months). The PdI describes how broad the size distribution is within the sample. The values of PdI range from 0.05 to 0.7. The smaller the value of PdI, the more monodisperse is the sample. An attenuator index of 7 was applied to the laser and the quartz cuvette was placed in a measurement position of 4.65 mm, every time.

The sound velocity was determined from the Brillouin frequency shift measured for different graphene concentrations contained in a transparent quartz cuvette. A diode laser with wavelength λ_0 = 532 nm was focused with a 10x microscope objective, and the Brillouin spectra was recorded on a JRS Tandem Fabry-Pérot TFP-1 interferometer in the backscattering configuration. The laser power was kept as low as possible (~ 2 mW) to avoid any possible heating effect from the laser.

The Raman spectra were recorded by T64000 Raman spectrometer manufactured by HORIBA Jobin Yvon. It was used in single grating mode with a spectral resolution better than 0.4 cm^{-1}. The liquid was placed in a transparent quartz cuvette. All the Raman measurements were carried out by focusing a diode laser (λ_0 = 532 nm) with 50x long working distance microscope objective. The power of the laser was kept as low as possible (~ 2 mW) to avoid any possible effect from self-heating. The reproducibility of the Raman setup was verified by measuring 30 times the same sample. From the numerical fit

of the Raman peak, the variation of the peak position was found to be ~0.06 cm^{-1} (standard deviation) within a range of 0.25 cm^{-1} (maximum and minimum peak deviation).

The three-omega (3ω) method has been mainly used to measure the thermal conductivity of solid materials [81,82]. In this work, we designed a modified version of the common 3ω cell. The idea was to make it suitable for the analysis of liquids. The design was based on the works of Chen et al. [83], Oh et al. [84] and Lubner et al. [85] .Our 3ω cell is shown in **Figure 5**. The liquid is placed on the 3 ω-heater which has been previously passivated with 200 nm of SiO_x (by plasma enhanced chemical vapor deposition) to avoid the leakage of current from the resistor to the conductive fluid. A 100 nm thick 3 ω-strip (5 nm of chromium and 95 nm of gold) was patterned on a 0.5 mm thick quartz substrate by photolithography and electron beam physical vapor deposition (EBPVD). The width of the heating line is defined as 2b = 10 um and the length as l = 1 mm, where 'l' is the distance between the voltage (inner) pads. Then, a 3 mm thick PDMS block is used to seal the circuit and to contain the liquid. An extended explanation of the method applied can be found in the supporting information of the article 1.

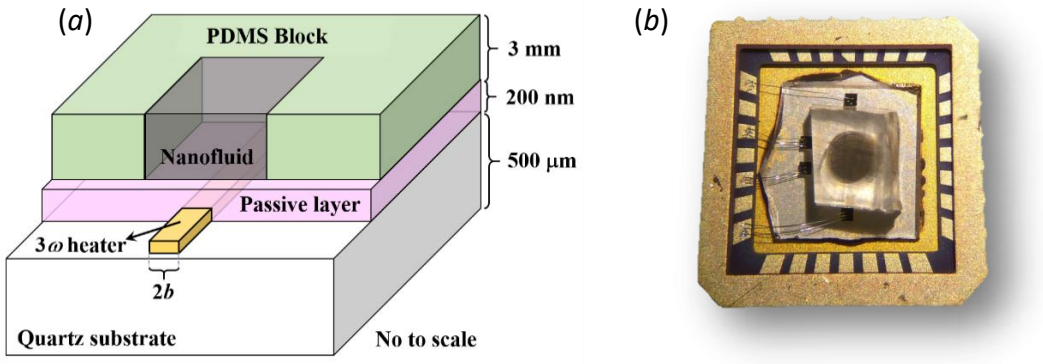

Figure 5 3ω cell for fluid samples: (a) Schematic representation (b) Top view photograph of the actual cell.

The same 3ω cell was used to measure other samples, from well-known liquids, e.g. water, ethylene glycol and ethanol, to edible oils and polymers. In all cases, the results were highly reproducible, as can be seen in **Table 1.** The information in **Table 1** was included in a manuscript led by A. Sachat et al. that was recently submitted to a journal (2019).

Table 1 Thermal conductivity for three polymers: PS, PEO and PS-PEO measured several times using the three-omega method. Data taken from submitted manuscript from Sachat et al. (2019).

	Samples					
	PS (W $m^{-1} K^{-1}$)		PEO (W $m^{-1} K^{-1}$)		PS-PEO (W $m^{-1} K^{-1}$)	
Run	*k*	error	*k*	error	*k*	error
1	0.199	0.0056	0.304	0.034	0.180	0.0075
2	0.197	0.0053	0.299	0.035	0.216	0.0034
3	0.198	0.0056	0.302	0.035	0.214	0.0031
4	0.197	0.0054	0.299	0.035	0.206	0.0030
5	0.197	0.0060	0.305	0.034	0.220	0.0039
6	-	-	-	-	0.191	0.0023
Mean & standard deviation	0.197	0.0012	0.302	0.003	0.204	0.0157

The specific heat (Cp) was measured by using differential scanning calorimetry (DSC) on a PerkinElmer DSC 8000. The difference in heat flow between an empty pan (standard aluminum pan) and the sample (inside the same pan) is recorded as a function of temperature. The conditions used for the measurement are described as follows: from 5-20 ºC at 2 ºC/min, adding two 10-minutes isotherms at the beginning and at end of the measurement. Platinum was used as a standard and analyzed by DSC in order to corroborate the proper operation of the equipment. The specific heat capacity of our samples was corrected by a factor of 1.13, obtained from the Pt measurements, in accordance with the standard procedure for DSC analysis.

The effective viscosity of the nanofluids was measured using a Haake RheoStress RS600 rheometer from Thermo Electron Corp. at T = 20-21 ºC. The shear rate used was 2880 s^{-1} with a measurement time of 30 seconds.

2.5.2 Long-term stability: Surfactant-free nanofluids

As mentioned in **section 2.4**, the preparation of stable dispersions is a challenging task. Graphene was selected as the additive material due to its exceptional thermal conductivity and lightness. This 2D material forms stable dispersions in DMF, DMAc and NMP without the aid of surfactants. Dynamic light scattering (DLS) technique was used to determine the stability of the dispersions over months. The samples were analyzed periodically to register the number of photons scattered by the sample. **Table 2** shows the DLS data from a graphene-DMAc nanofluid. The photon count rate was kept practically constant for four

months. And both, the hydrodynamic diameter and the polydispersity index remained unchanged as well.

The simplicity of these nanofluids makes them perfect candidates to be modeled. The absence of an additional component, such as a surfactant, facilitates the study of heat transfer phenomena in nanofluids.

Table 2 DLS data from a graphene-nanofluid sample based on DMAc

Features / Time	Day 1	After 2 months	After 3 months	After 4 months
Hydrodynamic diameter (nm)	187 ± 9	184 ± 4	174 ± 6	179 ± 5
Photon count rate (kcps)	310 ± 2	334 ± 3	336 ± 2	333 ± 2
Polydispersity index	0.120 ± 0.031	0.111 ± 0.008	0.123 ± 0.018	0.102 ± 0.014

2.5.3 Thermal and physical-chemical characterization of graphene-amides nanofluids

i) Thermal conductivity, specific heat and viscosity

The thermal conductivity (*k*) of graphene-DMAc, graphene-DMF and graphene-NMP nanofluids was determined using the 3-ω technique, as a function of graphene concentration. The **Table 3** shows the thermal conductivity for different graphene concentrations (C) in the nanofluids. A progressive enhancement of *k* was observed in DMAc and DMF-based nanofluids (NFs) as C increased, with a maximum enhancement of ~48% for C = 0.18 wt.% in DMAc-based NF as shown in **Figure 6a**. Concentrations between 0.01–0.05 wt.% in DMF and DMAc produced relatively large enhancements of *k* of ~6–25% and 3–17%, respectively. On the other hand, NMP nanofluids with concentrations of graphene in the same order showed no significant enhancement of *k*.

The thermal conductivity as a function of graphene concentration for two different temperatures, T = 298 K/25 ºC (green solid squares) and 324 K/51 ºC (light green solid circles), is shown in **Figure 6b**. As can be seen, the thermal conductivity of DMF-NFs tends to decrease as temperature increases, exhibiting the same temperature behavior as with common organic fluids [86].

Table 3 Thermal conductivity and viscosity of graphene-amide nanofluids

Concentration		Samples					
		DMAc		DMF		NMP	
mg/mL	wt.%	k (W m^{-1} K^{-1})	Viscosity (mPa·s)	k (W m^{-1} K^{-1})	Viscosity (mPa·s)	k (W m^{-1} K^{-1})	Viscosity (mPa·s)
0.00	0	0.175	1.19	0.183	0.94	0.235	2.07
0.05	0.005	-	-	-	-	0.234	2.19
0.10	0.01	0.180	1.17	0.194	0.99	0.236	2.21
0.25	0.03	0.196	1.18	0.203	1.01	-	-
0.50	0.05	0.206	1.26	0.228	1.08	0.213	2.92
1.13	0.12	-	-	-	1.26	-	-
1.50	0.18	0.259	1.68	-	-	-	-

As mentioned in **section 2.4**, viscosity is a very relevant property that limits the use of nanofluids in certain applications. The viscosity of DMAc, DMF and NMP sets of nanofluids was measured using a rheometer at 20 ºC. The **Table 3** shows the modification of the viscosity with increasing graphene concentration. The maximum increase in viscosity was ~41% for 0.05 wt.% graphene in NMP. It is important to mention that although the viscosity increases significantly as the concentration of graphene increases, the effective viscosity of the nanofluids can still be considered low.

An increase in viscosity as the nanoparticle concentrations rise has been frequently observed in graphene-based [87–92] and other NFs [89,90].

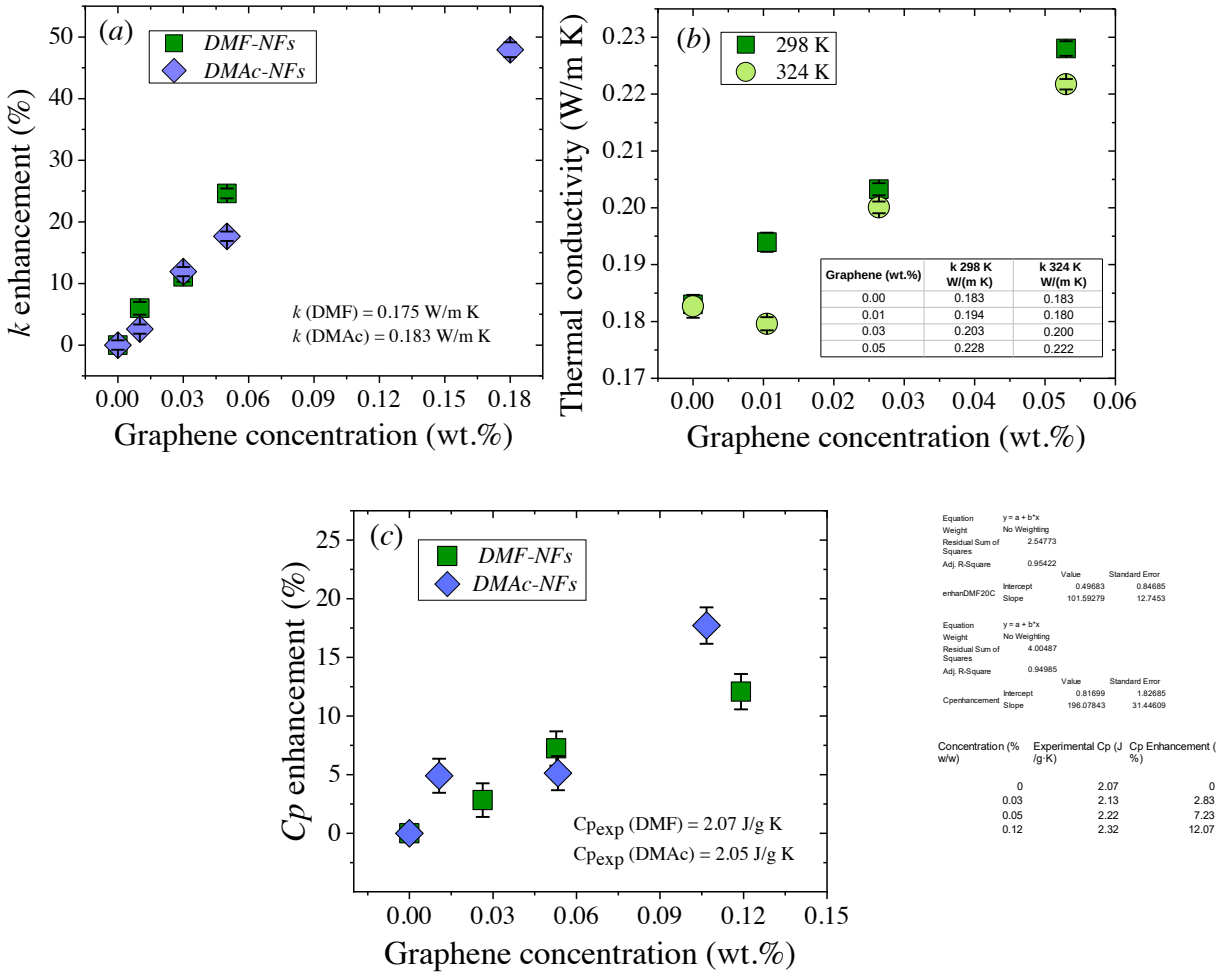

Figure 6 Thermal conductivity and specific heat of graphene-DMAc and graphene-DMF nanofluids: (a) thermal conductivity enhancement at room temperature (b) Thermal conductivity of DMF nanofluids as a function of graphene concentration at 298 K and 324 K and (c) heat capacity enhancement as a function of graphene concentration at 293 K. The figures were taken from article 1.

The heat capacity (Cp) was measured using differential scanning calorimetry (DSC). As can be seen in **Figure 6c**, the specific heat capacity was also affected by the presence of graphene, and shows an upward trend with increasing graphene concentration. The largest enhancement, 18%, was obtained with 0.11 wt.% of graphene in DMAc.

ii) Analysis of vibrational spectra: Raman and Brillouin light scattering

Raman spectroscopy analyses were performed to determine a possible modification of the intramolecular interactions in the solvent molecules induced by graphene. Several Raman bands of DMF and DMAc were found to shift in frequency with increasing graphene concentration. The corresponding vibrational modes are ascribed to vibrations of bonds related to the nitrogen atom. As can be seen in **Figure 7** and **Figure 8**, the shift is quite significant. It can be observed that the entire band is displaced, in all the affected vibrational modes. This means that all the molecules of the liquid are affected to a greater or lesser extent by the presence of graphene. This can be understood as a modification of the rigidity of some bonds in the solvent molecule, as higher energy is needed to make them vibrate.

Graphene-DMAc nanofluids

The Raman spectra of DMAc for different graphene concentrations and the corresponding peak positions as a function of concentration are displayed in **Figure 7a-c**. A clear blue-shift and a broadening of the Raman bands can be observed as the graphene concentration increases. The largest displacement was found to be ~4 cm^{-1} for a band around ~470 cm^{-1} (see **Figure 7b**). This band corresponds to a scissoring vibration from the bond (CH_3–N–CH_3) of the DMAc molecule [93]. The displacement of this and the other bands to higher frequencies in the presence of graphene is an indicator of a strong modification of interatomic forces within the nanofluid.

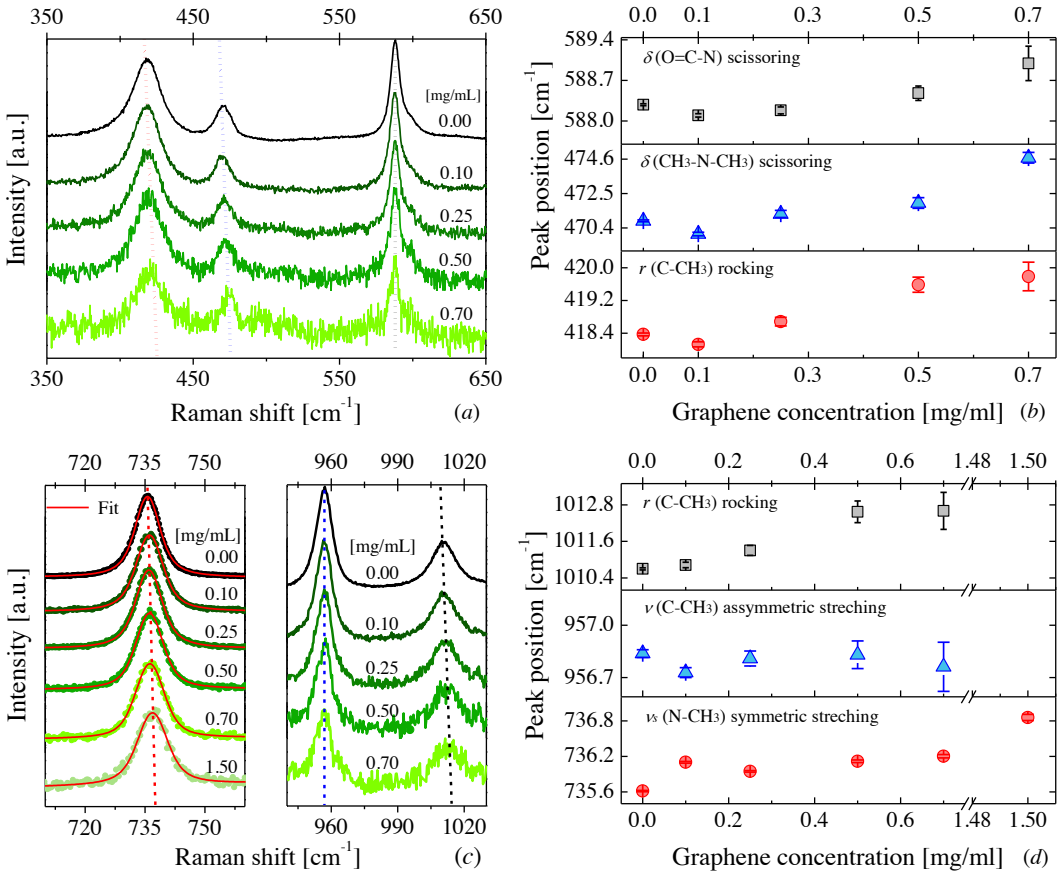

Figure 7 Raman scattering of DMAc-based NFs and peak positions of several Raman bands: (a) and (c) Raman spectra of DMAc-based NFs for different graphene concentrations, (b) and (d) peak positions of six Raman bands shown in (a) and (c) as a function of graphene concentration

Graphene-DMF nanofluids

A similar effect can also be observed in DMF-based nanofluids as displayed in **Figure 8b-d**. Here, the largest displacement ~4 cm^{-1} occurred for a rocking vibration of the bond (CH_3)–N of the DMF molecule [93].

The delocalization of π electrons in graphene seems to play an important role in the interaction (stacking) between layers. Similarly, the nitrogen, oxygen and carbonyl carbon atoms in both DMF and DMAc all have sp^2 hybridization, and hence p orbitals perpendicular to the O–C–N plane allow electron delocalization [94,95]. The parallel orientation of the DMF/DMAc molecules with respect to the graphene flakes can favor the overlap of two adjacent p-orbitals. It can favor a π-π bond between the solvent molecules

and the graphene surface. This interaction thus increases the rigidity of the internal bonds of the molecules closest to graphene and, consequently, modifies their Raman spectra.

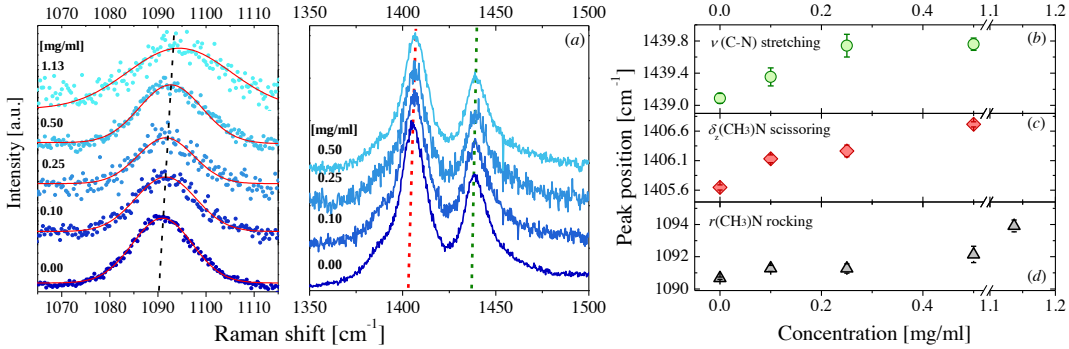

Figure 8 Raman scattering of DMF-based NFs and peak positions of several Raman bands: (a) Raman spectra of DMF-based NFs for different graphene concentrations, (b)–(d) peak positions of three Raman bands shown in (a) as a function of graphene concentration.

Graphene-NMP nanofluids

The case of NMP-based fluids is quite different, **Figure 9** shows the full Raman spectra of NMP-based NFs for three different graphene concentration of C = 0, 0.05 and 0.10 mg/mL (0, 0.005 and 0.01 wt.%). At first glance, a very small displacement of certain Raman modes can be detected (see **Figure 10**). However, the displacement is within the range of the spectral reproducibility of the equipment (~0.25 cm^{-1}) and within the error determination of each peak position. In conclusion, there is not a significant displacement of the Raman bands as the graphene concentration increases.

The Raman spectroscopy results from graphene-NMP NFs are not surprising if we consider the structure of the organic compound. N-methyl-2-pyrrolidone is a five-membered cyclic amide, and therefore, the bonds tend to be more rigid than those of amides having a linear structure. Consequently, it is conceivable that small amounts of graphene do not affect or modify the intramolecular vibrations of inner bonds in the solvent. Furthermore, Adams et al. [96] suggested that NMP molecules tend to spontaneously form dimers in the liquid state. NMP molecules strongly interact in pairs. Therefore, the impact of the presence of graphene flakes on the vibration of the bonds should be negligible. The findings of Adam et al. reinforce the idea that the solvent creates a natural barrier that prevents graphene from modifying the intramolecular interactions of

the solvent. Moreover, Basma et al. [97] reported that pure NMP has a well-developed intrinsic order compared to other solvents.

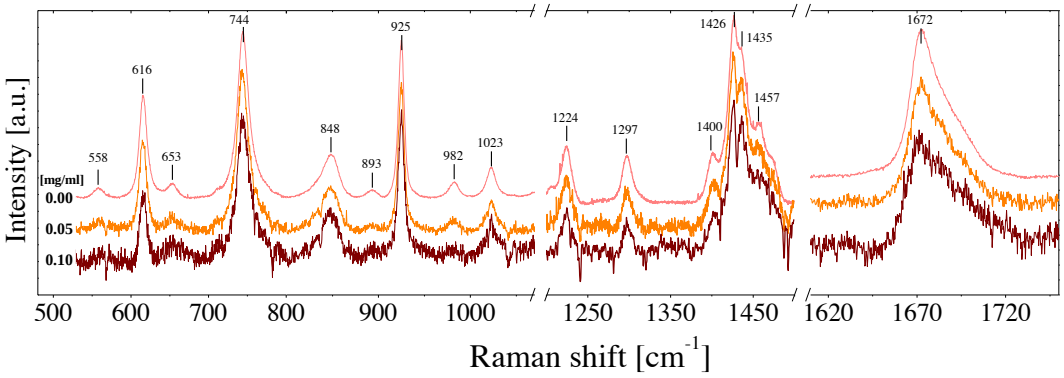

Figure 9 Raman spectra of NMP-based nanofluids for three different graphene concentrations

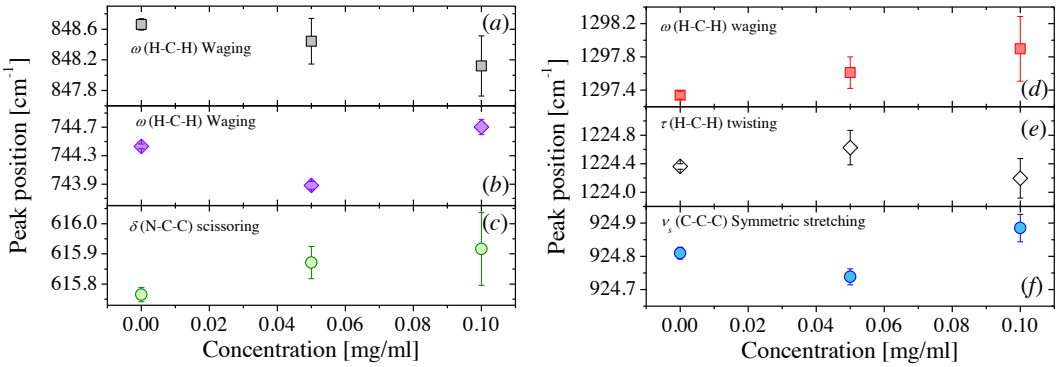

Figure 10(a)–(f) Peak positions of six Raman bands of NMP shown in Figure 3 as a function of graphene concentration.

The sound velocity in DMAc- and DMF-NFs was determined from Brillouin light scattering (BLS) measurements. BLS is a well-established technique to measure the sound velocities in solids, liquids and gases [98–100]. It probes the light frequency shift resulting from inelastic light scattering by thermally populated acoustic waves (sound waves) in the medium. In the backscattering configuration, the Brillouin shift is related to the frequency of the scattering of acoustic wave through the following expression [101]:

$$f = \frac{v_s}{\lambda_s} = \frac{2nv_s}{\lambda_0}, \quad (1)$$

where f is the Brillouin frequency, v_s and λ_s are the velocity and the wavelength of the acoustic wave, respectively, λ_0 is the laser wavelength (λ_0 = 532 nm), and n is the refractive index of the medium. The refractive index of the nanofluids was determined

using the knife edge method [102]. The refractive indexes remained constant as a function of graphene concentration. A schematic representation of the setup used and a graph with the refractive index values are included in the supporting information of article 1. To calculate the sound velocity, an average of the refractive indexes for the fluids was used, n = 1.44 and n = 1.43, for DMF and DMAc, respectively, which are in good agreement with the values in the literature [103]. A small shift in the frequency as a function of graphene concentration can be observed in **Figure 11**, which is consistent with a concentration dependence of the sound velocity shown in **Figure 12**.

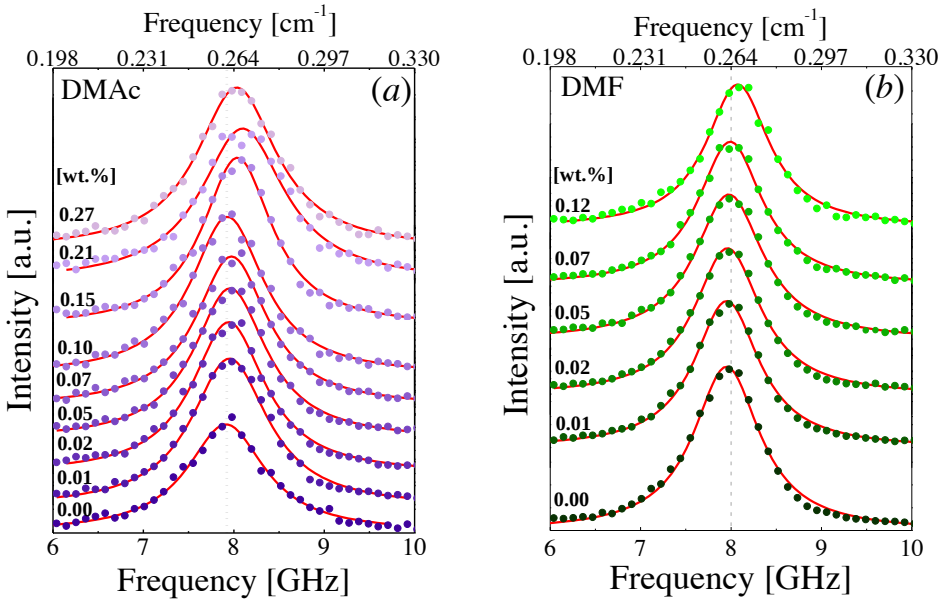

Figure 11 Brillouin spectra of DMAc (a) and DMF (b) NFs with different concentrations of graphene.

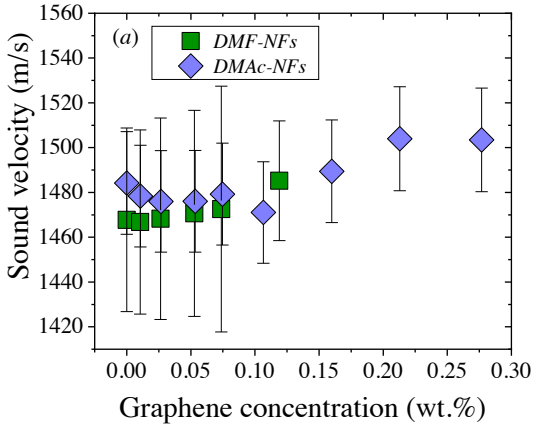

Figure 12 Sound velocity of DMAc and DMF nanofluids as a function of graphene concentration. This Figure was taken from article 1.

These experimental findings finally connect the molecular and macroscopic world in nanofluids. At the end of this chapter, we will discuss and discard some of the heat transfer mechanisms proposed in the literature in the light of these results. However, we stop here to list some of the questions these findings have opened:

- How such small concentrations of graphene are able to affect all the molecules in the liquid?
- Why only some vibrational modes of certain bonds of DMF and DMAc are affected?
- If the intramolecular forces of the molecules of liquid are affected and graphene is the external force, the intermolecular interactions may be affected as well. How does this affect heat transfer in the nanofluid?
- What type of interaction exists between graphene and the molecules of liquid? Could that be a π-π interaction? (both have sp^2 hybridization and hence p available orbitals)
- Does graphene induce a certain order in the nearby liquid molecules?

2.5.4 Theoretical studies

An attempt was made to answer all the questions posed above. We decided to run DFT and MD simulations of a simple graphene-DMF system to better understand their interactions. These simulations revealed that there is a weak and attractive graphene-DMF interaction. In addition, it was discovered that graphene induces a parallel orientation of the closest molecules of liquid, as can be seen in **Figure 13**. These two results and the fact that both graphene and DMF/DMAc/NMP molecules have sp^2 hybridization, available p orbitals and electron delocalization, suggest that the interaction can be of the π-π type.

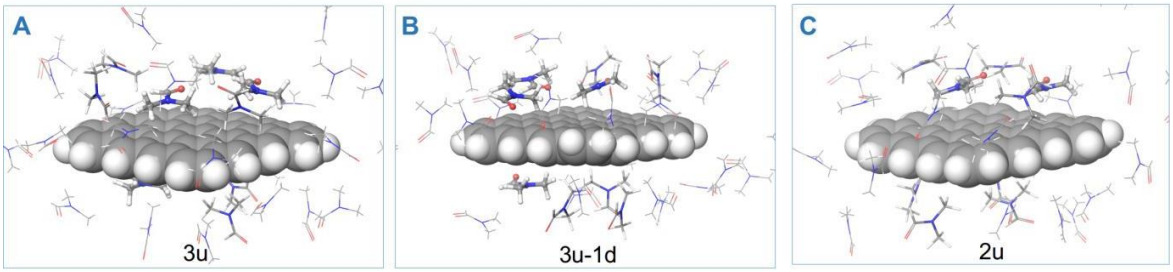

Figure 13 The three different SLG-DMF configurations with the highest occurrence: A (59.7%), B (17.6%) and C (8.1%).

We were interested in finding out if graphene was able to induce a local order in solvent molecules. A simulation of a graphene flake surrounded by 4350 DMF molecules was run and the results were analyzed. The nitrogen-nitrogen (N-N) pair-correlation function (PCF) of DMF was calculated as a function of graphene height. **Figure 14a** shows the contour plot of the N-N PCF as a function of graphene distance and N-N pair distances. This plot represents the relative density of nitrogen atoms around a central nitrogen atom as a function of its distance to graphene. In this particular case, the plot provides information about the distance between DMF molecules (N-N distance) in all possible parallel planes with respect to graphene. **Figure 14c** schematically illustrates the surroundings of a graphene flake, where layers of DMF at different distances from the graphene flake are represented. The scheme shows that in the nearest layers of DMF to the graphene flake (orange planes) DMF molecules are parallel oriented towards the graphene flake. A central molecule of DMF and its first, second and third neighbors are represented in the layers on top and above the graphene flake.

Three vertical cuts of the contour plot (**Figure 14a**) at 3.6, 8.1 and 25.5 Å distance from the graphene are displayed in **Figure 14b**. These representative cuts were selected based on the relative high density of DMF molecules at certain N-N distances as shown in **Figure 14a**. At a distance of 3.6 Å from the graphene flake, DMF molecules show a large degree of ordering, similar to that of a crystal where first (~ 6.5 Å), second (~ 11.6 Å) and third (~ 16.5 Å) neighbors can be identified (also called coordination shells). At least three layers of ordered DMF can be observed at 3.6, 8.1 and 13.5 Å from the graphene flake, which is remarkable considering that the flake radius is only 16.5 Å; hence, on larger flakes even longer-ranged ordering may be expected. The **Figure 14a** clearly shows that these three layers of DMF molecules have a higher density of DMF molecules at different N-N distances, although the effect is lost thereafter (see the supporting information of article 1 for further details). As the distance of DMF molecules from the graphene flake increases, the dynamic solid-like behavior of DMF is lost and it starts to behave as a normal liquid (just the first neighbors can be identified). Akıner et al. reported a similar nanolayer formation of water in the vicinity of hexagonal boron nitride [104].

As a conclusion, the special type of interaction, π-π, and the induced local order around graphene may contribute to the enhancement of the fluid's thermal properties.

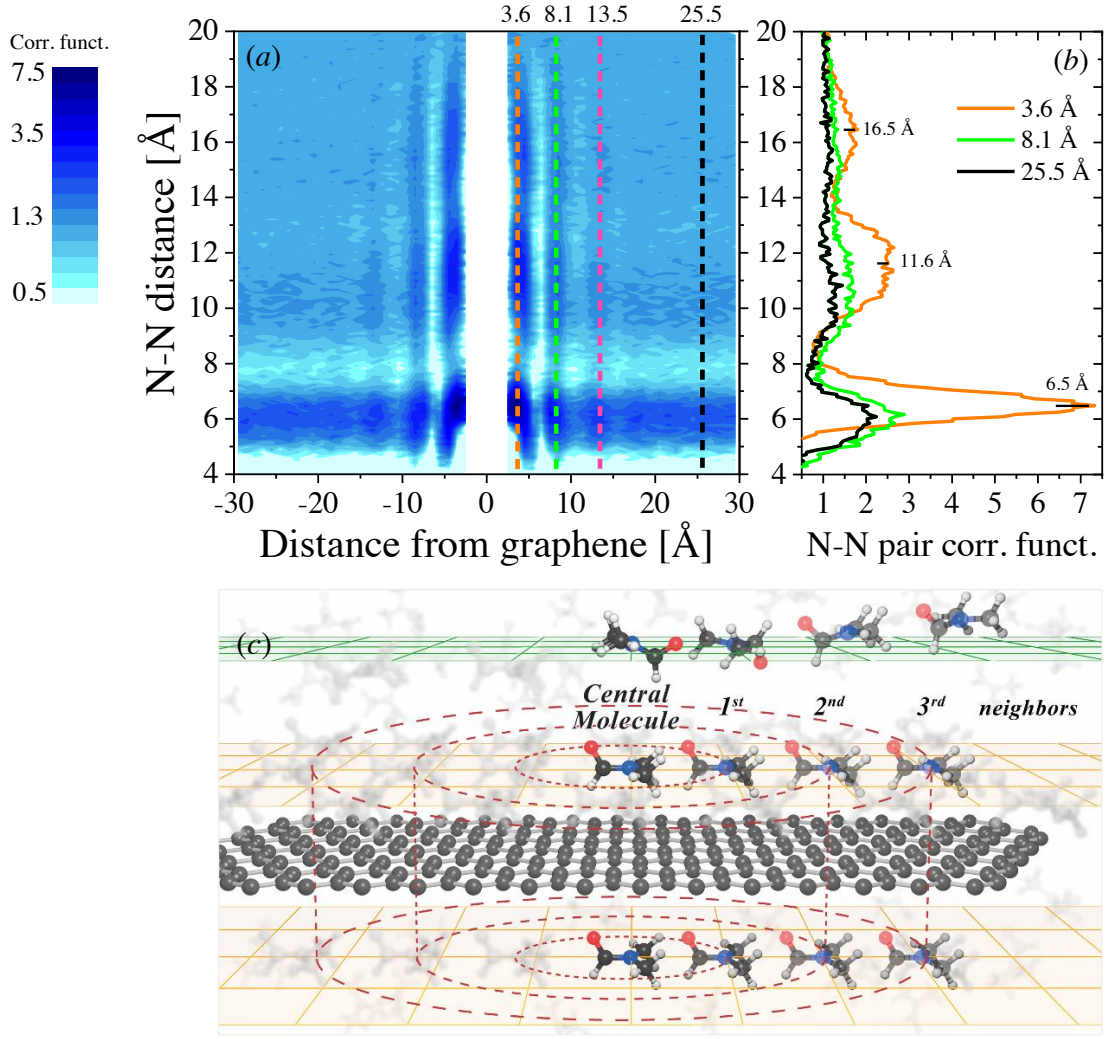

Figure 14 Calculated correlation function of nitrogen to nitrogen (N-N) distance from DMF molecules as a function of graphene distance, and an illustration (a) Contour plot of the N-N pair correlation function as function of graphene distance (b) N-N pair correlation function N-N pair distance. (c) Schematic representation of the surroundings of a graphene flake. These figures were taken from article 1.

2.5.5 The heat transfer mechanisms suggested in the literature discussed in the light of the results of thermally enhanced graphene-amide nanofluids

The NP **agglomeration** model (i) can explain the enhancement of *k* in unstable NFs. In these systems the thermal conductivity will depend on the degree of agglomeration and its dynamics, consequently, *k* will be time dependent [105].The formation of large aggregates, up to a certain size, can enhance *k* even further due to local percolation behavior. In our case, the DLS results showed a constant particle size and concentration over time. Additionally, the average graphene size observed using TEM is in good agreement with the DLS results, demonstrating that no agglomeration occurred (see the supporting information from article1). Moreover, a constant *k* was measured in different samples as a function of time (months), demonstrating that this mechanism cannot explain our results. To investigate the formation of layering and increased order in the DMF solvent near graphene, pair correlation distribution function of DMF was calculated as a function of graphene distance. A local order of DMF molecules was found around graphene, as mechanism (ii) (**solid-like structure of the liquid**) suggested. This local layering may impact on the effective thermal performance of the nanofluid.

Raman spectroscopy was used as a tool to determine the plausibility of applying theory (iii) to our nanofluids. If graphene induces a modification of the interatomic interactions in the fluid, the Raman spectrum should be affected. As can be seen in **Figure 7** and **Figure 8** several Raman modes shift to higher frequencies with increasing graphene concentration, especially those related to nitrogen. In all cases, the entire band is displaced, which means that all the molecules of the liquid are affected by the presence of graphene to a greater or lesser extent. This can be understood as a modification of the rigidity of some bonds in DMF and DMAc, as higher energy is needed to make them vibrate. This interpretation leads us to suggest that graphene somehow affects the interaction between the solvent molecules, resulting in a strong modification of the **interatomic potential** as a function of graphene concentration, as model (iii) suggests.

If we assume that the **Brownian motion** mechanisms (iv) and (v) are responsible for the enhancement of thermal conductivity in the fluids, when the temperature increases, it is well known that the overall speed of the particles will be higher and consequently *k* should also increase. However, as shown in **Figure 6b**, *k* decreases when the temperature increases, therefore such a mechanism does not explain our results. In addition, Keblinski

et al. [29] showed that the movement of nanoparticles, due to Brownian motion, is too slow to transport significant amounts of heat through a nanofluid, even in the case of extremely small particles. This conclusion is supported by molecular dynamics simulations [29]. Similarly, a localized convection caused by Brownian motion can also be discarded [106].

Additional research

2.5.6 Raman analysis as a function of time

In order to confirm the reproducibility of the measurements, Raman spectra of the three types of graphene nanofluids (DMAc, DMF and NMP- NFs) were recorded as a function of time for different concentrations of graphene. **Table 4** shows a summary of the set of measurements.

Table 4 Summary of the Raman measurements taken on different days over a period of time greater than one year

Sample name	Date (day No.)		
Graphene-DMAc NFs	2017/11/30 (day 1)	2017/12/22 (day 22)	2019/05/07 (day 524)
Graphene-NMP NFs	2018/02/05 (day 1)	2019/03/15 (day 404)	2019/05/08 (day 458)
Graphene-DMF NFs	2017/09/28 (day 1)	-	2019/05/08 (day 588)

Figure 15, Figure 16 and **Figure 17** show the Raman spectra of DMAc-, NMP- and DMF-based nanofluids for different graphene concentrations measured on different days, respectively. As can be seen, the Raman spectra do not change significantly as a function of time. We did not observe any modification and/or displacement of the Raman bands of the samples. Taking into account that the Raman spectra of nanofluids recorded after one year are practically identical to those performed on day 1, we can assure that the quality of the dispersion is maintained after more than one year. These results indicate the good quality and long-term stability of the samples.

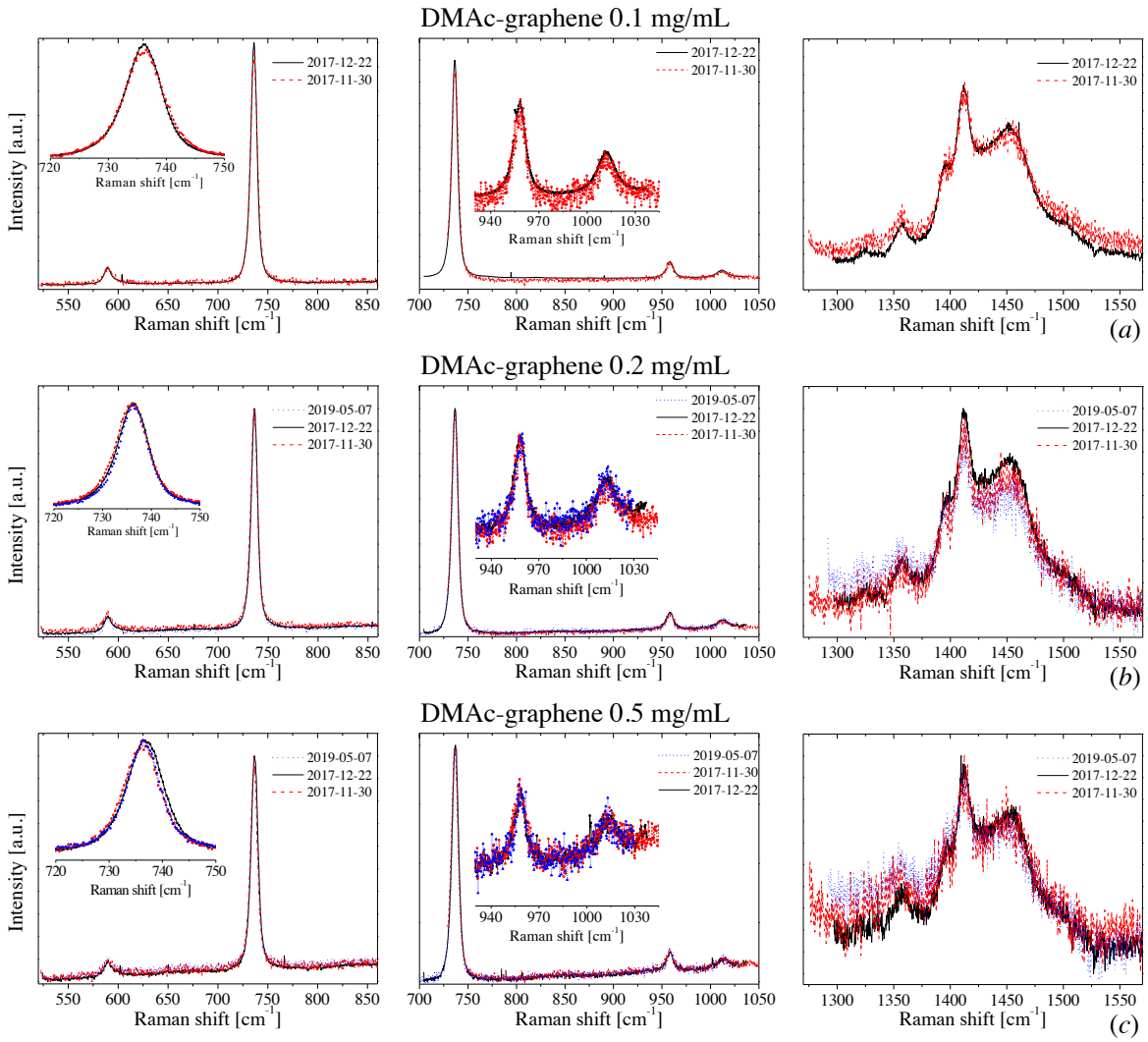

Figure 15 Raman spectra of graphene DMAc-NFs recorded on different dates as a function of graphene concentration: (a) 0.1 mg/mL, (b) 0.2 mg/mL and (c) 0.5 mg/mL

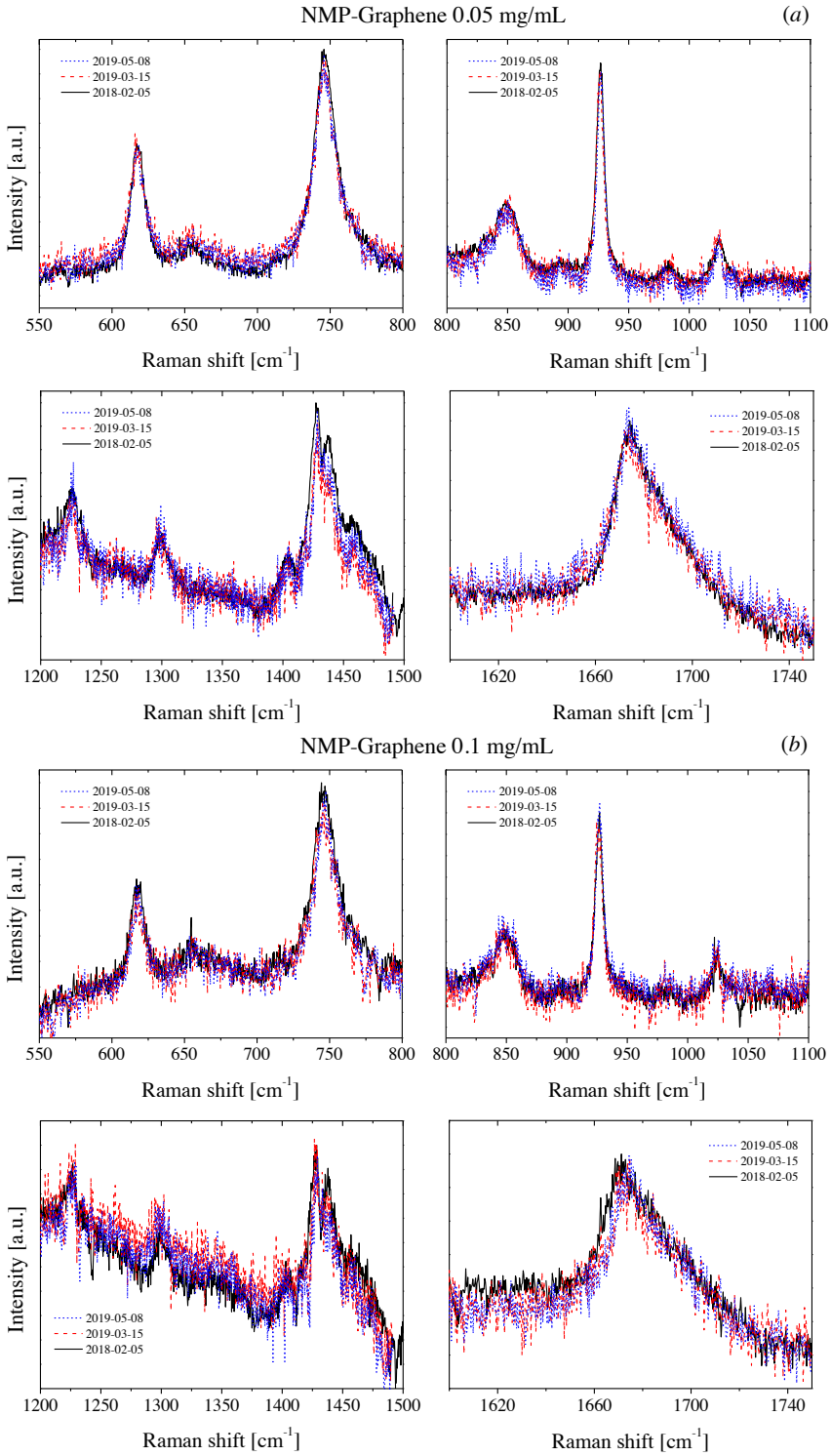

Figure 16 Raman spectra of NMP-NFs recorded on different dates as a function of graphene concentration: (a) 0.05 mg/mL and (b) 0.1 mg/mL.

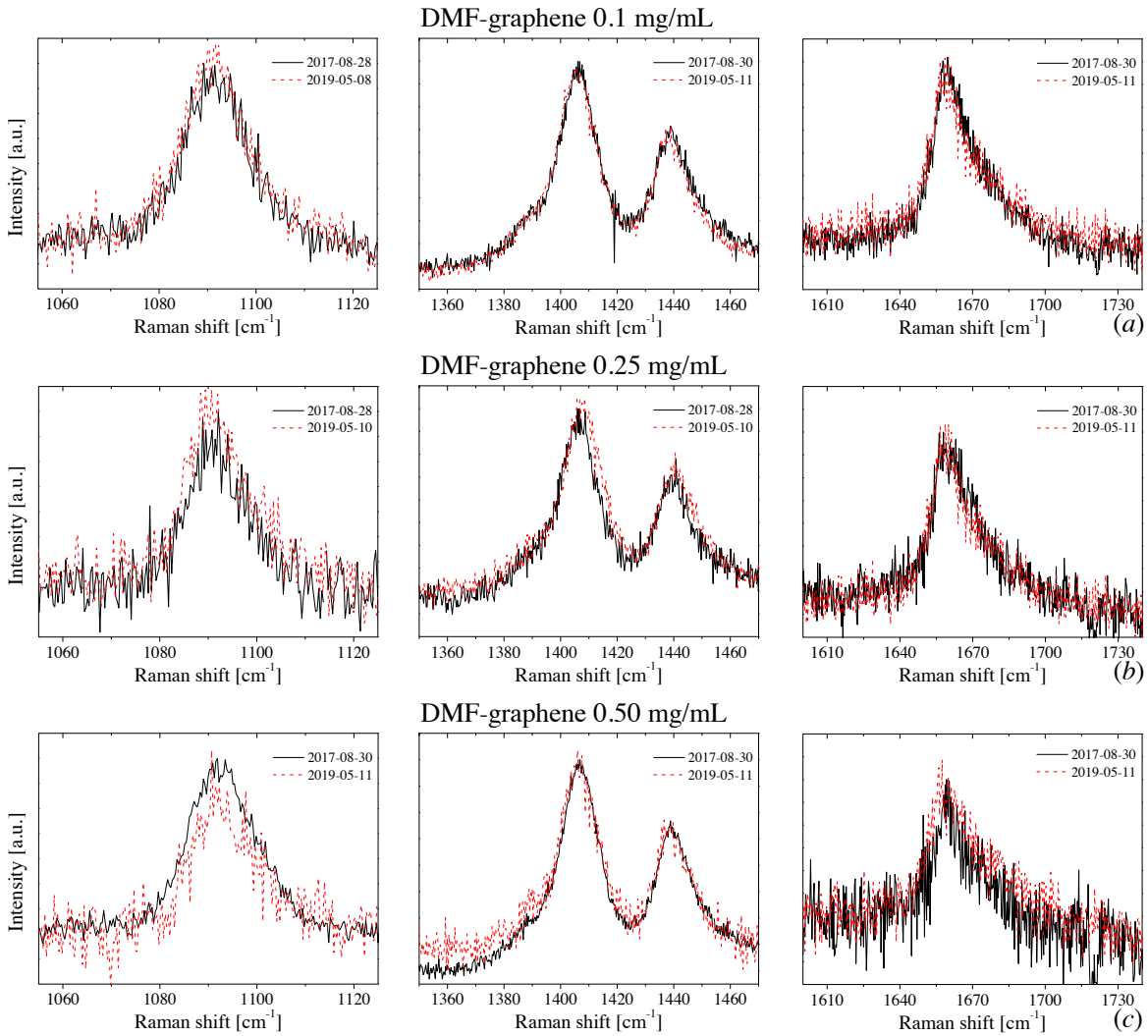

Figure 17 Raman spectra of DMF-based nanofluids recorded on different dates as a function of graphene concentration: (a) 0.10 mg/mL, (b) 0.25 mg/mL and (b) 0.50 mg/mL.

2.6 Summary and conclusions

Highly stable graphene dispersions in DMAc and DMF with enhanced thermal properties were prepared. The influence of graphene concentration on thermal conductivity, specific heat capacity, viscosity and speed of sound was measured showing an enhancement of all these properties with increasing graphene concentration. The main achievements are summarized as follows:

i. We measured a 48% enhancement in the thermal conductivity of 0.18% DMAc-based nanofluid, demonstrating that only a small amount of dispersed graphene is required to induce a large enhancement of the overall thermal properties compared with the base fluid.

ii. An 18% of improvement in specific heat capacity was measured in 0.11 wt% of graphene in DMAc-based NF.

iii. Raman measurements indicated that the intramolecular interactions in DMF and DMAc molecules are modified when graphene is present, affecting the whole liquid.

iv. The theoretical studies (DFT and MD simulations) suggested that the interaction between graphene and the nearest DMF molecules is stronger than initially thought. These molecules tend to lay parallel to the graphene flake favoring a possible π–π stacking. A local order of the DMF molecules up to three layers was also observed in the simulations.

v. Although no simulations were performed on the system of graphene-DMAc, the Raman measurements showed similar displacements to those of the system graphene-DMF. These findings, together with the similarities between DMF and DMAc molecules, suggest that the same mechanism can be behind the Raman displacement of DMAc-based nanofluids.

In order to evaluate if this behavior was characteristic of other organic solvents, a set of highly stable graphene dispersions was prepared, with N-methyl-2-pyrrolidone (NMP) as the base fluid. NMP is an amide, such as DMAc and DMF; however is a cyclic compound, whereas DMAc and DMF have linear geometries. In this nanofluid, we studied the impact of different graphene concentrations on the thermal conductivity, viscosity and Raman spectra of NMP. Our observations can be summarized as follows:

i. We found that the thermal conductivity of NMP was not affected by concentrations of graphene in the order of those that do affect DMAc and DMF.

ii. Similarly, the Raman spectra of NMP as function of graphene concentration were also not affected.

iii. The Raman results of graphene-NMP nanofluids can be explained taking into account the geometry and structure of NMP. As it is a five-membered cyclic amide, the bonds tend to be more rigid than those of amides having a linear structure. Therefore, these concentrations of graphene or perhaps graphene itself might not be strong enough as external force to induce a modification of the intramolecular bonds of NMP. Furthermore, there are studies [96,97] showing that NMP tends to form dimers and have a well-developed intrinsic order in liquid state, which also hurdles the possible impact graphene can have on the fluid, speaking in vibrational terms.

Taking all the above into consideration, we can conclude that there is a clear correlation between the shift of some Raman modes to higher frequencies and the enhancement of heat transfer in the fluid. These results represent an excellent initial step toward understanding the manner in which NPs modify the fluid arrangement directly affecting thermal transport. NFs are commonly highly diluted systems; therefore, it is the properties of the NPs and fluid molecule atoms at the points of intermolecular contact which are important in assessing the type of interaction. It clearly depends on the nature of the NPs and fluid molecules. It is also important to remark that the interaction between graphene and the amides is the key factor explaining the high dispersibility of graphene in DMF, DMAc and NMP. Our results suggest that the presence of graphene produces important changes at the macroscopic level in organic base fluids, with the result that the dispersal of tiny concentrations of graphene produces a large improvement in the overall thermal properties of DMF and DMAc. This revealing finding demonstrates the applicability of these types of nanofluids as efficient, heat transfer materials.

Article 1

Nanoscale

PAPER

View Article Online
View Journal | View Issue

Cite this: *Nanoscale*, 2018, **10**, 15402

Mechanisms behind the enhancement of thermal properties of graphene nanofluids†

M. R. Rodríguez-Laguna, *[a,b] A. Castro-Alvarez, [c] M. Sledzinska, [a] J. Maire, [a] F. Costanzo, [a] B. Ensing, [a,d] M. Pruneda, [a] P. Ordejón, [a] C. M. Sotomayor Torres, [a,e] P. Gómez-Romero [a] and E. Chávez-Ángel *[a]

While the dispersion of nanomaterials is known to be effective in enhancing the thermal conductivity and specific heat capacity of fluids, the mechanisms behind this enhancement remain to be elucidated. Herein, we report on highly stable, surfactant-free graphene nanofluids, based on *N*,*N*-dimethylacetamide (DMAc) and *N*,*N*-dimethylformamide (DMF), with enhanced thermal properties. An increase of up to 48% in thermal conductivity and 18% in specific heat capacity was measured. The blue shift of several Raman bands with increasing graphene concentration in DMF indicates that there is a modification in the vibrational energy of the bonds associated with these modes, affecting all the molecules in the liquid. This result indicates that graphene has the ability to affect solvent molecules at long-range, in terms of vibrational energy. Density functional theory and molecular dynamics simulations were used to gather data on the interaction between graphene and solvent, and to investigate a possible order induced by graphene on the solvent. The simulations showed a parallel orientation of DMF towards graphene, favoring π–π stacking. Furthermore, a local order of DMF molecules around graphene was observed suggesting that both this special kind of interaction and the induced local order may contribute to the enhancement of the fluid's thermal properties.

Received 5th April 2018,
Accepted 12th July 2018

DOI: 10.1039/c8nr02762e

rsc.li/nanoscale

Introduction

Heat transfer fluids (HTFs) play an important role in a wide range of applications. Vehicles, microelectronics and industrial processes require the use of coolants to dissipate the heat produced and thus prevent overheating. However, the functionality of HTFs is not limited to this single role: heat transfer plays a key part in energy conversion applications and thermal storage.

Water, ethylene glycol, oils, *etc*. are widely used as HTFs,[1] but a major problem with these conventional coolants is the low heat exchange rate and thermal conductivity (k), typically between 0.06–0.6 W m^{-1} K^{-1}.[1] These values are not high enough to meet the coming needs and challenges of the industry, such as in the field of microelectronics, where temperature control has become crucial for an adequate and reliable performance of the electronic components. The high demand for HTFs with superior performance in terms of heat transfer efficiency has led to the development of a variety of novel nanofluid (NF) materials, formed by solid nanoparticles (NPs) dispersed in a base fluid. Numerous studies have revealed that the thermal properties of a fluid can be improved remarkably by the dispersion of nanoparticles, such as specific heat capacity and thermal conductivity,[2–9] and in the case of the latter by more than 20%.[5–11]

The enhancement of k has been commonly observed in NFs and there is still an ongoing debate to explain it. This work sheds some light on the possible causes of this enhancement. In previous studies, various mechanisms have been suggested to explain thermal conductivity enhancement, such as: (i) an increase in thermal transfer due to Brownian motion of nanoparticles;[12,13] (ii) localized convection created in the fluid due to Brownian motion of nanoparticles;[13–15] (iii) agglomeration of nanoparticles;[12,16,17] (iv) enhanced thermal energy transfer due to increased interatomic interactions arising from the interatomic potential;[15,18] (v) layer-like ordered liquid around the solid;[12] and (vi) ballistic phonon transport of heat through solid nanoparticles.[12]

[a]*Catalan Institute of Nanoscience and Nanotechnology (ICN2), CSIC and BIST, Campus UAB, Bellaterra, 08193 Barcelona, Spain. E-mail: rocio.rodriguez@icn2.cat, emigdio.chavez@icn2.cat*
[b]*Departament de Química, Universitat Autònoma de Barcelona, Cerdanyola del Vallès, 08193 Barcelona, Spain*
[c]*Organic Chemistry Section, Facultat de Química, Universitat de Barcelona, Av. Diagonal 645, 08028 Barcelona, Catalonia, Spain*
[d]*Van't Hoff Institute for Molecular Sciences, University of Amsterdam, 1098 XH Amsterdam, The Netherlands*
[e]*ICREA, Pg. Lluís Companys 23, 08010 Barcelona, Spain*
†Electronic supplementary information (ESI) available. See DOI: 10.1039/c8nr02762e

In this paper, all of these mechanisms are discussed and considered in the particular case of graphene–amide NFs. Herein, we report a simple NF system in which a surfactant free nanomaterial is dispersed in an organic fluid. This approach was chosen because the presence of a surfactant can result in additional complexity in modeling and interpreting the enhancement of the thermal properties.[19,20] Consequently, the experimental and theoretical data obtained from this book-example system can provide valuable information regarding the interaction between a nano-solid and the fluid molecules. This work also seeks to address how the presence of a small concentration of nanomaterial is capable of modifying the macro-properties of the fluid. The solvents, *N*,*N*-dimethylacetamide (DMAc) and *N*,*N*-dimethylformamide (DMF), were used to prepare graphene NFs because they form highly stable graphene dispersions. Moreover, these fluids possess a higher boiling point than most coolants, *e.g.* water. Graphene was selected as the additive material due to its extraordinary thermal conductivity (above 2000 W m^{-1} K^{-1}) and non-toxicity.[21,22] Furthermore, graphene-based nanofluids have also attracted great attention due to the wide range of fields they can be applied in, including liquid electrodes for energy storage and flexible electronics, among others.[23–26] We determined experimentally the influence of graphene concentration on thermal conductivity, heat capacity (C_p), sound velocity (v_s) and Raman spectra. Additionally, molecular dynamics (MD) and density functional theory (DFT) were used to study the interaction between graphene and amide molecules and a possible local order close to the graphene flake, as previously done with other nanofluid systems.[27] Our study provides considerable insight into the field of thermal transport in dynamic systems, such as liquids and NFs, thereby addressing a fundamental problem in NFs.

Results

Thermal conductivity and specific heat capacity studies

Thermal conductivity measurements of the DMAc and DMF graphene NFs were performed using the 3ω technique at 298 K and 324 K. In contrast to other techniques used for thermal conductivity characterization (*e.g.* hot transient wire), the three-omega method works in a very fast time window (10–200 Hz). Therefore, it mostly suppresses the interference from convection, for which the effect decreases with frequency.[28] Three concentrations of DMF nanofluids ranging from 0.01 to 0.05 wt% of graphene dispersed in DMF and four concentrations of graphene dispersed in DMAc nanofluids ranging from 0.01 to 0.18 wt% were measured along with the bare fluids. Hereafter, for convenience, sample names will be shortened by omitting 'wt% of graphene dispersed in', for example: 0.01 wt% of graphene dispersed in DMAc will henceforth be written as 0.01% DMAc. The thermal conductivity enhancement of the NFs at room temperature compared to the bare fluids is shown in Fig. 1a as a function of graphene concentration. A progressive and almost linear enhancement can be observed in both sets of NFs as a function of graphene concentration. The largest enhancement (~48%) was obtained with 0.18% DMAc NF. The thermal conductivity data are summarized in Tables S3 and S4 in the ESI.†

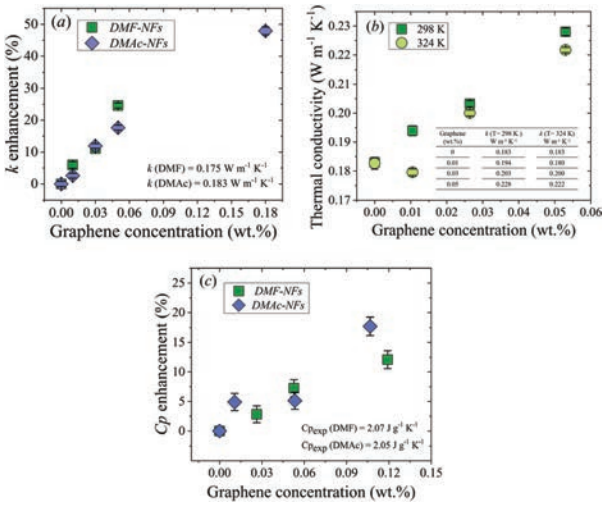

Fig. 1 Thermal conductivity and specific heat capacity of the DMF and DMAc nanofluids as a function of graphene concentration; (a) Room temperature thermal conductivity enhancement as a function of graphene concentration for DMF and DMAc-based nanofluids; (b) thermal conductivity of DMF nanofluids as a function of graphene concentration at 298 K and 324 K; (c) specific heat capacity enhancement as a function of graphene concentration for DMF and DMAc-based nanofluids at 293 K.

The thermal conductivity as a function of graphene concentration for two different temperatures, T = 298 K (green solid squares) and 324 K (light green solid circles), is shown in Fig. 1b. As can be seen, the thermal conductivity of DMF-NFs tends to decrease as temperature increases, exhibiting the same temperature behavior as with common organic fluids.[29]

The specific heat capacities (C_p) of the base fluids and graphene–DMAc and –DMF NFs were measured using differential scanning calorimetry (DSC) at 293 K. The study of the influence of graphene concentration on the specific heat capacity of the nanofluids was carried out using concentrations in the range of 0.01–0.12% for both DMAc and DMF.

The progressive enhancement of the specific heat capacity as a function of graphene concentration for DMAc and DMF-based fluids is shown in Fig. 1c. The largest enhancement (~18%) was obtained with 0.11% DMAc NF.

The viscosity of the NFs was also measured as a function of graphene concentration. A relevant increment of the viscosity was found on increasing graphene loadings (see the ESI†).

Analysis of vibrational spectra

Brillouin and Raman light scattering. The sound velocity in the NFs was determined from Brillouin light scattering (BLS) measurements. BLS is a well-established technique for measuring sound velocities in solids, liquids and gases.[30–32] It probes

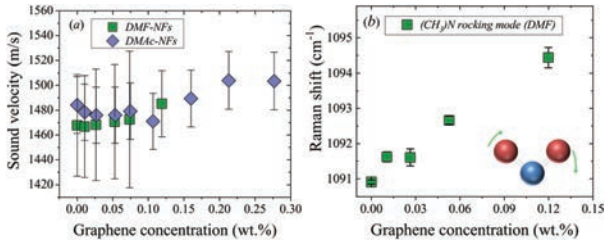

Fig. 2 Brillouin and Raman light scattering of NFs; (a) sound velocity as a function of graphene concentration for DMF and DMAc-based nanofluids measured at 298 K. (b) Shift of the 1090 cm^{-1} mode ascribed to the $(CH_3)N$ rocking mode (DMF) as a function of graphene concentration and a simple representation of the rocking mode.

the light frequency shift resulting from inelastic light scattering by thermally populated acoustic waves in the medium. In the backscattering configuration, the Brillouin shift is related to the frequency of the scattering acoustic wave through the following expression:[33]

$$f = \frac{v_s}{\lambda_s} = \frac{2nv_s}{\lambda_0}, \quad (1)$$

where f is the Brillouin frequency, v_s and λ_s are the velocity and the wavelength of the acoustic wave, respectively, λ_0 is the laser wavelength (λ_0 = 532 nm), and n is the refractive index of the medium. The refractive index of the nanofluids was determined using the knife edge method.[34] The refractive indexes remained constant as a function of graphene concentration. A schematic representation of the setup used and a graph with the refractive index values are included in the ESI.† To calculate the sound velocity, an average of the refractive indexes for the fluids was used, n = 1.44 and n = 1.43, for DMF and DMAc, respectively, which are in good agreement with the values in the literature.[35] A small shift in the frequency as a function of graphene concentration can be observed in Fig. S2 in the ESI,† which is consistent with a concentration dependence of the sound velocity shown in Fig. 2.

The Raman spectra of DMF NFs and the bare fluid were recorded, as shown in Fig. S4 in the ESI.† The peak position of the Raman mode at 1090 cm^{-1} is plotted in Fig. 2b as a function of graphene concentration. This band corresponds to an asymmetric bending vibration in a plane (rocking) of the bond '$(CH_3)N$' of the DMF molecule.[36] The Raman spectra at 1090 cm^{-1} at different concentrations of graphene show a continuous displacement to higher frequencies and a broadening of the mode with increasing graphene concentration (see Fig. S4 in the ESI†). Similarly, the band centered at 1438 cm^{-1}, ν(C–N) stretching, undergoes a shift to higher frequencies with increasing graphene concentration, as shown in Table 1.

Discussion

As the results show, the presence of graphene in the NFs impacts all the measured properties, *i.e.*, thermal conductivity,

Table 1 Experimental Raman frequencies of pure DMF and 0.05% DMF and calculated frequencies of a simple system (*A*) consisting of three molecules of DMF parallel to a graphene flake, obtained by DFT using the functionals: B3LYP/6-311G (p, d) and wB97X-D3/6-311G (p, d)

		Theoretical frequencies [cm^{-1}]			
Experimental frequencies [cm^{-1}]		B3LYP/6-311G(d, p)		ωB97X-D3/6-311G(d, p)	
DMF	0.05 wt%	DMF	*A*	DMF	*A*
1090.9	1092.6	1092.9	1096.3	1103.0	1108.5
1438.5	1439.8	1430.7	1443.7	1452.0	1448.2

specific heat capacity, sound velocity and vibrational Raman modes. The enhancement of k has been commonly observed in NFs and there is still an ongoing debate to explain it. Different mechanisms have been suggested, such as: (i) an increase in thermal transfer due to Brownian motion of nanoparticles;[12,13] (ii) localized convection created in the fluid due to Brownian motion of nanoparticles;[13–15] (iii) agglomeration of nanoparticles;[12,16] (iv) enhanced thermal energy transfer due to increased interatomic interactions arising from the interatomic potential;[15,18] (v) layer-like ordered liquid around the solid;[12] and (vi) ballistic phonon transport of heat through solid nanoparticles.[12]

Assuming that the Brownian motion mechanisms (i and ii) are correct, if the temperature increases, then the overall speed of the particles will be higher and consequently k should also increase. However, as shown in Fig. 1b, k decreases when the temperature increases, therefore such a mechanism does not explain our results. In addition, Keblinski *et al.*[12] showed that the movement of nanoparticles, due to Brownian motion, is too slow to transport significant amounts of heat through a nanofluid, even in the case of extremely small particles. This conclusion is supported by molecular dynamics simulations.[12] Similarly, a localized convection caused by Brownian motion can also be discarded.[13] The NP agglomeration model (iii) can explain the enhancement of k in unstable NFs and is time dependent.[16] The formation of large aggregates, up to a certain size, can enhance k even further due to local percolation behavior. In our case, the DLS results showed a constant particle size and concentration over time. Additionally, the average graphene size observed using TEM is in good agreement with the DLS results, demonstrating that no agglomeration occurred (see the ESI†). Moreover, a constant k was measured in different samples as a function of time (months), demonstrating that this mechanism cannot explain our results.

Raman spectroscopy was used as a tool to determine the plausibility of applying theory (iv) to our nanofluids. If graphene induces a modification of the interatomic interactions in the fluid, the Raman spectrum should be affected. As can be seen in Fig. 2b and Table 1, two Raman modes of DMF shifted to higher frequencies with increasing graphene concentration. Remarkably, the bands exhibiting larger displacements were the ones corresponding to carbon–nitrogen bonds:

N–(CH_3) (≈ 1090 cm^{-1}) and C–N (≈ 1438 cm^{-1}). The displacement of the band ≈1090 cm^{-1} was around 4 cm^{-1} for 0.12% graphene–DMF nanofluid. This band corresponds to an asymmetric rocking vibration from the bond 'N–(CH_3)'.[36] The displacement of these bands to higher frequencies in the presence of graphene physically could be interpreted as the C–N bond becoming more rigid, needing more energy to vibrate, with increasing graphene concentration. This interpretation leads us to suggest that graphene somehow affects the interaction between the solvent molecules, resulting in a strong modification of the interatomic potential as a function of graphene concentration, as model (iv) suggests.

Some authors claim that the weak interplanar bonding in graphite is merely due to van der Waals interactions. However, graphite does not show the same behavior as typical molecular (van der Waals) crystals.[37] Nevertheless, the delocalization of π electrons seems to play an important role in the interaction (stacking) between layers. Similarly, the nitrogen, oxygen and carbonyl carbon atoms in both DMF and DMAc all have sp^2 hybridization, and hence p orbitals perpendicular to the O–C–N plane which allow electron delocalization.[38] The quasi-planarity of the solvent molecules and the sp^2 hybridization favor the π–π stacking if the solvent molecules are in a parallel orientation with respect to the graphene flakes. Therefore, it is reasonable to suggest that a π–π bond is formed between the solvent molecules and the graphene surface. This interaction would then increase the rigidity of C–N bonds of the molecules closest to the graphene, and consequently, modify their Raman spectra, as shown in Table 1. This table shows the calculated Raman frequencies of a simple system (*A*), consisting of three molecules of DMF parallel to a graphene flake and the experimental Raman frequencies of DMF and 0.05% DMF. As can be seen, the calculated Raman modes as a function of graphene concentration exhibit a consistent shift to higher frequencies by an amount in agreement with the experimental spectra.

Gong *et al.*[39] reported a similar interaction, particularly a π–π+ stacking, between sp^2 carbon in an amorphous carbon surface and imidazolium cation. The imidazolium ring is a delocalized π system and could adopt a parallel orientation to the solid substrate interacting with sp^2 π electrons, as argued by Gong *et al.*[39] Xu *et al.* described a comparable scenario where chemically converted graphene induced molecular flattening of a porphyrin-based molecule through electrostatic and π–π stacking cooperative interactions.[40] However, this interaction does not explain the shift of the whole band at 1090 cm^{-1} with increasing graphene concentration.

In order to test our interpretation in terms of orientation of the solvent molecules to graphene surfaces, theoretical simulations using a combination of density functional theory (DFT) and molecular dynamics (MD) calculations were performed (see the ESI†). The MD calculations showed that the most frequent DMF orientation with respect to graphene was the parallel one. We found that three parallel configurations, labelled as A, B and C, presented the highest occurrence of 59.7%, 17.6% and 8.1%, respectively, compared to all other possible DMF orientations (see Fig. S12 in the ESI†). These configurations represent simple systems consisting of three (A and B) or two (C) DMF molecules around a graphene flake. Subsequently, these configurations were used as inputs for DFT simulations. It was found that these parallel configurations were the most energetically favorable, facilitating π–π stacking (see Fig. S10, and 12–14 in the ESI†).

To investigate a possible order of DMF molecules near graphene (model v), the nitrogen–nitrogen (N–N) pair-correlation function (PCF) of DMF molecules was calculated. Fig. 3a shows the contour plot of the N–N PCF as a function of graphene distance and N–N pair distances. This plot represents the relative density of nitrogen atoms around a central nitrogen atom as a function of its distance to graphene. In this particular case, the plot provides information about the distance between DMF molecules (N–N distance) in all possible parallel planes with respect to graphene. Fig. 3c schematically illustrates the surroundings of a graphene flake, where layers of DMF at different distances from the graphene flake are represented. The scheme shows that in the nearest layers of DMF to the graphene flake (orange planes) DMF molecules are parallelly oriented towards the graphene flake. A central molecule of DMF and its first, second and third neighbors are represented in the layers on top and above the graphene flake.

Three vertical cuts of the contour plot (Fig. 3a) at 3.6, 8.1 and 25.5 Å distance from the graphene are displayed in Fig. 3b. These representative cuts were selected based on the relatively high density of DMF molecules at certain N–N distances as shown in Fig. 3a. At a distance of 3.6 Å from the graphene flake, DMF molecules show a large degree of ordering, similar to that of a crystal: the first (~6.5 Å), second (~11.6 Å)

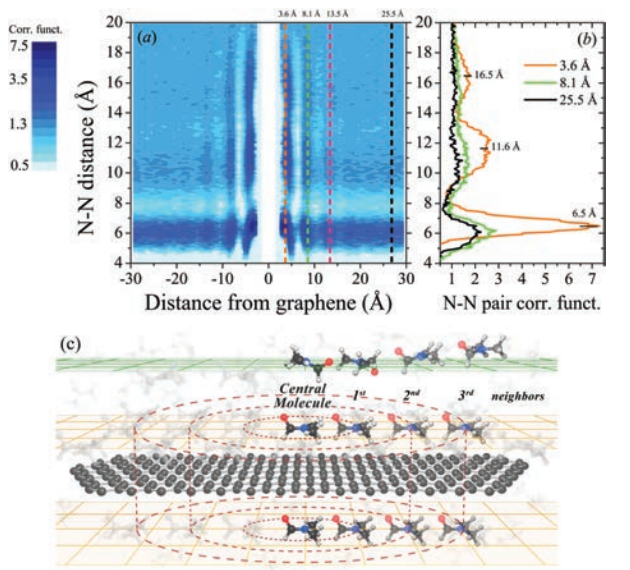

Fig. 3 Calculated correlation function of nitrogen to nitrogen (N–N) distance from DMF molecules as a function of graphene distance, and an illustration (a) contour plot of the N–N pair correlation function as a function of graphene distance; (b) N–N pair correlation function as a function of N–N distances at three different distances with respect to graphene. (c) Schematic representation of the surroundings of a graphene flake.

and third (~16.5 Å) neighbors can be identified (also called coordination shells). At least three layers of ordered DMF can be observed at 3.6, 8.1 and 13.5 Å from the graphene flake, which is remarkable considering that the flake radius is only 16.5 Å; hence, on larger flakes even longer-ranged ordering may be expected. Fig. 3a clearly shows that these three layers of DMF molecules have a higher density of DMF molecules at different N–N distances, although the effect is lost thereafter (see the ESI† for details). As the distance of DMF molecules from the graphene flake increases, the dynamic solid-like behavior of DMF is lost and it starts to behave as a normal liquid (just the first neighbors can be identified). Akıner *et al.* reported a similar nanolayer formation of water in the vicinity of hexagonal boron nitride.[41]

The interaction between the graphene and DMF molecules also induces a shift in the maxima of peaks in PCF as shown in Fig. 3b. The first peak (first neighbors) corresponding to a plane of molecules of DMF at 3.6 Å of graphene is shifted compared to the first peaks corresponding to the planes at 8.1 and 25.5 Å from the graphene flake. This indicates a rearrangement of the molecules on the graphene flake. Close to graphene DMF molecules tend to lay parallel to the flake, as mentioned before, requiring a larger N–N distance in the first coordination shell (see orange solid line in Fig. 3b). A shifting of the second peak is also observed.

The above discussion suggests that the local order of solvent molecules near the graphene flake, the parallel configuration and the possible π–π stacking are plausible key factors to explain the high dispersibility of graphene in DMF and DMAc.[42] The same mechanism can also explain the high dispersibility of graphene in other amides, such as *N*-methyl-2-pyrrolidone (NMP).[42]

Delving deeper into the experimental Raman spectra of DMF NFs, the associated symmetric shape of the band at ~1090 cm^{-1}, indicates that, to a greater or lesser extent, all DMF molecules are affected by the graphene flakes, in terms of the energy associated with this DMF vibrational mode. This unexpected result has been studied theoretically here; however, no explicit order was found beyond the third DMF layer above the graphene flake. If the DMF molecules near graphene were the only molecules affected by the presence of the graphene flake, the band at 1090 cm^{-1} should not shift and a weak shoulder would appear at higher frequencies as evidence of a fraction of DMF molecules acquiring a stronger bond.

Finally, our findings demonstrate that both this particular molecular interactions and local order mechanisms of the solvent molecules around graphene are present in the NFs as models (iv) and (v) suggested. Concerning model (vi), as the mean free path of phonons in graphene covers a large range (40–800 nm)[43,44] and the size of our graphene flakes varies from 150 to 450 nm, it is conceivable that phonons with a certain range of mean free path also contribute to the enhancement of *k*.

In fact, flakes of such sizes have been reported to display very high thermal conductivity.[45] As mentioned above, graphene flakes with those sizes were able to induce a liquid layering effect, in agreement with model (v), which in turn reduces the thermal boundary resistance between the flakes and the liquid.[46] Shahil *et al.*[47] separately showed that the thermal conductivity of a graphene-based nanocomposite increased with the graphene loading due to the low thermal boundary resistance between the flakes and the matrix. Both studies highlighted the fact that a strong enhancement of thermal conductivity requires the presence of thin flakes, albeit not exclusively. One of the reasons for the smaller thermal conductivity enhancement of nanofluids compared to nanocomposites might be attributed to the higher interface thermal resistance between graphene flakes and liquids, as can be seen on comparing the results from Shahil *et al.*[47] and Alexeev *et al.*[46]

In a nanocomposite, the thermal conductivity enhancement can also be further improved by giving a specific orientation to the flakes,[48] which might also occur in our nanofluids.

Regarding the enhancement of C_p exhibited by our NFs, similar enhancements in analogous NFs have been reported previously, *e.g.* for graphite nanoplatelets (NPts), Nelson *et al.*[49] showed a 50% enhancement of C_p of polyalphaolefin with 0.6 wt% of graphite NPts with a thickness of ~100 nm and diameters ~20 μm. Xie *et al.*[50] reported enhancements of ~8% and 17% for molten salt-based NFs with concentrations of 0.5% and 1.0 wt% graphite NPts (thickness ~2–5 nm and diameters ~10–20 μm).

In the case of oxide nanoparticles (NPs), Shin and Banerjee also reported a 26%[51] and 14.5%[3] enhancement in molten salt using SiO_2 NPs with a concentration of 1 wt%. Similarly, Qiao *et al.*[52] found an enhancement of 15.7% in other molten salts with the same concentration and NPs. Sang and Liu[53] also showed a huge enhancement of C_p in ternary-based NFs with different NPs. They measured enhancement of 79.9–113.7% for SiO_2, 50.6–73.9% for CuO, 31.1–56.5% for TiO_2 and 50.6–66.5% for Al_2O_3 nanoparticles with concentrations up to 1 wt%.

While it is well known that the addition of small amounts of nanomaterials (<1 wt%) could lead to the enhancement of C_p, the mechanism behind is still under debate. In certain simple cases it has been shown that the C_p of the NFs can be explained using the mixing theory of ideal gas mixtures.[54] However, it has been demonstrated that this approach fails for some NFs, where the C_p of the NPs is lower or in the order of the bare fluids. Shin and Banerjee identified three mechanisms to understand the enhancement of C_p:[3] (i) *higher C_p of NPs in comparison with their bulk counterpart*: this enhancement of C_p is well known and it comes from the discretization of the phonon spectra and the modification of the phonon density of states.[55–58] (ii) *High solid–fluid interaction*: the high surface area per unit mass of the NPs induces an increase in the interfacial thermal resistance (ITR) between the NPs and the surrounding fluid molecules. The increase in the ITR acts as additional thermal storage.[14,59] (iii) *Nanolayering of the liquid molecules around the NPs*: the existence of this solid-like layer is likely to have enhanced specific heat due to the smaller intermolecular spacing in comparison with the bare fluid.[3]

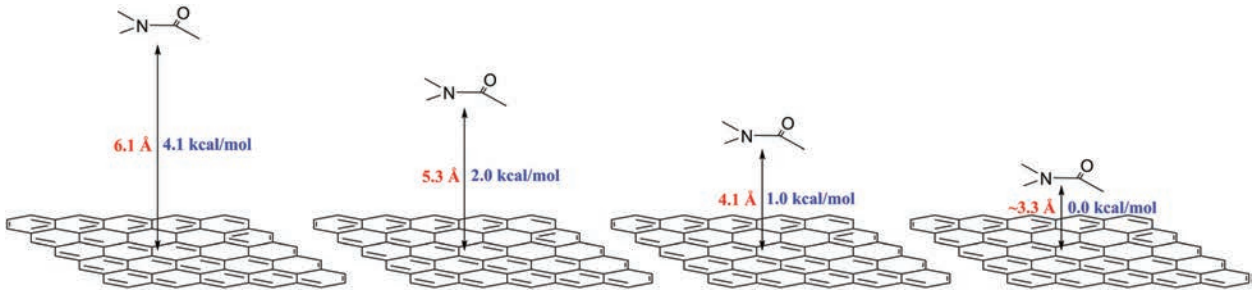

Fig. 4 Strength of π–π stacking calculated at different distances from the graphene flake.

Mechanism (i) cannot explain completely the enhancement of C_p in our samples. Due to the lateral sizes of the graphene flakes, it is not small enough to see the "phonon confinement effect", and we do not expect a strong modification in the phonon spectra. But, if we consider that as the thickness of the flakes is below 10 nm, the heat capacity can be affected by the emergence of new phonon modes, such as breathing and shear vibrations.[60] However, due to these modes having a very low energy (~20–80 cm^{-1}, 2.5–10 meV) we do not expect an important contribution at room temperature.[61,62]

Regarding model (ii) (high solid-fluid interaction), Xue *et al.*[63] demonstrated that for nanofluids characterized by weak atomic bonding (compared with solid–solid) at the particle–fluid interface, they exhibit high thermal resistance. In our case, the strength of the π–π interaction for the parallel configuration fluctuates between 4.1–1.0 [kcal mol^{-1}] (see Fig. 4). The weak strength of the π–π stacking and the possible high thermal resistance together with the formation of the nanolayering (model iii) around the graphene flakes could explain the enhanced C_p observed in this work.

Recently, Hentschke[64] discussed other possible mechanisms caused by mesolayers of the liquid molecules around the NPs and their interaction with other mesolayers. These mesolayers should have higher C_p compared with the bare fluid and they should extend far beyond the NPs with extensions about 4 times the diameters of the NPs. While this theory matches quite well with the cases presented in the work of Hentschke, our results did not show a layering beyond 18 Å, *i.e.*, in the same order as the lateral size of the graphene flakes.

Conclusions

Highly stable graphene dispersions over time in DMAc and DMF with enhanced thermal properties were prepared. The influence of graphene concentration on thermal conductivity, specific heat capacity and speed of sound was measured showing an enhancement of all these properties with increasing graphene concentration. We measured a 48% enhancement in the thermal conductivity of 0.18% DMAc-based nanofluid, demonstrating that only a small amount of dispersed graphene is required to induce a large enhancement of the overall thermal properties compared with the base fluid. Furthermore, a 0.11 wt% of graphene in the same fluid resulted in an 18% improvement in specific heat capacity. Finally, the Raman scattering results and the simulations lend support to the idea of stronger intermolecular interaction between the solvent and the graphene flakes than initially thought.

The Raman spectra analysis indicated that the intermolecular interaction between DMF molecules is modified when graphene is present, affecting the whole liquid. Furthermore, the theoretical studies suggested that the interaction between graphene and the nearest DMF molecules is stronger than initially thought. These molecules tend to lay parallel to the graphene flake favoring a possible π–π stacking. A local order of the DMF molecules up to three layers was also observed in the simulations.

These results represent an excellent initial step toward understanding the manner in which NPs modify the fluid arrangement directly affecting thermal transport. NFs are commonly highly diluted systems; therefore, it is the properties of the NPs and fluid molecule atoms at the points of intermolecular contact which are important in assessing the type of interaction. It clearly depends on the nature of the NPs and fluid molecules. It is also important to remark that the interaction between graphene and DMF is the key factor explaining the high dispersibility of graphene in DMF, DMAc and NMP.

Our results suggest that the presence of graphene produces important changes at the macroscopic level in organic base fluids, with the result that the dispersal of tiny concentrations of graphene produces a large improvement in the overall thermal properties of DMF and DMAc. This revealing finding demonstrates the applicability of these types of nanofluids as efficient, heat transfer materials. Furthermore, the small concentrations of graphene help to minimize contamination and can reduce possible sedimentation problems and the final costs of heat transfer fluids.

Methodology

Sample fabrication

Graphene flakes with lateral sizes ~150–450 nm and thicknesses from 1 to 10 layers were prepared from graphite (Sigma-

Aldrich, purity >99+% and size <20 μm) by a mechanical exfoliation method, similar to that used by Hermann *et al.*[65] An extended explanation of sample preparation is included in the ESI.†

Characterization

Several experimental techniques were used to obtain a complete structural, thermal and spectroscopic characterization of the fluids, including transmission electron microscopy (TEM), differential scanning calorimetry (DSC) and Raman and Brillouin spectroscopy. The thermal conductivity was obtained using a modified three-omega (3ω) method based on the work of Oh *et al.*[66] (see the ESI†). Finally, the stability of the dispersions was studied over time by regular tests every month for four months using dynamic light scattering (DLS). An extended description of the preparation of the NFs and characterization techniques can be found in the ESI.†

Author contributions

MRRL and PGR fabricated the samples. MRRL carried out DSC, DLS and TEM measurements and analyses. MRRL, ECA and MS fabricated 3ω devices and measured the thermal conductivities. MRRL and ECA performed the Raman analyses. MRRL, ECA and JM designed and performed the Brillouin measurements. ECA designed and performed the refractive index measurements. ACA carried out the Raman simulations, and studied the non-covalent interaction and orientation of the solvent molecules toward graphene. FC, BE, MP and PO calculated the N–N pair correlation function and provided support for the theoretical analysis. PGR and CMST supervised the work and discussed the experimental results. MRRL and ECA analysed and discussed the data and wrote the manuscript. All authors discussed the results and commented on the manuscript.

Conflicts of interest

There are no conflicts to declare.

Acknowledgements

The Catalan Institute of Nanoscience and Nanotechnology (ICN2) acknowledges support from the Severo Ochoa Program (MINECO, Grant SEV-2013-0295) and funding from the CERCA Programme/Generalitat de Catalunya. Funding from the Spanish Ministry (MINECO/FEDER: MAT2015-68394-R NaCarFLOW, FIS2015-70862-P PHENTOM and FIS2015-64886-C5-3-P SIESTA) is also acknowledged. FC, BE, MP and PO acknowledge support from the EU Center of Excellence MaX-Materials Design at the Exascale (Grant No. 676598), Generalitat de Catalunya (Grant No. 2014SGR301) and supercomputing resources from the Red Española de Supercomputación (RES). ACA acknowledges Fundació Cellex de Barcelona for financial support. We would also like to thank Andrew Hudson for the assistance provided with the use of English in the manuscript and Dr Torres for designing Fig. 3c.

References

1 S. M. Sohel Murshed and C. A. Nieto de Castro, *Renewable. Sustainable Energy Rev.*, 2017, **78**, 821–833.
2 P. Andreu-Cabedo, R. Mondragon, L. Hernandez, R. Martinez-Cuenca, L. Cabedo and J. Julia, *Nanoscale Res. Lett.*, 2014, **9**, 582.
3 D. Shin and D. Banerjee, *Int. J. Heat Mass Transfer.*, 2011, **54**, 1064–1070.
4 H. Tiznobaik and D. Shin, *Int. J. Heat Mass Transfer.*, 2013, **57**, 542–548.
5 O. Manca, Y. Jaluria and D. Poulikakos, *Adv. Mech. Eng.*, 2010, 1–2.
6 A. Turgut, I. Tavman, M. Chirtoc, H. P. Schuchmann, C. Sauter and S. Tavman, *Int. J. Thermophys.*, 2009, **30**, 1213–1226.
7 D. Kwek, A. Crivoi and F. Duan, *J. Chem. Eng. Data*, 2010, **55**, 5690–5695.
8 S. Jana, A. Salehi-Khojin and W.-H. Zhong, *Thermochim. Acta*, 2007, **462**, 45–55.
9 M. M. Tawfik, *Renewable Sustainable Energy Rev.*, 2017, **75**, 1239–1253.
10 B. T. Branson, P. S. Beauchamp, J. C. Beam, C. M. Lukehart and J. L. Davidson, *ACS Nano*, 2013, **7**, 3183–3189.
11 P. M. Sudeep, J. Taha-Tijerina, P. M. Ajayan, T. N. Narayanan and M. R. Anantharaman, *RSC Adv.*, 2014, **4**, 24887.
12 P. Keblinski, S. R. Phillpot, S. U. S. Choi and J. A. Eastman, *Int. J. Heat Mass Transfer*, 2002, **45**, 855–863.
13 P. Keblinski and J. Thomin, *Phys. Rev. E: Stat., Nonlinear, Soft Matter Phys.*, 2006, **73**, 10502.
14 R. Prasher, P. Bhattacharya and P. E. Phelan, *J. Heat Transfer*, 2006, **128**, 588.
15 S. Sarkar and R. P. Selvam, *J. Appl. Phys.*, 2007, **102**, 74302.
16 R. Prasher, P. E. Phelan and P. Bhattacharya, *Nano Lett.*, 2006, **6**, 1529–1534.
17 M. Liu, C. Ding and J. Wang, *RSC Adv.*, 2016, **6**, 3571–3577.
18 N. H. Abou-tayoun, *Molecular Dynamics Simulation of Thermal Conductivity Enhancement of Copper-water Nanofluid*, American University of Sharjah, 2012.
19 Y. Xuan, Q. Li and P. Tie, *Exp. Therm. Fluid Sci.*, 2013, **46**, 259–262.
20 G. Xia, H. Jiang, R. Liu and Y. Zhai, *Int. J. Therm. Sci.*, 2014, **84**, 118–124.
21 K. P. Loh, Q. Bao, P. K. Ang and J. Yang, *J. Mater. Chem.*, 2010, **20**, 2277.
22 A. A. Balandin, *Nat. Mater.*, 2011, **10**, 569–581.
23 D. P. Dubal and P. Gomez-Romero, *2D Mater.*, 2016, **3**, 31004.
24 X. Han, Y. Chen, H. Zhu, C. Preston, J. Wan, Z. Fang and L. Hu, *Nanotechnology*, 2013, **24**, 205304.

25 Y. Liang, D. Wu, X. Feng and K. Müllen, *Adv. Mater.*, 2009, **21**, 1679–1683.
26 K. V. Wong and O. De Leon, *Adv. Mech. Eng.*, 2010, **2**, 519659.
27 V. V. Chaban and E. E. Fileti, *Phys. Chem. Chem. Phys.*, 2016, **18**, 26865–26872.
28 Z. L. Wang, D. W. Tang, S. Liu, X. H. Zheng and N. Araki, *Int. J. Thermophys.*, 2007, **28**, 1255–1268.
29 D. S. Viswanath and M. Bhagwant Rao, *J. Phys. D: Appl. Phys.*, 1970, **3**, 1444–1450.
30 J. G. Dil, *Rep. Prog. Phys.*, 1982, **45**, 285–334.
31 G. Benedek and T. Greytak, *Proc. IEEE*, 1965, **53**, 1623–1629.
32 T. Yogi, K. Sakai and K. Takagi, *J. Appl. Phys.*, 2006, **100**, 23505.
33 H. Bohidar, T. Jossang and J. Feder, *J. Phys. D: Appl. Phys.*, 1988, **21**, S53–S55.
34 S. Nemoto, *Appl. Opt.*, 1992, **31**, 6690.
35 T. M. Aminabhavi and B. Gopalakrishna, *J. Chem. Eng. Data*, 1995, **40**, 856–861.
36 V. Venkata Chalapathi and K. Venkata Ramiah, *Proc. - Indian Acad. Sci., Sect. A*, 1968, **68**, 109–122.
37 F. Rozpłoch, J. Patyk and J. Stankowski, *Acta Phys. Pol., A*, 2007, **112**, 557–562.
38 C. R. Kemnitz and M. J. Loewen, *J. Am. Chem. Soc.*, 2007, **129**, 2521–2528.
39 X. Gong, A. Kozbial, F. Rose and L. Li, *ACS Appl. Mater. Interfaces*, 2015, **7**, 7078–7081.
40 Y. Xu, L. Zhao, H. Bai, W. Hong, C. Li and G. Shi, *J. Am. Chem. Soc.*, 2009, **131**, 13490–13497.
41 T. Akıner, J. K. Mason and H. Ertürk, *J. Chem. Phys.*, 2017, **147**, 44709.
42 C.-J. Shih, S. Lin, M. S. Strano and D. Blankschtein, *J. Am. Chem. Soc.*, 2010, **132**, 14638–14648.
43 H. Zhang, X. Chen, Y. D. Jho and A. J. Minnich, *Nano Lett.*, 2016, **16**, 1643–1649.
44 J. Zou and B. Cao, *Appl. Phys. Lett.*, 2017, **110**, 103106.
45 D. L. Nika and A. A. Balandin, *Rep. Prog. Phys.*, 2017, **80**, 36502.
46 D. Alexeev, J. Chen, J. H. Walther, K. P. Giapis, P. Angelikopoulos and P. Koumoutsakos, *Nano Lett.*, 2015, **15**, 5744–5749.
47 K. M. F. Shahil and A. A. Balandin, *Nano Lett.*, 2012, **12**, 861–867.
48 J. Renteria, S. Legedza, R. Salgado, M. P. Balandin, S. Ramirez, M. Saadah, F. Kargar and A. A. Balandin, *Mater. Des.*, 2015, **88**, 214–221.
49 I. C. Nelson, D. Banerjee and R. Ponnappan, *J. Thermophys. Heat Transfer*, 2009, **23**, 752–761.
50 Q. Xie, Q. Zhu and Y. Li, *Nanoscale Res. Lett.*, 2016, **11**, 306.
51 D. Shin and D. Banerjee, *J. Heat Transfer*, 2011, **133**, 24501.
52 G. Qiao, M. Lasfargues, A. Alexiadis and Y. Ding, *Appl. Therm. Eng.*, 2017, **111**, 1517–1522.
53 L. Sang and T. Liu, *Sol. Energy Mater. Sol. Cells*, 2017, **169**, 297–303.
54 J. Buongiorno, *J. Heat Transfer*, 2006, **128**, 240.
55 V. N. Likhachev, G. A. Vinogradov and M. I. Alymov, *Phys. Lett. A*, 2006, **357**, 236–239.
56 B.-X. Wang, L.-P. Zhou and X.-F. Peng, *Int. J. Thermophys.*, 2006, **27**, 139–151.
57 M.-J. Huang, T.-M. Chang, C.-K. Liu and C.-K. Yu, *Int. J. Heat Mass Transfer.*, 2008, **51**, 4470–4479.
58 E. Chávez, J. Cuffe, F. Alzina and C. M. Sotomayor Torres, *J. Phys.: Conf. Ser.*, 2012, **395**, 12105.
59 L. Xue, P. Keblinski, S. R. Phillpot, S. U. S Choi and J. A. Eastman, *Int. J. Heat Mass Transfer*, 2004, **47**, 4277–4284.
60 C. H. Lui, Z. Ye, C. Keiser, X. Xiao and R. He, *Nano Lett.*, 2014, **14**, 4615–4621.
61 E. Chávez-Àngel, *Confined acoustic phonons in Si nano-membranes: impact on thermal properties*, PhD thesis, Universitat Autònoma de Barcelona, 2014.
62 M. Mouis, in *Beyond-CMOS Nanodevices 1*, ed. F. Balestra, John Wiley, 2014, pp. 142–152.
63 L. Xue, P. Keblinski, S. R. Phillpot, S. U. S. Choi and J. A. Eastman, *J. Chem. Phys.*, 2003, **118**, 337–339.
64 R. Hentschke, *Nanoscale Res. Lett.*, 2016, **11**, 88.
65 H. Hermann, T. Schubert, W. Gruner and N. Mattern, *Nanostruct. Mater.*, 1997, **8**, 215–229.
66 D.-W. Oh, A. Jain, J. K. Eaton, K. E. Goodson and J. S. Lee, *Int. J. Heat Fluid Flow*, 2008, **29**, 1456–1461.

Supporting information of Article 1

Electronic Supplementary Material (ESI) for Nanoscale.

Mechanisms behind the enhancement of thermal properties of graphene nanofluids

M. R. Rodríguez-Laguna[1,2], A. Castro-Alvarez[3], M. Sledzinska[1], J. Maire[1], F. Costanzo[1], B. Ensing[1,5], M. Pruneda[1], P. Ordejón[1], C. M. Sotomayor Torres[1,4], P. Gómez-Romero[1] and E. Chávez-Ángel[1]

[1] Catalan Institute of Nanoscience and Nanotechnology (ICN2), CSIC and BIST, Campus UAB, Bellaterra, 08193 Barcelona, Spain

[2] Departament de Química, Universitat Autònoma de Barcelona, Cerdanyola del Vallès, 08193 Barcelona, Spain

[3] Organic Chemistry Section, Facultat de Química, Universitat de Barcelona, Av. Diagonal 645, 08028 Barcelona, Catalonia, Spain

[4] ICREA, Pg. Lluís Companys 23, 08010 Barcelona, Spain

[5] Van't Hoff Institute for Molecular Sciences, University of Amsterdam, 1098 XH Amsterdam, The Netherlands

E-mail: rocio.rodriguez@icn2.cat; emigdio.chavez@icn2.cat

Keywords: Nanofluids, Graphene, enhancement of thermal properties, π–π stacking, liquid layering, Raman of nanofluids, intermolecular forces.

Nomenclature

Abbreviations and Latin letters

BLS	Brillouin light scattering	*MD*	Molecular dynamics
Cp	Specific heat capacity at constant pressure (J/g K)	*n*	Refractive index of the medium
DFT	Density functional theory	*N-N*	Nitrogen-nitrogen
DLS	Dynamic light scattering	*NFs*	Nanofluids
DMAc	N,N-dimethylacetamide	*NMP*	N-Methyl-2-pyrrolidone
DMF	N,N-dimethylformamide	*NP*	Nanoparticles
DSC	Differential scanning calorimetry	*PCF*	Pair-correlation function
f	Brillouin frequency (Hz)	*TEM*	Transmission electron microscopy
HTFs	Heat transfer fluids	v_s	Sound velocity (m/s)
k	Thermal conductivity (W/m K)	*wt. %*	by weight (%)

Greek letters

λ_0	Laser wavelength (nm)	ν	Stretching (vibrational mode)
λ_s	Wavelength of the acoustic wave (nm)	3ω	Three-omega method

(*i*) Experimental methods

1. Sample preparation

Graphene flakes with lateral sizes ~ 150-450 nm and thicknesses from 1 to 10 layers were prepared from graphite (Sigma-Aldrich, purity > 99+% and size < 20 um) by a mechanical exfoliation method, similar to that used by Hermann et al.[61]. Thus, 0.4 g of graphite were ball-milled in a 100mL stainless steel jar with zirconia beads (5 and 12 mm diameter) in a high-energy planetary ball mill (All-direction planetary ball mill 0.4L, model CIT-XBM4X-V0.4L, Columbia International) at 378 rpm for 64 hours. From the resulting material, graphene nanofluids were prepared as follows. Graphene NFs were prepared based on DMAc (ACROS Organics, 99+ %) with concentrations ranging from 0.01-0.27 wt.% and DMF (Scharlau, HPLC grade) with concentrations ranging from 0.01-0.12 wt.%. Hereafter, for convenience, sample names will be shortened by omitting 'wt.% of graphene dispersed in', for example: 0.01 wt.% of graphene dispersed in DMAc will henceforth be written as 0.01 % DMAc. The preparation of the nanofluids consisted of direct mixing of the base fluid with graphene flakes. To suppress particle clustering and obtain stable dispersions[62], graphene was dispersed in the fluid using a high energy-planetary ball mill. Graphene and the solvent were mixed in a proportion of 1:31 in weight and were ball milled for 1 h, employing 5 and 12 mm diameter zirconia beads and 100 mL stainless steel jars. The ball to powder weight ratio used was 16:1 and the rotating speed of the jars was 378 rpm. Soft ultrasonic vibration, 1000 W (Ovan, model ATM40-6LCD) was then applied for 1h. After this procedure, the samples were centrifuged at 6000 rpm for one hour to ensure the stability of the nanofluids (Digicen 21 centrifuge, Orto alresa).

2. Dynamic light scattering

The stability of the graphene-based nanofluid dispersions was determined as a function of time using dynamic light scattering (DLS) system (ZetaSizer nano ZS, ZEN3600, Malvern Instruments, Ltd. Malvern). The samples were analysed periodically to register the number of photons scattered by the sample (one measurement per month). An attenuator index of 7 was applied to the laser and a quartz cuvette with a measurement position of 4.65 mm was used every time. The hydrodynamic diameter and the polydispersity index (PdI) of the sample were also obtained. Our measurements show that the total number of photons remained constant throughout the duration of the investigation. **Table S1** shows constant hydrodynamic diameter of the nanoflakes, photon count rate and PdI for a nanofluid based on DMAc during 4 months. The PdI describes how broad the size distribution is within the sample. Values range from 0.05-0.7, the smaller the PdI, the more monodisperse is a sample. Therefore, PdIs shown in Table S1 indicate that the sample is moderately monodisperse and together with the photon count rate values it can be said that there is no precipitation of graphene flakes throughout time.

Table S1 *DLS data from a graphene-nanofluid sample based on DMAc.*				
Features / Time	**Day 1**	**After 2 months**	**After 3 months**	**After 4 months**
Hydrodynamic diameter (nm)	187 ± 9	184 ± 4	174 ± 6	179 ± 5
Photon count rate (kcps)	310 ± 2	334 ± 3	336 ± 2	333 ± 2
Polydispersity index	0.120 ± 0.031	0.111 ± 0.008	0.123 ± 0.018	0.102 ± 0.014

3. High-resolution transmission electron microscopy analysis

The dispersions were deposited on 300-mesh carbon grids, which were analyzed using the JEOL 1210 microscope, operating at 120 kV to obtain transmission electron microscopy (TEM) images. **Figure S1** shows a TEM image (*a*) of representative graphene flakes with different sizes (260-330 nm). The inset of **Figure S1*a*** shows selected area electron diffraction (SAED) from a graphene flake. As can be seen, single spots are obtained, which means a high crystallinity of the selected flake. Furthermore, the simulated SAED patter displayed in **Figure S1*b*** is in total accordance with the experiment, demonstrating the single crystal nature of the graphene flakes.

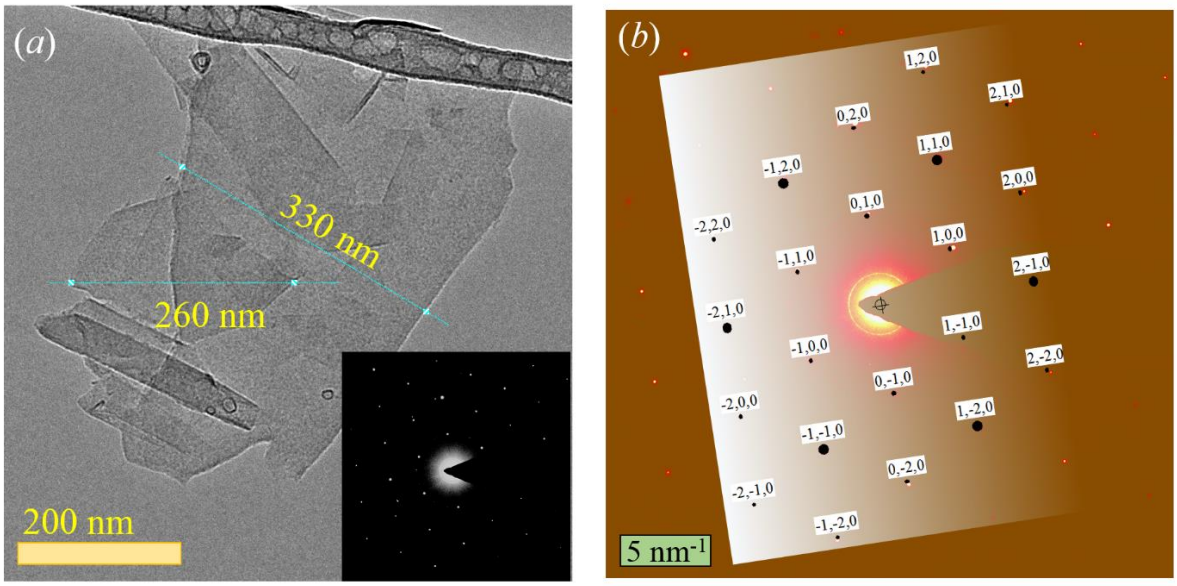

Figure S1 (*a*) *Representative TEM image of graphene from a DMAc dispersion (DMAc-NF) showing folded graphene sheets. (inset) Selected area electron diffraction (SAED) from the same graphene flake.* (*b*) *Simulated and experimental SAED pattern of multilayer graphene showing the different crystallographic planes.*

4. Brillouin Light Scattering

The sound velocities were determined from the Brillouin frequency shift measured for different graphene concentrations contained in a transparent quartz cuvette. A diode laser with wavelength λ_0 = 532 nm was focused with a 10x microscope objective, and the Brillouin spectra was recorded on JRS Tandem Fabry-Pérot TFP-1 interferometer in the backscattering configuration. The laser power was kept as low as possible (~ 2 mW) to avoid any possible heating effect from the laser.

Figure S2 displays the anti-stoke component of the Brillouin spectra for DMF and DMAc at different graphene concentrations. A small shift in the frequency as a function of graphene concentration is observed.

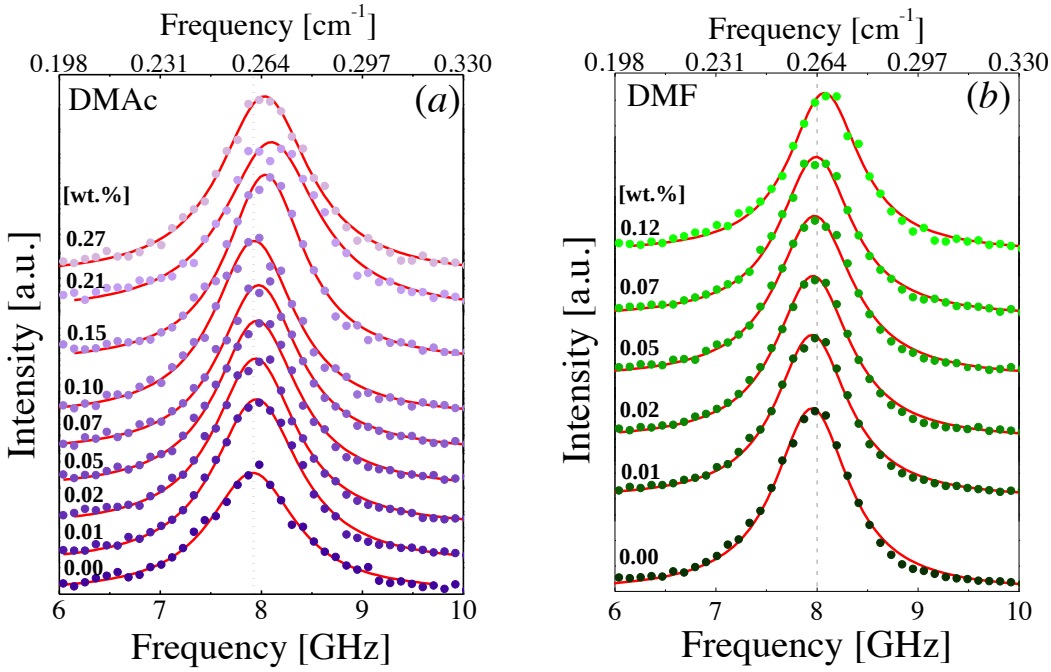

Figure S2 *Brillouin spectrum of DMAc (a) and DMF (b) NFs with different concentrations of graphene.*

5. Refractive index

The refractive index of the nanofluids were determined using the knife edge method.[3] This method consists of passing a laser light obliquely through a transparent container filled with the liquid to be measured. Due to the light passing through different media, the transmitted beam is displaced from its incident direction. This displacement depends on the refractive index of the liquid and the wall of the container. To eliminate the influence of the container wall, it is necessary to measure an empty cell and then, by subtracting the difference between both displacements, it is possible to estimate the refractive index of the liquid without reference to the refractive index of the container.[3]

A scheme of the set up used to measure the refractive index is illustrated in **Figure S3**. The measured refractive indices are displayed in the **Figure S4.** We can see that the refractive indices do not vary within of the experimental error bars.

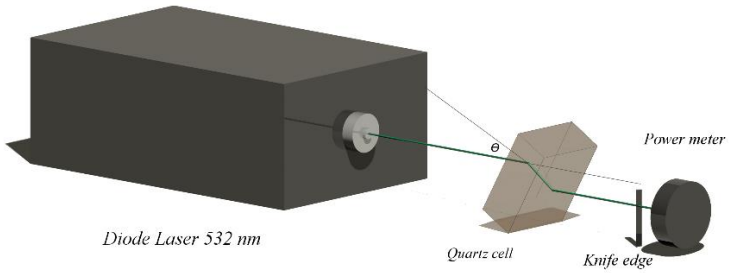

Figure S3 *Schematic representation that was used to measure the refractive index of the nanofluid.*

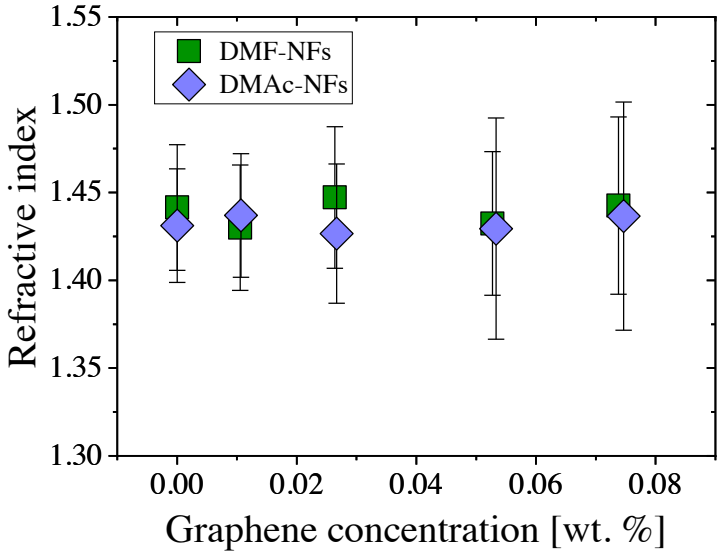

Figure S4 *Refractive index as a function of graphene concentration.*

6. Raman light scattering

The Raman spectra were recorded by T64000 Raman spectrometer manufactured by HORIBA Jobin Yvon. It was used in single grating mode with a spectral resolution better than 0.4 cm^{-1}. The liquid was placed in a transparent quartz cuvette, the same one used for Brillouin analysis. All the Raman measurements were carried out by focusing a diode laser (λ_0 = 532 nm) with 50x long working distance microscope objective. The power of the laser was kept as low as possible (~ 2 mW) to avoid any possible effect from self-heating.

The **Figure S5*a*** shows the Raman peak position of '$(CH_3)N$' rocking mode of pure DMF for several measurements. As can be seen, the reproducibility of the experimental setup varies in the order of 0.06 cm^{-1} (standard deviation, green parallel bar) within a range of 0.25 cm^{-1} (maximum and minimum peak deviation). It is important to mention that another possible factor that could produce a displacement of the Raman modes is the temperature fluctuation. To discard this effect, Raman measurements as a function of the laser power were performed. **Figure S5*b*** shows that the variation of the peak position of the "$(CH_3)N$" rocking mode of 0.5 mg/ml graphene-DMF is completely uncorrelated with the laser power. The range of variation was in ~ 0.24 cm^{-1} and with a standard deviation of 0.1 cm^{-1}, i.e., in the

same range than the reproducibility of the equipment. Therefore, the displacements of the Raman band shown in this work are completely related to the strong interaction between graphene and DMF and cannot be associated with temperature fluctuation of the sample.

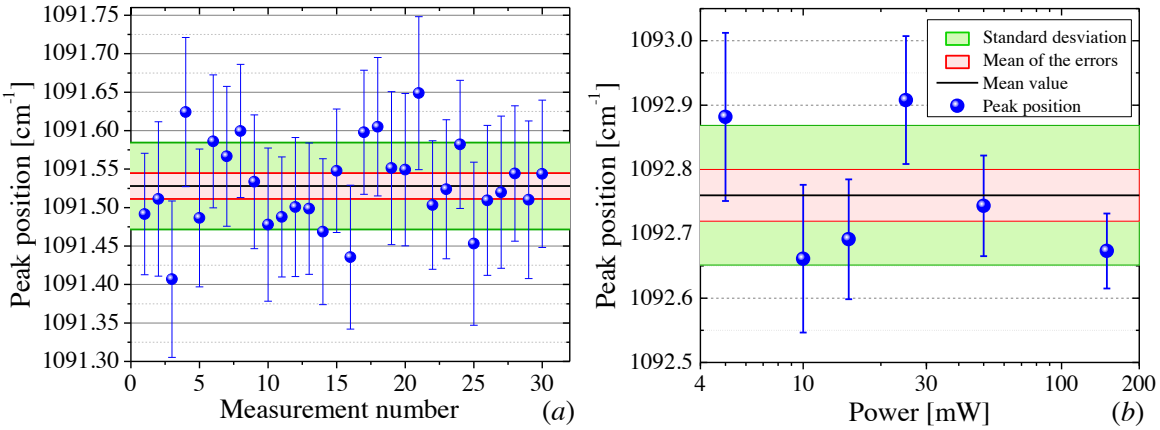

Figure S5 *Peak position of ~ 1091 cm^{-1} the rocking mode as function of: (a) measurement number (pure DMF) and (b) laser power (0.5 mg/m graphene-DMF nanofluid). The error bar of each measured point comes from the Lorentzian fit of the band. The average peak position is displayed in black solid line. The standard error of the averaged and mean errors are displayed with green and red parallel bars, respectively.*

The experimental Raman spectra from DMF-NFs at different graphene concentrations is plotted in **Figure S6**. This band corresponds to an asymmetric bending vibration in a plane (rocking) of the bond '$(CH_3)N$' of DMF molecule [5]. **Figure S6** shows a continuous displacement to higher frequencies and a broadening of the mode with increasing graphene concentration. The peak position was determined by a Lorentzian fit of the Raman spectra showed in solid red line.

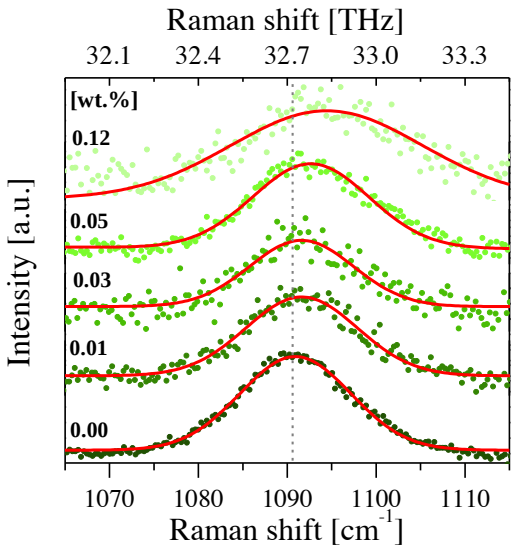

Figure S6 *Raman scattering from DMF NFs with different graphene flake concentrations: shift and broadening of the Raman spectra and the Lorentzian fit (solid red lines).*

7. Three-omega method

The three-omega (3ω) method is widely used to measure the thermal conductivity of solid materials[6,7]. In this work, we designed a modified version suitable for the measurement of liquids, based on the works of Chen et al.[8], Oh et al.[9] and Lubner et al.[10] Our cell is shown in **Figure S7**. The liquid is placed on the 3ω-heater which has been previously passivated with 200 nm of SiO_x, by plasma enhanced chemical vapor deposition, to avoid current leakage from the resistor to the conductive fluid. A 100 nm thick 3ω-strip (5 nm of chromium and 95 nm of gold) was patterned on a 0.5 mm thick quartz substrate by photolithography and electron beam physical vapor deposition (EBPVD). The width of the heating line is defined as $2b$ = 10 μm and the length as l = 1 mm, the latter considered as the distance between the voltage (inner) pads. Then, a 3 mm thick PDMS block is used to seal the circuit and to contain the liquid (as a well).

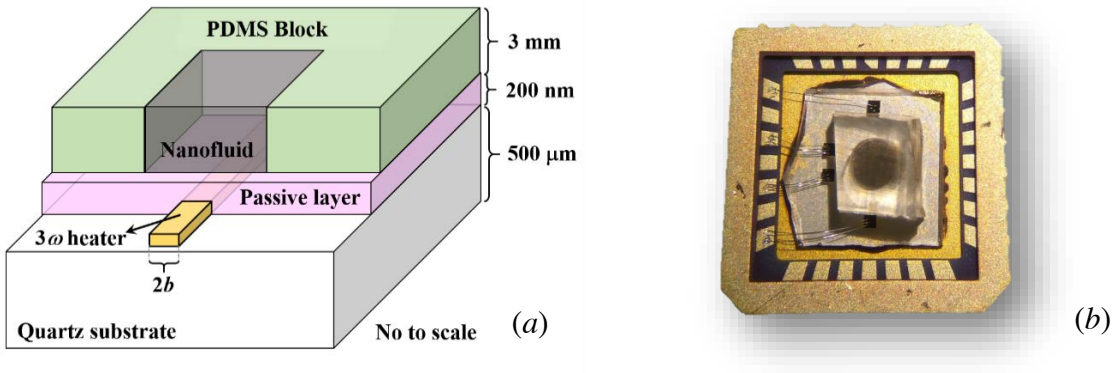

Figure S7 *3ω cell for fluid samples: (a) Schematic representation (b) Top view photograph of the actual cell containing a graphene nanofluid sample.*

The 3ω method consists of applying an alternating current (AC) through the metal strip which is in direct contact with the liquid. It is simultaneously a heater and thermometer. An AC signal with an angular frequency ω ($\omega = 2\pi f$, where f is the frequency) flows through the strip generating heat which oscillates at 2ω. The injected heat generates a temperature rise (ΔT) which will depend on the thermal properties of the sample. Since the electrical resistivity is linearly proportional to the temperature, see **Figure S8*a***, the ΔT can be obtained from this dependence. The temperature oscillations is obtained by measuring the third harmonic component of the voltage ($U_{3\omega}$) across the resistor using [6,7]:

$$\Delta T = \frac{2U_{3\omega}}{\beta U_0} \approx 2\frac{U_{3\omega,rms}}{\beta U_{\omega,rms}} \qquad (1)$$

where U_0 is the voltage amplitude and β is the temperature coefficient of the electrical resistivity of the strip. Since the first harmonic amplitude is at least three order of magnitude larger than the third harmonic amplitude, one can approximate U_0 with U_ω. Finally, the thermal conductivity of the samples

can be obtained by measuring the frequency dependence of the $U_{3\omega}$. The 3ω signal was recorded by 7260 DSP lock-in amplifier (EG&G Instruments) using a passive circuit.

The thermal conductivity of the substrate of an empty cell can be obtained by solving the transient heat conduction equation for a finite width line heater, deposited on the semi-infinite surface of a film-on-substrate system. The temperature rise is given by [6,7]:

$$\Delta T = \frac{P_l}{k\pi}\int_0^\infty \frac{\sin^2(xb)}{(xb)^2\sqrt{x^2+q^2}}dx = \frac{P_l}{k\pi}F(qb) \tag{2}$$

where b is half heater width, $q \equiv 1/\lambda = \sqrt{2i\omega/\alpha}$ is the inverse of the thermal penetration depth (λ) α and k are the thermal diffusivity and conductivity of the substrate, respectively, and P_l is the AC power per unit length, i.e., P/l where l is the heater length.

7.1 Thermal conductivity determination of liquids

For the thermal conductivity determination of the liquid, the 3ω-strip was considered to be in the middle of the two semi-infinite media *S* (for substrate) and *NF* (for nanofluid). Then, assuming that the heat transfer occurs only across the interface liquid-heater-substrate, as in the boundary mismatch approximation, the total measured temperature oscillation of the heater (ΔT_{total}), including the substrate on one side and the nanofluid on the other, can be expressed as [8,9]:

$$\frac{1}{\Delta T_{total}} = \frac{1}{\Delta T_S} + \frac{1}{\Delta T_{NF}} \tag{3}$$

where ΔT_S is the temperature rise of the substrate (measured in an empty cell) and the ΔT_{NF} is the temperature rise in the fluid. Lubner et al.[10] showed that the error using this approach is less than 1% at low-frequency limit (hundreds of Hz) when the ratio of the thermal diffusivities of the NF and S $\alpha_{NF}/\alpha_S > 10^{-1}$ (in our case $\alpha_{NF}/\alpha_S > 0.2$) and the thermal conductivities ratio $10^{-2} < k_{NF}/k_S < 1$ (in our case $k_{NF}/k_S < 0.22$). Finally, the thermal conductivity of the fluid can be estimated by solving Eq. (2) using least squares fit.

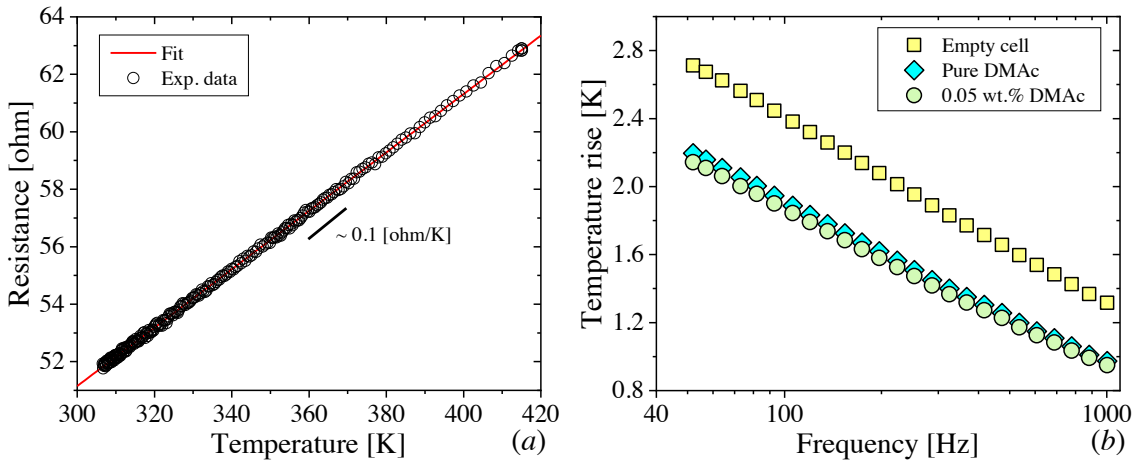

Figure S8 (*a*) *Electrical resistance against temperature of 3ω strip*. (*b*) *Typical temperature rise as a function of the frequency showing: empty cell (yellow solid squares) and filled cell with DMAc (blue solid diamonds) and 0.05 wt% graphene-DMAc (green solid circles).*

A summary of the thermal conductivity data in this work is shown in **Table S2** and **Table S3**. The measured values of the thermal conductivity were corrected using a factor to allow the comparison of data from different 3ω cells. The measurement of *k* of DMAc NFs was performed using different 3ω cells, on the other hand, a single 3ω cell was used to measure the whole set of concentrations of DMF-NFs. The bare fluids were used as standards and analyzed in order to corroborate the proper operation of each cell. The thermal conductivity of our samples was corrected by a factor, obtained from the bare fluids measurements. Previous to the measurement of each sample, the thermal conductivity of the bare fluid is measured and compared with the well-accepted value from the literature. Then a correction factor is obtained and the thermal conductivity of the bare fluid is corrected. After that the *k* of NF is measured and corrected by the same factor. In order to check the reproducibility of the measurement, at least four measurements for each sample were repeated with a standard deviation smaller than 0.01 W/m K .

The experimental thermal conductivity values of the base fluids are in broad agreement with the widely accepted values of k = 0.17 W/m K and 0.18 W/m K for DMAc and DMF, respectively [11].

Table S2 *Thermal conductivity data from graphene-DMAc nanofluids at 298 K.*

Concentration wt.%	*k* (W/mK)	Correction factor	corrected *k* (W/mK)	*k* enhancement (%)
0.00	0.184±0.001	0.95	0.175±0.001	0±0.8
0.01	0.191±0.001	0.94	0.180±0.001	2.6±0.8
0.03	0.168±0.001	1.17	0.196±0.001	11.9±0.8
0.05	0.174±0.001	1.18	0.206±0.001	17.7±0.8
0.18	0.281±0.003	0.92	0.259±0.003	47.9±1.2

Table S3 *Thermal conductivity data from graphene-DMF nanofluids at 298 K.*

Concentration wt.%	*k* (W/mK)	Correction factor	corrected *k* (W/mK)	*k* enhancement (%)
0.00	0.172±0.001	1.06	0.183±0.001	0.0±0.8
0.01	0.183±0.002	1.06	0.194±0.002	6.0±1.0
0.03	0.191±0.001	1.06	0.203±0.001	11.1±0.8
0.05	0.215±0.001	1.06	0.228±0.001	24.6±0.8

8. Differential scanning calorimetry

Specific heat capacity (Cp) was measured by using differential scanning calorimetry (DSC) on a PerkinElmer DSC 8000, using a common procedure. The difference in heat flow between an empty pan (standard aluminum pan) and the sample (inside the same pan) is recorded as a function of temperature; both measurements are taken using the same thermal program, heating rate and temperature range. In particular, the conditions used in this work are described as follows: from 5-20ºC at 2ºC/min, adding two 10-minutes isotherms at the beginning and at end of the measurement. Platinum was used as a standard and analyzed by DSC in order to corroborate the proper operation of the equipment. The specific heat capacity of our samples was corrected by a factor of 1.13, obtained from the Pt measurements, in accordance with the standard procedure for DSC analysis.

Table S4 shows a summary of the results and the corresponding *Cp* enhancement of the NFs. The results obtained for the base fluids are in good agreement with the values found in the literature: 2.06 J/gK and 2.016 J/gK for DMF and DMAc, respectively, at 298 K [11].

Table S4 *Specific heat capacity data from graphene-DMAc and DMF nanofluids at 293K.*

Concentration wt.%	DMAc		DMF	
	Corrected *Cp* (J/gK)	*Cp* enhancement (%)	Corrected *Cp* (J/gK)	*Cp* enhancement (%)
0.00	2.05±0.02	0.00	2.07±0.02	0.00
0.01	2.15±0.02	4.89±1.45	--	--
0.03	--	--	2.13±0.02	2.83±1.44
0.05	2.16±0.02	5.11±1.45	2.22±0.02	7.23±1.47
0.11-0.12	2.41±0.02	17.71±1.56	2.32±0.02	12.07±1.51

It is important to remark that, as the enhancement of *Cp* is not as large as for *k* (see **Table S2** and **Table S3**), the overall thermal diffusivity ($\alpha = k/(\rho\, Cp)$, with ρ being the material density) of NFs will also increase as a function of graphene concentration. For example, taking the experimental *k* and *Cp* data for 0.05 wt.% graphene-DMAc NF, the thermal diffusivity enhancement is $\alpha \sim 12$ %. This result demonstrates the potential of these NFs as heat transfer fluid for cooling applications.

9. Effective viscosity measurements

The effective viscosity of the nanofluids was measured using a Haake RheoStress RS600 rheometer from Thermo Electron Corp. at T = 20-21ºC. The shear rate used was 2880 s^{-1} with a measurement time of 30 seconds.

Figure S9 displays the viscosity of the nanofluids as a function of graphene concentration at room temperature. The viscosity of both sets of graphene nanofluids increases considerably as a function of graphene concentration. DMAc nanofluids with low graphene loading (0.00-0.03 wt. %) have similar viscosity values.

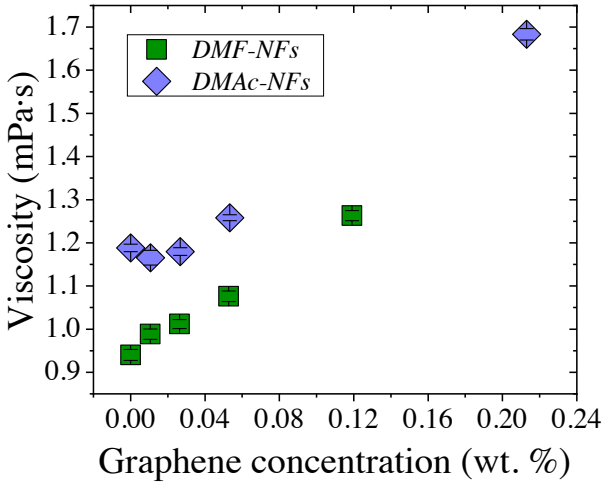

Figure S9 *Viscosity of graphene-DMAc and DMF nanofluids as a function of graphene concentration.*

(*ii*) Theoretical modelling

1. Molecular dynamics and DFT calculations: procedure

A combination of density functional theory (DFT) and molecular dynamic (MD) simulations was used to calculate the most frequent DMF-graphene configurations (DMF molecules orientation to graphene) and their respective Raman frequencies. Geometry optimization, energies and Raman modes were calculated using DFT methods (B3LYP). The DMF-graphene configurations were obtained from MD simulations, using a OPLS-2005 [12,13] classical force field. Then, singlet-point calculations were carried out at a higher DFT level (ωB97XD). The methodology used in this work is summarized in **Figure S10.**

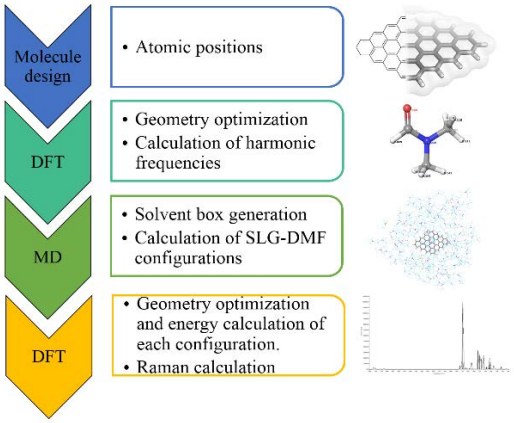

Figure S10 *Flow diagram of the method used.*

2. Molecule design and first DFT optimization

Initially, a 4x4 unit cell for SLG and a single DMF molecule were generated using the Avogadro software [14] (see **Figure S11**). The resulting structures were optimized with the Becke's three-parameter exchange (B3) + Lee-Yang-Parr (LYP) correlation functional (B3LYP) [15–18] using Pople 6-31G(d)[19] basis set. The calculations were done with Gaussian 09 [20]. The map of electrostatic potential (ESP) [21,22] allowed to calculate the partial atomic charge distributions of the molecules, which were used as point charges in the OPLS force field. Once the energy was minimized, the harmonic frequencies were calculated to corroborate the energy minimization. Our compute frequencies are corrected by a scaling factor [23] of 0.961.

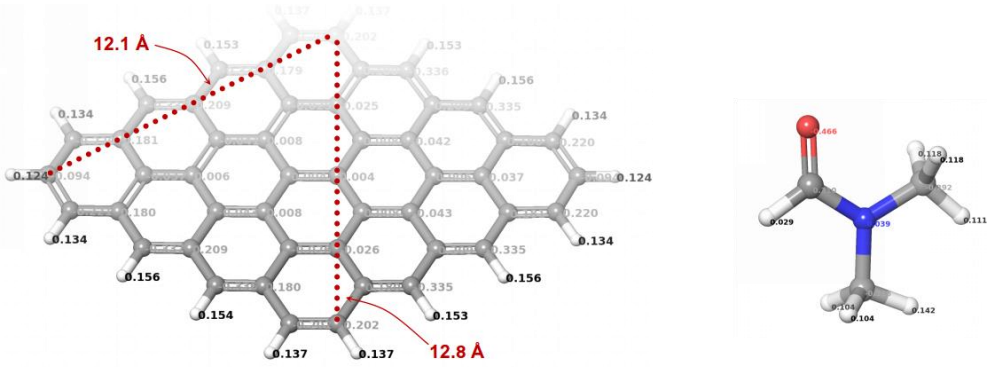

Figure S11 *Molecular geometries and partial charges of the graphene flake (left) and DMF molecule (right). The partial charges were those calculated with B3LYP/6-31G(d).*

3. Molecular dynamics simulations

Starting with the optimized DMF molecule, we generated a cubic solvent box for the MD simulations. For this purpose, the Disordered System Builder module of the Schrödinger material suite [24] was used to create a multicomponent system of randomly distributed molecules of DMF consisting of 512 molecules with a van der Waals scalar factor of 0.80. The system was optimized for a period of 200 ps; the ESP partial charges were those calculated by B3LYP/6-31G(d). Once this model was generated, the

equilibration of the complete system (SLG+DMFs) was performed for 100 ps at T = 300 K and constant volume. This was followed by MD simulations for 100 ns maintaining a cubic solvation model at constant temperature and pressure of 1.013 bars. A schematic representation of the calculation is shown in the

Figure S12**.**

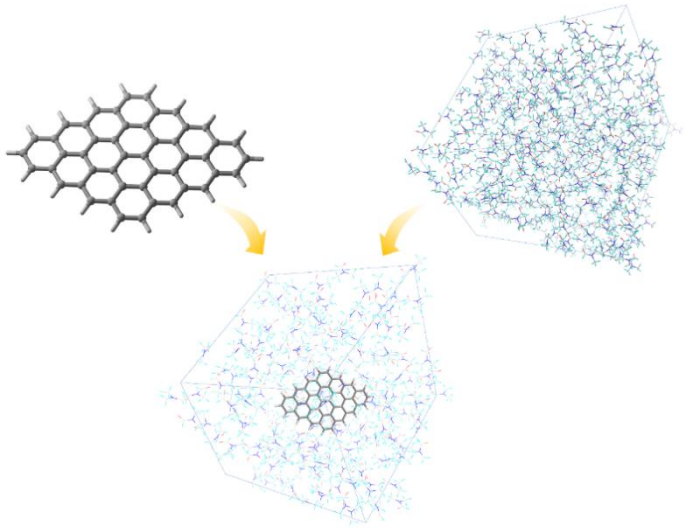

Figure S12 *Schematic representation of the studied system: graphene surrounded by 512 DMF molecules.*

The data from 100 ns long MD simulations were performed using scripts written in Python. Firstly, the trajectory of the system was divided into 1000 frames, i.e., we have an image of the whole system every 0.1 ns. These frames were analyzed identifying ten configurations containing two or three molecules of DMF with different orientations (with respect to graphene) were identified as the most frequent ones. Three different SLG-DMF configurations, identified as **A**, **B** and **C** (see **Figure S13**), were found with the highest occurrence of 59.7%, 17.6% and 8.1%, respectively. The rest of configurations showed an occurrence below 5% and 1% (see red and blue regions depicted in **Figure S14**).

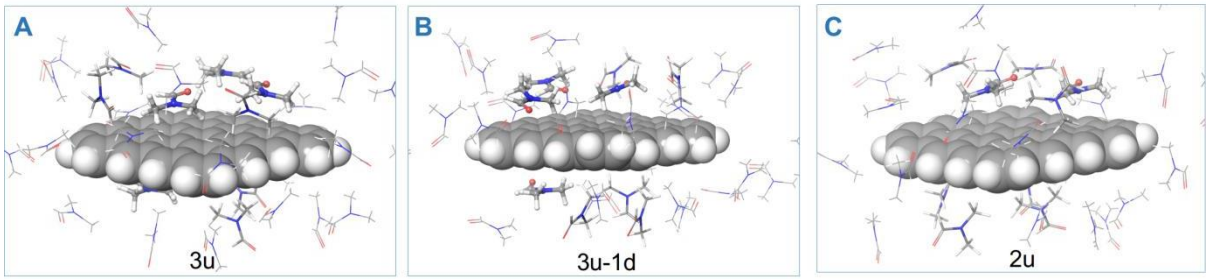

Figure S13 *The three different SLG-DMF configurations with the highest occurrence: A (59.7%), B (17.6%) and C (8.1%).*

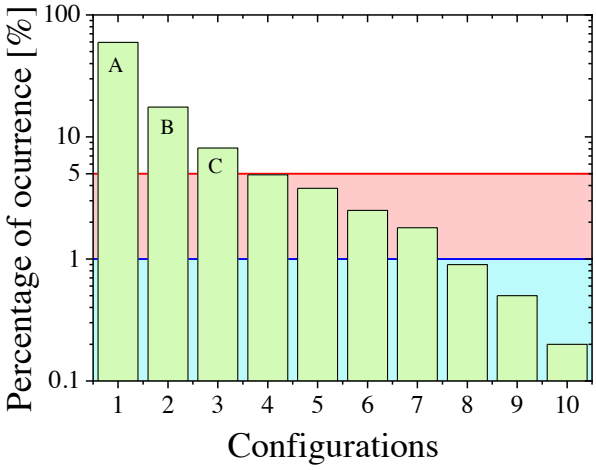

Figure S14 *Percentage of occurrence of the different identified configurations.*

A snapshot of SLG and some DMF molecules around of it is displayed in **Figure S15**. The natural formation of the hydrogens bonds with distances ~ 2.6-3.0 Å are shown with pink dotted lines.

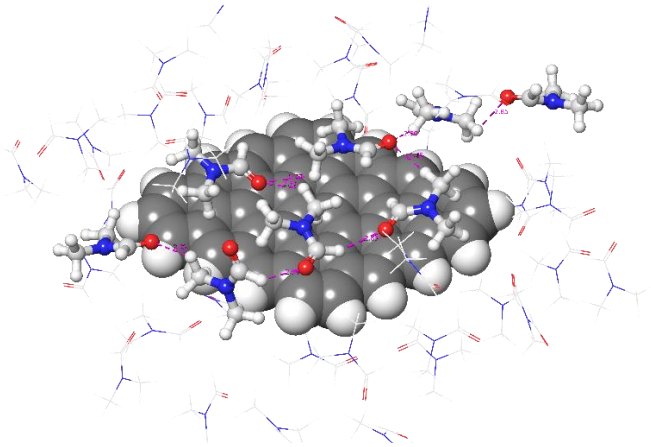

Figure S15 *Representative snapshot of the MD simulation showing the natural formation of hydrogen bonds among DMF molecules.*

4. DFT energy calculation, second geometry optimization and Raman modes

4.1 Energy calculation of MD configurations

The energy calculations of SLG-DMF systems were carried out for each configuration using the hybrid functional B3LYP, including London dispersion corrections suggested by Grimme [25]. This correction helps in the distribution of charges in hydrocarbon molecules and in molecules where inter and intramolecular van der Waals interactions are very important, as in the case of graphene structures. The ωB97X-D3 functional [26,27] with the 6-311+G(d,p) basis set was also used.

Configuration **A** turned out to be the most energetically favorable system, containing three DMF molecules that were oriented in parallel to the SLG. Configuration **B** presented a similar configuration to **A** but with an extra DMF molecule located under graphene, also with a parallel orientation. This extra molecule produces an energy imbalance of the system of 5.2 kcal/mol as compared to **A**, as shown

in **Figure S16**. Configuration **C** is the simpler system, which contains 2 molecules of DMF in a parallel orientation located in the center of SLG and was found 7.3 kcal/mol above **A**.

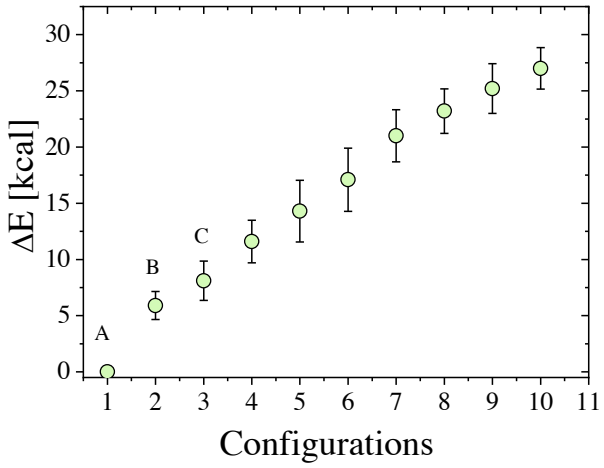

Figure S16 *DFT energy difference between the most energetic favorable SLG-DMF configurations (A) and the remaining two configurations.*

4.2 Molecular orbitals and non-covalent interactions (NCI)

To better understand the nature of SLG-DMFs interaction, we examined the electronic properties of the bound states. The highest occupied molecular orbital (HOMO) and the lowest unoccupied molecular orbitals (LUMO) of SLG-DMFs systems (**A**, **B** and **C**) are shown in **Figure S17**. The HOMO-LUMO gap is similar for the three studied configurations. Both the LUMO and the HOMO, HOMO-1 and HOMO-2 orbitals are mainly located in the SLG, which defines the gap of the system. The HOMO-3 shows the best delocalization of the electronic density, being a mixture of DMF and SLF states. On the DMF molecule, it is located mainly on the nitrogen and oxygen (where the available p orbitals for π-π interactions), and delocalized over the entire SLG. As expected, the electronic density is concentrated on the amide group due to the delocalization of the nitrogen electron pair onto the C=O group. Configuration **A** clearly shows the highest electron density in comparison with the other configurations. In all the cases, the gap between the sub-level HOMO-3, and its corresponding LUMO is ~0.22 eV. In other words, the parallel geometry of the DMF molecules in respect to SLG favors the formation of a molecular orbital, with participation of the DMF p-orbitals (HOMO-3), and delocalized π states of graphene.

Another method to evaluate non-covalent interactions (NCIs) is based on the analysis of reduced density gradient [28,29]. We analyzed the electron densities and their reduced gradients obtained in the DFT calculations, for the three configurations (**A**, **B** and **C**) using NCIPlot[30]. This method enables the identification of NCIs by plotting the isosurfaces of the reduced density gradient in the real space. This approach allows to distinguish a wide range of binding energies, encompassing strong and weak

(attractive and repulsive) intermolecular interactions such as: CH-π and π-π, van der Waals, hydrogen and halogen bonds, etc. As is shown in **Figure S18**, weak interactions are present in all the SLG-DMF configurations. However, the configuration A shows the largest interaction area in relation with the other configurations.

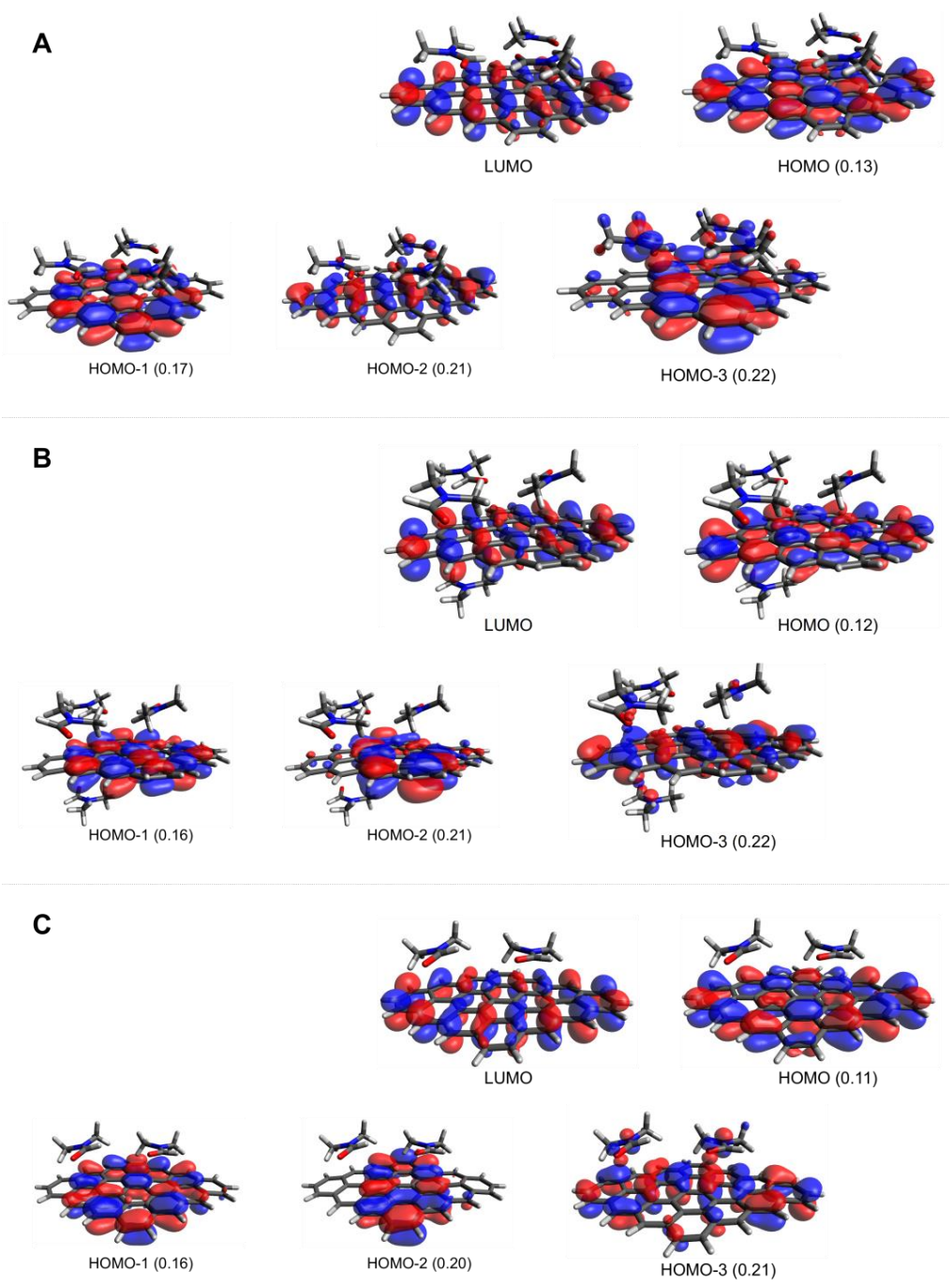

Figure S17 *HOMO and LUMO orbitals of the **A**, **B** and **C** configurations. The number in parentheses are the energy differences between the corresponding frontier orbitals. The red and blue clouds represent the regions positive and negative values of the wavefunctions, respectively.*

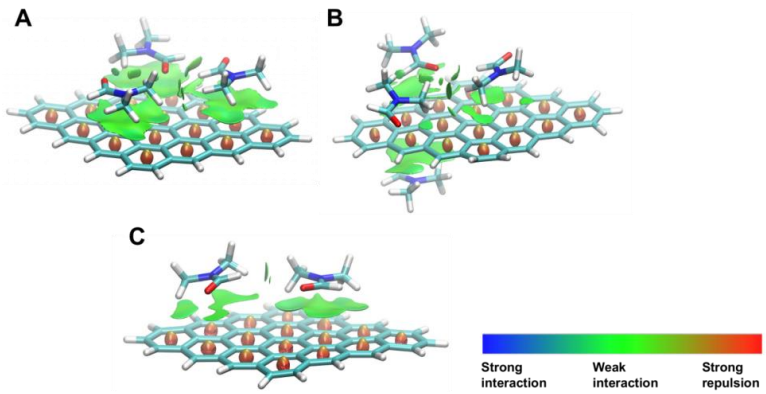

Figure S18 *Analysis of non-covalent interactions of the three studied configurations.*

4.3 Raman calculation

The Raman frequencies were calculated at gamma point for the three optimized configurations. We used two different functionals B3LYP and ωB97X-D3 with 6-311+G(d, p) as the basis set. The calculations also included the dispersion correction suggested by Grimme [25]. **Table S5** shows the comparison between the experimental Raman peaks of pure DMF and 0.05 wt% NF and the theoretical results. We identified two Raman modes as: rocking (1091 cm^{-1}) and stretching (1438 cm^{-1}). It can be seen that both the experimental data and the theoretical modelling of the Raman peaks are blue shifted in respect to the pure DMF.

Table S5 *Calculated Raman frequencies for the SGL–DMF configurations using B3LYP-D/6-311+G (p,d) and ωB97X-D3/6-311+G (p,d).*

Experimental frequencies (cm^{-1})		Theoretical frequencies (cm^{-1})							
		B3LYP-D/6-311+G(d,p)				ωB97X-D3/6-311+G(d,p)			
DMF	0.05 wt.%	DMF	A	B	C	DMF	A	B	C
1090.9	1092.6	1092.9	1096.3	1113.0	1094.2	1103.0	1108.5	1110.1	1111.5
1438.5	1439.8	1430.7	1443.7	1442.5	1440.3	1452.0	1448.2	1458.0	1454.0

4.4 Height dependent radial distribution of DMF

To investigate the formation of layering and increased order in the DMF solvent interacting with the SLG flake, we computed the nitrogen-nitrogen pair-correlation function of DMF as a function of the height above (or below) the SLG from a 10 ns NPT simulation of a single flake in DMF. Here, a disk-like SLG of 348 carbon atoms was built with the Avogadro software, positioned in a cubic box with its normal vector along the z-axis, and dissolved in 4350 DMF molecules using the Packmol software [31]. The NPT (constant temperature and pressure) simulation was performed with the LAMMPS [32] program using the fully flexible OPLS-AA force field [33], after energy minimizing and performing 100 ps runs for (*i*) isochoric warming up, (*ii*) NVT (constant temperature and volume) equilibration, and (*iii*) NPT equilibration. The RESPA multi-time step algorithm [34] was used with an outer time step of 1 fs. The temperature was controlled at T =300 K by a CSVR thermostat [35] with a period of 0.1 ps, while a Parrinello-Rahman barostat [36] set to p =1 atm was employed with a period of 1 ps. In each stage of these

simulations, the SLG was constrained to remain with its normal vector along the *z*-axis by removing every MD step any total angular velocity from the SLG.

The height dependent pair-correlation function (or radial distribution function) was obtained by computing over the 10 ns trajectory (1 ps frame interval) the relative density of nitrogen atoms around a central nitrogen atom as a function of its distance in a 2D slab with thickness $d\boldsymbol{z}$. Note that, at variance with the usual radial distribution, which quantifies the relative density on a 3D sphere ($g(\boldsymbol{r})= 4\pi r^2 \rho d\boldsymbol{r}$), here we obtain the density on the surface of a cylinder with height $d\boldsymbol{z}$ ($g(\boldsymbol{r})= 2\pi \boldsymbol{r} \rho d\boldsymbol{r} d\boldsymbol{z}$), centered at the central nitrogen atom. In the loop over central nitrogen atoms, only atoms were selected that were within 4 Å of the main axis of the 33-Å diameter SLG, and their $\boldsymbol{z}$-height above (or below) the flake was histogrammed with a bin size of $d\boldsymbol{z}$. The radial bin size, $d\boldsymbol{r}$, was set to 0.1 Å and $d\boldsymbol{z}$ was set to 1.0 Å. For convenience we will rename the coordinates as: $\boldsymbol{z}$ = *x*-axis and $\boldsymbol{r}$ = *y*-axis following the axis nomenclature of the **Figure S19*a***.

Figure S19*a* shows three dimensional color map of nitrogen-nitrogen (N-N) pair as function of graphene distance (*x*-axis) and N-N pair distance (*y*-axis). Far from the flake, at $x \approx \pm$ 29.5 Å, is seen a high density centered at $y \approx$ 6.0 Å as is shown green solid lines of **Figure S19*b***, i.e., the typical liquid behavior. Where the contribution of the first coordination shell is always higher than non-existing second, third shells, etc. due the non-long range order in a liquid. However, near the flake at $x \sim \pm$3.45 Å three well defined peaks are seen at N-N distance $y \approx$ 6.5, 11.6 and 16.5 Å, corresponding to first, second and third coordination shells, respectively (see black solid line in **Figure S19*b***). These results show a strongly ordered (although still liquid) structure of the DMF molecules close to the graphene.

Figure S19*b* shows that the first peak at $x \approx$ 3.45 Å is shifted ~ 0.5 Å in respect with the analogous peak at higher distances from the graphene flake. This can be explained in terms of the preferential orientation of the DMF molecules. Further from graphene there is not a preferential orientation of DMF molecules, but close to graphene they tend to lay parallel to the flake, requiring a larger N-N distance in the first coordination shell.

Figure S19*c* shows an interesting behavior of the liquid as a function of graphene distance (*x*), as can be seen the plot shows an oscillatory trend of the N-N correlation function as a function of graphene distance. The minimum and maximum profile in the *x*-direction, reveal that there is a short range structuring of DMF molecules extending to ~ 20 Å out from the flake. Certainly, three DMF layers can be distinguished, reaching at least 15 Å from the flake. The maximum height of the peaks can be seen at a distance of $x \approx$ 3.45 Å (black solid line in **Figure S19*b*** and grey dotted line in **Figure S19*c***) and followed by a minimal density at $x \approx$ 6.2 Å from the flake (see grey dotted line in **Figure S19*b*** and first dip of **Figure S19*c***), which separates the first DMF layer from the second. Therefore, graphene is affecting not only the 'layer' of DMF molecules which is in direct contact with the flake but the second and third layers. The effect is lost thereafter. In the *y* direction, the DMF structuring ranges at least 18

Å, which is remarkable considering that the flake radius is only 16.5 Å; hence, on larger flakes even longer-ranged ordering may be expected.

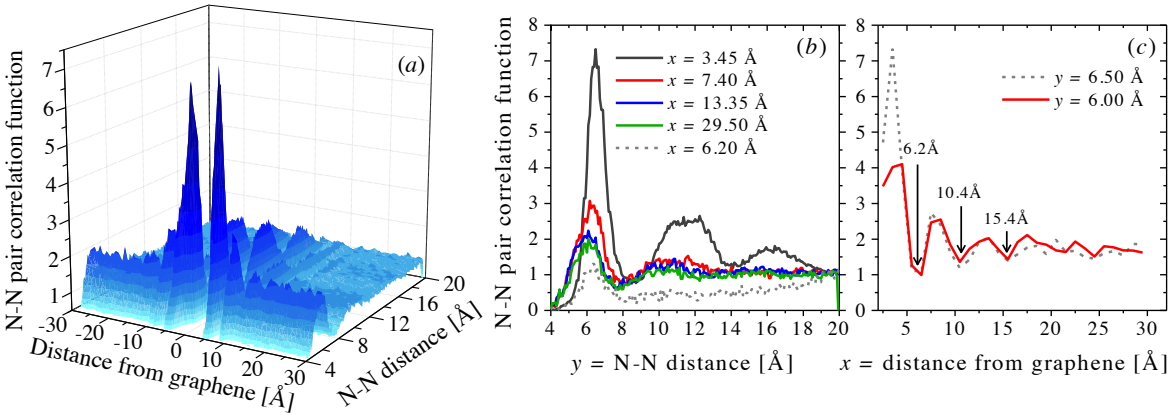

Figure S19 (*a*) *Three dimensional (3D) color map of nitrogen-nitrogen pair correlation function (z-axis) as function of graphene distance (x-axis) and N-N distance (y-axis).* (*b*) *Five vertical cuts of the 3D color map at different distances of the graphene flake (x) in the zy-plane.* (*c*) *Two vertical xz-plane cuts centered at different N-N distances (y).*

References

1 H. Hermann, T. Schubert, W. Gruner and N. Mattern, *Nanostructured Mater.*, 1997, **8**, 215–229.

2 V. Trisaksri and S. Wongwises, 2007, **11**, 512–523.

3 S. Nemoto, *Appl. Opt.*, 1992, **31**, 6690.

4 T. M. Aminabhavi and B. Gopalakrishna, *J. Chem. Eng. Data*, 1995, **40**, 856–861.

5 V. Venkata Chalapathi and K. Venkata Ramiah, *Proc. Indian Acad. Sci. - Sect. A*, 1968, **68**, 109–122.

6 D. G. Cahill, *Rev. Sci. Instrum.*, 1990, **61**, 802–808.

7 D. G. Cahill, *Rev. Sci. Instrum.*, 2002, **73**, 3701.

8 F. Chen, J. Shulman, Y. Xue, C. W. Chu and G. S. Nolas, *Rev. Sci. Instrum.*, 2004, **75**, 4578–4584.

9 D.-W. Oh, A. Jain, J. K. Eaton, K. E. Goodson and J. S. Lee, *Int. J. Heat Fluid Flow*, 2008, **29**, 1456–1461.

10 S. D. Lubner, J. Choi, G. Wehmeyer, B. Waag, V. Mishra, H. Natesan, J. C. Bischof and C. Dames, *Rev. Sci. Instrum.*, , DOI:10.1063/1.4905680.

11 D. R. Lide, *CRC Handbook of Chemistry and Physics*, Boca Raton, FL, CRC Press., 2005.

12 J. L. Banks, H. S. Beard, Y. Cao, A. E. Cho, W. Damm, R. Farid, A. K. Felts, T. A. Halgren, D. T. Mainz, J. R. Maple, R. Murphy, D. M. Philipp, M. P. Repasky, L. Y. Zhang, B. J. Berne, R. A. Friesner, E. Gallicchio and R. M. Levy, *J. Comput. Chem.*, 2005, **26**, 1752–1780.

13 G. A. Kaminski, R. A. Friesner, J. Tirado-Rives and W. L. Jorgensen, *J. Phys. Chem. B*, 2001, **105**, 6474–6487.

14 M. D. Hanwell, D. E. Curtis, D. C. Lonie, T. Vandermeersch, E. Zurek and G. R. Hutchison, *J. Cheminform.*, 2012, **4**, 17.

15 S. H. Vosko, L. Wilk and M. Nusair, *Can. J. Phys.*, 1980, **58**, 1200–1211.

16 C. Lee, W. Yang and R. G. Parr, *Phys. Rev. B*, 1988, **37**, 785–789.

17 A. D. Becke, *J. Chem. Phys.*, 1993, **98**, 5648–5652.

18 P. J. Stephens, F. J. Devlin, C. F. Chabalowski and M. J. Frisch, *J. Phys. Chem.*, 1994, **98**, 11623–11627.

19 R. Ditchfield, W. J. Hehre and J. A. Pople, *J. Chem. Phys.*, 1971, **54**, 724–728.

20 M. J. Frisch, G. W. Trucks, H. B. Schlegel, G. E. Scuseria, M. A. Robb, J. R. Cheeseman, G. Scalmani, V. Barone, B. Mennucci, G. A. Petersson, H. Nakatsuji, M. Caricato, X. Li, H. P. Hratchian, A. F. Izmaylov, J. Bloino, G. Zheng, J. Sonnenb and D. J. Fox, 2009.

21 U. C. Singh and P. A. Kollman, *J. Comput. Chem.*, 1984, **5**, 129–145.

22 B. H. Besler, K. M. Merz and P. A. Kollman, *J. Comput. Chem.*, 1990, **11**, 431–439.

23 J. P. Merrick, D. Moran and L. Radom, *J. Phys. Chem. A*, 2007, **111**, 11683–11700.

24 2017.

25 S. Grimme, *Wiley Interdiscip. Rev. Comput. Mol. Sci.*, 2011, **1**, 211–228.

26 J.-D. Chai and M. Head-Gordon, *Phys. Chem. Chem. Phys.*, 2008, **10**, 6615.

27 J.-D. Chai and M. Head-Gordon, *J. Chem. Phys.*, 2008, **128**, 84106.

28 E. R. Johnson, S. Keinan, P. Mori-Sa´nchz, J. Contreras-Garc a, A. J. Cohen and W. Yang, *J. Am. Chem. Soc.*, 2010, **132**, 6498–6506.

29 G. Saleh, C. Gatti and L. Lo Presti, *Comput. Theor. Chem.*, 2012, **998**, 148–163.

30 J. Contreras-Garc a, E. R. Johnson, S. Keinan, R. Chaudret, J.-P. Piquemal, D. N. Beratan and W. Yang, *J. Chem. Theory Comput.*, 2011, **7**, 625–632.

31 L. Martínez, R. Andrade, E. G. Birgin and J. M. Martínez, *J. Comput. Chem.*, 2009, **30**, 2157–2164.

32 S. Plimpton, *J. Comput. Phys.*, 1995, **117**, 1–19.

33 W. L. Jorgensen and J. Tirado-Rives, *J. Am. Chem. Soc.*, 1988, **110**, 1657–1666.

34 M. Tuckerman, B. J. Berne and G. J. Martyna, *J. Chem. Phys.*, 1992, **97**, 1990–2001.

35 G. Bussi, D. Donadio and M. Parrinello, *J. Chem. Phys.*, 2007, **126**, 14101.

36 M. Parrinello and A. Rahman, *J. Appl. Phys.*, 1981, **52**, 7182–7190.

Article 2

nanomaterials

MDPI

Article

Modification of the Raman Spectra in Graphene-Based Nanofluids and Its Correlation with Thermal Properties

María del Rocío Rodríguez-Laguna [1,2,*], Pedro Gómez-Romero [1,*], Clivia M. Sotomayor Torres [1,3] and Emigdio Chavez-Angel [1,*]

1 Catalan Institute of Nanoscience and Nanotechnology (ICN2), CSIC and The Barcelona Institute of Science and Technology (BIST), Campus UAB, Bellaterra, 08193 Barcelona, Spain; clivia.sotomayor@icn2.cat
2 Department of Chemistry, Universitat Autònoma de Barcelona, Campus UAB, Bellaterra, 08193 Barcelona, Spain
3 ICREA- Institució Catalana de Recerca i Estudis Avançats, Pg. Lluís Companys 23, 08010 Barcelona, Spain
* Correspondence: rodriguez3laguna@gmail.com (M.d.R.R.-L.); pedro.gomez@icn2.cat (P.G.-R.); emigdio.chavez@icn2.cat (E.C.-A.); Tel.: +34-93-7373616 (M.d.R.R.-L.); +34-93-7373608 (P.G.-R.); +34-93-7371617 (E.C.-A.)

Received: 13 May 2019; Accepted: 24 May 2019; Published: 26 May 2019

Abstract: It is well known that by dispersing nanoparticles in a fluid, the thermal conductivity of the resulting nanofluid tends to increase with the concentration of nanoparticles. However, it is not clear what the mechanism behind this phenomenon is. Raman spectroscopy is a characterization technique connecting the molecular and macroscopic world, and therefore, it can unravel the puzzling effect exerted by the nanomaterial on the fluid. In this work, we report on a comparative study on the thermal conductivity, vibrational spectra and viscosity of graphene nanofluids based on three different amides: *N*, *N*-dimethylacetamide (DMAc); *N*, *N*-dimethylformamide (DMF); and *N*-methyl-2-pyrrolidinone (NMP). A set of concentrations of highly stable surfactant-free graphene nanofluids developed in-house was prepared and characterized. A correlation between the modification of the vibrational spectra of the fluids and an increase in their thermal conductivity in the presence of graphene was confirmed. Furthermore, an explanation of the non-modification of the thermal conductivity in graphene-NMP nanofluids is given based on its structure and a peculiar arrangement of the fluid.

Keywords: raman of nanofluids; enhancement of thermal conductivity; nanofluids; graphene

1. Introduction

The continuous trend towards miniaturization in the electronics industry has led to smaller devices with more processing power. However, as dimension decreases, the effective thermal conductivity (k) of each component also decreases and, consequently, energy losses increase [1]. In the case of the emerging charge-based nanoelectronic switches, the density of these devices is limited by a maximum allowable power dissipation of ~100 W/cm^2, and not by their size [2].

Therefore, it is a matter of high priority to design effective and novel cooling strategies, at a reasonable price to meet the cooling needs of the electronics industry. To guarantee proper performance and reliability of electronic components, excess heat must be carried away from critical components and hot spots, and then dissipated to the environment. Conduction and convection are the primary modes of heat transfer in cooling strategies of electronics, where radiation expels only a small part of the total thermal load. Conventional cooling strategies can be divided into active and passive. Passive cooling does not consume energy and is mainly based on natural convection, radiation, and heat conduction by utilizing heat spreader or a heat sink with very high thermal conductivity.

Metal materials, such as aluminum, copper, zinc, are the most used as heat sinks [3]. Passive cooling technology relies on maximizing heat transfer by conduction, radiation, and convection using heat sinks, heat spreaders, heat pipes, or thermal interface materials to maintain optimal operating temperatures. These components can be found in all electronic devices and only require an architectural design of heat sinks and choice of the right material [4]. Active cooling, on the other hand, requires an external device (e.g., a fan) to force the cooling of the system. However, a major drawback of this technology is related to the consumption of extra energy to keep the device in operation although the rate of heat removal is much larger than that provided by passive cooling methods (except strategies using latent heat) [5]. Thus, active cooling can deal with higher power densities, and current cooling strategies include: Forced-air and forced-liquid cooling, direct liquid immersion, thermoelectric coolers, and forced convection [5–7].

The vast majority of active cooling systems include a heat sink or heat spreader in direct contact with the heat source. Excess heat is transported away from the electronic component by (1) conduction towards the cold edges of the solid piece or to a second piece (heat sink, pipe or cold plate) and then, by (2) forced convection in air or liquid. It is clear that the material, together with the structural and architectural design of heat sink, is crucial to increase efficiency levels of active cooling systems. Great efforts have been made to improve the performance of current heat sinks, such as the modification of the architectural designs [8–11], development of composite materials with enhanced thermal properties (metal-SiC, metal-graphene/diamond) [3,12–14], and study and control of the structure to enhance their thermal conductivity (e.g., porosity) [14]. Therefore, to improve the efficiency of active cooling systems, there must be an optimization of solid materials acting as heat sinks/spreaders/pipes and active components, such as fluids and those related to mechanical forces (fan, pump, etc.).

Among these active methods, the air-based (heat-sink-and-fan) can be found in many electronic devices from the cheapest laptop to the most expensive laboratory equipment. However, this is an old technology and not always efficient. Furthermore, it is not cost-effective for the dissipation of large amounts of heat. Murshed and Nieto de Castro [5] demonstrated that forced convection of air has very low heat removal rates compared with forced convection of liquids and that natural convection has the lowest heat removal rate among all cooling modes.

In this context, liquid-cooling technology has proven to be an efficient and low-cost method to cool high-power components [5,15,16], despite the potential risk of having liquid close to an electronic device. This becomes evident in the designs of high-density boards, where air cooling can become so challenging that the only viable option is the use of liquid cold plate technologies. [17] In any case, it is important to remark that the implementation of an effective cooling strategy in both high-power and low-power components may require the use of a combination of liquid- and air-cooling technologies, as well as a proper design of the passive components (heat sinks and heat spreaders).

Within liquid-based active cooling, the most common is the use of heat transfer fluids (or coolants) confined in basins. The coolant flows from tower pumps through pipes along the hot side of the device, thereby reducing the temperature.

Conventional coolants are mainly classified into dielectric and non-dielectric fluids. Dielectric coolants are organic-based fluids with quite low thermal conductivity but widely used in direct liquid immersion systems, while, the non-dielectric coolants are preferred for heat pipes and microfluidics due to their superior thermal properties compared to their dielectric counterparts. They are normally aqueous solutions and thus exhibit quite a high heat capacity and low viscosity. Water, ethylene glycol, and mixtures of these two are the most popular and widely used as coolants for many electronic devices [5]. However, a major problem of conventional coolants is the low heat exchange rate and thermal conductivity, which is too small to meet the coming needs and challenges in the field. One way to overcome this barrier is by using solid particles dispersed in fluids to improve their thermal properties [18–20].

Nanofluids (NFs) are colloidal dispersions of nanoparticles (1–100 nm) suspended in a base liquid [21]. The presence of well-dispersed nanoparticles in a fluid can provide remarkable improvements in thermal properties, such as thermal conductivity [18,22–27] and in some cases, specific heat capacity [27–34]. The heat transfer performance of a number of nanofluids has been tested compared to that of their base fluids in commercial electronic cooling units for CPUs and chips, as well as in heat pipes (passive cooling). The results are promising, showing an effective decrease in the temperature of the electronic components (CPUs and chips) [35–39] as well as an enhancement in the heat transfer performance of heat pipes [40–44].

Several studies have been reported on the enhancement of thermophysical properties in nanofluids, however, the mechanism behind this phenomenon is not clear [45–49]. In the literature, at least six different mechanisms have been suggested for explaining this enhancement: (*i*) Increase of the thermal transfer due to Brownian motion of nanoparticles, (*ii*) localized convection created in the fluid due to Brownian motion of nanoparticles, (*iii*) agglomeration of nanoparticles, (*iv*) enhanced thermal energy transfer due to increased interatomic interactions arising from the modification of interatomic potential, (*v*) ordered layering of liquid around the solid, and (*vi*) ballistic phonon transport of heat through solid nanoparticles [45–49]. In a previous report [27], we showed that for these kinds of fluids (amides) the mechanisms: (*i*), (*ii*) and (*iii*) cannot explain our experimental observations. In addition, the displacement of some Raman modes of DMF-graphene NFs led us to conclude that there is a strong modification of the interatomic potential as a function of graphene concentration, as the model (*iv*) suggests.

Taking into account all of the above, in this paper, we report an extension of our previous work related to the enhancement of thermophysical properties of graphene-based nanofluids [27]. Here, we present a thorough study of the vibrational properties of two previously reported NFs based on: N, N-dimethylacetamide (DMAc) and N, N-dimethylformamide (DMF) and we extend the work to a NF based on N-methyl-2-pyrrolidinone (NMP). The thermophysical properties of each NF are discussed based on the Raman observations.

2. Materials and Methods

Graphene flakes were prepared from graphite (Sigma-Aldrich, purity > 99% and size < 20 um, St. Louis, MO, USA) by mechanical exfoliation. An extended description of the sample preparation can be found in the section on experimental methods in the supporting information of Reference [27]. The produced graphene size was around 150–450 nm and the number or layers varied from 2–10. *N*, *N*-dimethylacetamide (ACROS Organics, 99+%, Fair Lawn, NJ, USA), *N*, *N*-dimethylformamide (Scharlau, HPLC grade, Barcelona, Spain) and *N*-methyl-2-pyrrolidinone (Sigma Aldrich, 99.5%, St. Louis, MO, USA) were used as the base fluids. The preparation of the nanofluids consisted of direct mixing of the base fluid with graphene nanosheets. Then, graphene was dispersed in the fluid using a planetary ball mill (All-direction planetary ball mill 0.4 L, model CIT-XBM4X-V 0.4 L, Columbia International, Irmo, SC, USA) and soft ultrasonic vibration (Ovan, model ATM40-6LCD, Barcelona, Spain) for 1 hour. These techniques were used to suppress the formation of particle clusters in order to obtain stable dispersions [50]. The samples were later centrifuged for one hour at 6000 rpm to ensure the stability of the NFs. The stability of the dispersions was evaluated by periodic analyses using dynamic light scattering (DLS) as is described in [27].

The measurements of thermal conductivity of the nanofluids were carried out by using the well-known three-omega (3ω) method [51,52] in the bidirectional configuration [53,54]. An extended description of the setup can be found in the section on experimental methods in the supporting information of References [27,55]. The effective viscosity of the nanofluids was measured using a Haake RheoStress RS600 rheometer from Thermo Electron Corp. at T = 20–21 °C. The shear rate used was 2880 s^{-1} with a measurement time of 30 seconds. The Raman spectra were recorded by T64000 Raman spectrometer manufactured by HORIBA Jobin Yvon (Chilly-Mazarin, France). It was used in single grating mode (2400 lines) with a spectral resolution better than 0.4 cm^{-1}. The NF was placed

in a transparent quartz cuvette. Then a green diode laser (λ = 532 nm) was focused on the cuvette by using a 50× long working distance microscope objective. The power of the laser was kept as low as possible (<2 mW) to avoid any possible effect from self-heating. Raman analyses of the samples were repeated under similar conditions as a function of time (day 1, after ~one month and more than one year later) to verify the reproducibility of the Raman spectra (See Figures S1–S3 in the supporting information for more details).

3. Results and Discussions

3.1. Thermal Conductivity and Viscosity Measurements

The Table 1 shows the thermal conductivity for different graphene concentrations (C) in nanofluids based on *N*, *N*-dimethylformamide (DMF), *N*, *N*-dimethylacetamide (DMAc) and *N*-methyl-2-pyrrolidinone (NMP). Progressive enhancement of *k* was observed in DMAc and DMF-based nanofluids (NFs) as C increased, with a maximum enhancement of ~48% for *C* = 1.50 mg/mL in DMAc-based NF. Concentrations between 0.1–0.5 mg/mL in DMF and DMAc produced relatively large enhancements of ~6–25% and 3–17%, respectively. While in the same set of concentrations no significant enhancement of *k* was detected in NMP-based NFs. In contrast, in the case of viscosity, a maximum enhancement of ~44% was observed for 0.50 mg/mL graphene in NMP.

Table 1. Thermal conductivity and viscosity of graphene based nanofluids.

Concentration		Samples					
		DMAc *		DMF *		NMP (This Work)	
mg/mL	wt%	*k* (W m^{-1} K^{-1})	Viscosity (mPa·s)	*K* (W m^{-1} K^{-1})	Viscosity (mPa·s)	*k* (W m^{-1} K^{-1})	Viscosity (mPa·s)
0.00	0	0.175	1.19	0.183	0.94	0.235	2.07
0.05	0.005	-	-	-	-	0.234	2.19
0.10	0.01	0.180	1.17	0.194	0.99	0.236	2.21
0.25	0.03	0.196	1.18	0.203	1.01	-	-
0.50	0.05	0.206	1.26	0.228	1.08	0.213	2.92
1.13	0.12	-	-	-	1.26	-	-
1.50	0.18	0.259	1.68	-	-	-	-

* Taken from Rodríguez-Laguna et al. [27].

An increase in viscosity as the nanoparticle concentrations rise has been frequently observed in graphene-based [23,26,56–59] and other NFs [23,26]. This enhancement has been commonly associated with the tendency of the nanoparticles to agglomerate under pressure. The agglomerates raise the internal shear stress and the resistance to flow in the NF, which leads to an increase in viscosity during measurement [58].

3.2. Raman Measurements

Firstly, we will discuss the Raman characterization of DMAc and DMF as a function of graphene concentration ranging from 0 < C < 1.5 and 0 < C < 1.13 mg/mL, respectively. Due to the very high light absorption of the most concentrated dispersions (C = 1.5 and 1.13 mg/mL for DMAc and DMF, respectively), we were only able to detect one peak in the entire Raman spectrum. The vibrational assignment for DMAc and DMF was done based on the work of Chalapathi and Ramiah [60]. Secondly, we will show and discuss the Raman spectra of NMP-NFs for three different graphene concentrations of *C* = 0, 0.05 and 0.10 mg/mL. The vibrational assignment was carried out based on the work of Peek and McDermott [61] and Xu et al. [62]. The peak positions of all the NFs were estimated using a Lorentzian fit considering a constant background. Raman analyses of the samples were repeated under similar conditions as a function of time: Day 1, after ~one month and one year later. We found excellent reproducibility of the Raman spectra of DMAc, DMF, and NMP-nanofluids as can be seen in

Figures S1–S3 that are shown in the supporting information. These results confirm the high stability of these dispersions over time and are in agreement with previously performed DLS analyses [27].

3.2.1. Raman of DMAc- and DMF-Based Nanofluids

Graphene-DMAc Nanofluids

The Raman spectra of DMAc for different graphene concentrations are displayed in Figure 1a,c. A clear shift can be observed for the Raman bands around 470 cm^{-1} (see Figure 1b). This band corresponds to the scissoring vibration of the bond (CH$_3$–N–CH$_3$) of the DMAc molecule [60]. The displacement of this band is a strong indicator of a strong modification of interatomic forces within the nanofluid.

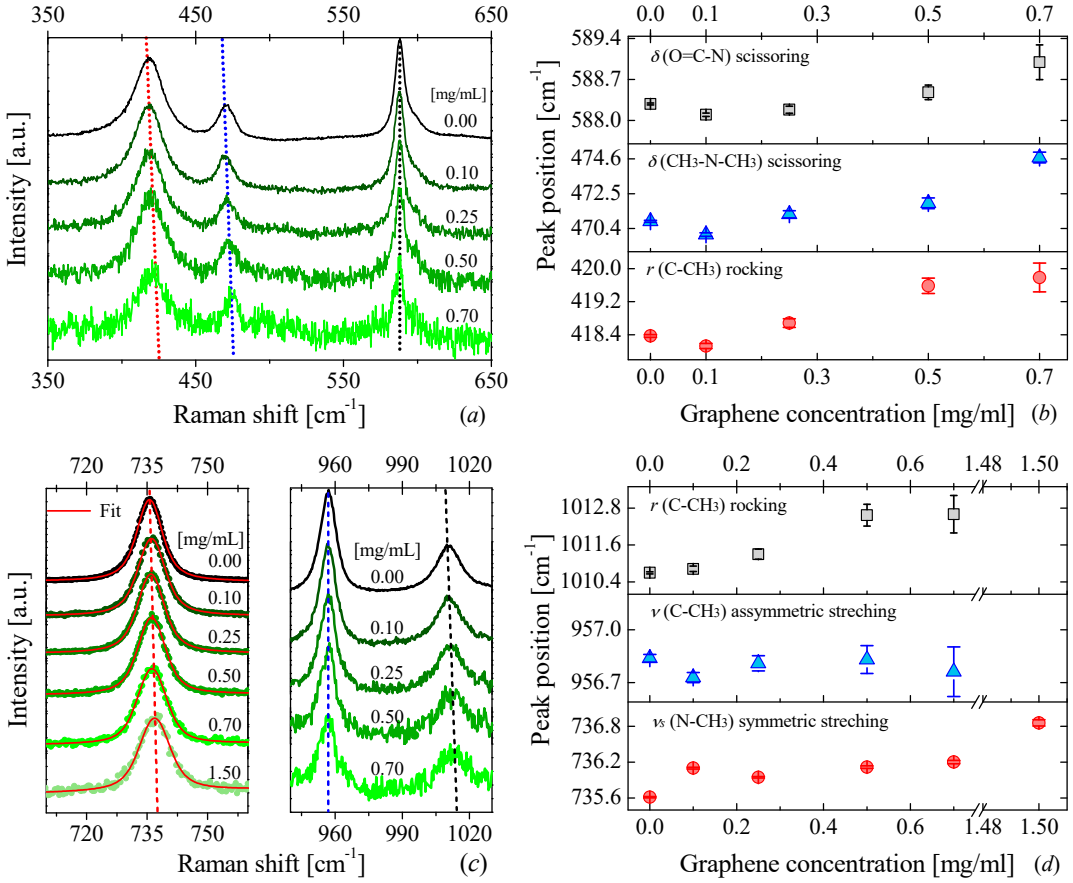

Figure 1. Raman scattering of DMAc-based NFs and peak positions of several Raman bands: (**a**,**c**) Raman spectra of DMAc-based NFs for different graphene concentrations, (**b**,**d**) peak positions of six Raman bands shown in (**a**,**c**) as a function of graphene concentration.

Graphene-DMF Nanofluids

A similar effect can also be observed in DMF-based nanofluids as displayed in Figure 2b,d Here, the largest displacement ~4 cm^{-1} occurred for a rocking vibration of the bond (CH$_3$)–N of the DMF molecule. In a previous study, we related such observations to the presence of the graphene flakes [27]. In this study, simulations based on density functional theory (DFT) and molecular dynamics (MD) suggested that the presence of the graphene flake acts as an external force field that induces a parallel orientation of the DMF molecules in the proximity of the graphene flakes.

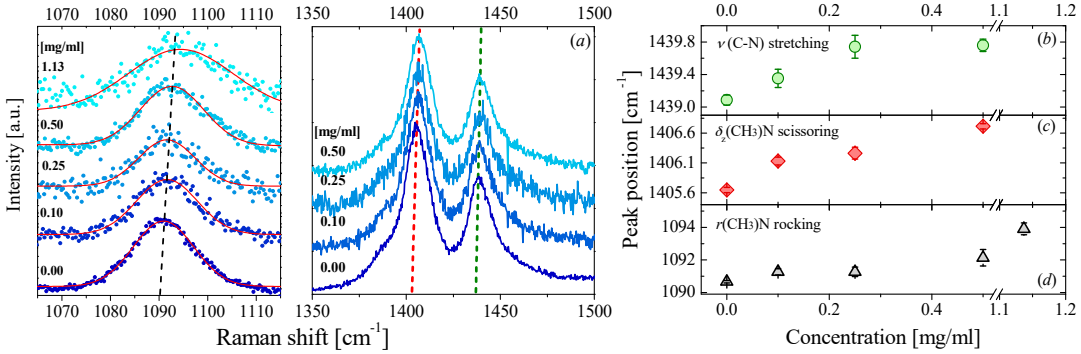

Figure 2. Raman scattering of DMF-based NFs and peak positions of several Raman bands: (**a**) Raman spectra of DMF-based NFs for different graphene concentrations, (**b**–**d**) peak positions of three Raman bands shown in (**a**) as a function of graphene concentration.

Figure 2. Raman scattering of DMF-based NFs and peak positions of several Raman bands: (**a**) Raman spectra of DMF-based NFs for different graphene concentrations, (**b**–**d**) peak positions of three Raman bands shown in (**a**) as a function of graphene concentration.

Taking into account that both graphene and DMF molecules contain a *p*-orbital with unshared electron pairs (delocalized electrons) along the flat plane direction [63,64], the parallel orientation of the DMF molecules with respect to the graphene flakes favor the overlap of two adjacent *p*-orbitals. It can favor a π-π bond between the solvent molecules and the graphene surface. This interaction thus increases the rigidity of the bonds of the molecules closest to graphene, consequently, modifies their Raman spectra. It is important to mention that our simulations suggest that this interaction is local, rather than global, i.e., just the molecules around of graphene flakes feel this change. It is not clear how the rest of the fluid is also affected by this interaction. Returning to DMAc NFs, a similar blue-shift in several Raman modes can be observed. If we consider that DMF and DMAc molecules are amides with quite similar structures and electron delocalization, then it is reasonable to suggest that a similar geometric configuration occurs in DMAc-based NFs. As a consequence, DMAc molecules may also tend to lay parallel to the graphene flakes favoring a π-π stacking between the graphene and the molecules thereby contributing to the blue-shift of the Raman spectra.

Taking into account that both graphene and DMF molecules contain a *p*-orbital with unshared electron pairs (delocalized electrons) along the flat plane direction [63,64], the parallel orientation of the DMF molecules with respect to the graphene flakes favor the overlap of two adjacent *p*-orbitals. It can favor a π-π bond between the solvent molecules and the graphene surface. This interaction thus increases the rigidity of the bonds of the molecules closest to graphene, consequently, modifies their Raman spectra. It is important to mention that our simulations suggest that this interaction is local, rather than global, i.e., just the molecules around of graphene flakes feel this change. It is not clear how the rest of the fluid is also affected by this interaction. Returning to DMAc NFs, a similar blue-shift in several Raman modes can be observed. If we consider that DMF and DMAc molecules are amides with quite similar structures and electron delocalization, then it is reasonable to suggest that a similar geometric configuration occurs in DMAc-based NFs. As a consequence, DMAc molecules may also tend to lay parallel to the graphene flakes favoring a π-π stacking between the graphene and the molecules thereby contributing to the blue-shift in the Raman spectra.

3.2.2. Raman in NMP-Based Nanofluids

The case of NMP-based fluids is quite different, Figure 3 shows the full Raman spectra of NMP-based NFs for three different graphene concentration of C = 0, 0.05 and 0.10 mg/mL. At first glance, a very small displacement of certain Raman modes can be detected (see Figure 4). However, the displacement is both within the range of the spectral reproducibility of the equipment (~0.25 cm^{-1}) and the error determination of each peak position. In conclusion, there is not a significant displacement of the Raman bands as the graphene concentration increases.

3.2.2. Raman in NMP-Based Nanofluids

The case of NMP-based fluids is quite different, Figure 3 shows the full Raman spectra of NMP-based NFs for three different graphene concentration of C = 0, 0.05 and 0.10 mg/mL. At first glance, a very small displacement of certain Raman modes can be detected (see Figure 4). However, the displacement is both within the range of the spectral reproducibility of the equipment (~0.25 cm^{-1}) and the error determination of each peak position. In conclusion, there is not a significant displacement of the Raman bands as the graphene concentration increases.

The Raman spectroscopy results from graphene-NMP NFs are not surprising if we consider the structure of the organic compound *N*-methyl-2-pyrrolidone is a five-membered cyclic amide (with a ring structure), and therefore, the bonds tend to be more rigid than those of amides having a linear structure. Consequently, it is conceivable that small amounts of graphene do not affect or modify the intramolecular vibrations of inner bonds in the solvent. Furthermore, Adams et al. [65] suggested that NMP molecules tend to spontaneously form dimers in the liquid state. NMP molecules strongly interact in pairs. Therefore, the impact of the presence of graphene flakes on the vibration of the bonds should be negligible. The findings of Adam et al. reinforce the idea that the solvent creates a natural barrier that prevents graphene from modifying the intramolecular interactions of the solvent. Moreover, Basma et al. [66] reported that pure NMP has a well-developed intrinsic order compared to other solvents. This inner order, together with the sp^2 hybridization of N-C=O (which allows a possible π-π interaction between NMP and graphene), can explain the long-term dispersion stability of graphene in NMP. However, the internal structure of NMP seems to be an obstacle to the improvement of the thermal properties of the fluid induced, in other cases, by graphene.

Nanomaterials **2019**, *9*, x FOR PEER REVIEW 7 of 12

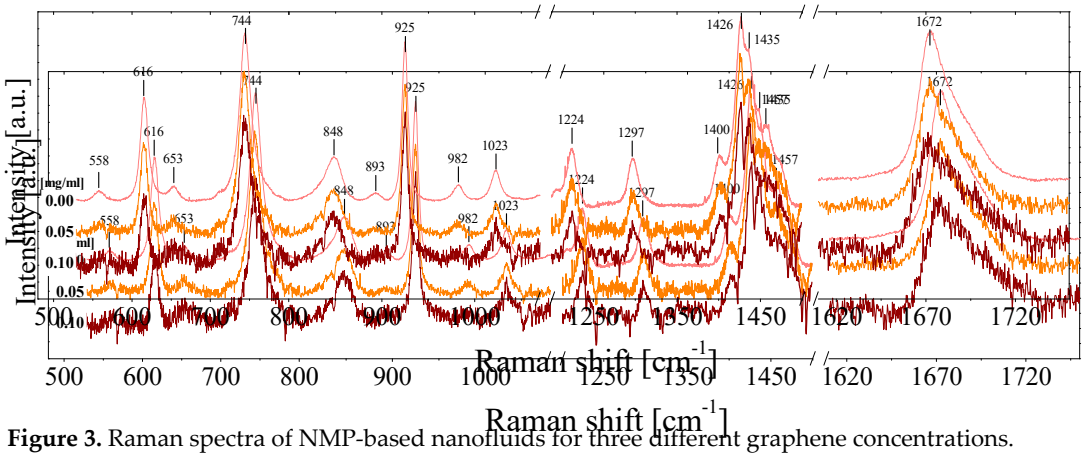

Figure 3. Raman spectra of NMP-based nanofluids for three different graphene concentrations.

Figure 3. Raman spectra of NMP-based nanofluids for three different graphene concentrations.

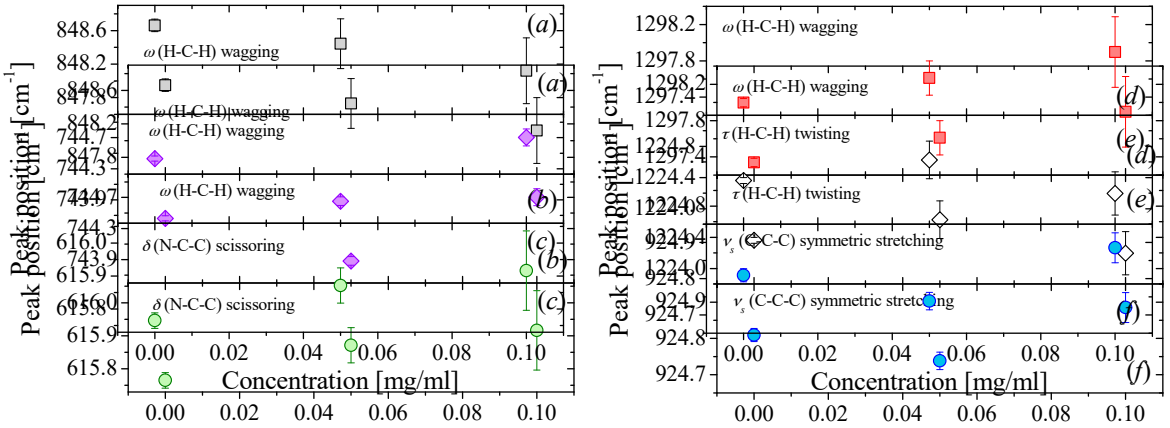

Figure 4. (**a**–**f**) Peak positions of six Raman bands of NMP shown in Figure 3 as a function of graphene concentration.

Figure 4. (**a**–**f**) Peak positions of six Raman bands of NMP shown in Figure 3 as a function of graphene concentration.

Figure 4. (**a**)–(**f**) Peak positions of six Raman bands of NMP shown in Figure 3 as a function of graphene concentration.

At this stage, one could consider as a possibility that higher concentrations of graphene may be preferable in order to observe a modification of the Raman spectra of NMP. However, although we prepared higher concentrations of this nanofluid, it was not possible to measure their Raman spectra. In addition to the high light absorption in the most concentrated samples, we also observed photoluminescence, which masks the Raman peaks. The origin of this photoluminescence has been attributed to the sonochemical degradation of the NMP suffered during the preparation of the NFs. Previous investigations [67,68] have demonstrated that sonication of pure NMP produces contaminating organic nanoparticles. Ogilvie et al. [68] also reported strong photoluminescence and enhancement of the optical absorbance of NMP-based NFs after a sonication treatment. In Figure 5a,b we can see the transmission electron microscopy (TEM) images of two graphene flakes sonicated in DMAc and NMP, respectively. It is interesting to observe in Figure 5b small particles on the graphene flakes. The sample of the image corresponds to a nanofluid of graphene-NMP, which was sonicated during the preparation stage. Similar particles were also found by Yau et al. [67] after the sonication of dispersion of NMP and single-walled carbon nanotubes. Their experimental data suggested that the sonication leads to the polymerization of the fluid, producing contamination by small organic nanoparticulate products (2–15 nm). Taking into account that the thermal conductivity of graphene-NMP NFs did not change with increasing graphene concentration, it seems that the degradation of NMP and the resulting organic contamination can affect the interaction between the additive nanomaterial (i.e., graphene) and the solvent, as well as the thermal performance of the NF. This causes a detrimental impact on the thermal conductivity of the nanofluid, in a manner that is still unknown.

At this stage, one could consider as a possibility that higher concentrations of graphene may be preferable in order to observe a modification of the Raman spectra of NMP. However, although we prepared higher concentrations of this nanofluid, it was not possible to measure their Raman spectra. In addition to the high light absorption in the most concentrated samples, we also observed photoluminescence, which masks the Raman peaks. The origin of this photoluminescence has been attributed to the sonochemical degradation of the NMP suffered during the preparation of the NFs. Previous investigations [67,68] have demonstrated that sonication of pure NMP produces contaminating organic nanoparticles. Ogilvie et al. [68] also reported strong photoluminescence and enhancement of the optical absorbance of NMP-based NFs after a sonication treatment. In Figure 5a,b we can see the transmission electron microscopy (TEM) images of two graphene flakes sonicated in DMAc and NMP, respectively. It is interesting to observe in Figure 5b small particles on the graphene flakes. The sample of the image corresponds to a nanofluid of graphene-NMP, which was sonicated during the preparation stage. Similar particles were also found by Yau et al. [67] after the sonication of dispersion of NMP and single-walled carbon nanotubes. Their experimental data suggested that the sonication leads to the polymerization of the fluid, producing contamination by small organic nanoparticulate products (2–15 nm). Taking into account that the thermal conductivity of graphene-NMP NFs did not change with increasing graphene concentration, it seems that the degradation of NMP and the resulting organic contamination can affect the interaction between the additive nanomaterial (i.e., graphene) and the solvent, as well as the thermal performance of the NF. This causes a detrimental impact on the thermal conductivity of the nanofluid, in a manner that is still unknown.

This causes a detrimental impact on the thermal conductivity of the nanofluid, in a manner that is still unknown.

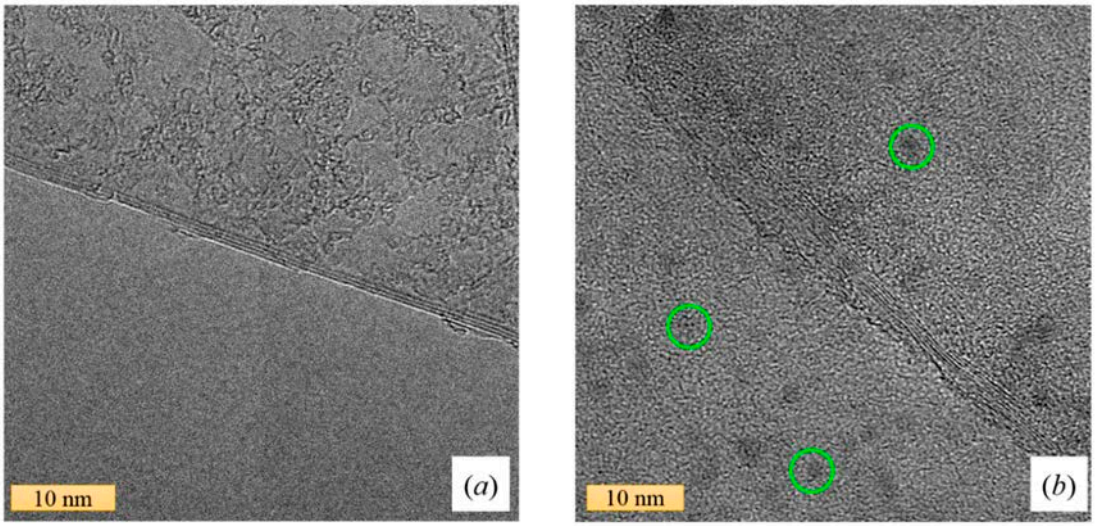

Figure 5. Representative transmission electron microscopy (TEM) images of graphene from: (**a**) a DMAc dispersion and (**b**) an NMP dispersion. Both images show the multilayer nature of the flakes folded graphene sheets. Highlighted by green circles, some nanoparticulates can be observed in the NMP-based nanofluid.

Figure 5. Representative transmission electron microscopy (TEM) images of graphene from: (**a**) a DMAc dispersion and (**b**) an NMP dispersion. Both images show the multilayer nature of the flakes folded graphene sheets. Highlighted by green circles, some nanoparticulates can be observed in the NMP-based nanofluid.

4. Conclusions

In this work, a correlation between the modification of the vibrational spectra of the fluids, and the increase of their thermal conductivity and viscosity in the presence of graphene is presented, where the base fluids were DMAc, DMF, and NMP. Our results suggest that the presence of graphene reflected in the displacement of some Raman bands, which could be attributed to changes in the produce shift of several Raman bands in DMAc and DMF and broadening of the bands. This is with those in the displacement of some Raman bands, which could be attributed to changes in the produce shift of several Raman bands in DMAc and DMF and broadening of the bands. This is associated with solvent–solvent interactions, which could be modified in the presence of graphene of the neighbor molecules. This interpretation suggests that graphene is able to modify, in an external force, the interactions between fluid molecules, in the presence of graphene flakes, which in turn seems to be directly connected with the enhancement of the thermal conductivity of the fluids. In the case of NMP-graphene-based nanofluids, modifications in the presence of graphene flakes, in addition to those observed in the bare fluid, could be directly associated with the enhancement of the thermal conductivity of the fluid. In the case of NMP-graphene-based fluids, modifications in the Raman spectra, either the structure of the NMP molecule and the peculiar arrangement of bare fluid (dimerization and inner order), can explain why the presence of graphene does not affect NMP and thermal conductivity results, that those concentrations of graphene are insufficient to impact on the fluid's thermal properties. We tested a higher concentration of graphene in NMP (C = 0.5 mg/mL), but the thermal conductivity was not enhanced, and the Raman spectrum showed photoluminescence, which masks the Raman peaks. Photoluminescence can be attributed to the degradation of NMP during sonication, which is a crucial step in the preparation of stable dispersions. The sonochemical degradation of NMP, together with the formation of the small organic contaminating particulates, affects the interaction between the graphene flakes, which could also contribute to a detrimental impact on the thermal conductivity.

In this work, a correlation between the modification of the vibrational spectra of the fluids, and the increase of their thermal conductivity and viscosity in the presence of graphene is presented, where the base fluids were DMAc, DMF, and NMP. Our results suggest that the presence of graphene reflected in the displacement of some Raman bands, which could be attributed to changes in the produce shift of several Raman bands in DMAc and DMF and broadening of the bands. This is associated with solvent–solvent interactions, which could be modified in the presence of graphene of the neighbor molecules. This interpretation suggests that graphene is able to modify, in an external force, the interactions between fluid molecules, in the presence of graphene flakes, which in turn seems to be directly connected with the enhancement of the thermal conductivity of the fluids. In the case of NMP-graphene-based nanofluids, modifications in the presence of graphene flakes, in addition to those observed in the bare fluid, could be directly associated with the enhancement of the thermal conductivity of the fluid. In the case of NMP-graphene-based fluids, modifications in the Raman spectra, either the structure of the NMP molecule and the peculiar arrangement of bare fluid (dimerization and inner order), can explain why the presence of graphene does not affect NMP and thermal conductivity results, that those concentrations of graphene are insufficient to impact on the fluid's thermal properties. We tested a higher concentration of graphene in NMP (C = 0.5 mg/mL), but the thermal conductivity was not enhanced, and the Raman spectrum showed photoluminescence, which masks the Raman peaks. Photoluminescence can be attributed to the degradation of NMP during sonication, which is a crucial step in the preparation of stable dispersions. The sonochemical degradation of NMP, together with the formation of the small organic contaminating particulates, affects the interaction between the graphene flakes, which could also contribute to a detrimental impact on the thermal conductivity.

Supplementary Materials: The following are available online at http://www.mdpi.com/2079-4991/9/5/804/s1, Table S1: Summary of the Raman measurements taken on different days over a period of time greater than one year, Figure S1: Raman spectra of graphene DMAc-NFs recorded on different dates as a function of graphene

Supplementary Materials: The following are available online at http://www.mdpi.com/2226-4310/4/2/18/s1, Table S1: Summary of the Raman measurements taken on different days over a period of time greater than one

concentration: (a) 0.1 mg/mL, (b) 0.2 mg/mL and (c) 0.5 mg/mL, Figure S2: Raman spectra of NMP-NFs recorded on different dates as a function of graphene concentration: (a) 0.05 mg/mL and (b) 0.1 mg/mL, Figure S3: Raman spectra of DMF-based nanofluids recorded on different dates as a function of graphene concentration: (a) 0.10 mg/mL, (b) 0.25 mg/mL and (b) 0.50 mg/mL.

Author Contributions: M.d.R.R.-L. and E.C.-A. wrote the article. M.d.R.R.-L. and P.G.-R. fabricated the samples. M.d.R.R.-L. and E.C.-A. measured the thermal conductivity, viscosity and Raman spectra. P.G.-R. and C.M.S.T. supervised the work. All authors discussed the results and commented on the manuscript.

Funding: ICN2 acknowledges support from Severo Ochoa Program (MINECO, Grant SEV-2017-0706) and funding from the CERCA Programme/ Generalitat de Catalunya. Funding from the Spanish Ministry (MINECO/FEDER: MAT2015-68394-R NaCarFLOW and FIS2015-70862-P PHENTOM) is also acknowledged. We would also like to thank Andrew Hudson for the assistance provided with the use of English in this manuscript.

Conflicts of Interest: The authors declare no conflict of interest.

References

1. Shi, L.; Dames, C.; Lukes, J.R.; Reddy, P.; Duda, J.; Cahill, D.G.; Lee, J.; Marconnet, A.; Goodson, K.E.; Bahk, J.-H.; et al. Evaluating Broader Impacts of Nanoscale Thermal Transport Research. *Nanoscale Microscale Thermophys. Eng.* **2015**, *19*, 127–165. [CrossRef]
2. International Roadmap for Devices and Systems (IRDS): Beyond CMOS. Available online: https://irds.ieee.org/images/files/pdf/2017/2017IRDS_BC.pdf (accessed on 26 May 2019).
3. Ekpu, M.; Bhatti, R.; Ekere, N.; Mallik, S. Advanced thermal management materials for heat sinks used in microelectronics. In Proceedings of the 18th European Microelectronics & Packaging Conference, Brighton, UK, 12–15 September 2011; pp. 1–8.
4. Ye, H.; Zhang, G. A review of passive thermal management of LED module. *J. Semicond.* **2011**, *32*, 14008. [CrossRef]
5. Sohel Murshed, S.M.; Nieto de Castro, C.A. A critical review of traditional and emerging techniques and fluids for electronics cooling. *Renew. Sustain. Energy Rev.* **2017**, *78*, 821–833. [CrossRef]
6. Bar-Cohen, A.; Arik, M.; Ohadi, M. Direct Liquid Cooling of High Flux Micro and Nano Electronic Components. *Proc. IEEE* **2006**, *94*, 1549–1570. [CrossRef]
7. Siddique, A.R.M.; Muresan, H.; Majid, S.H.; Mahmud, S. An adjustable closed-loop liquid-based thermoelectric electronic cooling system for variable load thermal management. *Therm. Sci. Eng. Prog.* **2019**, *10*, 245–252. [CrossRef]
8. Tasaka, M.; Shinohara, K.; Hayashi, C.; Kashima, S.; Koyama, K. Cooling performance of heat sinks with corrugated-fins. In Proceedings of the ITherm'98. Sixth Intersociety Conference on Thermal and Thermomechanical Phenomena in Electronic Systems (Cat. No.98CH36208), Seattle, WA, USA, 27–30 May 1998; pp. 104–111.
9. Budelman, G.A. US-Patent: Heatsink with integrated blower for improved heat transfer. No. 6244331, 2001.
10. Mahajan, R.; Chia-pin Chiu; Chrysler, G. Cooling a Microprocessor Chip. *Proc. IEEE* **2006**, *94*, 1476–1486. [CrossRef]
11. Leng, C.; Wang, X.-D.; Wang, T.-H. An improved design of double-layered microchannel heat sink with truncated top channels. *Appl. Therm. Eng.* **2015**, *79*, 54–62. [CrossRef]
12. Molina, J.; Prieto, R.; Narciso, J.; Louis, E. The effect of porosity on the thermal conductivity of Al–12wt.% Si/SiC composites. *Scr. Mater.* **2009**, *60*, 582–585. [CrossRef]
13. Caccia, M.; Rodríguez, A.; Narciso, J. Diamond Surface Modification to Enhance Interfacial Thermal Conductivity in Al/Diamond Composites. *JOM* **2014**, *66*, 920–925. [CrossRef]
14. Molina, J.-M.; Rodríguez-Guerrero, A.; Louis, E.; Rodríguez-Reinoso, F.; Narciso, J. Porosity Effect on Thermal Properties of Al-12 wt % Si/Graphite Composites. *Materials (Basel)* **2017**, *10*, 177. [CrossRef]
15. Kheirabadi, A.C.; Groulx, D. Cooling of server electronics: A design review of existing technology. *Appl. Therm. Eng.* **2016**, *105*, 622–638. [CrossRef]
16. Lv, L.C.; Li, J. Micro Flat Heat Pipes for Microelectronics Cooling: Review. *Recent Patents Mech. Eng.* **2013**, *6*, 169–184. [CrossRef]
17. Garimella, S.V.; Persoons, T.; Weibel, J.A.; Gektin, V. Electronics Thermal Management in Information and Communications Technologies: Challenges and Future Directions. *IEEE Trans. Compon. Packag. Manuf. Technol.* **2017**, *7*, 1191–1205. [CrossRef]

18. Patil, M.; Kim, S.; Seo, J.; Lee, M. Review of the Thermo-Physical Properties and Performance Characteristics of a Refrigeration System Using Refrigerant-Based Nanofluids. *Energies* **2015**, *9*, 22. [CrossRef]
19. Mahian, O.; Kianifar, A.; Kalogirou, S.a.; Pop, I.; Wongwises, S. A review of the applications of nanofluids in solar energy. *Int. J. Heat Mass Transf.* **2013**, *57*, 582–594. [CrossRef]
20. Safaei, M.; Ahmadi, G.; Goodarzi, M.; Safdari Shadloo, M.; Goshayeshi, H.; Dahari, M. Heat Transfer and Pressure Drop in Fully Developed Turbulent Flows of Graphene Nanoplatelets–Silver/Water Nanofluids. *Fluids* **2016**, *1*, 20. [CrossRef]
21. Choi, S.U.S.; Eastman, J.A. Enhancing thermal conductivity of fluids with nanoparticles. *ASME Int. Mech. Eng. Congr. Expo.* **1995**, *66*, 99–105.
22. Branson, B.T.; Beauchamp, P.S.; Beam, J.C.; Lukehart, C.M.; Davidson, J.L. Nanodiamond Nanofluids for Enhanced Thermal Conductivity. *ACS Nano* **2013**, *7*, 3183–3189. [CrossRef]
23. Patil, M.; Seo, J.-H.; Kang, S.-J.; Lee, M.-Y. Review on Synthesis, Thermo-Physical Property, and Heat Transfer Mechanism of Nanofluids. *Energies* **2016**, *9*, 840. [CrossRef]
24. Azmi, W.H.; Sharma, K.V.; Mamat, R.; Najafi, G.; Mohamad, M.S. The enhancement of effective thermal conductivity and effective dynamic viscosity of nanofluids – A review. *Renew. Sustain. Energy Rev.* **2016**, *53*, 1046–1058. [CrossRef]
25. Bhanushali, S.; Jason, N.N.; Ghosh, P.; Ganesh, A.; Simon, G.P.; Cheng, W. Enhanced Thermal Conductivity of Copper Nanofluids: The Effect of Filler Geometry. *ACS Appl. Mater. Interfaces* **2017**, *9*, 18925–18935. [CrossRef] [PubMed]
26. Sekrani, G.; Poncet, S. Ethylene- and Propylene-Glycol Based Nanofluids: A Litterature Review on Their Thermophysical Properties and Thermal Performances. *Appl. Sci.* **2018**, *8*, 2311. [CrossRef]
27. Rodríguez-Laguna, M.R.; Castro-Alvarez, A.; Sledzinska, M.; Maire, J.; Costanzo, F.; Ensing, B.; Pruneda, M.; Ordejón, P.; Sotomayor Torres, C.M.; Gómez-Romero, P.; et al. Mechanisms behind the enhancement of thermal properties of graphene nanofluids. *Nanoscale* **2018**, *10*, 15402–15409. [CrossRef]
28. Wei, C.; Nan, Z.; Wang, X.; Tan, Z. Investigation on Thermodynamic Properties of a Water-Based Hematite Nanofluid. *J. Chem. Eng. Data* **2010**, *55*, 2524–2528. [CrossRef]
29. Shin, D.; Banerjee, D. Enhanced Specific Heat of Silica Nanofluid. *J. Heat Transf.* **2011**, *133*, 24501. [CrossRef]
30. Tiznobaik, H.; Shin, D. Enhanced specific heat capacity of high-temperature molten salt-based nanofluids. *Int. J. Heat Mass Transf.* **2013**, *57*, 542–548. [CrossRef]
31. Ho, M.X.; Pan, C. Optimal concentration of alumina nanoparticles in molten Hitec salt to maximize its specific heat capacity. *Int. J. Heat Mass Transf.* **2014**, *70*, 174–184. [CrossRef]
32. Shahrul, I.M.; Mahbubul, I.M.; Khaleduzzaman, S.S.; Saidur, R.; Sabri, M.F.M. A comparative review on the specific heat of nanofluids for energy perspective. *Renew. Sustain. Energy Rev.* **2014**, *38*, 88–98. [CrossRef]
33. Riazi, H.; Murphy, T.; Webber, G.B.; Atkin, R.; Tehrani, S.S.M.; Taylor, R.A. Specific heat control of nanofluids: A critical review. *Int. J. Therm. Sci.* **2016**, *107*, 25–38. [CrossRef]
34. Hu, Y.; He, Y.; Zhang, Z.; Wen, D. Enhanced heat capacity of binary nitrate eutectic salt-silica nanofluid for solar energy storage. *Sol. Energy Mater. Sol. Cells* **2019**, *192*, 94–102. [CrossRef]
35. Roberts, N.A.; Walker, D.G. Convective Performance of Nanofluids in Commercial Electronics Cooling Systems. *Appl. Therm. Eng.* **2010**, *30*, 2499–2504. [CrossRef]
36. Escher, W.; Brunschwiler, T.; Shalkevich, N.; Shalkevich, A.; Burgi, T.; Michel, B.; Poulikakos, D. On the Cooling of Electronics With Nanofluids. *J. Heat Transf.* **2011**, *133*, 51401. [CrossRef]
37. Rafati, M.; Hamidi, A.A.; Shariati Niaser, M. Application of nanofluids in computer cooling systems (heat transfer performance of nanofluids). *Appl. Therm. Eng.* **2012**, *45–46*, 9–14. [CrossRef]
38. Ijam, A.; Saidur, R. Nanofluid as a coolant for electronic devices (cooling of electronic devices). *Appl. Therm. Eng.* **2012**, *32*, 76–82. [CrossRef]
39. Nazari, M.; Karami, M.; Ashouri, M. Comparing the thermal performance of water, Ethylene Glycol, Alumina and CNT nanofluids in CPU cooling: Experimental study. *Exp. Therm. Fluid Sci.* **2014**, *57*, 371–377. [CrossRef]
40. Liu, Z.-H.; Li, Y.-Y. A new frontier of nanofluid research – Application of nanofluids in heat pipes. *Int. J. Heat Mass Transf.* **2012**, *55*, 6786–6797. [CrossRef]
41. Sureshkumar, R.; Mohideen, S.T.; Nethaji, N. Heat transfer characteristics of nanofluids in heat pipes: A review. *Renew. Sustain. Energy Rev.* **2013**, *20*, 397–410. [CrossRef]

42. Alawi, O.A.; Sidik, N.A.C.; Mohammed, H.A.; Syahrullail, S. Fluid flow and heat transfer characteristics of nanofluids in heat pipes: A review. *Int. Commun. Heat Mass Transf.* **2014**, *56*, 50–62. [CrossRef]
43. Das, S.; Giri, A.; Samanta, S.; Kanagaraj, S. Role of graphene nanofluids on heat transfer enhancement in thermosyphon. *J. Sci. Adv. Mater. Devices* **2019**, *4*, 163–169. [CrossRef]
44. Poplaski, L.M.; Benn, S.P.; Faghri, A. Thermal performance of heat pipes using nanofluids. *Int. J. Heat Mass Transf.* **2017**, *107*, 358–371. [CrossRef]
45. Sarkar, S.; Selvam, R.P. Molecular dynamics simulation of effective thermal conductivity and study of enhanced thermal transport mechanism in nanofluids. *J. Appl. Phys.* **2007**, *102*, 074302. [CrossRef]
46. Prasher, R.; Bhattacharya, P.; Phelan, P.E. Brownian-Motion-Based Convective-Conductive Model for the Effective Thermal Conductivity of Nanofluids. *J. Heat Transf.* **2006**, *128*, 588. [CrossRef]
47. Prasher, R.; Phelan, P.E.; Bhattacharya, P. Effect of Aggregation Kinetics on the Thermal Conductivity of Nanoscale Colloidal Solutions (Nanofluid). *Nano Lett.* **2006**, *6*, 1529–1534. [CrossRef]
48. Keblinski, P.; Thomin, J. Hydrodynamic field around a Brownian particle. *Phys. Rev. E* **2006**, *73*, 10502. [CrossRef]
49. Keblinski, P.; Phillpot, S.R.; Choi, S.U.S.; Eastman, J.A. Mechanisms of heat flow in suspensions of nano-sized particles (nanofluids). *Int. J. Heat Mass Transf.* **2002**, *45*, 855–863. [CrossRef]
50. Trisaksri, V.; Wongwises, S. Critical review of heat transfer characteristics of nanofluids. *Renew. Sustain. Energy Rev.* **2007**, *11*, 512–523. [CrossRef]
51. Cahill, D.G. Thermal conductivity measurement from 30 to 750 K: the 3ω method. *Rev. Sci. Instrum.* **1990**, *61*, 802. [CrossRef]
52. Cahill, D.G. Erratum: "Thermal conductivity measurement from 30 to 750 K: The 3ω method" [Rev. Sci. Instrum. 61, 802 (1990)]. *Rev. Sci. Instrum.* **2002**, *73*, 3701. [CrossRef]
53. Oh, D.W.; Jain, A.; Eaton, J.K.; Goodson, K.E.; Lee, J.S. Thermal conductivity measurement and sedimentation detection of aluminum oxide nanofluids by using the 3ω method. *Int. J. Heat Fluid Flow* **2008**, *29*, 1456–1461. [CrossRef]
54. Lubner, S.D.; Choi, J.; Wehmeyer, G.; Waag, B.; Mishra, V.; Natesan, H.; Bischof, J.C.; Dames, C. Reusable bi-directional 3 ω sensor to measure thermal conductivity of 100-μ m thick biological tissues. *Rev. Sci. Instrum.* **2015**, *86*, 014905. [CrossRef]
55. Chavez-Angel, E.; Reuter, N.; Komar, P.; Heinz, S.; Kolb, U.; Kleebe, H.-J.; Jakob, G. Subamorphous Thermal Conductivity of Crystalline Half-Heusler Superlattices. *Nanoscale Microscale Thermophys. Eng.* **2019**, *23*, 1–9. [CrossRef]
56. Kole, M.; Dey, T.K. Investigation of thermal conductivity, viscosity, and electrical conductivity of graphene based nanofluids. *J. Appl. Phys.* **2013**, *113*, 84307. [CrossRef]
57. Mehrali, M.; Sadeghinezhad, E.; Tahan Latibari, S.; Mehrali, M.; Togun, H.; Zubir, M.N.M.; Kazi, S.N.; Metselaar, H.S.C. Preparation, characterization, viscosity, and thermal conductivity of nitrogen-doped graphene aqueous nanofluids. *J. Mater. Sci.* **2014**, *49*, 7156–7171. [CrossRef]
58. Vallejo, J.P.; Żyła, G.; Fernández-Seara, J.; Lugo, L. Rheological behaviour of functionalized graphene nanoplatelet nanofluids based on water and propylene glycol:water mixtures. *Int. Commun. Heat Mass Transf.* **2018**, *99*, 43–53. [CrossRef]
59. Vallejo, J.; Żyła, G.; Fernández-Seara, J.; Lugo, L. Influence of Six Carbon-Based Nanomaterials on the Rheological Properties of Nanofluids. *Nanomaterials* **2019**, *9*, 146. [CrossRef] [PubMed]
60. Chalapathi, V.V.; Ramiah, K.V. Normal vibrations of N-Dimethylformamide and N, N-Dimethylacetamide. *Proc. Indian Acad. Sci.* **1968**, *91*, 109–122. [CrossRef]
61. Peek, P.S.; McDermott, D.P. Vibrational modes and frequencies of 2-pyrrolidinones and their deutero-isotopomers. *Spectrochim. Acta Part A Mol. Spectrosc.* **1988**, *44*, 371–377. [CrossRef]
62. Xu, W.; Wang, H.; Tao, Y.; Zheng, X. The structural organization of *N*-methyl-2-pyrrolidinone in binary mixtures probed by Raman spectroscopy: Experimental and quantum chemical results. *J. Raman Spectrosc.* **2018**, *49*, 362–371. [CrossRef]
63. Rozpłoch, F.; Patyk, J.; Stankowski, J. Graphenes Bonding Forces in Graphite. *Acta Phys. Pol. A* **2007**, *112*, 557–562. [CrossRef]
64. Kemnitz, C.R.; Loewen, M.J. "Amide Resonance" Correlates with a Breadth of C−N Rotation Barriers. *J. Am. Chem. Soc.* **2007**, *129*, 2521–2528. [CrossRef] [PubMed]

65. Adams, W.A.; Kruus, P.; Patraboy, T.J. The system sulfur dioxide–*N*-methyl-2-pyrrolidinone. *Can. J. Chem.* **1983**, *61*, 37–44. [CrossRef]
66. Basma, N.S.; Headen, T.F.; Shaffer, M.S.P.; Skipper, N.T.; Howard, C.A. Local Structure and Polar Order in Liquid N -Methyl-2-pyrrolidone (NMP). *J. Phys. Chem. B* **2018**, *122*, 8963–8971. [CrossRef] [PubMed]
67. Yau, H.C.; Bayazit, M.K.; Steinke, J.H.G.; Shaffer, M.S.P. Sonochemical degradation of *N*-methylpyrrolidone and its influence on single walled carbon nanotube dispersion. *Chem. Commun.* **2015**, *51*, 16621–16624. [CrossRef] [PubMed]
68. Ogilvie, S.P.; Large, M.J.; Fratta, G.; Meloni, M.; Canton-Vitoria, R.; Tagmatarchis, N.; Massuyeau, F.; Ewels, C.P.; King, A.A.K.; Dalton, A.B. Considerations for spectroscopy of liquid-exfoliated 2D materials: Emerging photoluminescence of N-methyl-2-pyrrolidone. *Sci. Rep.* **2017**, *7*, 16706. [CrossRef] [PubMed]

Supporting information of Article 2

Supporting information

Modification of the Raman Spectra in Graphene-Based Nanofluids and Its Correlation with Thermal Properties

María del Rocío Rodríguez-Laguna [1,2,*], Pedro Gómez-Romero [1,*], Clivia M. Sotomayor Torres [1,3] and Emigdio Chavez-Angel [1,*]

[1] Catalan Institute of Nanoscience and Nanotechnology (ICN2), CSIC and The Barcelona Institute of Science and Technology (BIST), Campus UAB, Bellaterra, 08193 Barcelona, Spain; clivia.sotomayor@icn2.cat (C.M.S.T)
[2] Department of Chemistry, Universitat Autònoma de Barcelona, Campus UAB, Bellaterra, 08193 Barcelona, Spain
[3] ICREA- Institució Catalana de Recerca i Estudis Avançats, Pg. Lluís Companys 23, 08010 Barcelona, Spain.
* Correspondence: rodriguez3laguna@gmail.com (M.R.R.L.); pedro.gomez@icn2.cat (P.G.R.); emigdio.chavez@icn2.cat (E.C.A.); Tel.: +34 93 7373616 (M.R.R.L.); +34 93 7373608 (P.G.R.); +34 93 7371617 (E.C.A.)

Raman spectra of nanofluids as a function of time

In order to confirm the reproducibility of the measurements, Raman spectra of the three types of graphene nanofluids (DMAc, DMF and NMP- NFs) were recorded as a function of time for different concentrations of graphene. **Table S1** shows a summary of the set of measurements.

Sample name	Date (day No.)		
Graphene-DMAc NFs	2017/11/30 (day 1)	2017/12/22 (day 22)	2019/05/07 (day 524)
Graphene-NMP NFs	2018/02/05 (day 1)	2019/03/15 (day 404)	2019/05/08 (day 458)
Graphene-DMF NFs	2017/09/28 (day 1)	-	2019/05/08 (day 588)

Table S1 Summary of the Raman measurements taken on different days over a period of time greater than one year.

Figure S1, Figure S2 and Figure S3 show the Raman spectra of DMAc-, NMP- and DMF-based nanofluids for different graphene concentrations measured on different days, respectively. As can be seen, the Raman spectra do not change significantly as a function of time. We did not observe any modification and/or displacement of the Raman bands of the samples. Taking into account that the Raman spectra of nanofluids recorded after one year are practically identical to those performed on day 1, we can assure that the quality of the dispersion is maintained after more than one year. These results indicate the good quality and long-term stability of the samples.

Supporting information

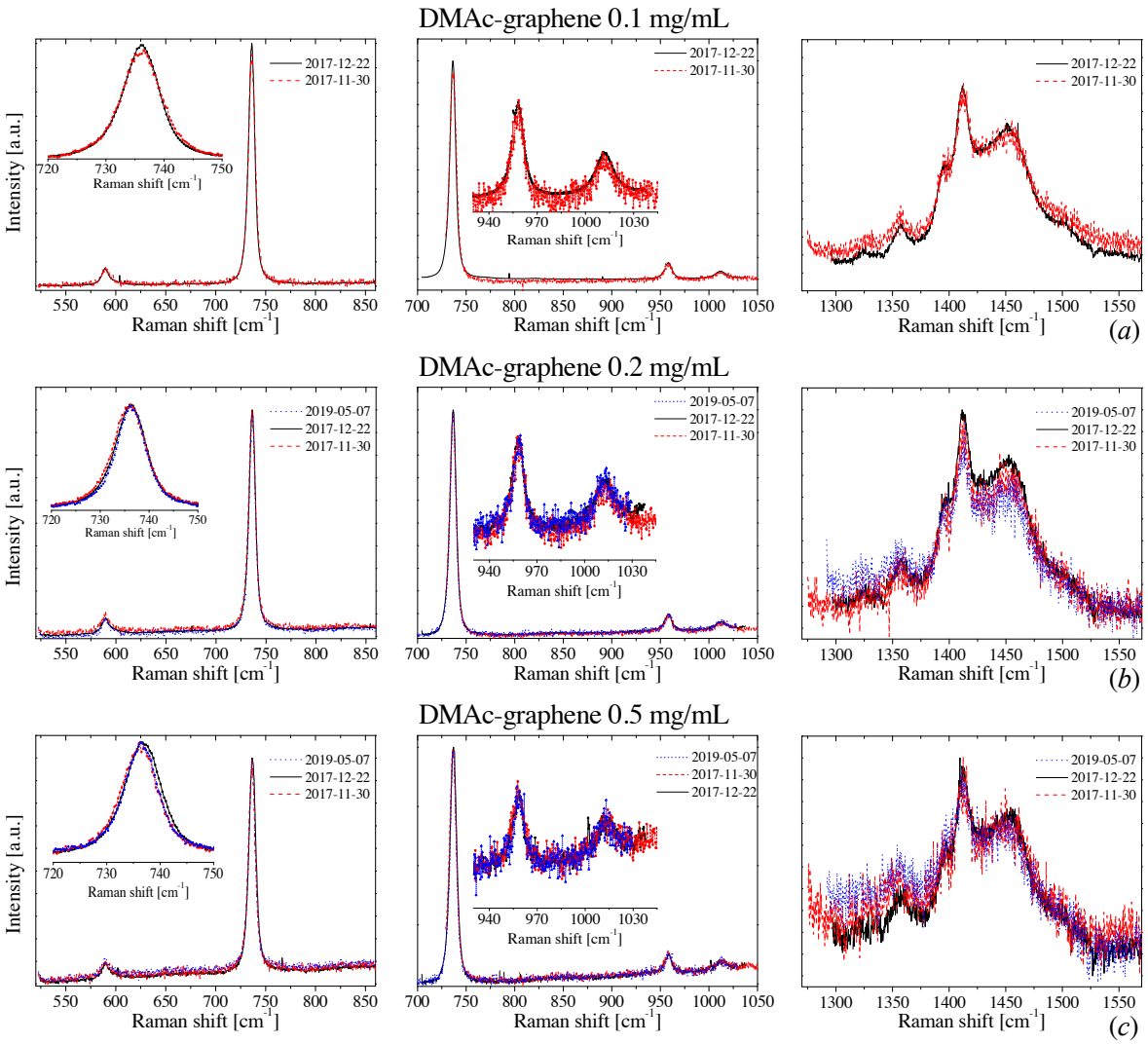

Figure S1 Raman spectra of graphene DMAc-NFs recorded on different dates as a function of graphene concentration: (a) 0.1 mg/mL, (b) 0.2 mg/mL and (c) 0.5 mg/mL.

Supporting information

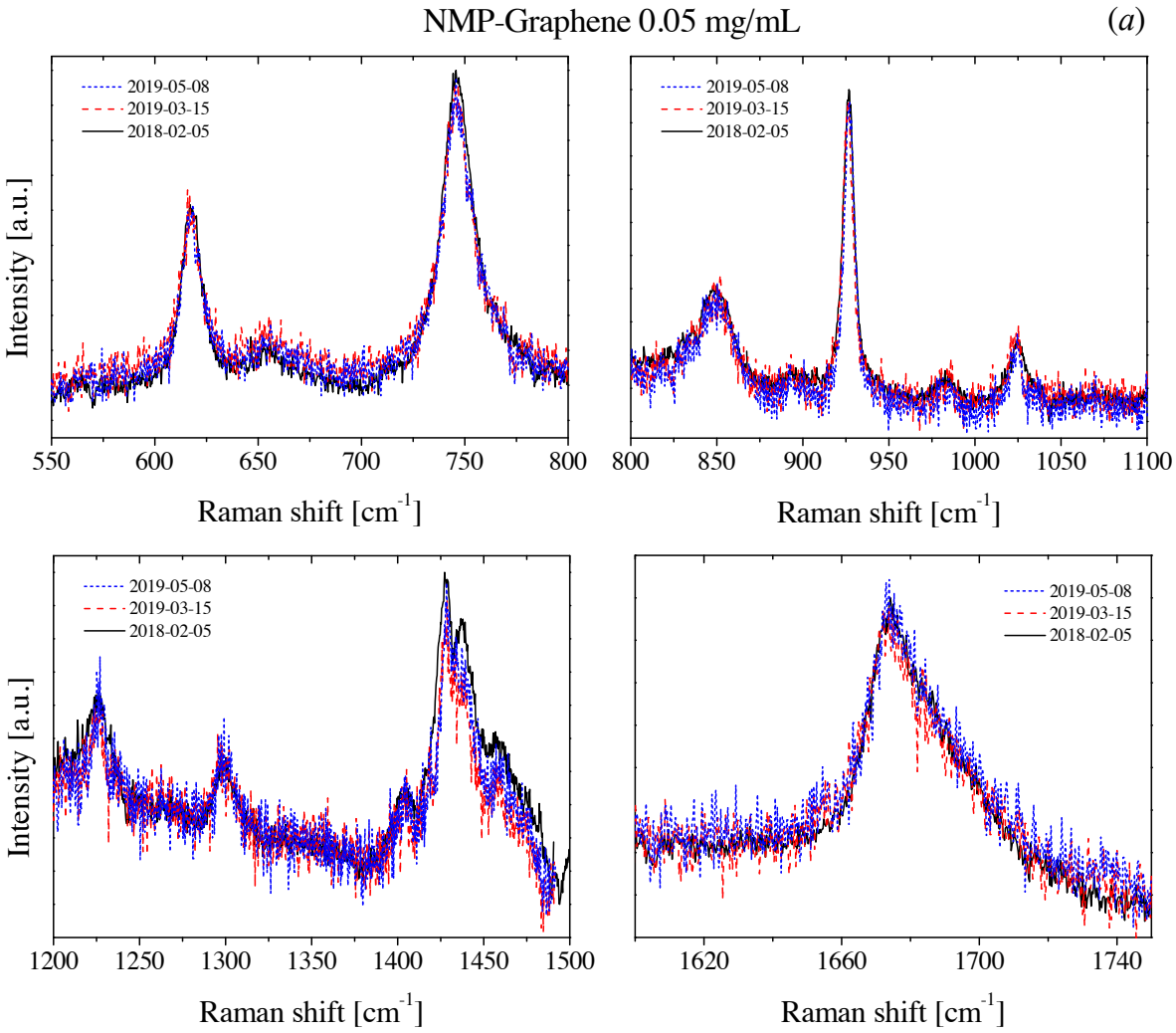

Supporting information

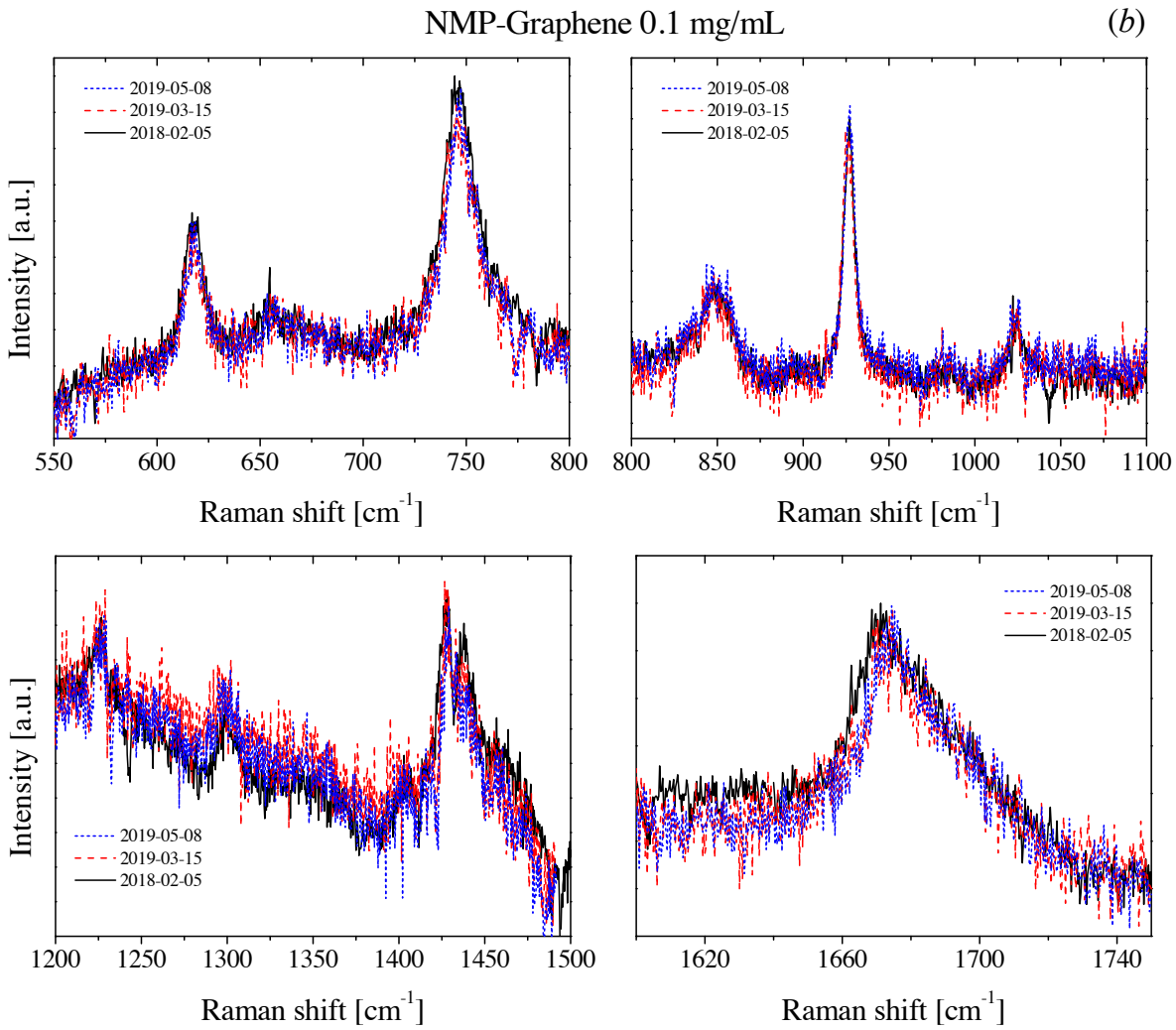

Figure S2 Raman spectra of NMP-NFs recorded on different dates as a function of graphene concentration: (a) 0.05 mg/mL and (b) 0.1 mg/mL.

Supporting information

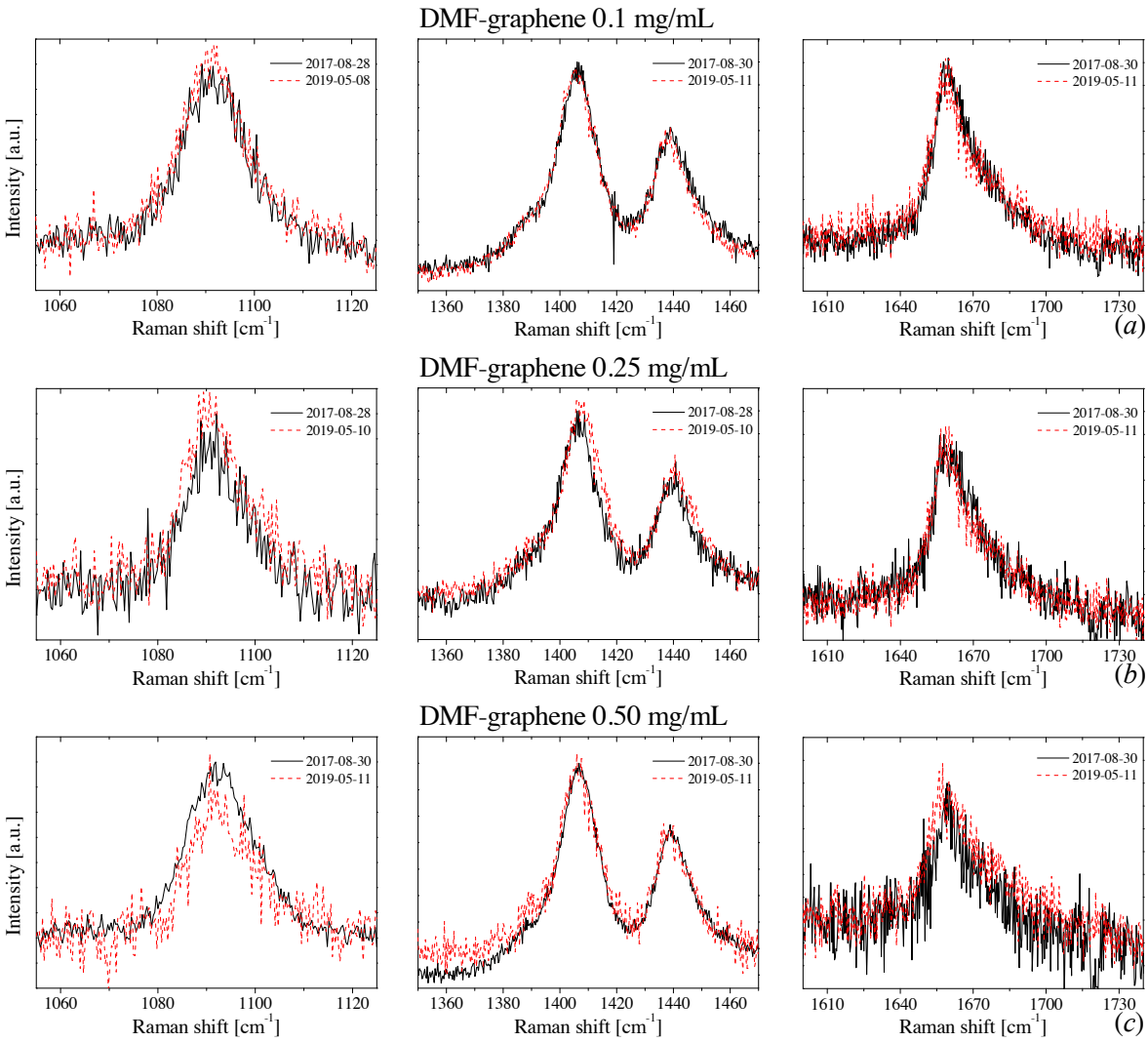

Figure S3 Raman spectra of DMF-based nanofluids recorded on different dates as a function of graphene concentration: (a) 0.10 mg/mL, (b) 0.25 mg/mL and (b) 0.50 mg/mL.

Chapter 3: Development of low-melting point molten salts and detection of solid-to-liquid transitions by alternative techniques to DSC

Chapter Summary

Inorganic salts in the molten state are extensively used in a variety of high temperature industrial applications. In this chapter, we describe the role of molten salts in some popular industries and delve into the function and performance of these materials in solar-thermal applications. Then, we will discuss the different strategies available to advance in CSP technology by tuning the thermo-physical properties of molten salts. Among all the strategies, the development of superior multi-component salts, made of more than 4 components, favors the expansion of the operating temperature (lower limit). Multi-component salts are combinations of different cations and anions. The difference in size of the ions hinders the crystallization of the material and provides lower melting temperatures. Multi-component salts are considered in this study to replace simpler combinations, such as binary and ternary eutectic mixtures. Herein, we report on two novel six-component nitrates with a melting temperature of 60-75 ºC and a thermal stability of up to ~ 500 ºC under a linear heating program in N_2 atmosphere. Properties such as the thermal conductivity in solid and molten state, heat capacity and vibrational spectra were evaluated. The study of the thermal behavior of these materials using differential scanning calorimetry was insufficient, hence alternative and complementary techniques were used, such as: the three-omega technique, optical transmission and Raman spectroscopy. Multi-component salts were found to solidify as amorphous solids even at slow cooling rates and water was found to behave as a catalyst of crystallization.

3.1 General applications of molten salts

Molten salts are inorganic salts which are in a solid state at room temperature but become liquids at higher temperature (> 250 ºC). These materials are extensively used in fields as diverse as nuclear and thermal-solar power [107–111]; waste management [112–114]; catalysis [109]; high-temperature batteries and fuel cells; and metallurgy, among others.

Molten salts are mainly used for high temperature applications. They are particularly useful as heat transfer fluids and storage materials due to their high boiling point, wide temperature range in the liquid state, low vapor pressure, good heat capacity and thermal conductivity.

Depending on the operating temperature range needed for a particular application, different molten salts are available and can be classified as follows:

Table 5 Molten salts classified by their operating temperature range (ºC)

Operating temperature range (ºC)	250 - 400	450-1000	400-1400
Molten salt	Nitrates, nitrites, hydroxide (alkaline)	Halides, sulfates, carbonates	Fluorides

The technology of molten salt oxidation (MSO) is a thermal treatment process essentially applied for **reprocessing of organic waste**. This technology is considered as a viable option to replace the regular incineration processes. The principle of this technology is based on flameless oxidation of materials in the molten salt with the subsequent capture of vapors in molten alkaline salts. Molten salts with low melting point and high viscosity are desirable. The ternary mixture of carbonates Na_2CO_3, K_2CO_3 and Li_2CO_3, is one of the most used materials in this application [113].

In the **metallurgy industry**, molten salts are involved in the extraction of metals (e.g. Hall-Heroult process) [115,116] and metal heat treating. The heat treatment of metals and alloys is crucial to achieve the desired shape and properties of the material. The hardening and softening of the metals as well as the modification of their surface are important processes that require an effective heat treatment technique. Baths of molten salts are an alternative to conventional furnaces and in some cases, are considered the ideal heat treating medium. Parts are immersed in the molten salt baths, where conduction is the

main heat transfer mechanism. Basic furnaces are based on convection and radiation, thus they are less effective heat treatments.

Other advantages are:

1) The absence of air in contact with the material (oxidation is avoided).

2) The uniform heat transfer through the material.

The main types of salt used in baths for metallurgy are molten alkali metal nitrates, mixture of these with their nitrites, molten chloride salts and molten cyanides [117].

Molten salt reactors (MSRs), which are a type of **nuclear fission reactor**, use molten salts as the primary coolant and in some cases, as the nuclear fuel. Molten salts such as alkali metal fluorides, ZrF_4- and BeF_4-salts are suitable for use in primary cooling circuits and chlorides are good candidates for heat transfer loops [111]. Pressurized water or molten metals (sodium, lead or lead-bismuth eutectic) are extensively used as nuclear coolants. Molten salts have the advantage of low vapor pressure, and are much less chemically reactive than sodium.

In addition to the properties mentioned above, molten salts were proven to be insensitive to radiation and present wide range solubility for actinides, which make them appealing for nuclear energy applications [107]. In conventional nuclear reactors, the fuel is solid and is composed of uranium dioxide (UO_2) or a mixture of the latter and plutonium dioxide (Mixed oxide fuel, MOX) in form of pellets stacked in corrosion-resistant metal rods. The main MSR concept is to have the fissile and fertile fuel dissolved in the molten salts. The most common fluoride salt used as a coolant in nuclear reactors is LiF-BeF_2 (2:1 stoichiometric mixture, FLiBe), with a melting point of 459 ºC and a boiling point of 1430 ºC. Thorium, uranium, and plutonium all form suitable fluoride salts that easily dissolve in LiF-BeF_2, and thorium and uranium can be effectively separated from one another in fluoride form.

Oak Ridge National laboratory (ORNL) researched on this technology through the 1960s by carrying out the Molten Salt Reactor Experiment (MSRE) [118]. The fuel used was LiF-BeF_2-ZrF_4-UF_4 (65-29-5-1, mole %) and the secondary coolant was LiF-BeF_2. The reactor operated safely and reliably for the equivalent of about 1.5 years of full power operation. Molten salt reactors are seen as a promising technology principally as a thorium fuel cycle prospect. There is a renewed interest in the development of novel MSR designs and new

molten salts [107,111] as well as in the compatibility of molten salts with metals/alloys (corrosion) [113] and with graphite (moderator) [119].

Lately, molten salts are attracting considerable attention in the thermo-solar energy field. Their nature and properties place them in an advantageous position to be used as sensible heat storage media and heat transfer fluids. Recent investigations are focused on the development of novel molten salts. The aim is to tune their properties to improve the energy conversion efficiency and to reduce the expenses of electricity production [11].

3.2 Molten salts in thermo-solar applications

Concentrated solar power (CSP) systems require a heat transfer fluid (HTF) to absorb and transport the solar energy to the heat exchanger and heat storage tank. It is well known that the wider the operating temperature of the fluid, the more efficient the energy conversion process will be. Concentrated technologies can reach very high temperatures, especially those based on point-focus collectors (≈500-1000 ºC). Therefore, the use of HTFs with high thermal stability is mandatory to preserve the original properties and performance of the fluid. Molten salts exhibit high thermal stability compared to water, common heat transfer oils, and organic compounds. Its only drawback is the relatively high melting temperatures (≥ 200 ºC).

Nowadays, the solar salt (60 $NaNO_3$-40 KNO_3, wt. %), with a melting temperature of 228 ºC [120], is the most commonly used HTF and thermal energy storage (TES) material in power tower systems. The high melting temperature of molten salts demands a supply of extra-energy to keep the material in the liquid state, thus, making the entire process costly and much less efficient. The current systems, such as that of 'Gemasolar' power tower plant[1], use freeze protection in pipes and tanks to minimize heat loss. Furthermore, they use a pipe trace system to monitor the temperature and act in case of massive heat loss. The protection system consists of insulation coatings, heat cables and heaters. All these accessories prevent the fluid from solidifying and damaging the pipes, however, it implies a cost.

[1] Available in http://torresolenergy.com/en/gemasolar/

3.3 Advancing CSP technology

To achieve desirable advances in CSP technology, fluids with low melting temperature and high thermal stability are required. During the last years, researchers have developed different strategies to design combinations of molten salts with low melting temperature, the so-called eutectic compositions. But, they also kept an eye on the thermal stability.

Novel molten salt mixtures with low melting points are being investigated to improve the energy conversion efficiency and to reduce the cost of electricity production [11]. Lowering the melting point of the HTF below room temperature could prevent the use of heaters and heat tracing systems. In addition, the risk of blocking the pipes due to the freezing of the salt would decrease considerably [121]. On the other hand, a fluid with a wide operational temperature range is beneficial both for energy conversion and for energy storage. Thus, producing high-temperature steam will substantially increase the efficiency of the steam turbine (Carnot's theorem) and that of the overall energy conversion. And in terms of sensible energy storage, a larger temperature difference in the storage system will result in a significantly increased specific storage capacity [12,13].

3.3.1 Strategies to improve the thermal performance of inorganic salts: recent studies

These strategies could imply 1) the design of new molten salts with superior thermo-physical properties or 2) the modification of the properties of conventional molten salts by using additives such as nanoparticles or small concentrations of other salts (e.g. chlorides). In any case, whether the HTF/TES is a new formulation or a composite, the aim is to improve the energy conversion efficiency and to reduce the cost of electricity production [11].

3.3.1.1 Dispersion of nanoparticles: improvement of Cp

The addition of nanoparticles to inorganic salts is considered one of the main strategies to improve the thermal properties of these materials. Choi and colleagues [122] led the way to the application of dispersions of nanoparticles as thermal fluids in 1996. Their first studies showed an enhancement of the thermal conductivity in water of 60% by dispersing 5% vol of CuO NPs. Based on this idea, Shin and Banerjee [123] added silica NPs into inorganic salt (Li_2CO_3:K_2CO_3 62:38 mol). The dispersion of 1 wt % of silica NPs of 1–20 nm size improved the specific heat of the salt by 25 %. Since then, there has been a rapid

rise in the number of studies on the dispersion of NPs in inorganic salts. Some recent studies are summarized below.

Liu et al. [124] studied the effect of nano- and micro-sized Si_3N_4, SiC and SiO_2 on the specific heat capacity of Solar salt. The specific heat capacity of silica composites with 3 wt. % were enhanced by 4-10 % compared to that of the pure salt, on the other hand, silicon nitride and silicon carbide NPs seem to have a negligible effect on this property. Sang and Liu [125] investigated the specific heat capacity of a ternary carbonate (K_2CO_3-Li_2CO_3-Na_2CO_3) with NPs of SiO_2, CuO, TiO_2 and Al_2O_3. Silica NPs demonstrated to be the most effective additive among all the chosen NPs, with a maximum enhancement of 78-117 % (500-540 °C). Even so, the other additives improved the Cp of the molten salt by 31-74 % for the same temperature range. However, the addition of NPs in molten salts has a major disadvantage for its application in the industry: the instability of NPs in dispersion at high temperatures and their tendency to agglomerate.

3.3.1.2 Expansion of the operating temperature range

a. Increase of the thermal stability

Dunlop et al [126] proposed the addition of chloride metals to molten salts to improve the thermal stability of the material. They used a ternary salt (53 wt% KNO_3, 40 wt% $NaNO_2$, 7 wt% $NaNO_3$) and they added different concentrations of a variety of chlorides (KCl, LiCl, $CaCl_2$, $ZnCl_2$, NaCl and $MgCl_2$). Thermogravimetric studies of the quaternary salt containing a 5 wt% addition of LiCl and KCl resulted in an increase in short-term thermal stability compared to the bare ternary nitrate salt. Furthermore, the long-term thermal stability was improved by 50 ºC. The addition of LiCl allowed the partial melting of the material at 80 ºC, in comparison to the 142 ºC of the ternary salt. Both, the increase in thermal stability and the drop in melting point widen the operating temperature range in 100 ºC in total, compared to the bare ternary nitrate.

Several studies have been conducted on the evaluation of the effect of different gas atmospheres on the thermal stability of salts [127–129]. In particular, Fereres et al. [128] evaluated the long-term thermal stability of the eutectic salt Li_2CO_3-Na_2CO_3-K_2CO_3 under air, nitrogen, carbon dioxide, and an 80/20 carbon dioxide/air mixture (in isothermal conditions). They found that the thermal stability of the salt improved in CO_2 atmosphere, as CO_2 gas shifts the equilibrium of the reaction of decomposition and slows down the decomposition rate.

b. Lower the melting point

In recent years, researchers have made an effort to develop low-melting point compositions to advance CSP technology. In 2011, Raade and Padowitz [130] developed a quinary composition with a melting point of 65 ºC using advanced experimental design and data analysis methods together with a powerful experimental workflow. More than 5000 combinations of inorganic salts were tested during the development process. To effectively design such a quantity of mixtures, they used powder and liquid dispensing systems coupled to a melting point apparatus.

Wang et al. [131] developed and predicted an eutectic quaternary system (17.5 $LiNO_3$-14.2 $NaNO_3$-50.2 KNO_3-17.8 $NaNO_2$, wt%) using thermodynamic modeling. They also confirmed the predicted melting temperature of 100 ºC using differential scanning calorimetry [11]. Wang and colleagues used a thermodynamic model based on regular solution theory, where the energies of mixing between components are required. However, since they did not have access to ternary and quaternary phase diagram information, they assumed no ternary and quaternary interactions between the components, only binary interactions were considered [11].

Ren et al. [132] prepared and characterized different mixing ratios of quaternary mixed nitrate based on KNO_3–$NaNO_3$–$LiNO_3$–$Ca(NO_3)_2 \cdot 4H_2O$ with melting temperatures below 100 ºC. They got inspired by a previous work done in Sandia National laboratories by Bradshaw and Siegel [133]. To lower the melting temperature of solar salt ($NaNO_3$-KNO_3) Bradshaw and Siegel added extra constituents, such as lithium nitrate and calcium nitrate, because all binary combinations of these nitrate salts display melting point depression, as well as eutectics, as do the ternary systems.

3.4 Multi component nitrate mixtures: nature and characteristics

Multi-component nitrates systems comprise binary, ternary, quaternary and higher mixtures of nitrates. They can be composed of diverse combinations of uni-, di-, trivalent cations and nitrate anions. Increasing the complexity of the mixture will make it more difficult for nucleation to take place [134]. This is due to the difficulty of these ions to regroup in crystal-forming compositions during cooling, since they appear to be mixed at random in the molten state[135]. For this reason, complex mixtures of five or more components often show a lower melting point than binary or ternary compositions. In certain conditions, complex mixtures preferentially form glasses during rapid-cooling.

As explained in the previous section, research on mixed-nitrates is currently focusing on the characterization and suitability of these materials for various applications [125,132,136]. However, in the last century, research on molten salts was fundamental rather than applied. In particular, from the 1950s to the 1980s, experts mainly focused on the study of how ions are associated in the molten state [134,137–139].

Cleaver et al. [140] studied the melting process in ionic crystals, particularly nitrates and nitrites. According to them, electrostatic charges in the unit of structure of ionic crystals are responsible for a strong mode of interaction between near neighbors, which in turn affect the mechanism of melting. By studying structural changes using X-ray and neutron diffractions, Cleaver et al. affirmed that long-range order disappears on melting, but the packing of nearest-neighbors in some melts is roughly the same than in solid state. Moreover, the authors indicate that in the liquid state, ionic crystals with non-spherical ions associate to form complexes. In these complexes, anions and cations tend to be more firmly packed together than in the crystal. Van Uitert and Grodkiewicz [134] considered the existence of 'clusters' in the melt formed of 'primary' cations which gather the anions around them, and 'secondary' cations that inhibit the motion of clusters. This explains why the ionic melt has difficulties in ordering and why the nucleation and phase separation are not favored. If we consider the salt in the liquid state, the movement of these ionic clusters must increase the viscosity. In this sense, earlier reports confirm that some binary and ternary mixtures of univalent nitrates (e.g. KNO_3, $NaNO_3$, etc.) with divalent cations (e.g. Ca^{2+}, Mg^{2+}) involve an increase of viscosity that can eventually terminate in glass formation [137].

3.5 Results: Multi-component salts with low melting point and detection of solid-liquid phase transition by alternative techniques to DSC

3.5.1 Materials and methods

(i) Preparation of molten salts with low-melting point

Three kinds of multi-component nitrates were prepared by the direct mixing of the pure chemicals in the proportions given in **Table 6.** The quinary salt named as Halotechnics SS-500 (Q) is a heat transfer fluid currently available for CSP applications [130,136]. The six-component formulations were reported for the first time in the manuscript attached below (article 3). The composition of the two novel salts, S-Al and S-Rb, was selected based on the quinary salt 'Q'. The proportion between the five original components in Q

(lithium, sodium, potassium, cesium and calcium nitrates) was maintained constant in the new formulations. The extra component, rubidium and aluminum nitrates, was added in a similar amount than lithium nitrate.

Table 6 Compositions of molten salts indicating the weight percentage (%) of individual components

	Components (%)						
Sample name	**$LiNO_3$**	**$NaNO_3$**	**KNO_3**	**$CsNO_3$**	**$Ca(NO3)_2$**	**$RbNO_3$**	**$Al(NO_3)_3$**
Halotechnics SS-500 (Q) [130]	8	6	23	44	19	-	-
Senary 1 (S-Al)	7.6	5.7	21.5	40.9	17.8	-	6.6
Senary 2 (S-Rb)	7.6	5.7	21.8	41.6	15.7	7.6	-

The schematic diagram of the preparation of the salts is shown in **Figure 18**, which includes the following steps:

1. Drying the pure salts in a vacuum desiccator for at least 24 h.
2. Direct mixing of the pure salts in an alumina crucible favoring the direct contact of the salts. Covering the crucible with a lid.
3. Introduction of the crucible inside a muffle furnace, where the sample is heated at 10 ºC/min up to 400 ºC for 2 hours.
4. Allow the sample to cool down naturally.

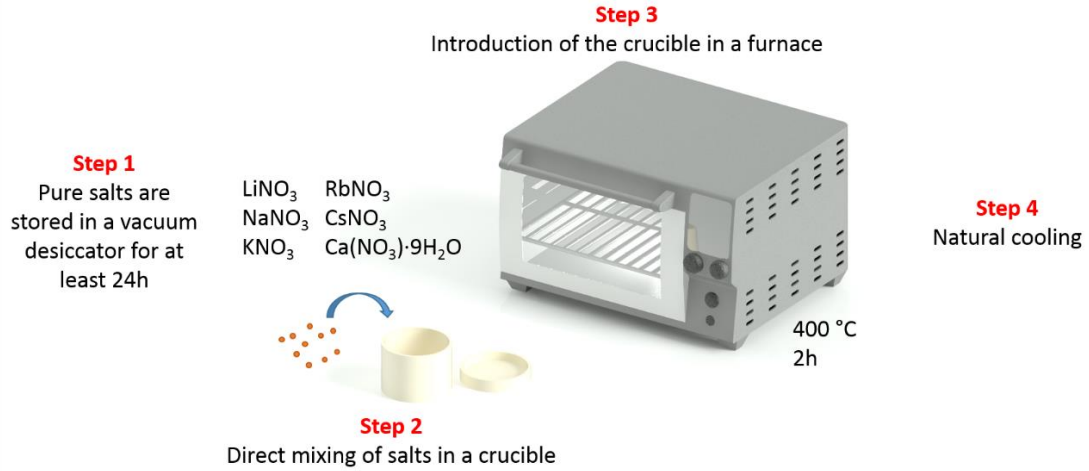

Figure 18 Schematic diagram of the preparation of the multi-component salts (particular example: sample S-Rb).

(ii) Methods

The behavior of the molten salts was studied as a function of temperature by DSC (PerkinElmer DSC 8000) from room temperature up to 300 ºC at different heating rates, using sealed aluminum pans in 20 ml/min nitrogen-flow atmosphere. Specific heat capacity was measured on a Mettler Toledo DSC822e 1 STAR^e system. The sapphire method was used and the heating program consisted on 'iso-dyn-iso' steps from 290-320 ºC in 60 ml/min nitrogen-flow atmosphere. An extended description of the experimental conditions is included in the supporting information of the manuscript (see page No. 3).

Thermogravimetric data was obtained from a Pyris 1 TGA (PerkinElmer) at 10 ºC/min, from room temperature up to 700 ºC in a 20 ml/min flow N_2 atmosphere. The thermal conductivity from solid to liquid states was measured by the 3ω technique in an in-house built setup. The details of the equipment and the conditions of measurement are detailed in an earlier work [49]. The Raman spectra of the samples were recorded with a HORIBA Jobin Yvon T64000 Raman spectrometer used in single grating mode with a spectral resolution better than 0.4 cm^{-1}. The salts were placed in a cryostat (Linksys32, Linkam Scientific Instruments) in a helium static atmosphere of 1 atm. All Raman measurements were carried out by focusing a diode laser (λ_0 = 532 nm) with 50x long working distance microscope objective. The power of the laser was kept at < 2 mW to avoid self-heating effects.

The transmission of a 635 nm red diode laser through two glass cuvettes, one empty and an identical cuvette filled with the sample, was recorded from room temperature to 140 ºC. The optical transmission measurements were performed in air atmosphere. The sample was heated using a hot plate inside an insulating box and the temperature was set manually. An extended description of the set-up is included in the supporting information (see pages 2-3).

The diffraction patterns were collected using a Malvern PANalytical X'pert PRO MPD diffractometer. It operated at 40 kV and 40 mA in theta-theta configuration using as the X-ray source a ceramic X-ray tube with Cu Kα anode (λ=1.5406 Å). Data were collected from 10 to 80º 2θ (step size=0.033º and time per step=219 s). The XRD analyses were carried out in transmission mode using a capillary spinner and the samples were filled inside

borosilicate glass capillaries with outer diameter of 0.7 mm. A focusing mirror was used for the incident beam and a lineal X'Celerator detector for the diffracted beam. Identification of the solid phases present in the mixture was performed using the PANalytical X'Pert HighScore Plus software and database.

The preparation of the samples for analysis required the melting of the samples to facilitate their handling. For this, a heat gun was used to heat above 100 ºC.

3.5.2 Thermal and physical-chemical characterization of the molten salts

In order to evaluate the potential of these molten salts for heat transfer and storage applications, an extensive examination of their thermal and structural properties was conducted. The thermal conductivity was measured for both solid and molten state, as well as the heat capacity and the temperature of degradation. For the structural study, X-ray diffraction and Raman spectroscopy analyses were performed. Differential scanning calorimetry (DSC) was used in the first place to study the thermal behavior of the samples. However, it was found that the determination of the solid-to-liquid transition of these materials by DSC was complex. To deepen into the thermal behavior of the materials, complementary and alternative techniques to DSC were used. The melting temperature of the salts was determined by three alternative techniques: optical transmission, the 3ω technique and Raman spectroscopy.

3.5.2.1 Thermogravimetric analysis: decomposition temperature under a linear heating program

A comparative study of the decomposition temperature of the new formulations was performed by thermogravimetric analysis, as shown in **Figure 19**. The materials were tested under N_2 flow and using a linear heating rate of 10 ºC/min**.** The three samples exhibited an initial weight loss at low temperature, which is ascribed to the evaporation of water absorbed by the material. Nitrates are in general very hygroscopic compounds. Therefore, the control of the storage conditions and atmospheric humidity during the preparation of the samples for the analysis is crucial to avoid water absorption.

Thermogravimetric analyses on salts S-Al and S-Rb were performed in our laboratory, hence the amount of absorbed water is similar in these samples. The thermogravimetric data from salt Q were taken from the literature [130]. A significant weight loss was observed for the three samples in the range of 550-700 ºC, which is attributed to the

decomposition of the salts. Under the same conditions, S-Al was thermally more stable than S-Rb. At 602 ºC, S-Rb had already lost 2.5% of its weight, in contrast, S-Al reached the same loss (2.5 % in weight) at 606 ºC. Raade and Padowitz [130] reported a 2.5 wt. % loss for the quinary mixture at 599 ºC in N_2 atmosphere, at a heating rate of 10 ºC/min. Therefore, the order in the thermal stability of the salts from most to least stable would be S-Al> S-Rb> Q, although the differences are marginal. However, it should be mentioned that these experimental datasets are not sufficient to predict the long-term thermal stability of the salts.

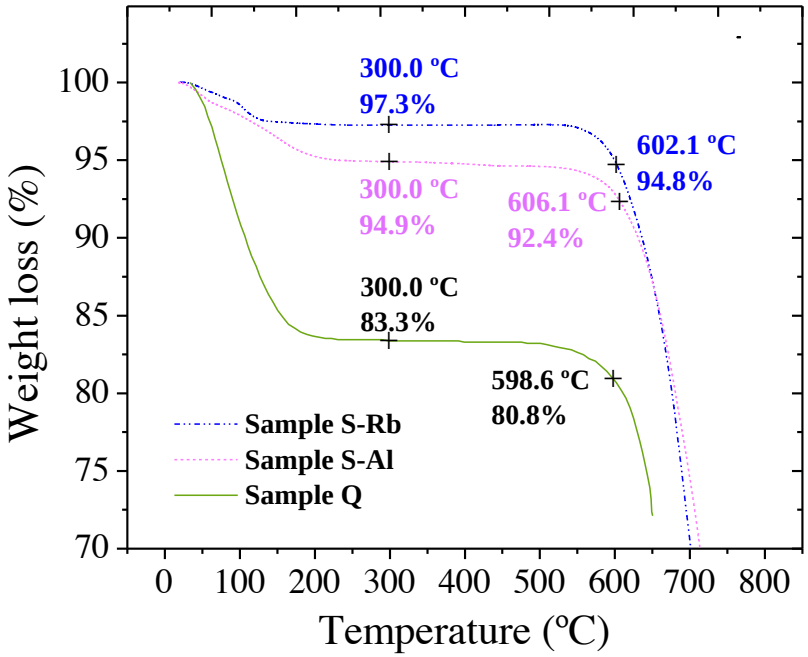

Figure 19 Thermogravimetric curves of the two senary salts and sample Q at a heating rate of 10 ºC/min in N_2 atmosphere. The thermogravimetric curve from salt Q was taken from the literature (data from ref. [130]).

3.5.2.2 Study of the thermal behavior of samples by differential scanning calorimetry

DSC curves of samples S-Al, S-Rb and Q were recorded with a thermal cycle of 10, 30 and 50 ºC/min as shown in **Figure 20a-c**. Multiple scan rates were applied to test the sensitivity of the equipment because no thermal events were observed under standard conditions (10 ºC/min). In addition, by varying the scan rate, temperature-time-dependent transitions can be easily identified, such as the glass transition. Hereafter, the temperature of first deviation of the baseline will be defined as the onset temperature of the phase transition (melting, crystallization, evaporation, etc.).

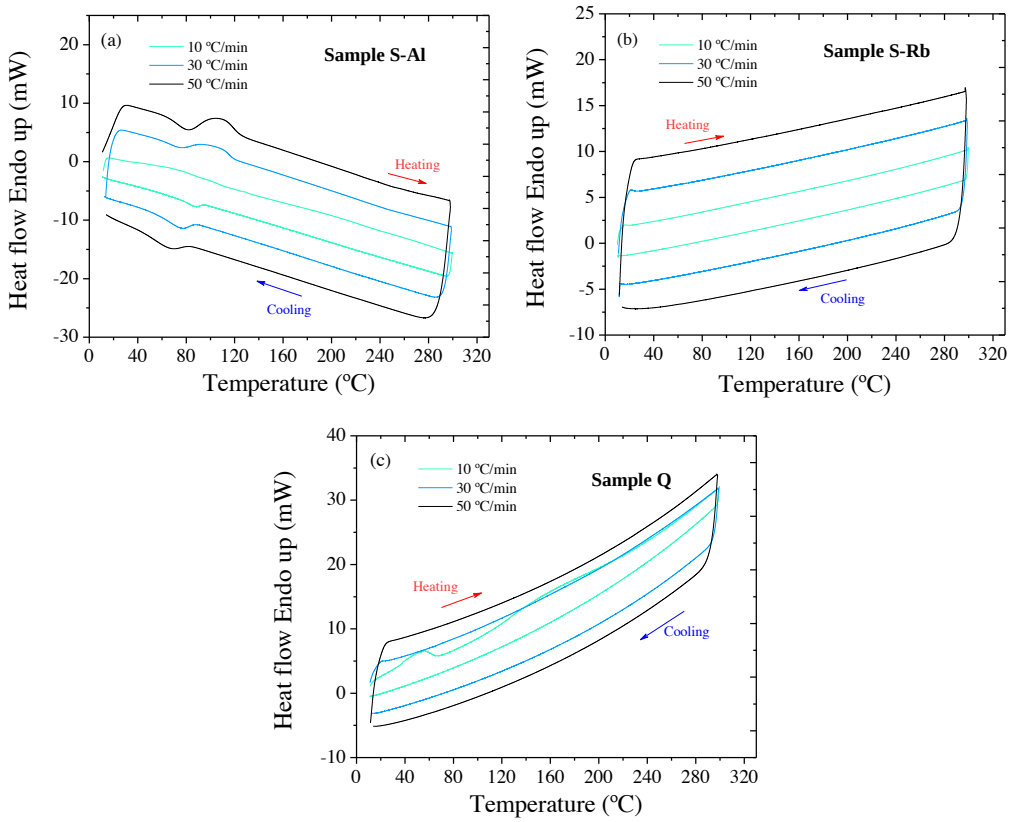

Figure 20 Calorimetric curves of the senary compositions and the previously reported quinary. (a) Calorimetric curves of S-Al at 10, 30 and 50 ºC/min, cooling and heating. (b) Calorimetric curves of S-Rb at 10, 30 and 50 ºC/min, cooling and heating. (c) Calorimetric curves of Q at 10, 30 and 50 ºC/min, cooling and heating.

As can be observed in **Figure 20a**, the DSC curve of sample S-Al shows no clear transitions during the heating step at the scan rate of 10 ºC/min, but an exothermic peak appeared during cooling at approx. 93 ºC. These results indicate that the sample is amorphous during the first heating at 10 ºC/min, hence, no phase change is observed. During the cooling step the salt crystallizes. At higher heating rates, a clear endothermic transition (peak onset ≈ 75 ºC) can be observed, as well as the corresponding exothermic peak during cooling. These peaks may correspond to the melting and crystallization of the salt, respectively, matching what was observed with the naked eye. The onset of the endothermic transition shifts only by 2-5 ºC over a heating rate range of 30-50 ºC/min, which indicates it is not a kinetic process (neither glass transition, nor decomposition), reinforcing the idea of a melting transition.

In contrast, samples Q and S-Rb did not show thermal transitions during the thermal cycle at any scan rate (**Figure 20b-c)**, with the exception of an endothermic peak at low

temperatures (onset ≈ 37 ºC), which appears only during the first heating cycle of the sample, see **Figure 20c** (10 ºC/min). The rest of the curves correspond to pre-heated samples.

The hygroscopic nature of the salts, together with the mass loss observed at low temperatures in the thermograms (**Figure 19)** indicate that the endothermic peak at ≈ 37 ºC corresponds to the vaporization of absorbed water in the sample. Pierced lids were used to avoid pressure problems or bursting. Consequently, as expected, no exothermic peak is observed during the cooling step.

The absence of thermal events in the calorimetric curves of samples Q and S-Rb can be explained by taking into consideration the nature and internal structure of multi-component mixtures. The presence of cations of different sizes and charges in the mixture hinders the crystallization of the material, thus promoting the amorphous state.

To better understand the structure of the materials and the factors that contribute to the vitrification or crystallization of the molten salts, X-ray diffraction (XRD) and Raman spectroscopy analyses were performed under different conditions.

3.5.2.3 Structural characterization

I. X-ray diffraction: structural characterization and water influence

The X-ray diffraction analyses were performed at room temperature, in air and under atmospheric humidity. The samples were melted with a heat gun before analysis to eliminate the absorbed water and ensure easy handling of the samples. **Figure 21a-c** shows the XRD patterns of the samples S-Al, S-Rb and Q as a function of time: right after melting (solid state), 1-2h after melting and more than 12h. The X-ray diffraction patterns show that samples Q and S-Rb do not crystallize right after the melting, but after 1 or 2 hours. On the contrary, S-Al presents a faster crystallization. These results support the interpretation of DSC curves given earlier. Therefore, it was perfectly reasonable not to detect the transition from solid to liquid in the Q and S-Rb samples by DSC, while the S-Al sample showed the transition regardless of the scanning rate used. This was possible due to the faster crystallization of this formulation. It is worth to remind the reader that the samples were melted with a heat gun before any measurement to favor an easy-handling.

The effect of humidity was also studied by XRD. The longer the samples were kept in air, the greater the exposure to humidity. The results indicate that the exposure to a humid

environment favors the crystallization of Q, S-Al and S-Rb, see **Figure 21 a-c**. Water facilitates the movement of the ions within the mixture, acting as a lubricant and catalyst for crystallization.

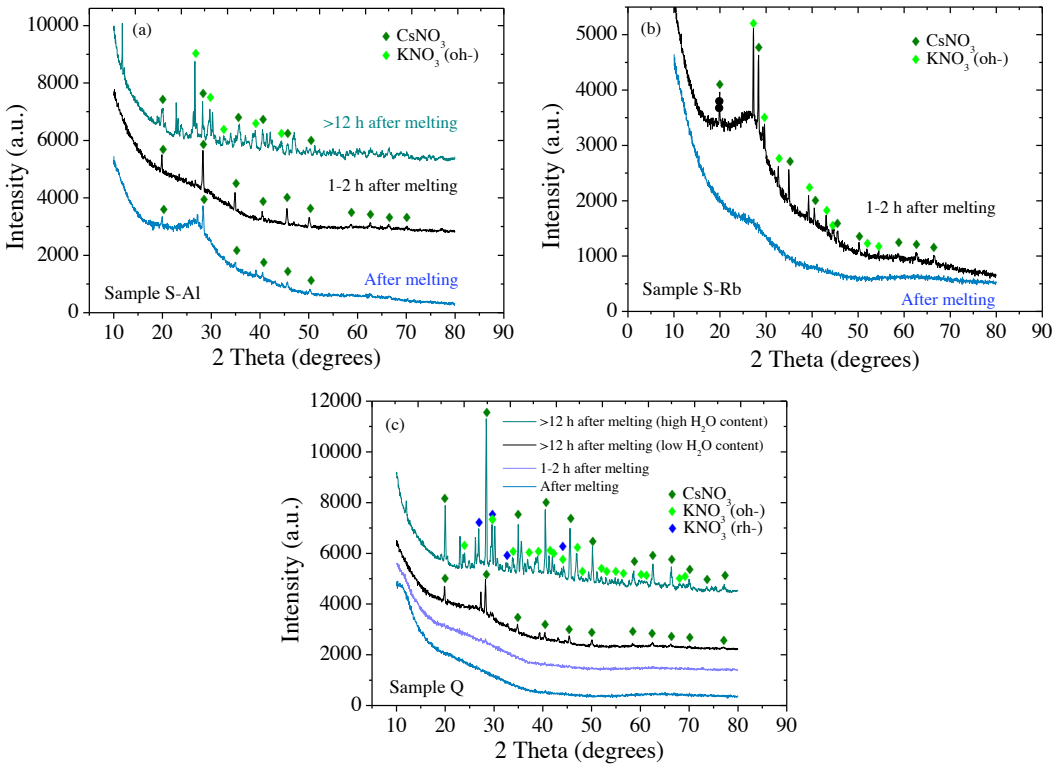

Figure 21 XRD patterns of samples (a) S-Al, (b) S-Rb and (c) Q, as a function of time elapsed after the melting and water content.

II. Raman spectroscopy as function of temperature and its impact on molecular vibrations

The Raman spectra of the samples were recorded as a function of temperature in steps of 10 ºC, approximately, from -10 to 149 ºC at a scan rate of 2 ºC/min (in a controlled He atmosphere, 1atm). Raman spectroscopy can provide information about the amount of disorder in the structure. In glasses all bands appear broadened typically with linewidths in the range of 20 cm^{-1}, which is an order of magnitude broader than that measured in ordered crystals [135]. Both, amorphous solids and liquids show bands substantially broader than the crystalline solid-phase. Therefore, this set of experiments provides information on the solid-to-liquid transition and the internal structure of the mixtures as a function of temperature. As can be seen in **Figure 22a-c** the band at ~ 1050 cm^{-1} was

followed for samples S-Al, S-Rb and Q as a function of temperature. This intense band is ascribed to a symmetric stretching mode of the nitrate ion, ω_1, if D_{3h} symmetry is assumed for the NO_3^- in the crystalline state, and no distortion of the geometry occurs, as Janz et al. assumed [141]. In addition, other very weak bands present at ~ 1350, 1380-1443 and 1650 cm^{-1} have been associated to antisymmetric stretching modes and an overtone of a bending mode (scissoring) of the nitrate ion [141]. However, their low Raman activity makes them difficult to detect. Therefore, we based our study on the symmetric stretching mode of NO_3^- as a function of temperature.

Janz et al. reported that the internal modes of NO_3^-, such as ω_1, are affected by the cationic environment. In fact, in pure salts this mode (ω_1) has been shown to be correlated with the polarizing power of the cationic species, e.g., in alkaline nitrates going from Li^+ to Cs^+, ω_1 decreases in frequency in a regular manner. Furthermore, in some alkaline binary mixtures, ω_1 appears as an additive function of the pure salts ω_1 frequencies multiplied by the fraction present [141].

In mixtures of nitrates of five or six cations of different sizes and charges, as is our case, it has been found that glassy structures are preferentially formed during rapid-cooling [134,135]. This is due to the inability of these ions to segregate into pure component crystals during cooling as they appear to be randomly mixed in the molten state [135].

Sample S-Al

The **Figure 22a** shows the Raman spectra of sample S-Al as a function of temperature recorded with increasing temperature at a rate of 2 ºC/min. As can be seen, at room temperature there is a band with a narrow linewidth (ΔE ~ 3 cm^{-1}) at ~ 1048 cm^{-1} and a small shoulder at higher frequencies. Both correspond to the stretching mode of NO_3^-. However, the narrow band at 1048 cm^{-1} corresponds to the salt in crystalline state whereas the shoulder can be associated with an amorphous domain existing in the salt due to the fast heating during the sample preparation. From room temperature to 65 ºC, the shoulder becomes smooth and at 76 ºC it becomes more intense up to 107 ºC dominating the spectrum. At 118 ºC the peak at 1048 cm^{-1} is completely masked by the shoulder which has become a wider band, indicating that the phase change to liquid state has come to its end.

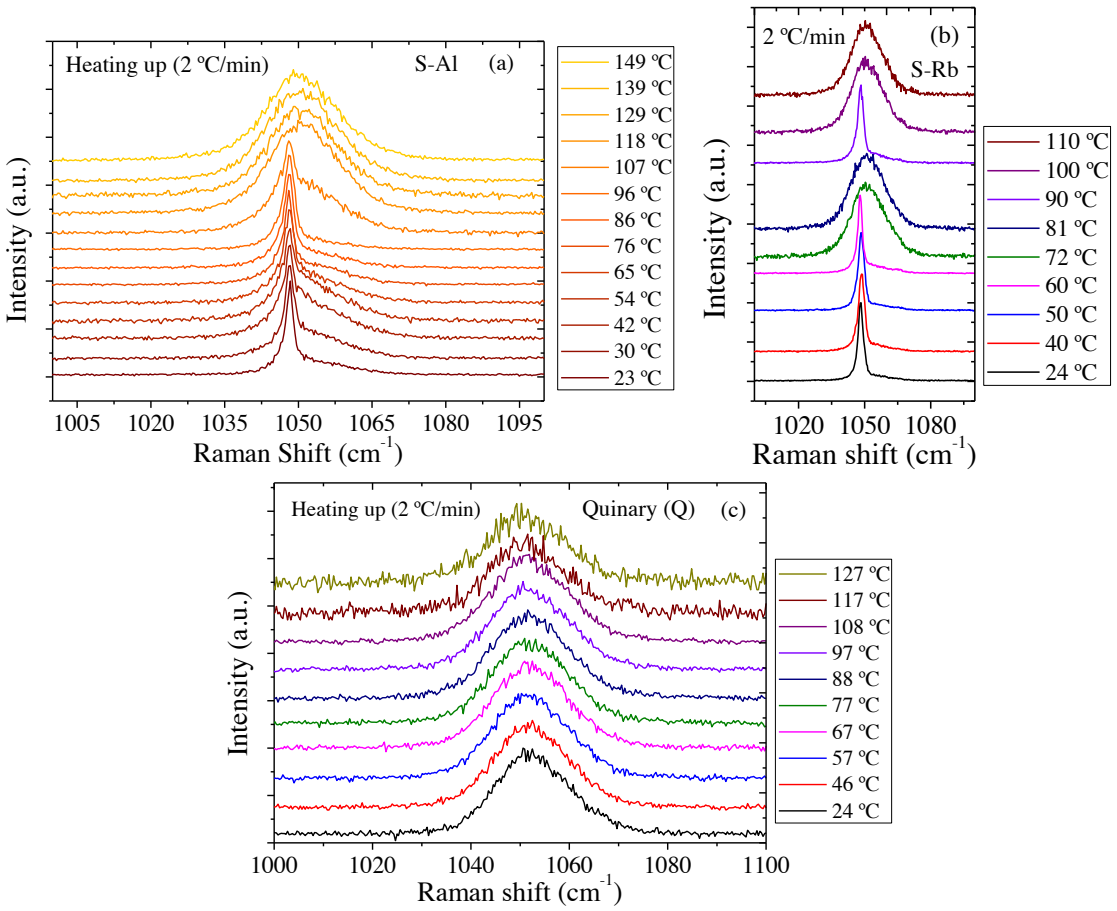

Figure 22 Raman spectra of the samples S-Al, S-Rb and Q recorded during heating at 2 ºC/min. The intensity and linewidth of the symmetric stretching NO_3^- mode are followed for the samples (a) S-Al (b) S-Rb and (c) Q.

Sample S-Rb

The symmetric stretching band (v ≈ 1050 cm^{-1}) is shown in **Figure 22b.** The frequency and line-shape were tracked from room temperature to 110 ºC at a heating rate of 2 ºC/min. Both frequency and line-shape remained unchanged up to 60 ºC above which the band suddenly broadens. At that point the band broadened around 20 cm^{-1} indicating a disorder in the surroundings of the nitrate anion. This result points to a phase change from solid (crystal) to liquid state occurring between 60-72 ºC. The spectrum at 90 ºC demonstrates that there are still solid (crystalline) domains, therefore, at 90 ºC the salt is still not homogeneous, i.e. not completely molten.

Sample Q

The symmetric stretching NO_3^- mode was recorded during heating at 2 ºC/min as a function of temperature, as shown in **Figure 22c**. As can be seen the band showed a broad linewidth and line-shape in the whole temperature range. However, the typical shift to lower frequencies when increasing temperature can still be observed. The intense broad band at low temperatures indicates the amorphous nature of the sample in solid state. Unfortunately, the linewidth and line-shape remained unaltered when temperature is increasing, without a drastic change at any temperature. Therefore, no information corresponding to the phase change can be obtained analyzing these spectra. These mixtures present a number of properties that change abruptly when turning from solid to liquid states, such as the internal vibrational energies, and others, like sample transparency and thermal conductivity. The thermal conductivity and the transparency variation of the material in solid and liquid states were used to determine the phase change using the 3-ω technique and optical transmission, respectively. In this sense, our findings open the possibility to use fast methods to gain thermal knowledge on molten salts and related samples at much reduced cost compared to a standard DSC.

3.5.2.4 Thermal conductivity and optical transmission: alternative techniques to detect solid-to-liquid transitions in molten salts.

The variation in transparency of the salts in the solid and liquid states, from white to transparent, respectively, allowed the detection of the phase change by optical transmission. **Figure 23d** shows the appearance of the S-Rb salt in solid (white) and liquid (transparent) states. The thermal conductivity was measured from room temperature to 140 ºC. **Figure 23a-c** shows a representation of the thermal conductivity and optical transmission data of S-Al, S-Rb and Q as a function of temperature. In all three cases, a decrease on the thermal conductivity can be observed as the temperature increases. On the contrary, the optical transmission increases as the solid to liquid phase change occurred. The onset temperature of the phase change from solid to liquid derived from optical transmission and thermal conductivity data were found to be in good agreement.

The **Figure 23a** shows the transmission and thermal conductivity curves of sample S-Al as a function of temperature. As can be seen, the light started to be transmitted above 60 ºC, in agreement with DSC data. The transmission increased up to a maximum at 96 ºC and above this temperature the transmission remained constant. On the other hand, a drop in

thermal conductivity (*k)* was more difficult to observe. It can be seen that above 76 ºC there was an important change in the thermal conductivity, which perfectly matched the corresponding transmission and DSC data.

The thermal conductivity of sample S-Rb underwent a noticeable drop in *k* values starting at 60 ºC, as shown in **Figure 23b.** Transmission also started to increase at 60 ºC. Furthermore, *k* and transmission values remained constant above 100 ºC, indicating the end of the phase change.

As shown in **Figure 23c**, there was a drastic change on the transmission of sample Q above 60 ºC, which is also the temperature at which the thermal conductivity begins to fall gradually. This change in transmission and thermal conductivity indicates the starting temperature of the melting, which is in complete agreement with the value reported by Raade and Padowitz [130]. As can be observed, *k* and transmission values remained constant above 100 ºC.

The decrease in transmission observed in **Figure 23b** from 25 to 45 ºC is due to water absorption by the salt. The presence of water has been proven to favor the crystallization of the salt, which results in the white color of the salt. Consequently, the initial state of the samples was semi-crystalline and translucent in some of the cases. This explains the change in transparency of the sample S-Rb to more opaque with time, until the material changed to the liquid state. The optical transmission measurements were performed in air atmosphere without controlling the humidity. A hot plate was used to heat the sample and the temperature was set manually. Consequently, the period of time required for the temperature to stabilize each time differs from one measurement to another (different time gaps). Hence, the absorption of water also varied from one sample to another.

Regarding thermal conductivity, we can conclude that there is not a significant difference in their values, at a given temperature, for the different molten salts. As can be seen in **Figure 23**, *k* values vary from 0.345 to 0.358 W $m^{-1}K^{-1}$ which are in the same range reported previously for other molten salts [142]. The average thermal conductivity of these salts in the liquid state is slightly smaller than that of the Solar salt (≈0.520 W m^{-1} K^{-1}) [143] and similar or even larger than that of Hitec (≈0.350 W m^{-1} K^{-1}) [144].

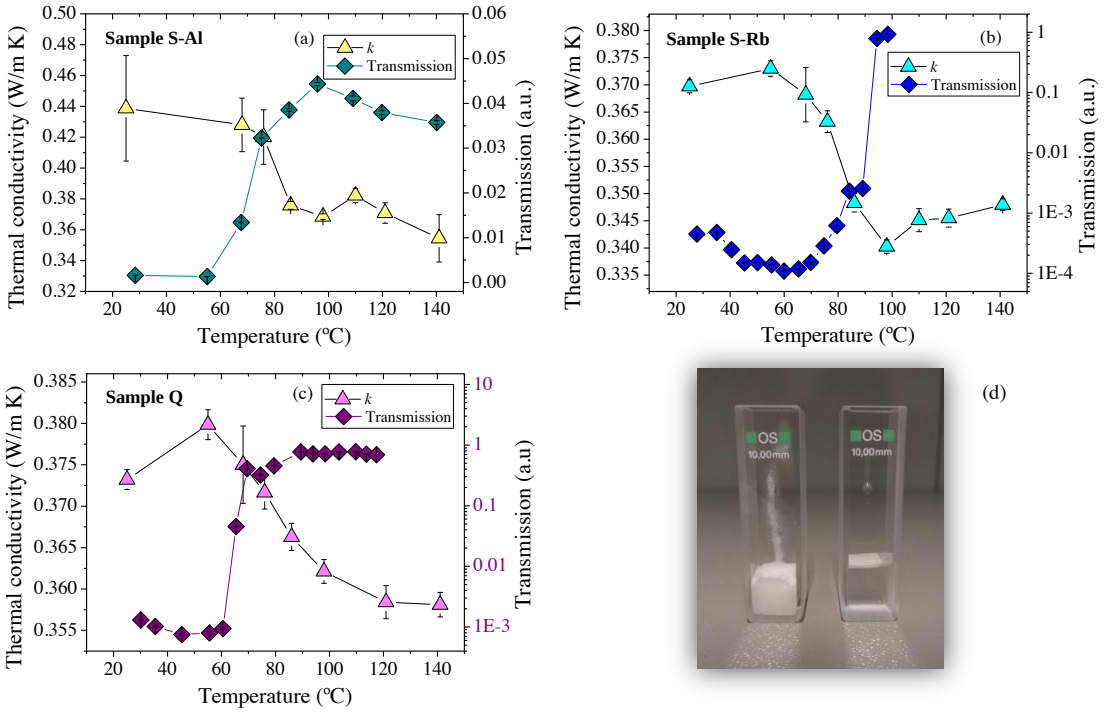

Figure 23 Optical transmission (full diamonds) and thermal conductivity (full triangles) of samples S-Al (a), S-Rb (b) and Q (c) as a function of temperature and (d) an image of sample S-Rb in solid (white) and liquid (transparent) states.

3.5.2.5 Specific heat capacity

The specific heat capacity (Cp) was determined using the Sapphire method (ASTM standard E1269 – 11) measured by DSC. The Cp measurement of each salt was repeated at least three times and the average values are shown in **Figure 24**, which shows the specific heat capacity of salts Q, S-Al and S-Rb as a function of temperature from 290-320 ºC. Cp values of salt Q were taken from the literature [136] to compare with the new formulations. The measured specific heat capacity of the new salts is close to that of the Halotechnics SS-500 (sample Q) and $NaKCsNO_3$ salts (1.20 and 1.18 J g^{-1} K^{-1}, respectively) [136]. These results support the potential of these salts to be used as thermal energy storage materials in CSP technology.

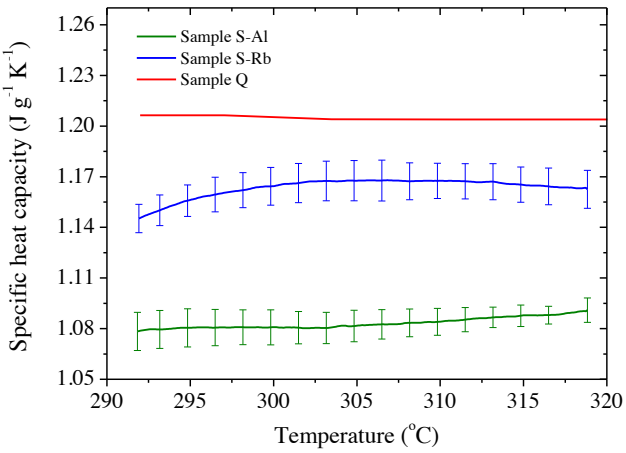

Figure 24 Specific heat capacity of samples S-Al, S-Rb (experimental data) and Q (the latter taken from reference [136]), as a function of temperature.

3.6 Additional results

3.6.1 Validation of alternative techniques to DSC by testing a sample with confirmed melting point

A well-known ternary eutectic mixture (30% $LiNO_3$,18% $NaNO_3$, 52% KNO_3, wt.%) was analyzed using both DSC and the suggested alternative techniques. This ternary nitrate was reported by R. Olivares et al. [129]. The **Figure 25** displays the differential scanning calorimetry curve from 25 to 200 ºC at a scanning rate of 10 ºC/min in N_2 flow. The analysis was performed by a Mettler Toledo DSC 1 STAR system using pierced Al crucibles. As can be observed, two endothermic peaks appear during the heating step. The first one, starting at ≈ 91 ºC, corresponds to a (α/β) solid-solid transformation. The second endothermic peak starts at ≈ 120 ºC and is attributed to the melting of the salt. The exothermic peak at 89 ºC during the cooling step indicates the crystallization of the eutectic composition. The results are in perfect agreement with the data reported by Olivares et al. [129].

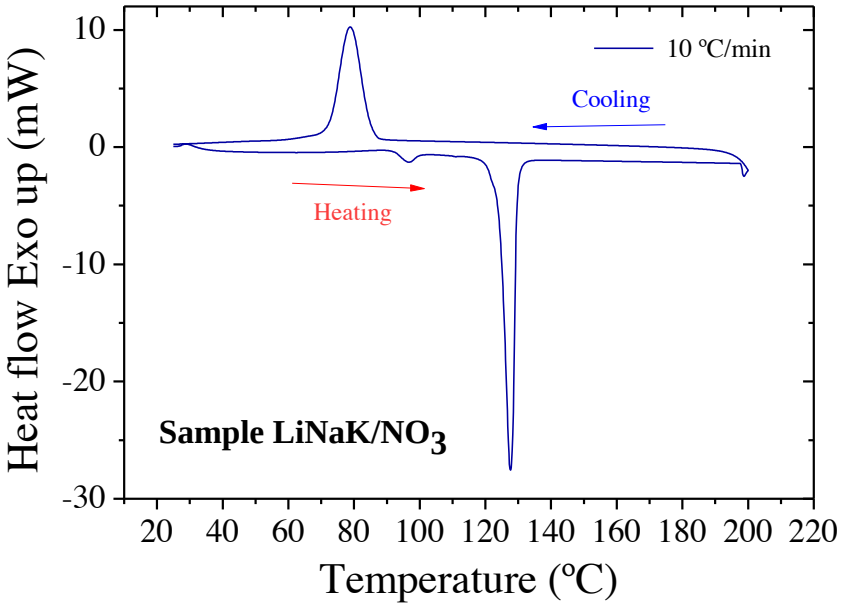

Figure 25 Calorimetric curve of $LiNaK/NO_3$ under heating and cooling rates of 10 ºC/min and N_2 flow.

The thermal conductivity of the ternary mixture ($LiNaK/NO_3$) was measured using the three-omega technique as a function of temperature (see **Figure 26a**). The thermal conductivity slightly decays from 25-55 ºC probably due to the absorption of water, as the atmosphere is not controlled in this experiment. Then, a small jump in the thermal conductivity can be observed at ~ 90-110 ºC, which can be ascribed to the solid-solid transition. Above 110 ºC the thermal conductivity decreases dramatically which is in agreement, in terms of temperature, with the solid-to-liquid transition observed with DSC. On the other hand, the optical transmission technique gives a starting melting temperature ≈ 110 ºC in the same range than the obtained by the DSC and the three-omega technique, see **Figure 26b**.

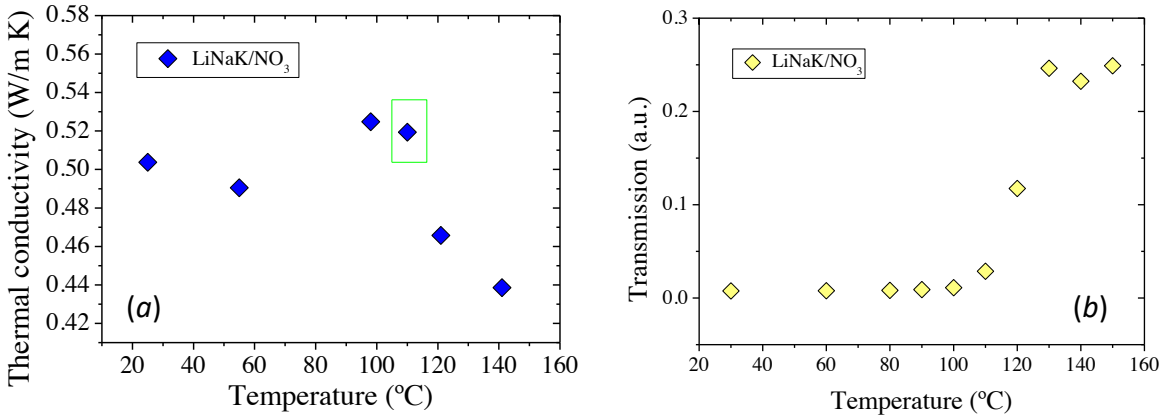

Figure 26 (a) Thermal conductivity of the sample LiNaK/NO_3 as a function of temperature, (b) optical transmission of the sample LiNaK/NO_3 as a function of temperature.

It is worth to mention the procedure used to register the thermal conductivity and optical transmission as a function of temperature. In both cases, the temperature is controlled manually. Once the set temperature is stable, the measurement begins (isothermal program). It is not a dynamic measurement as the DSC analysis (linear program). This can explain why the starting of the melting occurs around 110 ºC using optical transmission and three-omega techniques.

To determine the solid-liquid phase change of LiNaK/NO_3 by Raman spectroscopy, we followed the symmetric stretching mode of NO_3^-, ω_1, as a function of temperature. A heating rate of 10 ºC/min was applied. To better interpret the results, it is necessary to take into account the frequencies of this vibrational mode (ω_1) in the individual components. In the solid state: $\omega_1(LiNO_3)$=1086 cm^{-1}, $\omega_1(NaNO_3)$=1069 cm^{-1}, $\omega_1(KNO_3)$=1050 cm^{-1} [141]. The ternary salt has different proportions of the three nitrates, and since this vibrational mode in the individual components appears at quite different frequencies, it is common to find several bands at frequencies resulting from the combination of the individual nitrates.

In this particular case, a double band around 1052 cm^{-1} and 1068 cm^{-1} can be observed for the salt in the solid state (see **Figure 27**). Since KNO_3 is the main component in the ternary, the band around 1052 cm^{-1} must correspond to domains where K^+ is the majoritarian cation. The **Figure 27** shows the Raman spectrum (vibrational mode: ω_1) of LiNaK/NO_3 registered under a heating rate of 10 ºC/min. If we analyze the results, it can be noticed that from 30-90 ºC the bands exhibit similar shape, the band at higher frequency remains the same but the other around 1052 cm^{-1} shows a light shift to lower

frequencies. Around 100 ºC there is a relevant blue-shift of the band positioned at lower frequency, while the other remains invariable. This change could correspond to the (α/β) solid-solid transformation, which seems directly related to a change in the arrangement of cation K^+ around NO_3^-. It is worth to mention that since the solid-solid phase change was registered at 91 ºC using DSC and that an evident jump of the thermal conductivity was detected at 90 ºC by the 3-ω technique, the blue shift in the ω_1 mode around this temperature can correspond to the (α/β) solid-solid transformation. After this, the spectrum changes completely between 130-140 ºC. The two bands merge in one, resulting in a band with wider linewidth. This indicates that the salt is in an amorphous state, in this case in the liquid form.

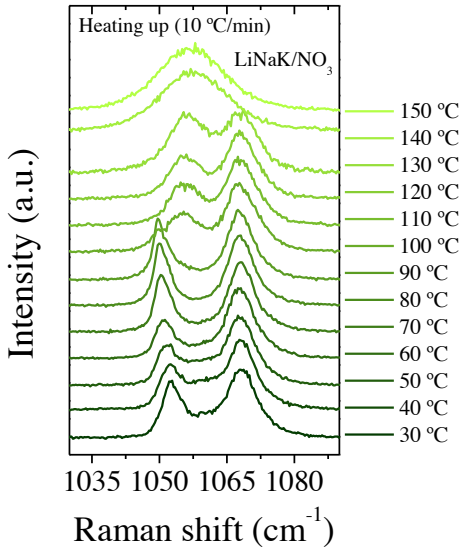

Figure 27 Raman scattering of sample LiNaK/NO_3 displayed as a function of temperature. Bands ascribed to the symmetry stretching of NO_3^- are followed under heating at a rate of 10 ºC/min.

The validity of these alternative techniques for the detection of solid-to-liquid transitions in molten salts was confirmed. The results were in perfect agreement with those from differential scanning calorimetry.

3.6.2 Comprehensive calorimetric analysis of the quinary salt

The study of the thermal behavior of the aforementioned multi-component salts was found to be complex. Therefore, we decided to conduct a more detailed analysis by differential scanning calorimetry using an external service. The quinary salt, Q, was measured using a Tzero™ DSC from TA Instrument. The sample was placed in a sealed Tzero aluminum

pan and a nitrogen-flow atmosphere was used during the experiments. The sample was not melted prior to the analysis. Several cycles of heating and cooling were conducted on the sample at different scanning rates and temperature ranges.

I. Cycle 1

The first heating was performed from -84 ºC to 150 ºC at a scan rate of 10 ºC/min. The lower curve in **Figure 28** shows a glass transition at ≈ -71.5 ºC. After that, it is not sufficiently clear if there is an exothermic peak with an onset starting at ≈ -11 ºC. However, the calorimetric curve shows two clear endothermic transitions, one following the other, at 13 ºC and 65 ºC, with an enthalpy of 4.7 J/g and 48 J/g, respectively.

The cooling step from 107 ºC to -90 ºC at a scan rate of 10 ºC/min shows a glass transition at ≈ -37 ºC. The change in slope after the glass transition occurs when reaching low temperatures (due to a variation of the cooling rate). This effect is produced by the cooling system and has nothing to do with the sample behavior.

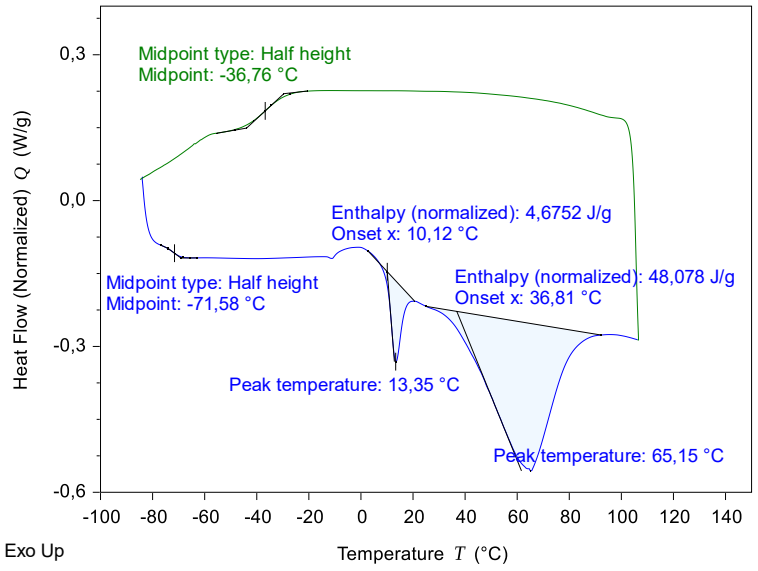

Figure 28 Calorimetric curves of sample Q under heating and cooling rates of 10 ºC/min and N_2 flow

II. Cycles 2 and 3

The second cycle consisted of a heating step from -85 ºC to 107 ºC (blue curve) and a cooling step from 110ºC to -90 ºC (pink curve), using a scan rate of 10 ºC/min and 1 ºC/min, respectively. **Figure 29** displays the curve corresponding to the heating step in cycle 2 (blue curve). The curve shows a glass transition at -33 ºC. This value is in agreement with the glass transition value found in the previous cooling curve (cycle 1, see **Figure 28**). There are other thermal effects above 0 ºC, however, they are difficult to interpret. The cooling step of cycle 2 (pink curve, **Figure 29**) shows a glass transition (Tg) around -19 ºC, the scan rate used is 1 ºC/min. As glass transition is a kinetic process, the shift in temperature of the glass transition from cycle 1 to cycle 2 can be understandable; however, the shift is too large. These materials are very complex and the arrangement of the species when going from the melt to the solid state depends on many factors, therefore, it is possible that after cooling at such a slow scan rate, the structure has changed considerably. The cycle 3 is composed of a single heating step from -90 ºC to 110 ºC at a scan rate of 10 ºC/min (green curve). The green curve in **Figure 29** shows a glass transition at -13 ºC.

These are preliminary results and a more detailed study is needed. The next step would be the analysis of this sample by using modulated differential scanning calorimetry (MDSC), which is a more sensitive technique. However, we can conclude from these results that this type of materials has a very complex behavior and has difficulties in crystallizing. No exothermic peak was observed during cooling, no matter which scan rate was used.

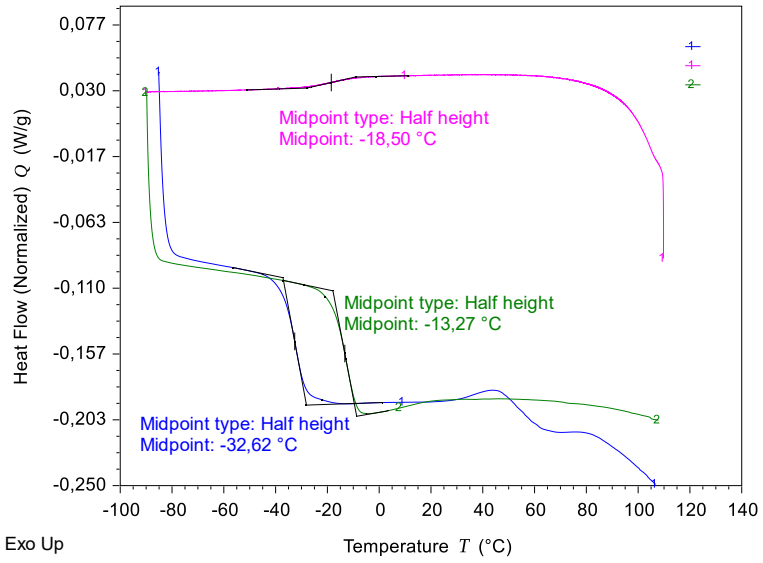

Figure 29 Calorimetric curves of sample Q under a heating rate of 10 ºC/min (blue and green curves, cycle 2 and 3, respectively) and under a cooling rate of 1 ºC/min (pink curve, cycle 2) in N_2 flow.

3.7 Conclusions

An important feature of multi-component salts is that the difference in size of the species hinders the crystallization and provides lower melting temperatures. Herein, two novel six-component nitrates 'S-Al' ($LiNaKCsCaAl/NO_3$) and 'S-Rb' ($LiNaKRbCsCa/NO_3$) were for the first time prepared and thermally characterized. These molten salts have low melting temperatures of ≈ 60-75 ºC and a thermal stability above 500 ºC under a linear heating program of 10 ºC/min in N_2 atmosphere. A complete study on the thermal properties of the materials was performed to evaluate their potential performance as heat transfer and storage materials. Their specific heat capacity values are close to that of the Halotechnics SS-500 and $NaKCsNO_3$ salts [136] and are slightly below that of the Solar salt [143]. The average thermal conductivity of these salts in the liquid state is slightly smaller than that of the Solar salt (≈0.520 W m^{-1} K^{-1}) [132] and similar or even larger than that of Hitec (≈0.350 W m^{-1} K^{-1}) [144]. A comparative study on the thermal stability of the salts by thermogravimetric analysis showed that samples S-Al and S-Rb are as thermally stable as Halotechnics SS-500 [130] and comparable to Na-K-Li nitrates [6].

The determination of the solid-to-liquid transition of these materials can be complex. The internal structure of multi-component salts can be affected by the cooling rate and water presence. These factors may influence the crystallization or amorphization of the material.

To deepen into the thermal behavior of the materials, complementary and alternative techniques were used. The melting temperature of the salts was determined by three alternative techniques: optical transmission, the 3ω technique and Raman spectroscopy. The monitoring of properties such as variation in transparency, thermal conductivity and internal vibrations of the salts as a function of temperature was demonstrated to be a useful indicator of the solid-to-liquid phase change.

The Raman spectra analysis revealed relevant information about the internal structure of the salts. The monitoring of the symmetric stretching mode of NO_3^- as a function of temperature provided information about the distribution of the cationic environment, the ordering of the solid below melting point and the onset melting temperature.

The difficulty in the ordering of these multi-cationic nitrate mixtures during cooling was also demonstrated, confirming previous findings in the literature [134,135] stating that a variable cationic environment favors glass formation during rapid cooling. X-ray diffraction analyses as a function of time and humidity showed that water acts as a catalyst for crystallization, providing mobility to the ions within the material. Furthermore, the addition of $RbNO_3$ and $Al(NO_3)_3$ to the original 5-component recipe of Halotechnics SS-500 (Q) favors the crystallization of the material, as displayed in the X-ray diffractograms as a function of time.

Our results suggest that these two new nitrate-based salts could be potential candidates for heat transfer and storage applications in CSP technology due to their low melting temperature, high thermal stability, good thermal conductivity and specific heat capacity, although further research is needed. Furthermore, three alternative techniques to DSC have been presented and validated to detect solid-to-liquid phase transitions of low energy. These unprecedented techniques for phase change detection widen the number of characterization methods in the field of thermal solar energy.

From the more complete calorimetric analysis performed on sample Q we can conclude that these multi-component salts are very complex materials and that their thermal behavior much depend on external factors, such as storage conditions, humidity, cooling rate, etc. However, the results obtained from DSC and the alternative techniques show that the melting temperature of these materials is consistent, regardless the technique used for the analysis. If the initial state of the material is crystalline, it can be stored above

its melting temperature and used as thermal storage material or heat transfer fluid for high-temperature applications.

There is little known about multi-component salts. Their amorphous nature is not necessarily an inconvenient for their application in CSP systems. All the results gathered show the complex behavior of this sort of materials. However, the complexity is nothing but gaps in the field. Future studies on the internal structure and amorphous behavior of multi-component salts are expected to fill those gaps. This knowledge will be crucial to the application of these materials in the field of thermal-solar energy, among others.

3.8 Acknowledgements

I would like to thank Dr. Carlos Gracia, TA Instruments, for helping me go further and perform a comprehensive calorimetric analysis of the quinary salt (Q). I would also like to acknowledge his priceless assistance in interpreting the results.

Article 3

Development of low-melting point molten salts and detection of solid-to-liquid transitions by alternative techniques to DSC

M. R. Rodríguez-Laguna*[1, 2], P. Gómez-Romero*[1], C. M. Sotomayor Torres[1, 3], M.-C. Lu[4] and E. Chávez-Ángel*[1]

[1] Catalan Institute of Nanoscience and Nanotechnology (ICN2), CSIC and BIST, Campus UAB, Bellaterra, 08193 Barcelona, Spain

[2] Departament de Química, Universitat Autònoma de Barcelona, Cerdanyola del Vallès, 08193 Barcelona, Spain

[3] ICREA, Pg. Lluís Companys 23, 08010 Barcelona, Spain

[4] Department of Mechanical Engineering, National Chiao Tung University, 1001 University Road, Hsinchu 30010, Taiwan

*Corresponding authors: rodriguez3laguna@gmail.com; pedro.gomez@icn2.cat, emigdio.chavez@icn2.cat

Keywords: Solar thermal conversion, molten salts, low melting point, heat transfer fluids, thermal conductivity, Raman spectroscopy, thermal energy storage.

Abstract

The 'Solar salt' (60% $NaNO_3$-40% KNO_3, wt. %) is the most used heat transfer and storage material in high temperature CSP systems. The main drawback is its high melting temperature of 228 ^oC, which requires extra-energy to keep it in the liquid state and avoid damage to pipes at low temperatures. Multi-component salts are combinations of different cations and anions. The difference in size of the ions hinders the crystallization of the material and provides lower melting temperatures. Multi-component salts are considered in this study to replace simpler combinations, such as binary and ternary eutectic mixtures. Herein, we report on two novel six-component nitrates with a melting temperature of 60-75 ^oC and a thermal stability up to ~ 500 ^oC under a linear heating program in N_2 atmosphere. Properties such as the thermal conductivity in solid and molten state, heat capacity and vibrational spectra were evaluated. The study of the thermal behaviour of these materials using differential scanning calorimetry was insufficient, hence alternative and complementary techniques were used, such as: the three-omega technique, optical transmission and Raman spectroscopy. Multi-component salts were found to solidify as amorphous solids even at slow cooling rates and water was found to behave as a catalyst of crystallization.

Introduction

Solar thermal conversion is now recognized as the soundest way to produce ecofriendly electrical energy [1,2]. The growing interest in this technology has opened new branches in the areas of heat transfer fluids (HTFs) and thermal energy storage (TES) materials [3–6]. In tower- and dish-type solar thermal power plants, temperatures higher than 1000 ^{o}C can be reached [7,8]. Consequently, these high-temperature collectors require fluids with high thermal stability to effectively absorb this concentrated solar energy and deliver it to a heat exchanger or to a heat storage tank, without decomposing. Furthermore, a low melting point fluid is essential to reduce the operational costs of heating the fluid at night to avoid it freezing [9]. A fluid with a wide operational temperature range is beneficial both for energy conversion and for energy storage. Thus, producing high-temperature steam will substantially increase the efficiency of the steam turbine (Carnot's theorem) and that of the overall energy conversion. And in terms of sensible energy storage, a larger temperature difference in the storage system will result in a significantly increased specific storage capacity. [10,11]

In this sense, molten salts are best positioned to be used as heat transfer fluids (HTF) and thermal energy storage (TES) materials in concentrated solar power (CSP) technology [12,13]. In fact, molten salts are the most widespread storage materials in commercial CSP and can be used as direct and indirect heat storage [13]. They are defined as ionic compounds that melt at high temperatures (≈ 200-1000 ^{o}C) and form homogeneous and stable liquids. They include, among others, nitrates, nitrites, chlorides, hydroxides, carbonates and their mixtures [1,14–23]. Among them, nitrates show the most desirable features including non-toxicity, low corrosion, low vapor pressure and a suitable combination of high thermal stability and medium-melting temperature. Other advantage of these types of fluids is the possibility of developing mixtures with a lower melting point than their individual components (eutectics).

A non-eutectic binary salt mixture of $NaNO_3$-KNO_3 (60-40 wt.%) [24] is the most widely used HTF/TES material in solar power towers. It is thermally stable up to 560 ^{o}C, however, it has a medium-high melting point of 228 ^{o}C. Another example is a ternary mixture of carbonates with a high melting point of 400 ^{o}C [25], the lowest for a carbonate-based mixture. The main drawback of molten salts as storage medium is their high freezing points. Currently, trace heating systems and tank heaters have to be installed to reduce thermal gradient and minimize freezing risks. As a consequence, unaffordable parasitic consumptions are generated to maintain the salts in a liquid state [13]. In this sense, the development and use of novel composition of molten salts with lower melting points can reduce dramatically these costs and, as a consequence, improve the overall efficiency of the CSP system.

In this work, two novel molten salts with significantly low melting points and composed of $LiNO_3$-$NaNO_3$-KNO_3-$CsNO_3$-$Ca(NO_3)_2$-$Al(NO_3)_3$ and $LiNO_3$-$NaNO_3$-KNO_3-$CsNO_3$-$Ca(NO_3)_2$-$RbNO_3$, respectively, are proposed and studied. They have a melting onset below 75 ^{o}C and a thermal stability above 500 ^{o}C under a linear heating program of 10 ^{o}C/min. The thermal conductivity, melting temperature, specific heat capacity and vibrational spectra of the salts were evaluated. The results reveal the potential of these salts to be used as heat transfer fluids and thermal energy storage materials in CSP technology.

These new molten salts are six-component multi-cationic nitrates. It is known that the combination of cations with different charges and sizes hinders the crystallization of the material [26,27]. Therefore, molten salt mixtures with five or more components often show a

lower melting point than binary or ternary compositions. However, the determination of the solid-to-liquid transition of these materials can be complex, due to several factors affecting their internal structure. To deepen into the thermal behavior of the materials, complementary and alternative techniques to the conventional differential scanning calorimetry (DSC) has been used. Some authors have used a capillary melting point apparatus to determine the solid-liquid phase transition [16]. However, these measurements are performed by image processing or eye observation, which are insufficiently accurate. To meet the challenge of determining the solid-to-liquid phase transition of molten salts, we have used, and report here, the following techniques: i) automatized optical transmission method, ii) the three-omega (3ω) technique and iii) Raman spectroscopy. All yielded similar results and agree with the melting temperature recorded by the naked eye, while providing a more reliable and objective determination of the melting range. Furthermore, these techniques provide important extra information regarding the thermal behavior of the mixtures and are proposed here as useful techniques for melting point and related phase-change studies. Other multi-cationic nitrate combination known as 'Halotechnics SS-500' [16] was also prepared for comparison with the new compositions and to complement the available data of the salt in the literature.

The specific heat, thermal stability and low melting point of these mixtures make them potentially good candidates for heat transfer and storage applications. Their increased range of operational temperature places them in a favorable position with respect to conventional HTFs for cost-effective concentrated solar power (CSP) technology. Furthermore, the characterization of these new materials has allowed us to get further insight on the behavior of multi-component salts, such as their glassy nature and water impact on their crystallization. On top of that, three different techniques have been used for the very first time to detect solid to liquid phase transitions as an alternative to DSC.

Materials and methods

Reagents and chemicals were supplied by Sigma Aldrich Chemical Co. Ltd. (www.sigmaaldrich.com) and Acros Organics (www.acros.com). Aluminum nitrate nonahydrate (98%), cesium nitrate (99%), potassium nitrate (99.0+%), rubidium nitrate (99.7%) and sodium nitrate (98%) were obtained from samples with ACS reagent grade from Sigma Aldrich. Extra pure calcium nitrate tetrahydrate (99+%) and lithium nitrate (99%) were obtained from Acros Organics, ACS reagent grade. Pure salts were dried and stored in a vacuum desiccator for at least 24 hours previous to the preparation of the mixtures, with the exception of $Al(NO_3)_3{\cdot}9H_2O$ and $Ca(NO_3)_2{\cdot}4\ H_2O$ which were used as provided. No additional purification of the salts was needed.

Molten salts preparation

Molten salts were prepared by the direct mixing of the pure chemicals in the proportions given in **Table 1**

Table 1 Compositions of molten salts indicating the weight percentage (%) of individual components

	Components (%)						
Sample name	**$LiNO_3$**	**$NaNO_3$**	**KNO_3**	**$CsNO_3$**	**$Ca(NO3)_2$**	**$RbNO_3$**	**$Al(NO_3)_3$**
Halotechnics SS-500 (Q) [16]	8	6	23	44	19	-	-
Senary 1 (S-Al)	7.6	5.7	21.5	40.9	17.8	-	6.6
Senary 2 (S-Rb)	7.6	5.7	21.8	41.6	15.7	7.6	-

Hereafter, for convenience, sample names will be shortened. The quinary salt 'Halotechnics SS-500' will be labeled as 'Q' and the senary salts 1 and 2 will be named in text as 'S-Al' and 'S-Rb', respectively.

The composition of the two novel salts, S-Al and S-Rb, was selected based on the quinary salt 'Q'. The proportion between the five original components (lithium, sodium, potassium, cesium and calcium nitrates) was maintained constant in the new compositions. The extra component, rubidium and aluminum nitrates, was added in a similar amount than lithium nitrate. To prepare approximately 6 g of S-Rb, the following amounts were added into an alumina crucible: 1.384 g of $Ca(NO_3)_2{\cdot}4H_2O$, 2.220 g of $CsNO_3$, 1.161 g of KNO_3, 0.407 g of $LiNO_3$, 0.406 g of $RbNO_3$ and 0.307 g of $NaNO_3$. The preparation of 6 g of S-Al consisted of weighting the following amounts: 1.381 g of $Ca(NO_3)_2{\cdot}4H_2O$, 2.210 g of $CsNO_3$, 1.159 g of KNO_3, 0.407 g of $LiNO_3$, 0.623 g of $Al(NO_3)_3{\cdot}9H_2O$ and 0.306 g of $NaNO_3$.

In order to obtain a homogeneous mixture, the samples were then located in a muffle furnace (Barnstead-Thermolyne muffle furnace, model No. FB1410M-33) and heated up to 400 ^{o}C at 10 ^{o}C/min, followed by a 2h-isotherm and natural cooling. All the molten salts showed a white or translucent white homogeneous appearance after this thermal treatment. Naked-eye inspections showed no trace of yellow in the mixture, indicating the absence of nitrites. This was also corroborated by X-Ray diffraction (XRD) (see supporting information). The molten salts were then kept in a vacuum desiccator prior to measurements.

The schematic diagram of the preparation of the salts is shown in **Figure 1**, which includes the following steps:

1. Drying the pure salts in a vacuum desiccator for at least 24 h.
2. Direct mixing of the pure salts in an alumina crucible favoring the direct contact of the salts. Covering the crucible with a lid.
3. Introduction of the crucible inside a muffle furnace, where the sample is heated at 10 ^{o}C/min up to 400 ^{o}C for 2 hours.
4. Allow the sample to cool down naturally.

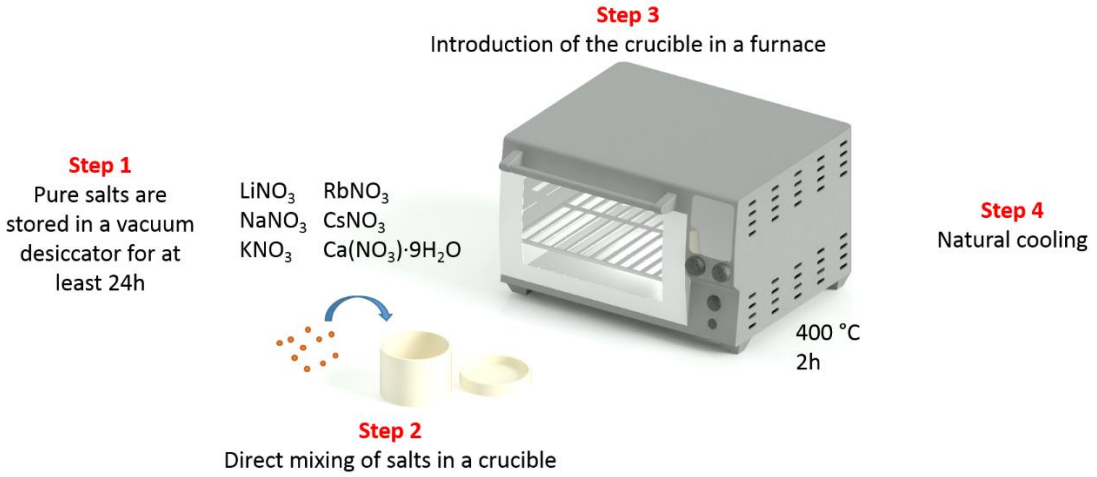

Figure 1. Schematic diagram of the preparation of the multi-component salts (particular example: sample S-Rb).

The solid to liquid phase transition of the molten salts was studied by DSC (PerkinElmer DSC 8000) from room temperature up to 300 ^{o}C at different heating rates, using sealed aluminum pans in 20 ml/min nitrogen-flow atmosphere. Specific heat capacity was measured on a Mettler Toledo DSC822e 1 STAR^{e} system. The sapphire method was used and the heating program consisted on 'iso-dyn-iso' steps from 290-320 ^{o}C in 60 ml/min nitrogen-flow atmosphere. An extended explanation of the experimental conditions is included in the supporting information. Thermogravimetric data was obtained from a Pyris 1 TGA (PerkinElmer) at 10 ^{o}C/min up to 700 ^{o}C in a 20 ml/min flow N_2 atmosphere. The thermal conductivity from solid to liquid states was measured by the 3ω technique in an in-house built set-up. The details of the equipment and the measurement are detailed in an earlier work [28]. Raman spectra were recorded with a HORIBA Jobin Yvon T64000 Raman spectrometer used in single grating mode with a spectral resolution better than 0.4 cm^{-1}. The salts were placed in a cryostat (Linksys32, Linkam Scientific Instruments) in a helium static atmosphere of 1 atm. All Raman measurements were carried out by focusing a diode laser (λ_0 = 532 nm) with 50x long working distance microscope objective. The power of the laser was kept at ~ 2 mW to avoid self-heating effects.

The transmission of a 635 nm red diode laser through two glass cuvettes, one empty and an identical cuvette filled with the sample, was recorded from room temperature to 140 ^{o}C. The optical transmission measurements were performed in air atmosphere. The sample was heated using a hot plate inside an insulating box and the temperature was set manually. An extended description of the set-up is included in the supporting information.

Prior to the characterization by DSC, the 3ω technique, transmission and Raman spectroscopy, the samples were melted using a heat gun above 100 ^{o}C.

Results and discussion

Differential scanning calorimetry and thermogravimetric analyses

DSC curves of samples S-Al, S-Rb and Q were recorded with a thermal cycle of 10, 30 and 50 ^{o}C/min as shown in **Figure 2a-c**. Multiple scan rates were applied to test the sensitivity of the equipment because no thermal events were observed under standard conditions (10 ^{o}C/min). In addition, by varying the scan rate, temperature-time-dependent transitions can be easily identified, such as the glass transition. Hereafter, the temperature of first deviation of the baseline will be defined as the onset temperature of the phase transition (melting, crystallization, evaporation, etc.).

As can be observed in **Figure 2a**, the DSC curve of sample S-Al shows no clear transitions during the heating step at the scan rate of 10 ^{o}C/min, but an exothermic peak appeared during cooling at approx. 93 ^{o}C. These results indicate that the sample is amorphous during the first heating at 10 ^{o}C/min, hence, no phase change is observed. During the cooling step the salt crystallizes. At higher heating rates, a clear endothermic transition (peak onset ≈ 75 ^{o}C) can be observed, as well as the corresponding exothermic peak during cooling. These peaks may correspond to the melting and crystallization of the salt, respectively, matching what was observed with the naked eye. The onset of the endothermic transition shifts only by 2-5 ^{o}C over a heating rate range of 30-50 ^{o}C/min, which indicates it is not a kinetic process (neither glass transition, nor decomposition), reinforcing the idea of a melting transition.

Interestingly, at the heating rate of 30 ^{o}C/min a subtle exothermic peak can be observed just before the endothermic peak, this exothermic peak is much better defined in the 50 ^{o}C/min curve. Multi-component systems have difficulties in ordering and tend to form glasses, hence this exothermic transition can be attributed to the crystallization of a residual amorphous portion of the sample.

In contrast, samples Q and S-Rb did not show thermal transitions during the thermal cycle at any scan rate (**Figure 2b-c)**, with the exception of an endothermic peak at low temperatures (onset ≈ 37 ^{o}C), which appears only during the first heating cycle of the sample, see **Figure 2c** (10 ^{o}C/min). The rest of the curves correspond to pre-heated samples.

The hygroscopic nature of the salts, together with the mass loss observed at low temperatures in the thermograms (**Figure 2d)**, indicate that the endothermic peak at ≈ 37 ^{o}C corresponds to the vaporization of absorbed water in the sample. Pierced lids were used to avoid pressure problems or bursting. Consequently, as expected, no exothermic peak is observed during the cooling step.

The absence of thermal events in the calorimetric curves of samples Q and S-Rb can be explained by taking into consideration the nature and internal structure of multi-component mixtures. The presence of cations of different sizes in the mixture hinders the crystallization of the material, thus promoting the amorphous state. The results obtained from X-Ray diffraction (XRD) support this idea (see supporting information for more details). The XRD analyses were performed at room temperature as a function of time and humidity. X-ray diffraction patterns show that samples Q and S-Rb do not crystallize right after the melting, but after 1 or 2 hours. On the contrary, S-Al presents a faster crystallization. The effect of humidity was also studied by XRD. The exposure to a humid environment favors the crystallization of Q, S-Al and S-Rb. Water facilitates the movement of the ions within the mixture, acting as a lubricant and catalyst for crystallization.

A comparative study of the thermal stability of the new compositions was performed by TGA, as shown in **Figure 2d.** The three samples exhibited an initial weight loss at low temperature, which is ascribed to the evaporation of water absorbed by the material. Nitrates are in general very hygroscopic compounds. Therefore, the control of the storage conditions and atmospheric humidity during the preparation of the samples for the analysis is crucial to avoid water absorption. Thermogravimetric analyses on salts S-Al and S-Rb were performed in our laboratory, hence the amount of absorbed water is similar in these samples. The thermogravimetric data from salt Q were taken from the literature [16]. A significant weight loss was observed for the three samples in the range of 550-700 ^{o}C, which is attributed to the decomposition of the salts. Under the same conditions, S-Al was thermally more stable than S-Rb. At 602 ^{o}C, S-Rb had already lost 2.5% of its weight, in contrast, S-Al reached the same loss (2.5 % in weight) at 606 ^{o}C. Raade and Padowitz [16] reported a 2.5 wt. % loss for the quinary mixture at 599 ^{o}C in N_2 atmosphere, at a heating rate of 10 ^{o}C/min.

It should be mentioned that these experimental datasets are not sufficient to predict the long-term thermal stability of the salts. However, running a linear heating rate program to the samples under the same experimental conditions permits a relative evaluation of their thermal stability.

To completely characterize the thermal behavior of multi-component salts, complementary and alternative techniques were used, namely, three omega technique (thermal conductivity), optical transmission and Raman spectroscopy. Multi-component mixtures have not yet been studied in depth. As mention above, the presence of a variety of species with different sizes and features hinders the crystallization of the material, nevertheless, several factors can modulate the crystallization e.g. cooling rate, presence of water, time. The research done in multi-component salts for thermal solar applications abstains from giving a complete view of the thermal behavior and internal structure of the samples [15,16,19].

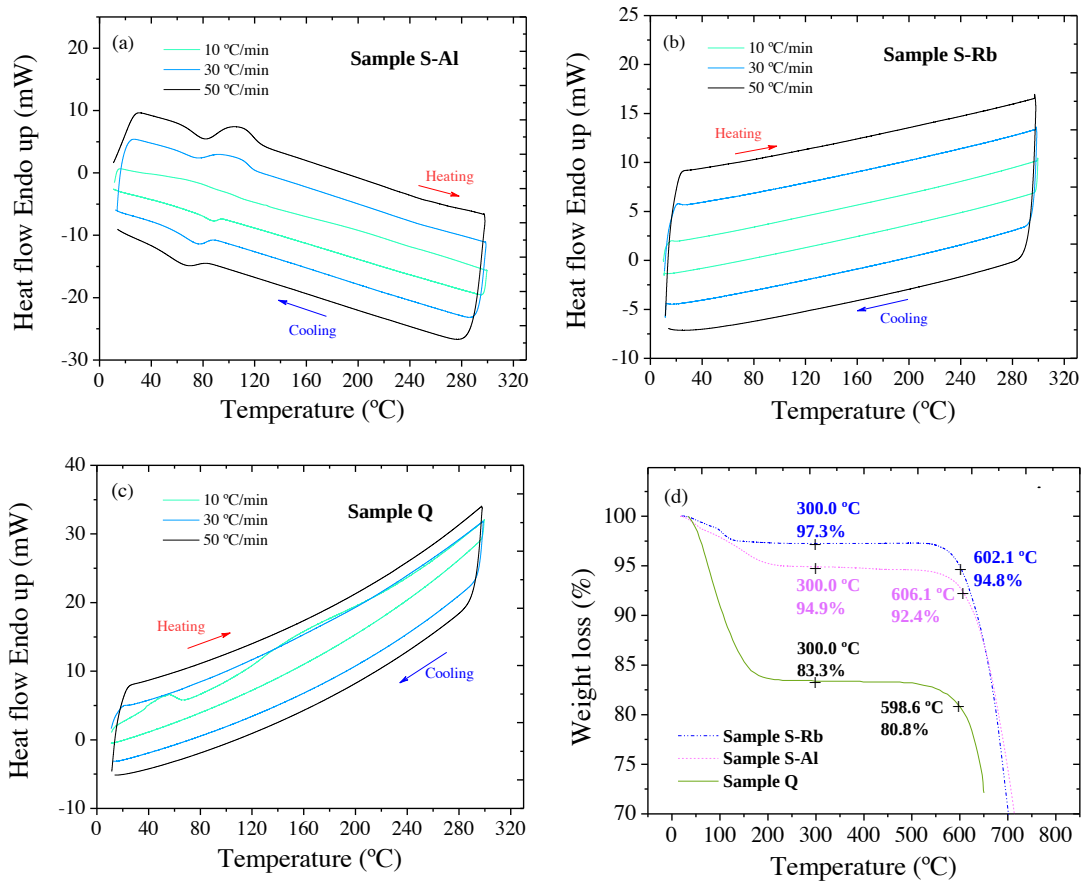

Figure 2. Calorimetric and thermogravimetric curves of the senary compositions and the previously reported quinary [16]. (a) Calorimetric curves of S-Al at 10, 30 and 50 °C/min, cooling and heating. (b) Calorimetric curves of S-Rb at 10, 30 and 50 °C/min, cooling and heating. (c) Calorimetric curves of Q at 10, 30 and 50 °C/min, cooling and heating. (d) Thermogravimetric curves of the two senary salts and sample Q at a heating rate of 10 °C/min in N_2 atmosphere. The thermogravimetric curve from salt Q was taken from the literature (data from ref. [16]).

These mixtures present a number of properties that change abruptly when turning from solid to liquid states, such as sample transparency, thermal conductivity and internal vibrational energies. The transparency variation of the molten material in solid and liquid states was used to determine the phase change by optical transmission. In this sense, our findings open the possibility to use fast methods to gain thermal knowledge on molten salts and related samples at much reduced cost compared to a standard DSC.

Optical transmission and thermal conductivity

The variation in transparency of the salts in the solid and liquid states, from white to transparent, respectively, allowed the detection of the phase change by optical transmission. **Figure 3d** shows the appearance of the S-Rb salt in solid (white) and liquid (transparent) states. The thermal conductivity was measured from room temperature to 140 °C. **Figure 3** shows a representation of the thermal conductivity and optical transmission data of S-Al, S-Rb and Q as a function of temperature. In all three cases, a decrease on the thermal conductivity can be observed as the temperature increases. On the contrary, the optical transmission increased as solid to liquid phase change occurred. The onset temperature of the phase change from solid to liquid derived from optical transmission and thermal conductivity data were found to be in good agreement.

Figure 3a shows the transmission and thermal conductivity curves of sample S-Al as a function of temperature. As can be seen, the light started to be transmitted above 60 ^{o}C, in agreement with DSC data. The transmission increased up to a maximum at 96 ^{o}C and above this temperature the transmission remained constant. On the other hand, a drop in thermal conductivity (*k)* was more difficult to observe. It can be seen that above 76 ^{o}C there was an important change in the thermal conductivity, which perfectly matched the corresponding transmission and DSC data.

The thermal conductivity of sample S-Rb underwent a noticeable drop in *k* values starting at 60 ^{o}C, as shown in **Figure 3b.** Transmission also started to increase at 60 ^{o}C. Furthermore, *k* and transmission values remained constant above 100 ^{o}C, indicating the end of the phase change.

As shown in **Figure 3c**, there was a drastic change on the transmission of sample Q above 60 ^{o}C, which is also the temperature at which the thermal conductivity begins to fall gradually. This change in transmission and thermal conductivity indicates the starting temperature of the melting, which is in complete agreement with the value reported by Raade and Padowitz [16]. As can be observed, *k* and transmission values remained constant above 100 ^{o}C.

The decrease in transmission observed in **Figure 3b** from 25 to 45 ^{o}C is due to water absorption by the salt. The presence of water has been proven to favor the crystallization of the salt, which results in the white color of the salt. Consequently, the initial state of the samples was semi-crystalline and translucent in some of the cases. This explains the change in transparency of the sample S-Rb to more opaque with time, until the material changed to the liquid state. The optical transmission measurements were performed in air atmosphere without controlling the humidity. The temperature of the hot plate used to heat the sample was set manually. Consequently, the required time gap for the temperature to stabilize each time, differs from one measurement to another. Hence, the absorption of water also varied from one sample to another.

Regarding thermal conductivity, we can conclude that there is not a significant difference in their values, at a given temperature, for the different molten salts. As can be seen in **Figure 3**, *k* values vary from 0.345 to 0.358 W $m^{-1}K^{-1}$ which are in the same range reported previously for other molten salts [20]. The average thermal conductivity of these salts in the liquid state is slightly smaller than that of the Solar salt (≈0.520 W m^{-1} K^{-1}) [29] and similar or even larger than that of Hitec (≈0.350 W m^{-1} K^{-1}) [30].

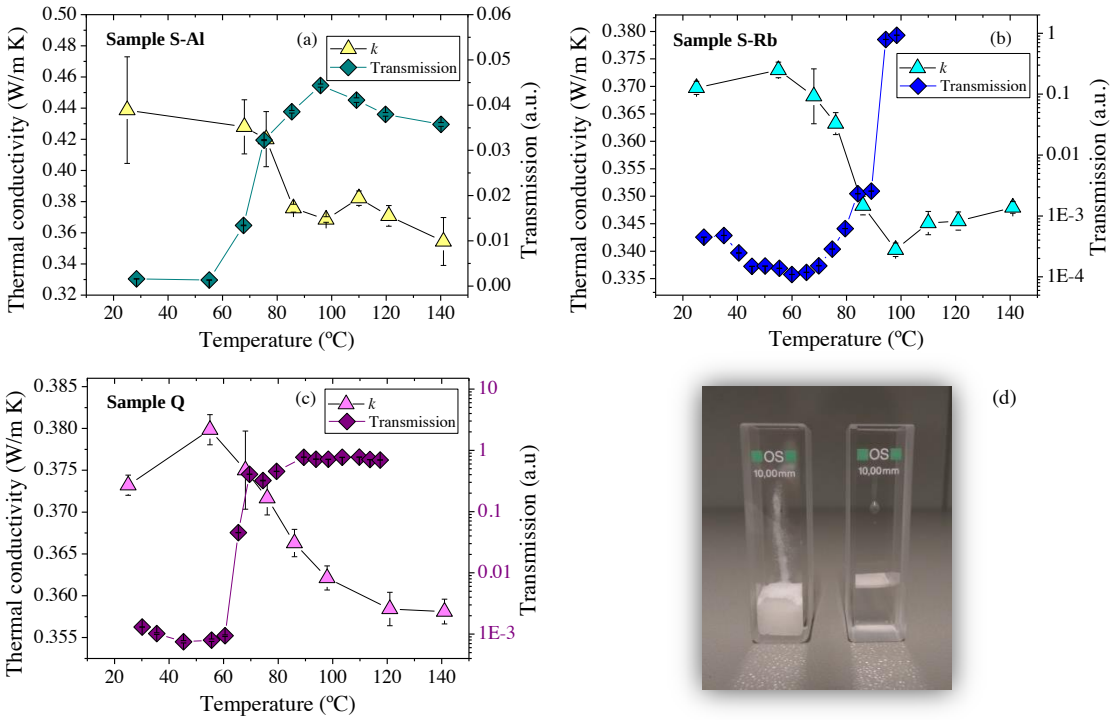

Figure 3. Optical transmission (full diamonds) and thermal conductivity (full triangles) of samples S-Al (a), S-Rb (b) and Q (c) as a function of temperature and (d) an image of sample S-Rb in solid (white) and liquid (transparent) states.

Specific heat capacity

The specific heat capacity (Cp) was determined using the Sapphire method (ASTM standard E1269 – 11) measured by DSC. The Cp measurement of each salt was repeated at least three times and the average values are shown in **Figure 4**, which shows the specific heat capacity of salts Q, S-Al and S-Rb as a function of temperature from 290-320 °C. Cp values of salt Q were taken from the literature [19] to compare with the new compositions. The measured specific heat capacity of the new salts is close to that of the Halotechnics SS-500 (sample Q) and $NaKCsNO_3$ salts (1.20 and 1.18 J g^{-1} K^{-1}, respectively) [19]. These results support the potential of these salts to be used as thermal energy storage materials in CSP technology.

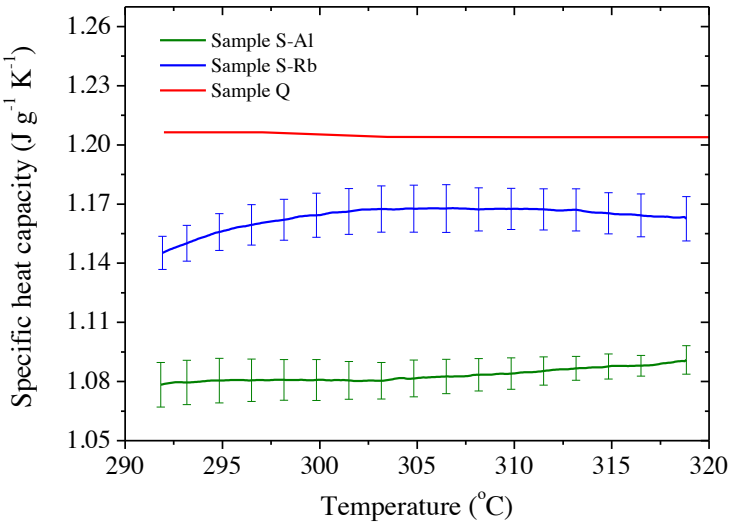

Figure 4. Specific heat capacity of samples S-Al, S-Rb (experimental data) and Q from reference [19] as a function of temperature.

Raman spectroscopy

The Raman spectra of the samples were recorded as a function of temperature in steps of 10 ^{o}C, approximately, from -10 to 149 ^{o}C at a scan rate of 2 ^{o}C/min. These data provided information on the melting onset and the internal structure of the mixtures as a function of temperature. The intense band at ~ 1050 cm^{-1} is ascribed to a symmetric stretching mode of the nitrate ion, ω_1, if D_{3h} symmetry is assumed for the NO_3^- in the crystalline state, and no distortion of the geometry occurs, as Janz et al. assumed [31]. In addition, other very weak bands present at ~ 1350, 1380-1443 and 1650 cm^{-1} have been associated to antisymmetric stretching modes and an overtone of a bending mode (scissoring) of the nitrate ion [31]. However, their low Raman activity makes them difficult to detect. Therefore, we based our study on the symmetric stretching mode of NO_3^- as a function of temperature.

Janz et al. reported that the internal modes of NO_3^-, such as ω_1, are affected by the cationic environment. In fact, in pure salts this mode (ω_1) has been shown to be correlated with the polarizing power of the cationic species, e.g., in alkaline nitrates going from Li^+ to Cs^+, ω_1 decreases in frequency in a regular manner. Furthermore, in some alkaline binary mixtures, ω_1 appears as an additive function of the pure salts ω_1 frequencies multiplied by the fraction present [31].

In mixtures of nitrates of five or six cations of different sizes and charges, as is our case, it has been found that glassy structures are preferentially formed during rapid-cooling [26,27]. This is due to the inability of these ions to segregate into pure component crystals during cooling as they appear to be randomly mixed in the molten state [27]. Raman spectroscopy can also provide information about the amount of disorder in the structure. In glasses all bands appear broadened typically with linewidths in the range of 20 cm^{-1}, which is an order of magnitude broader than that measured in ordered crystals [27].

Sample S-Al

Figure 5a shows the Raman spectra of sample S-Al as a function of temperature recorded with increasing temperature at a rate of 2 ^{o}C/min. As can be seen, at room temperature there is a band with a narrow linewidth (ΔE ~ 3 cm^{-1}) at ~ 1048 cm^{-1} and a small shoulder at higher frequencies. Both correspond to the stretching mode of NO_3^-. However, the narrow band at 1048 cm^{-1} corresponds to the salt in crystalline state whereas the shoulder can be associated with an amorphous domain existing in the salt due to the fast heating during the sample preparation. From room temperature to 65 ^{o}C, the shoulder becomes smooth and at 76 ^{o}C it becomes more intense up to 107 ^{o}C dominating the spectrum. At 118 ^{o}C the peak at 1048 cm^{-1} is completely masked by the shoulder which has become a wider band, indicating that the phase change to liquid state has come to its end. This vibrational mode was also registered during the cooling of the salt at a rate of 2 ^{o}C/min, as shown in **Figure 5b**. The spectra are dominated by a broad peak, indicating the amorphous nature of the salt. This illustrates the difficulty in ordering the multi-component mixtures, even at slow cooling rates (2 ^{o}C/min). A typical shift to higher frequencies is observed during cooling of the broad peak. **Figure 5c** shows the change in frequency as a function of temperature during cooling at a rate of 2 ^{o}C/min.

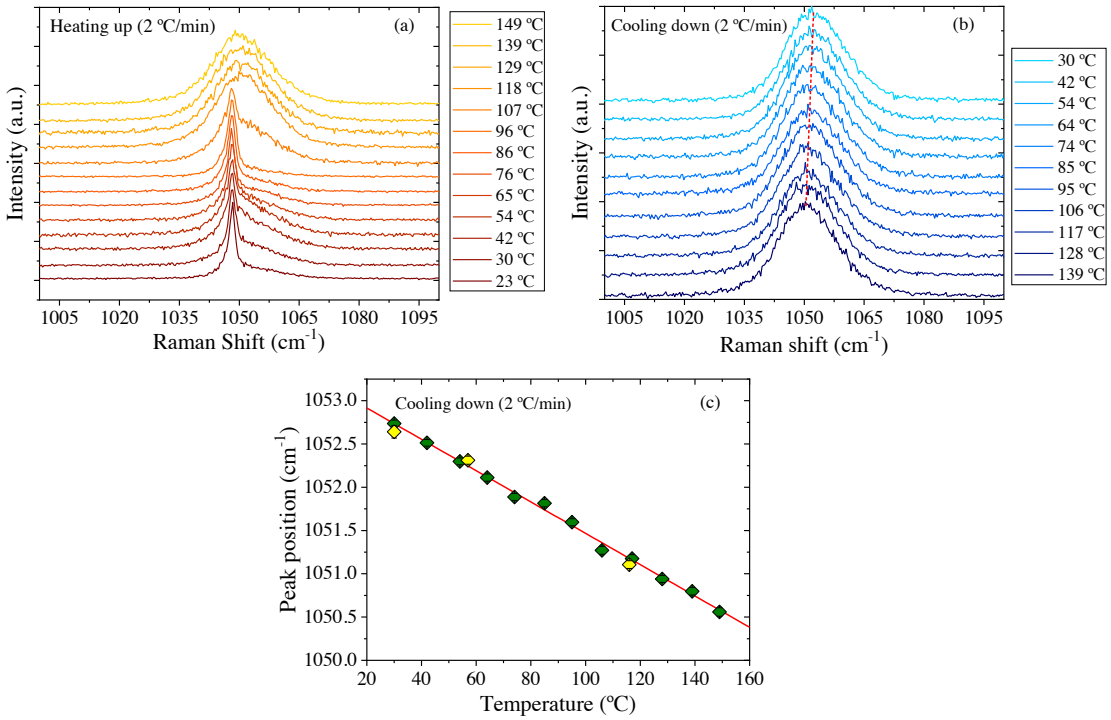

Figure 5. Raman spectra of sample S-Al under (a) heating at 2 °C/min (b) cooling at 2 °C/min and (c) peak position of the symmetric stretching NO_3^- mode as a function of temperature during cooling at 2 °C/min.

Sample S-Rb

The symmetric stretching band (ν ≈ 1050 cm^{-1}) is shown in **Figure 6a.** The frequency and line-shape were tracked from room temperature to 110 °C at a heating rate of 2 °C/min. Both frequency and line-shape remained unchanged up to 60 °C above which the band suddenly broadens. At that point the band broadened around 20 cm^{-1} indicating a disorder in the surroundings of the nitrate anion. This result points to a phase change from solid (crystal) to liquid state occurring between 60-72 °C. The spectrum at 90 °C demonstrates that there are still solid (crystalline) domains, therefore, at 90 °C the salt is still not homogeneous, i.e. not completely molten. These values are in agreement with the data obtained from transmission and thermal conductivity vs T. **Figure 6b** shows a slow crystallization taking place during cooling at 2 °C/min.

In **Figure 6b** the band is somehow distorted at certain temperatures. This is due to the kinetic nature of crystallization; crystals are growing in the material, but part of the salt is still in the liquid state. Temperatures labelled as 'T °C-2' correspond to domains with growing crystals visible with the camera, while the unlabeled temperature values correspond to liquid domains. As can be observed, in mixed domains (T °C-2) the spectrum shows two overlapped bands. The narrower band can be ascribed to the crystalline material and the broader band to the molten or amorphous fraction.

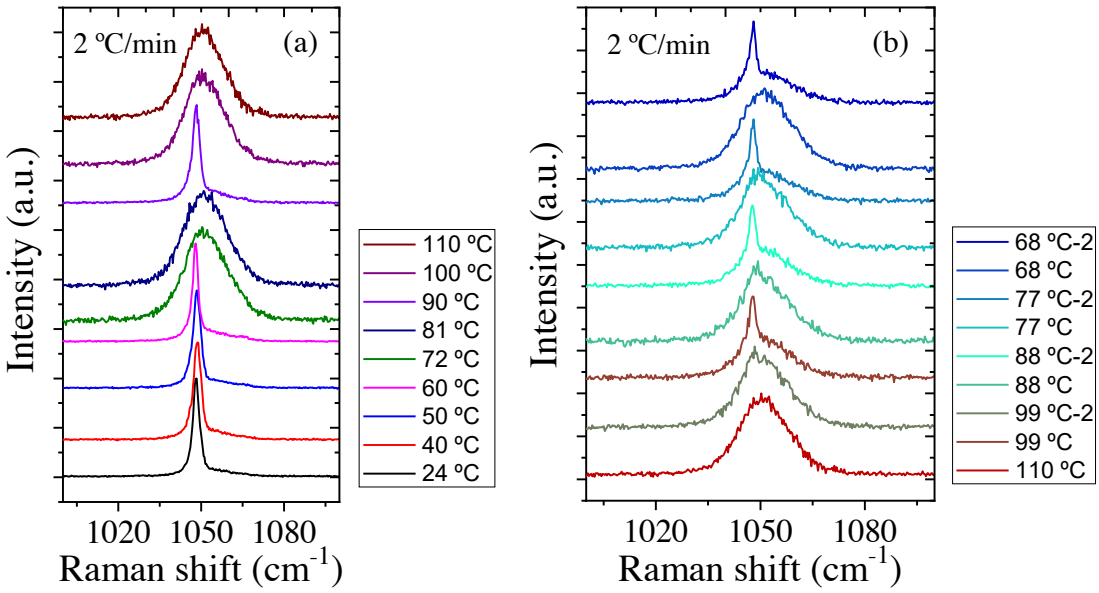

Figure 6. Raman scattering of sample S-Rb. The symmetric stretching NO_3^- mode intensity and linewidth are followed under heating (a) and cooling (b) both at a rate of 2 °C/min.

Sample Q

The symmetric stretching NO_3^- mode was recorded during heating and cooling at 2 °C/min as a function of temperature, as shown in **Figure 7**. As can be seen the band showed a broad linewidth and line-shape in the whole temperature range. However, the typical shift to lower frequencies when increasing temperature as well as the opposite behavior during cooling can be observed in **Figure 7c**. The observed broad band at low temperatures indicates the amorphous nature of the sample in solid state. Unfortunately, the linewidth and line-shape remained unaltered when temperature is increasing (or decreasing), without a drastic change at any temperature. Therefore, no information corresponding to the phase change can be obtained analyzing these spectra.

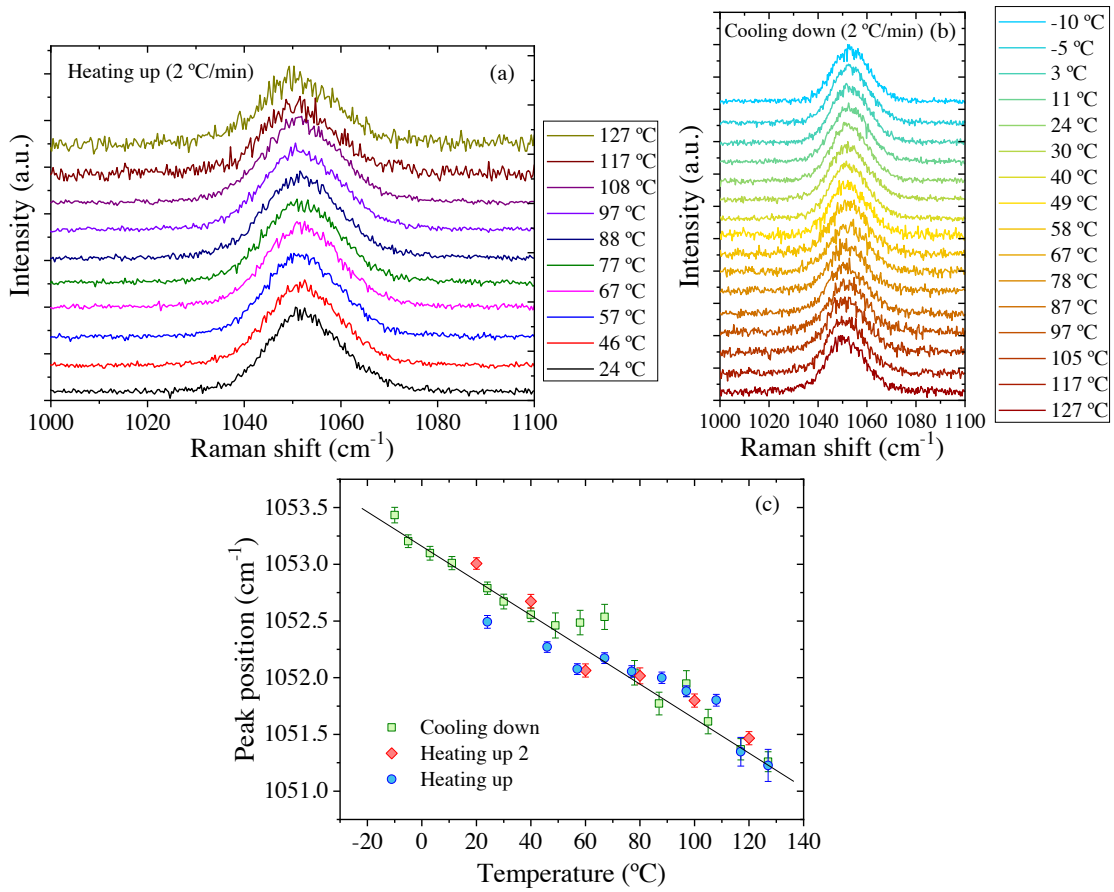

Figure 7. Raman spectra of the sample Q at 2 °C/min and peak position of the symmetric stretching mode of NO_3^- under (a) heating and (b) cooling both at 2 °C/min and (c) peak position as a function of temperature during cooling and heating at 2 °C/min.

In multi-cationic mixtures, as the samples studied here, without a priori knowledge if the composition was close to the eutectic point, we expected a splitting of the ω_1 mode due to the presence of different cationic domains. **Table 2** shows the frequencies of the symmetric stretching mode of NO_3^- for pure salts in liquid and solid state. As can be seen in the table, there is a substantial shift in frequency of the vibrational mode that depends on the environment of NO_3^-. However, no splitting of the ω_1 band was observed that could be associated to different cationic domains in the samples.

Table 2. Raman frequencies (cm^{-1}) corresponding to the symmetric stretching of NO_3^- for pure salts in liquid and solid states [31,32]

	Salt					
Raman mode	**$LiNO_3$**	**$NaNO_3$**	**KNO_3**	**$RbNO_3$**	**$CsNO_3$**	**$Ca(NO_3)_2$**
ω_1 (liquid state)	1067	1053	1048	1046	1043	
ω_1 (solid state)	1086	1069	1050	1056	1050	1069*[32]

*Shoulder at 1066 cm^{-1}

The distortion of the band in the spectra of S-Al and S-Rb has been clearly associated to the amorphous fraction of the samples. Therefore, the narrow linewidth of the band in the solid state, for samples S-Al and S-Rb, denotes that the cationic environment is homogeneous.

The difficulty of samples Q and S-Al to crystallize is evident even at low cooling rates, as can be observed in the Raman spectra recorded under cooling conditions at a rate of 2 ^{o}C/min (**Figure 5b** and **Figure 7b**).

It is clear that the handling of the material before the Raman analyses is crucial for the interpretation of the spectra. As can be observed in **Figure 7**, for sample Q, from room temperature to 127 ^{o}C, the broad linewidth and line-shape of the band remained unaltered as a function of temperature. Similar behavior was observed during the cooling process (from 127 to -10 ^{o}C). As was mentioned in the methodology section, the samples were melted prior to the characterization in order to properly place the sample in the equipment. In the case of sample Q, it was observed that the kinetic of crystallization of the salt was very slow. This statement is supported by the data from the Raman spectra and XRD data taken right after melting the sample and 1-2 hours later (see **Figure S1** in the supporting information).

Finally, it has been demonstrated that the solid-to-liquid transition in nitrate salts can be detected by Raman spectroscopy by monitoring the linewidth and line-shape of internal vibrational modes. In glass and molten states the internal modes of NO_3^- become an order of magnitude broader than in crystalline state, as was observed in the spectra.

Furthermore, the 3ω technique and the optical transmission equipment have also been proven to be suitable techniques to detect solid-to-liquid transitions in molten salts. **Table 3** summarizes the values for the melting temperature range of the salts using DSC, 3ω technique, optical transmission and Raman spectroscopy.

Table 3. Melting temperature range of the salts measured by DSC, optical transmission, 3ω technique and Raman spectroscopy.

	Melting temperature range (^{o}C)		
Techniques	**Samples**		
	S-Al	***S-Rb***	***Q***
DSC	75 – 115	-	-
Optical transmission	60 – 96	60 - 100	60 - 100
3ω technique	76 – 100	60 - 100	60 - 100
Raman spectroscopy	76 – 118	60 - 100	-

Conclusions

An important feature of multi-component salts is that the difference in size of the species hinders the crystallization and provides lower melting temperatures. Herein, two novel six-component nitrates 'S-Al' ($LiNaKCsCaAl/NO_3$) and 'S-Rb' ($LiNaKRbCsCa/NO_3$) were for the first time prepared and thermally characterized. These molten salts have low melting temperatures of ≈ 60-75 ^oC and a thermal stability above 500 ^oC under a linear heating program of 10 ^oC/min in N_2 atmosphere. A complete study on the thermal properties of the materials was performed to evaluate their possible performance as heat transfer and storage materials. Their specific heat capacity values are close to that of the Halotechnics SS-500 and $NaKCsNO_3$ salts [19] and are slightly below that of the Solar salt [29]. The average thermal conductivity of these salts in the liquid state is slightly smaller than that of the Solar salt (≈0.520 W m^{-1} K^{-1}) [29] and similar or even larger than that of Hitec (≈0.350 W m^{-1} K^{-1}) [30]. A comparative study on the thermal stability of the salts by thermogravimetric analysis showed that samples S-Al and S-Rb are as thermally stable as Halotechnics SS-500 [16] and comparable to Na-K-Li nitrates [1].

The determination of the solid-to-liquid transition of these materials can be complex. The internal structure of multi-component salts can be affected by the cooling rate and/or water presence. These factors may influence the crystallization or amorphization of the material. To deepen into the thermal behavior of the materials, complementary and alternative techniques were used. The melting temperature of the salts was indirectly estimated by three alternative techniques: optical transmission, the 3ω technique and Raman spectroscopy. The monitoring of properties such as variation in transparency, thermal conductivity and internal vibrations of the salts as a function of temperature was demonstrated to be a useful indicator of the solid-to-liquid phase change.

The Raman spectra analysis revealed relevant information about the internal structure of the salts. The monitoring of the symmetric stretching mode of NO_3^- as a function of temperature provided information about the distribution of the cationic environment, the ordering of the solid below melting point and the onset melting temperature.

The difficulty in the ordering of these multi-cationic nitrate mixtures during cooling was also demonstrated, confirming previous findings in the literature [26,27] stating that a variable cationic environment (cations with different sizes) favors glass formation during fast cooling. X-ray diffraction analyses as a function of time and humidity (see supporting information), showed that water acts as a catalyst for crystallization, providing mobility to the ions within the material. Furthermore, the addition of $RbNO_3$ and $Al(NO_3)_3$ to the original 5-component recipe of Halotechnics SS-500 (Q) favors the crystallization of the material, as displayed in the X-ray diffractograms as a function of time.

Our results suggest that these two new nitrate-based salts could be potential candidates for heat transfer and storage applications in CSP technology due to their low melting temperature, high thermal stability, good thermal conductivity and specific heat capacity, although further research is needed. Furthermore, three alternative techniques to DSC have been presented and validated to detect solid-to-liquid phase transitions of low energy. These unprecedented techniques for phase change detection widen the number of characterization methods in the field of thermal solar energy.

There is little known about multi-component salts. Their amorphous nature is not necessarily an inconvenient for their application in CSP systems. All the results gathered show the complex behavior of this sort of materials. However, the complexity is nothing but gaps in the field. Future studies on the internal structure and amorphous behavior of multi-component salts are expected to fill those gaps. This knowledge will be crucial to the application of these materials in the thermal-solar field, among others.

Acknowledgments

The Catalan Institute of Nanoscience and Nanotechnology (ICN2) acknowledges support from the Severo Ochoa Program (MINECO, Grant SEV-2017-0706) and funding from the CERCA Programme/Generalitat de Catalunya. Funding from the Spanish Ministry MINECO/FEDER: FIS2015-70862-P PHENTOM and MAT2015-68394-R NaCarFLOW are also acknowledged. M.-C. L acknowledges support from the Ministry of Science and Technology in Taiwan, MOST 104-2221-E-009-147-MY3. We thank Dr. Jessica Padilla for the assistance provided with XRD analysis. MRRL would like to thank Dr. Carlos Gracia for the valuable discussions. We would also like to thank Andrew Hudson and Dr. Guy L. Whitworth for the assistance provided with English writing in the manuscript.

References

[1] K. Vignarooban, X. Xu, A. Arvay, K. Hsu, A.M. Kannan, Heat transfer fluids for concentrating solar power systems – A review, Appl. Energy. 146 (2015) 383–396. doi:10.1016/j.apenergy.2015.01.125.

[2] H.L. Zhang, J. Baeyens, J. Degrève, G. Cacères, Concentrated solar power plants: Review and design methodology, Renew. Sustain. Energy Rev. 22 (2013) 466–481. doi:10.1016/j.rser.2013.01.032.

[3] M. Liu, N.H. Steven Tay, S. Bell, M. Belusko, R. Jacob, G. Will, W. Saman, F. Bruno, Review on concentrating solar power plants and new developments in high temperature thermal energy storage technologies, Renew. Sustain. Energy Rev. 53 (2016) 1411–1432. doi:10.1016/j.rser.2015.09.026.

[4] L. Miró, J. Gasia, L.F. Cabeza, Thermal energy storage (TES) for industrial waste heat (IWH) recovery: A review, Appl. Energy. 179 (2016) 284–301. doi:10.1016/j.apenergy.2016.06.147.

[5] J. Gasia, L. Miró, L.F. Cabeza, Review on system and materials requirements for high temperature thermal energy storage. Part 1: General requirements, Renew. Sustain. Energy Rev. 75 (2017) 1320–1338. doi:10.1016/j.rser.2016.11.119.

[6] G. Alva, L. Liu, X. Huang, G. Fang, Thermal energy storage materials and systems for solar energy applications, Renew. Sustain. Energy Rev. 68 (2017) 693–706. doi:10.1016/j.rser.2016.10.021.

[7] E. Zarza, Medium Temperature Solar Concentrators (Parabolic-Troughs Collectors), in: Sol. Energy Convers. Photoenergy Syst., 2005.

[8] H. Müller-Steinhagen, F. Trieb, Concentrating Solar Power: A review of the technology, Ingenia. 18 (2004) 43–50.

[9] C. Villada, A. Bonk, T. Bauer, F. Bolívar, High-temperature stability of nitrate/nitrite molten salt mixtures under different atmospheres, Appl. Energy. 226 (2018) 107–115. doi:10.1016/j.apenergy.2018.05.101.

[10] T. Bauer, N. Breidenbach, N. Pfleger, D. Laing, M. Eck, Overview of molten salt storage systems and material development for solar thermal power plants, Proc. 2012 Natl. Sol. Conf. (SOLAR 2012) Denver. (2012).

[11] I. Sarbu, C. Sebarchievici, A comprehensive review of thermal energy storage, Sustain. 10 (2018). doi:10.3390/su10010191.

[12] U. Pelay, L. Luo, Y. Fan, D. Stitou, M. Rood, Thermal energy storage systems for concentrated solar power plants, Renew. Sustain. Energy Rev. 79 (2017) 82–100. doi:10.1016/j.rser.2017.03.139.

[13] E. González-Roubaud, D. Pérez-Osorio, C. Prieto, Review of commercial thermal energy storage in concentrated solar power plants: Steam vs. molten salts, Renew. Sustain. Energy Rev. 80 (2017) 133–148. doi:10.1016/j.rser.2017.05.084.

[14] R.I. Olivares, W. Edwards, LiNO3-NaNO3-KNO3 salt for thermal energy storage: Thermal stability evaluation in different atmospheres, Thermochim. Acta. 560 (2013) 34–42. doi:10.1016/j.tca.2013.02.029.

[15] T. Wang, D. Mantha, R.G. Reddy, Novel low melting point quaternary eutectic system for solar thermal energy storage, Appl. Energy. 102 (2013) 1422–1429. doi:10.1016/j.apenergy.2012.09.001.

[16] J.W. Raade, D. Padowitz, Development of Molten Salt Heat Transfer Fluid With Low Melting Point and High Thermal Stability, J. Sol. Energy Eng. 133 (2011) 31013. doi:10.1115/1.4004243.

[17] N. Ren, Y. Wu, C. Ma, L. Sang, Preparation and thermal properties of quaternary mixed nitrate with low melting point, Sol. Energy Mater. Sol. Cells. 127 (2014) 6–13. doi:10.1016/j.solmat.2014.03.056.

[18] A.G. Fernández, S. Ushak, H. Galleguillos, F.J. Pérez, Development of new molten salts with LiNO3 and Ca(NO3)2 for energy storage in CSP plants, Appl. Energy. 119 (2014) 131–140. doi:10.1016/j.apenergy.2013.12.061.

[19] P. Zhang, J. Cheng, Y. Jin, X. An, Evaluation of thermal physical properties of molten nitrate salts with low melting temperature, Sol. Energy Mater. Sol. Cells. 176 (2018) 36–41. doi:10.1016/j.solmat.2017.11.011.

[20] R. Serrano-López, J. Fradera, S. Cuesta-López, Molten salts database for energy applications, Chem. Eng. Process. Process Intensif. 73 (2013) 87–102. doi:10.1016/j.cep.2013.07.008.

[21] K. Wang, B. Xu, P. Lucas, S.M. Jeter, Experimental Investigation to the Properties of Eutectic Salts by NaCl-KCl-ZnCl2 for Application as High Temperature Heat Transfer Fluids, Proc. ASME 2014 8th Int. Conf. Energy Sustain. (2014) 1–6.

[22] L. Sang, M. Cai, N. Ren, Y. Wu, C. Burda, C. Ma, Improving the thermal properties of ternary carbonates for concentrating solar power through simple chemical modifications by adding sodium hydroxide and nitrate, Sol. Energy Mater. Sol. Cells. 124 (2014) 61–66. doi:10.1016/j.solmat.2014.01.025.

[23] Q. Peng, J. Ding, X. Wei, J. Yang, X. Yang, The preparation and properties of multi-component molten salts, Appl. Energy. 87 (2010) 2812–2817. doi:10.1016/j.apenergy.2009.06.022.

[24] C. Martin, T. Bauer, H. Müller-Steinhagen, An experimental study of a non-eutectic mixture of KNO3 and NaNO3 with a melting range for thermal energy storage, Appl. Therm. Eng. 56 (2013) 159–166. doi:10.1016/j.applthermaleng.2013.03.008.

[25] R.I. Olivares, C. Chen, S. Wright, The Thermal Stability of Molten Lithium–Sodium–Potassium Carbonate and the Influence of Additives on the Melting Point, J. Sol. Energy Eng. 134 (2012) 41002. doi:10.1115/1.4006895.

[26] L.G. van Uitert, W.H. Grodkiewicz, Nitrate glasses, Mater. Res. Bull. 6 (1971) 283–291. doi:10.1016/0025-5408(71)90042-0.

[27] T. Furukawa, S.A. Brawer, W.B. White, Raman spectroscopic study of nitrate glasses, J. Chem. Phys. 69 (1978) 2639. doi:10.1063/1.436912.

[28] M.R. Rodríguez-Laguna, A.. Castro-Alvarez, M. Sledzinska, J. Maire, F.. Costanzo, B.. Ensing, M.. Pruneda, P. Ordejón, C.M. Sotomayor Torres, P. Gómez-Romero, E. Chávez-Ángel, Mechanisms behind the enhancement of thermal properties of graphene nanofluids, Nanoscale. 10 (2018) 15402–15409. doi:10.1039/C8NR02762E.

[29] N. Ren, Y.T. Wu, C.F. Ma, L.X. Sang, Preparation and thermal properties of quaternary mixed nitrate with low melting point, Sol. Energy Mater. Sol. Cells. 127 (2014) 6–13. doi:10.1016/j.solmat.2014.03.056.

[30] L.L.C. Coastal Chemical Co., HITEC ® Heat Transfer Salt. Technical Data Guide, (2009).

[31] G.J. Janz, D.W. James, Raman Spectra and Ionic Interactions in Molten Nitrates, J. Chem. Phys. 35 (1961) 739–745. doi:10.1063/1.1731994.

[32] M.H. Brooker, Raman and i.r. spectra of zinc, cadmium and calcium nitrate: A study of the low temperature phase transitions in calcium nitrate, Spectrochim. Acta Part A Mol. Spectrosc. 32 (1976) 369–377. doi:10.1016/0584-8539(76)80090-6.

Supporting information of Article 3

Supporting information

Development of low-melting point molten salts and detection of solid-to-liquid transitions by alternative techniques to DSC

M. R. Rodríguez-Laguna*[1,2], P. Gómez-Romero*[1], C. M. Sotomayor Torres[1,3], M.-C. Lu[4] and E. Chávez-Ángel*[1]

[1] Catalan Institute of Nanoscience and Nanotechnology (ICN2), CSIC and BIST, Campus UAB, Bellaterra, 08193 Barcelona, Spain

[2] Departament de Química, Universitat Autònoma de Barcelona, Cerdanyola del Vallès, 08193 Barcelona, Spain

[3] ICREA, Pg. Lluís Companys 23, 08010 Barcelona, Spain

[4] Department of Mechanical Engineering, National Chiao Tung University, 1001 University Road, Hsinchu 30010, Taiwan

*E-mail: rodriguez3laguna@gmail.com; pedro.gomez@icn2.cat; emigdio.chavez@icn2.cat

Keywords: Solar thermal conversion, molten salts, low melting point, heat transfer fluids, thermal conductivity, thermal energy storage.

XRD analysis

XRD measurements at room temperature were carried out for qualitative identification of the phases present in the mixture. Analyses of the samples were performed under different conditions: I) after melting, II) 1-2h after melting, III) more than 12 h after melting with low content of water and IV) more than 12 h after melting with high content of water. The diffraction patterns were collected using a Malvern PANalytical X'pert PRO MPD diffractometer. It operated at 40 kV and 40 mA in theta-theta configuration using as the X-ray source a ceramic X-ray tube with Cu K_α anode (λ=1.5406 Å). Data were collected from 10 to 80° 2θ (step size=0.033° and time per step=219 s). The XRD analysis were carried in transmission mode using a capillary spinner and the samples were filled inside borosilicate glass capillaries with outer diameter of 0.7 mm. A focusing mirror was used for the incident beam and a lineal X'Celerator detector for the diffracted beam. Identification of the solid phases present in the mixture was performed using the PANalytical X'Pert HighScore Plus software and database.

Figure S1 shows XRD of samples S-Al, S-Rb and Q under different conditions, such as time after melting and content of water. It can be observed that right after melting samples S-Rb and Q are mainly amorphous, in contrast, S-Al starts to crystalize sooner. Sample Q has more difficulty in crystallizing after 1-2h of melting than samples S-Al and S-Rb. In addition, it can be observed in **Figure S1c** that water favors the crystallization of the salt. XRD spectra did not show any decomposition of the salts or peak corresponding to any nitrite phase. However, the main components of the salts are easily identified, cesium and potassium nitrates.

Supporting information

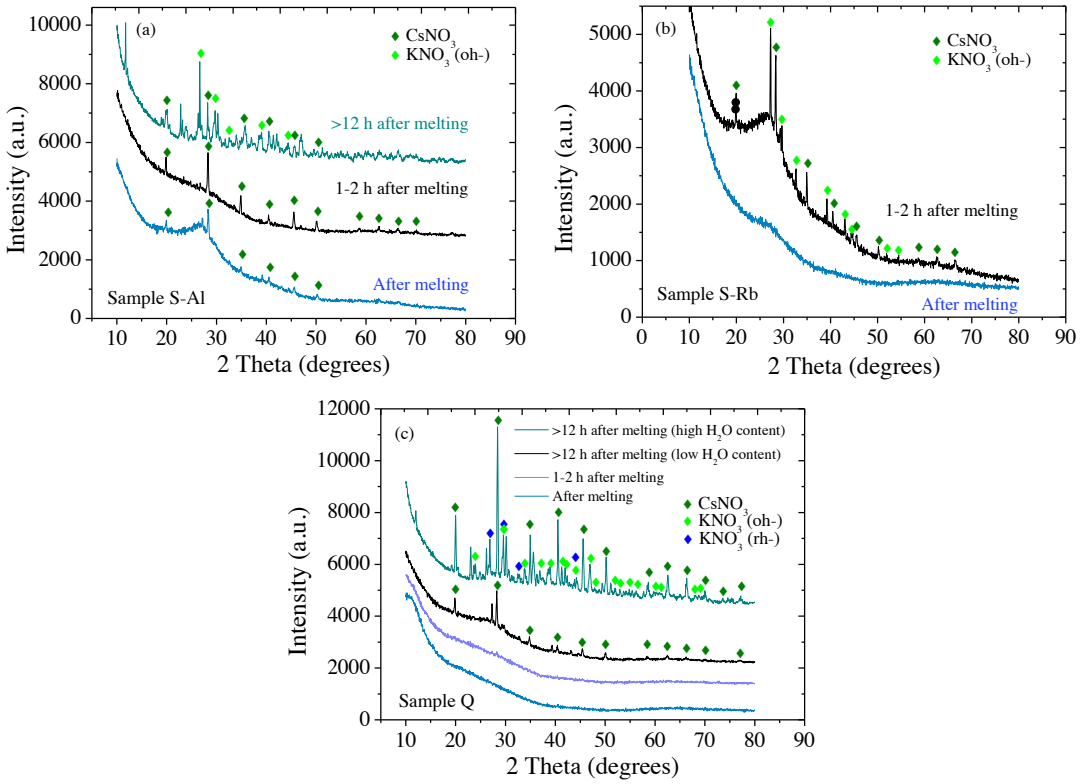

Figure S1. XRD of samples Q, S+Al and S+Rb right after melting, 1-2 h after melting and more than 12 h after melting with low or high content of water.

Optical transmission

Transmission measurements were performed in air atmosphere from room temperature to 140 ºC in a homemade setup, which is schematically depicted in **Figure S2**. The samples were placed in a glass cuvette (HELLMA, 100-OS, 10 mm light path) using a heat gun above 100 ºC to melt the salts and favor their handling. A 635 nm collimated diode-laser was passed through two identical cuvettes (one empty and other containing the sample) and the transmitted light was measured at the same time. The empty cell was used as a reference in order to avoid any possible effect from the cuvette. Finally, the transmitted light of the cuvette containing the sample was divided by the transmitted light from the empty one to obtain the transmission signal from the sample.

Supporting information

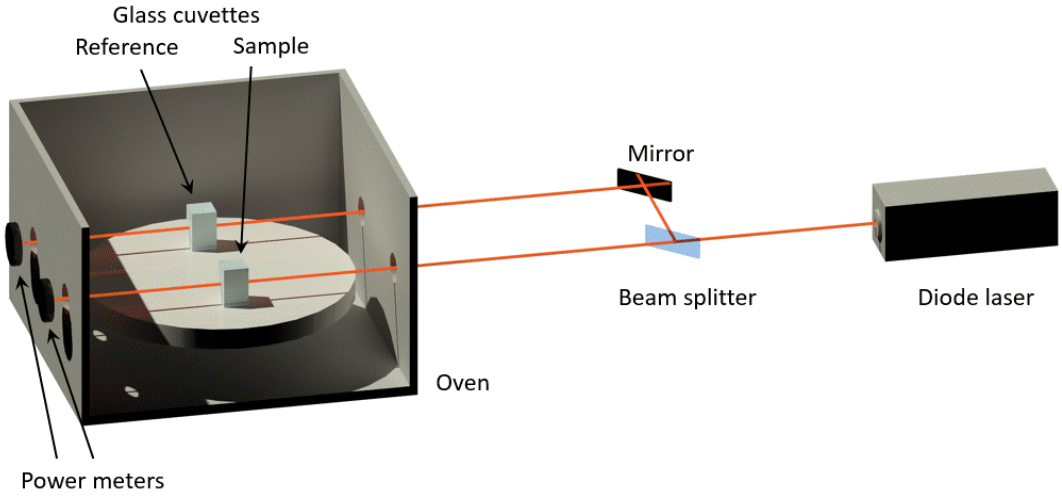

Figure S2 schematic representation of the experimental setup

Differential scanning calorimetry - specific heat capacity

Specific heat capacity was measured using differential scanning calorimetry on a Mettler Toledo DSC822e 1 STAR^e system in 60 ml/min nitrogen-flow atmosphere. ASTM standard test method 'E1269 – 11' was followed. The heating program consisted on 'iso-dyn-iso' steps from 290-320 ^oC. The isothermal segments lasted 5 minutes and the dynamic segment heating rate was 5 ^oC/min. A slower heating rate than the advised in the ASTM method was used to shorten the initial deflection segment of the signal in the dynamic step. The standard method E1269 – 11 requires performing three different measurements using/with the same conditions each time to determine the Cp of the sample: blank, sapphire and sample measurements. The Cp measurement of each salt was repeated at least three times and average values are shown in this manuscript. Aluminum (Al) crucibles of 40 µl with Al pierced lid were used to perform the experiments. The same reference and sample crucibles were used to perform the three measurements: blank, sapphire and sample to avoid errors in Cp due to a weight difference. The crucible was sealed using the Mettler Toledo press only before the sample measurement. The sample weight ranged from 5-10 mg.

Chapter 4: Conclusions and future perspectives

Chapter Summary

In this chapter, I start recalling the demands of the heat transfer industry and the gaps in the scientific knowledge regarding nanofluids, low melting temperature compositions and multi-component salts. Then, the achievements of this investigation are listed in the form of bullet points. Finally, a summary of the unfinished work and future perspectives are presented.

4.1 Conclusions

Heat transfer fluids dissipate, transfer or carry away heat to heat exchangers, heat spreaders or steam turbines, depending on the application. The selection of the fluid involves taking into consideration multiple factors, such as chemical stability, operating temperature range (melting point and thermal stability), vapor pressure, viscosity, thermal conductivity, specific heat, etc. The problem arises when the conventional fluids do not meet the needs and challenges of the industry. Examples of industries presently facing this problem are electronics and solar-thermal energy.

The relentless development of technology has led to the miniaturization of electronic components to achieve faster performances. As a consequence, the power densities of the electronic item increases, resulting in a rapid and localized increase in temperature. In this application, fluids are called to have high thermal conductivities and high heat dissipation rate. Water, ethylene glycol, oils, etc. are widely used as HTFs [145], but the major problem of these conventional coolants is the low heat exchange rate and thermal conductivity (k), typically between 0.06–0.6 Wm^{-1} K^{-1} [145]. These values are not high enough. One way to overcome this barrier is by using solid nanoparticles dispersed in fluids to improve their thermal properties [20,21].

In the case of solar-thermal energy, the most efficient solar power stations are those using point-focus configurations, i.e. solar power tower, T=1000 ºC and dish concentrators, T >2000 ºC. Sun's rays are focused onto a receiver located along the focal point of the reflector, which is a smaller area than that irradiated using other type of configurations. As a result, these technologies reach very high temperatures. Then, HTFs with wider the operating temperatures range can increase the efficiency of the overall energy conversion. Nowadays, the solar salt (60 wt. % $NaNO_3$ and 40 wt. % KNO_3), with a melting temperature of 228 ºC [120] is the most commonly used HTF and thermal energy storage (TES) material in power tower systems. The high melting temperature of molten salts demands a supply of extra-energy to keep the material in the liquid state, hence, making the entire process costly and less efficient. As a consequence, solar thermal power industry is in urgent need for novel formulations with lower melting point (ideally room-temperature) and higher thermal stability.

In addition to the demands of the heat transfer industries, the scientific community is attempting to understand the fundamentals of the enhanced heat transfer in nanofluids. But still there is no consensus on the phenomenon behind. At the same time, researchers

in the high-temperature field are looking for strategies to expand the operation temperature range of molten salts and come up with new compositions.

In this thesis, we have attempted to cover the needs of the industry as well as diving into the fundamentals of the materials. We have studied both nanofluids and molten salts, in terms of thermal behavior and materials characterization. The primary idea was to learn about these outstanding materials and to contribute our bit to the scientific knowledge.

The achievements of this investigation are exposed below in the form of bullet points. They are divided into two sections, labeled as low-temperature fluids and high-temperature fluids.

Low-temperature fluids

- Highly stable dispersions of graphene-based nanofluids were prepared. They have been stable over years and still are.
- The influence of graphene concentration on thermal conductivity (*k*), specific heat capacity (Cp), viscosity, speed of sound and Raman spectra was investigated and measured.
- Graphene nanofluids based on DMAc and DMF showed enhanced thermal properties, with a maximum enhancement in thermal conductivity of up to 48% (0.18 wt.%) and an 18 % improvement in specific heat capacity (0.11 wt.%).
- The Raman spectra analysis indicated that the intra- and intermolecular interactions between DMF (or DMAc) molecules are modified when graphene is present, affecting the whole liquid.
- The theoretical studies suggested that
  - The interaction between graphene and the nearest DMF molecules is stronger than initially thought.
  - These molecules tend to lay parallel to the graphene flake favoring a possible π–π stacking.
  - A local order of the DMF molecules up to three layers was observed in the simulations.

- The heat transfer mechanisms suggested in the literature to explain the enhanced heat transfer in nanofluids have been discussed and some of them discarded when applied to our nanofluids.
- Graphene-NMP nanofluids neither showed an enhancement of the thermal conductivity, nor a modification of the Raman spectra. Although the viscosity was affected by a maximum of ≈41 %.
- The results on the three types of graphene-amides nanofluids led us to the conclusion that there is a correlation between the modification of the vibrational spectra of the fluids, and the increase of their thermal conductivity.
- The non-modification of the thermal conductivity and Raman spectra of graphene-NMP nanofluids were explained taking into consideration the geometry, structure and behavior of NMP molecules.
- We consider that the special interaction graphene-amide suggested by the simulations is the key factor explaining the high dispersibility of graphene in these fluids.

These results represent an excellent initial step toward understanding the manner in which NPs modify the fluid arrangement directly affecting thermal transport. NFs are commonly highly diluted systems; therefore, it is the properties of the NPs and fluid molecule atoms at the points of intermolecular contact which are important in assessing the type of interaction. It clearly depends on the nature of the NPs and fluid molecules

High-temperature fluids

- Two novel six-component nitrates 'S-Al' ($LiNaKCsCaAl/NO_3$) and 'S-Rb' ($LiNaKRbCsCa/NO_3$) were prepared and thermally characterized for the first time.
- These molten salts have low melting temperatures of ≈ 60-75 ºC and a thermal stability above 500 ºC under a linear heating program of 10 ºC/min in N_2 atmosphere.
- The manner the salts were designed (based on a quinary salt and adding an extra component) demonstrates that multi-component salts provide lower melting temperatures.

- The thermal properties of the materials (i.e., thermal conductivity, degradation temperature and specific heat) were analyzed to evaluate their potential performance as heat transfer and thermal storage materials.
- The values of their thermal properties were comparable to those of common HTFs used in solar thermal applications.
- The determination of the solid-to-liquid transition of these materials can be complex.
- Factors, such as the cooling rate, storage conditions and humidity affect the internal structure of the materials, and can promote the crystallization or amorphization of the material.
- The monitoring of properties such as variation in transparency, thermal conductivity and internal vibrations of the salts as a function of temperature was demonstrated to be a useful indicator of the solid-to-liquid phase change.
- The melting temperature of the salts was determined by three alternative techniques: optical transmission, the 3ω technique and Raman spectroscopy.
- The monitoring of the symmetric stretching mode of NO_3^- as a function of temperature provided information about the melting temperature range and the order the solid (crystalline or amorphous).
- It was demonstrated that a variable cationic environment favors glass formation during fast cooling.
- X-ray diffraction analyses as a function of time and humidity showed that water acts as a catalyst for crystallization, providing mobility to the ions within the material.
- The addition of $RbNO_3$ and $Al(NO_3)_3$ to the original 5-component formulation of Halotechnics SS-500 (Q) favors the crystallization of the material.

The amorphous nature of these materials is not necessarily a drawback for their application in CSP systems. If the initial state of the material is crystalline, it can be stored above its melting temperature and used as thermal storage material or heat transfer fluid for high-temperature applications.

4.2 Future perspectives

As a result of all the data gathered and the experience gained along these four years, we designed and performed a series of studies that unfortunately could not be completed. We consider them to be like seeds in the fertile field of scientific knowledge. The unfinished work (so far) is briefly described below:

Low-temperature fluids

- Experimental study on the liquid re-arrangement in the presence of dispersed graphene. For that purpose, we performed some preliminary analyses of graphene-DMF and –DMAc nanofluids using synchrotron radiation for X-ray diffraction. With the acquired data we could calculate the pair-pair distribution function (PPDF) of the nanofluids. The results are promising, but unfortunately, we are in the waiting list for beam time. Work done in collaboration with Dr. Alicia Manjon (MSPD beamline, Alba synchrotron).

High-temperature fluids

- The study of eutectic formation in well-known molten salts: diffusion of ionic species.
- The development of low-melting point compositions, where binary phase diagrams are employed to determine the proportion of nitrate to be added in relation to the main components of the original mixture. We achieved to design two quaternary mixtures with medium-low melting points.
- The addition of ionic inorganic clusters to molten salts to modify their thermo-physical properties. We achieved to reduce the melting temperature of the salt.
- The addition of encapsulated phase change material (Sn/C core shell particles) in the aforementioned novel molten salts. Work in collaboration with Prof. Ming-Chang Lu and Yen-Ta Lee, Department of Mechanical Engineering, National Chiao Tung University, Hsinchu, Taiwan.
- The fabrication of a set-up for the measurement of thermal conductivity at high temperatures (up to 400-500 ºC). We achieved to design and fabricate a suitable 3-ω cell for high-temperatures, which is also resistant to the possible corrosion caused by molten salts.

References

1. Moore, G.M. Cramming more components onto integrated circuits. *Electronics* **1965**, *38*, 114.

2. Zarza, E. Medium Temperature Solar Concentrators (Parabolic-Troughs Collectors). In *Solar Energy Conversion and Photoenergy Systems*; 2005; Vol. I.

3. Situmbeko, S.; Inambao, F. Low temperature solar thermal energy conversion. *Energize* **2010**, 21–24.

4. *Advances in Solar Heating and Cooling*; Wang, R.Z., Ge, T.S., Eds.; Woodhead Publishing, 2016; ISBN 9780081003015.

5. Zhang, H.L.; Baeyens, J.; Degrève, J.; Cacères, G. Concentrated solar power plants: Review and design methodology. *Renew. Sustain. Energy Rev.* **2013**, *22*, 466–481.

6. Vignarooban, K.; Xu, X.; Arvay, A.; Hsu, K.; Kannan, A.M. Heat transfer fluids for concentrating solar power systems – A review. *Appl. Energy* **2015**, *146*, 383–396.

7. Kearney, D.; Kelly, B.; Herrmann, U.; Cable, R.; Pacheco, J.; Mahoney, R.; Price, H.; Blake, D.; Nava, P.; Potrovitza, N. Engineering aspects of a molten salt heat transfer fluid in a trough solar field. *Energy* **2004**, *29*, 861–870.

8. Gil, A.; Medrano, M.; Martorell, I.; Lázaro, A.; Dolado, P.; Zalba, B.; Cabeza, L.F. State of the art on high temperature thermal energy storage for power generation. Part 1—Concepts, materials and modellization. *Renew. Sustain. Energy Rev.* **2010**, *14*, 31–55.

9. Peng, Q.; Ding, J.; Wei, X.; Yang, J.; Yang, X. The preparation and properties of multi-component molten salts. *Appl. Energy* **2010**, *87*, 2812–2817.

10. Peng, Q.; Wei, X.; Ding, J.; Yang, J.; Yang, X. High-temperature thermal stability of molten salt materials. *Int. J. Energy Res.* **2008**, *32*, 1164–1174.

11. Wang, T.; Mantha, D.; Reddy, R.G. Novel low melting point quaternary eutectic system for solar thermal energy storage. *Appl. Energy* **2013**, *102*, 1422–1429.

12. Bauer, T.; Breidenbach, N.; Pfleger, N.; Laing, D.; Eck, M. Overview of molten salt storage systems and material development for solar thermal power plants. *Proc. 2012 Natl. Sol. Conf. (SOLAR 2012) Denver.* **2012**.

13. Sarbu, I.; Sebarchievici, C. A Comprehensive Review of Thermal Energy Storage. *Sustainability* **2018**, *10*, 191.

14. Lv, L.; Li, J. Micro Flat Heat Pipes for Microelectronics Cooling: Review. *Recent Patents Mech. Eng.* **2013**, *6*, 169–184.

15. Ekpu, M.; Bhatti, R.; Ekere, N.; Mallik, S. Advanced thermal management materials for heat sinks used in microelectronics. In Proceedings of the 18th European Microelectronics & Packaging Conference; 2011; pp. 1–8.

16. Ye, H.; Zhang, G. A review of passive thermal management of LED module. *J.*

Semicond. **2011**, *32*, 014008.

17. Sohel Murshed, S.M.; Nieto de Castro, C.A. A critical review of traditional and emerging techniques and fluids for electronics cooling. *Renew. Sustain. Energy Rev.* **2017**, *78*, 821–833.

18. Bar-Cohen, A.; Arik, M.; Ohadi, M. Direct Liquid Cooling of High Flux Micro and Nano Electronic Components. *Proc. IEEE* **2006**, *94*, 1549–1570.

19. Siddique, A.R.M.; Muresan, H.; Majid, S.H.; Mahmud, S. An adjustable closed-loop liquid-based thermoelectric electronic cooling system for variable load thermal management. *Therm. Sci. Eng. Prog.* **2019**, *10*, 245–252.

20. Patil, M.S.; Kim, S.C.; Seo, J.; Lee, M. Review of the Thermo-Physical Properties and System Using Refrigerant-Based Nanofluids. *Energies* **2015**, *9*, 22.

21. Mahian, O.; Kianifar, A.; Kalogirou, S. a.; Pop, I.; Wongwises, S. A review of the applications of nanofluids in solar energy. *Int. J. Heat Mass Transf.* **2013**, *57*, 582–594.

22. Choi, S.U.S.; Eastman, J.A. Enhancing thermal conductivity of fluids with nanoparticles. In Proceedings of the ASME International Mechanical Engineering Congress and Exposition; 1995; Vol. 66, pp. 99–105.

23. Manca, O.; Jaluria, Y.; Poulikakos, D. Heat Transfer in Nanofluids. *Adv. Mech. Eng.* **2010**, *2*, 380826.

24. Das, S.K.; Choi, S.U.S.; Yu, W.; Pradeep, T. *Nanofluids: Science and Technology*; John Wiley & Sons, Inc.: Hoboken, NJ, USA, 2007; ISBN 9780470180693.

25. Chinnaraj, A.N. Thermal Conductivity Enhancement in Nanofluids -Mathematical Model, Southern Illinois University, 2011.

26. Javadi, F.S.; Saidur, R.; Kamalisarvestani, M. Investigating performance improvement of solar collectors by using nanofluids. *Renew. Sustain. Energy Rev.* **2013**, *28*, 232–245.

27. ÖZERİNÇ, S. Heat Transfer Enhancement With Nanofluids, Middle East Technical University, 2010.

28. Zhou, L.-P.; Wang, B.-X.; Peng, X.-F.; Du, X.-Z.; Yang, Y.-P. On the Specific Heat Capacity of CuO Nanofluid. *Adv. Mech. Eng.* **2010**, *2*, 172085.

29. Keblinski, P.; Phillpot, S.R.; Choi, S.U.S.; Eastman, J.A. Mechanisms of heat flow in suspensions of nano-sized particles (nanofluids). *Int. J. Heat Mass Transf.* **2002**, *45*, 855–863.

30. Hong, K.S.; Hong, T.-K.; Yang, H.-S. Thermal conductivity of Fe nanofluids depending on the cluster size of nanoparticles. *Appl. Phys. Lett.* **2006**, *88*, 031901.

31. Putnam, S.A.; Cahill, D.G.; Braun, P. V.; Ge, Z.; Shimmin, R.G. Thermal conductivity of nanoparticle suspensions. *J. Appl. Phys.* **2006**, *2006*, 155–158.

32. Sundar, L.S.; Singh, M.K.; Ramana, E.V.; Singh, B.; Grácio, J.; Sousa, A.C.M.

Enhanced Thermal Conductivity and Viscosity of Nanodiamond-Nickel Nanocomposite Nanofluids. *Sci. Rep.* **2015**, *4*, 4039.

33. Baby, T.T.; Ramaprabhu, S. Investigation of thermal and electrical conductivity of graphene based nanofluids. *J. Appl. Phys.* **2010**, *108*.

34. Jana, S.; Salehi-Khojin, A.; Zhong, W.-H. Enhancement of fluid thermal conductivity by the addition of single and hybrid nano-additives. *Thermochim. Acta* **2007**, *462*, 45–55.

35. Salehi, J.M.; Heyhat, M.M.; Rajabpour, A. Enhancement of thermal conductivity of silver nanofluid synthesized by a one-step method with the effect of polyvinylpyrrolidone on thermal behavior. *Appl. Phys. Lett.* **2013**, *102*, 231907.

36. Kwek, D.; Crivoi, A.; Duan, F. Effects of Temperature and Particle Size on the Thermal Property Measurements of Al_2O_3 −Water Nanofluids. *J. Chem. Eng. Data* **2010**, *55*, 5690–5695.

37. Gimeno-Furio, A.; Navarrete, N.; Mondragón, R.; Cervantes, E.; Hernandez, L.; Martinez Cuenca, R.; Cabedo, L.; Julia, J.E. Thermophysical properties of a nanofluid based on a eutectic mixture of diphenyl and diphenyl oxide and carbon black nanoparticles. In Proceedings of the 13th International Conference on Heat Transfer, Fluid Mechanics and Thermodynamics; 2017; pp. 601–605.

38. Gao, Y.; Wang, H.; Sasmito, A.P.; Mujumdar, A.S. Measurement and modeling of thermal conductivity of graphene nanoplatelet water and ethylene glycol base nanofluids. *Int. J. Heat Mass Transf.* **2018**, *123*, 97–109.

39. Mohebbi, A. Prediction of specific heat and thermal conductivity of nanofluids by a combined equilibrium and non-equilibrium molecular dynamics simulation. *J. Mol. Liq.* **2012**, *175*, 51–58.

40. Kumar, D.H.; Patel, H.E.; Kumar, V.R.R.; Sundararajan, T.; Pradeep, T.; Das, S.K. Model for Heat Conduction in Nanofluids. *Phys. Rev. Lett.* **2004**, *93*, 144301.

41. Yu, W.; Choi, S.U.S. The role of interfacial layers in the enhanced thermal conductivity of nanofluids: A renovated Maxwell model. *J. Nanoparticle Res.* **2003**, *5*, 167–171.

42. Abou-tayoun, N.H. Molecular Dynamics Simulation of Thermal Conductivity Enhancement of Copper-Water Nanofluid, American University of Sharjah, 2012.

43. Prasher, R.; Bhattacharya, P.; Phelan, P.E. Brownian-Motion-Based Convective-Conductive Model for the Effective Thermal Conductivity of Nanofluids. *J. Heat Transfer* **2006**, *128*, 588.

44. Fan, J.; Wang, L. Review of Heat Conduction in Nanofluids. *J. Heat Transfer* **2011**, *133*, 040801.

45. Prasher, R.; Evans, W.; Meakin, P.; Fish, J.; Phelan, P.; Keblinski, P. Effect of aggregation on thermal conduction in colloidal nanofluids. *Appl. Phys. Lett.* **2006**, *89*, 143119.

46. Evgin, T.; Koca, H.D.; Horny, N.; Turgut, A.; Tavman, I.H.; Chirtoc, M.; Omastová,

M.; Novak, I. Effect of aspect ratio on thermal conductivity of high density polyethylene/multi-walled carbon nanotubes nanocomposites. *Compos. Part A Appl. Sci. Manuf.* **2016**, *82*, 208–213.

47. Choi, S.U.S.; Zhang, Z.G.; Yu, W.; Lockwood, F.E.; Grulke, E.A. Anomalous thermal conductivity enhancement in nanotube suspensions. *Appl. Phys. Lett.* **2001**, *79*, 2252–2254.

48. Xue, L.; Keblinski, P.; Phillpot, S.R.; Choi, S.U.S.; Eastman, J.A. Effect of liquid layering at the liquid–solid interface on thermal transport. *Int. J. Heat Mass Transf.* **2004**, *47*, 4277–4284.

49. Rodríguez-Laguna, M.R.; Castro-Alvarez, A.; Sledzinska, M.; Maire, J.; Costanzo, F.; Ensing, B..; Pruneda, M.; Ordejón, P.; Sotomayor Torres, C.M.; Gómez-Romero, P.; et al. Mechanisms behind the enhancement of thermal properties of graphene nanofluids. *Nanoscale* **2018**, *17*, 15402–15409.

50. Alexeev, D.; Chen, J.; Walther, J.H.; Giapis, K.P.; Angelikopoulos, P.; Koumoutsakos, P. Kapitza Resistance between Few-Layer Graphene and Water: Liquid Layering Effects. *Nano Lett.* **2015**, *15*, 5744–5749.

51. Yu, C.-J.; Richter, A.G.; Datta, A.; Durbin, M.K.; Dutta, P. Observation of Molecular Layering in Thin Liquid Films Using X-Ray Reflectivity. *Phys. Rev. Lett.* **1999**, *82*, 2326–2329.

52. Yu, C.J.; Richter, A.G.; Datta, A.; Durbin, M.K.; Dutta, P. Molecular layering in a liquid on a solid substrate: An X-ray reflectivity study. *Phys. B Condens. Matter* **2000**, *283*, 27–31.

53. Gong, X.; Kozbial, A.; Rose, F.; Li, L. Effect of π-π+ Stacking on the Layering of Ionic Liquids Confined to an Amorphous Carbon Surface. *ACS Appl. Mater. Interfaces* **2015**, *7*, 7078–7081.

54. Xue, L.; Keblinski, P.; Phillpot, S.R.; Choi, S.U.-S.; Eastman, J.A. Two regimes of thermal resistance at a liquid–solid interface. *J. Chem. Phys.* **2003**, *118*, 337–339.

55. Sarkar, S.; Selvam, R.P. Molecular dynamics simulation of effective thermal conductivity and study of enhanced thermal transport mechanism in nanofluids. *J. Appl. Phys.* **2007**, *102*, 074302.

56. Bhattacharya, P.; Saha, S.K.; Yadav, A.; Phelan, P.E.; Prasher, R.S. Brownian dynamics simulation to determine the effective thermal conductivity of nanofluids. *J. Appl. Phys.* **2004**, *95*, 6492–6494.

57. Gupta, A.; Kumar, R. Role of Brownian motion on the thermal conductivity enhancement of nanofluids. *Appl. Phys. Lett.* **2007**, *91*, 223102.

58. Buongiorno, J. Convective Transport in Nanofluids. *J. Heat Transfer* **2006**, *128*, 240.

59. Bringuier, E.; Bourdon, A. Kinetic theory of colloid thermodiffusion. *Phys. A Stat. Mech. its Appl.* **2007**, *385*, 9–24.

60. Babu, S.R.; Babu, P.R.; Rambabu, V. Effects of Some Parameters on Thermal Conductivity of Nanofluids and Mechanisms of Heat Transfer Improvement. *Int. J.*

Eng. Res. Appl. **2013**, *3*, 2136–2140.

61. Wang, L.; Wei, X. Nanofluids: Synthesis, Heat Conduction, and Extension. *J. Heat Transfer* **2009**, *131*, 033102.

62. Cardellini, A.; Alberghini, M.; Govind Rajan, A.; Misra, R.P.; Blankschtein, D.; Asinari, P. Multi-scale approach for modeling stability, aggregation, and network formation of nanoparticles suspended in aqueous solutions. *Nanoscale* **2019**, *11*, 3979–3992.

63. Arshad, W.; Ali, H.M. Graphene nanoplatelets nanofluids thermal and hydrodynamic performance on integral fin heat sink. *Int. J. Heat Mass Transf.* **2017**, *107*, 995–1001.

64. Ali, H.M.; Arshad, W. Effect of channel angle of pin-fin heat sink on heat transfer performance using water based graphene nanoplatelets nanofluids. *Int. J. Heat Mass Transf.* **2017**, *106*, 465–472.

65. Fu, Y.; Mei, T.; Wang, G.; Guo, A.; Dai, G.; Wang, S.; Wang, J.; Li, J.; Wang, X. Investigation on enhancing effects of Au nanoparticles on solar steam generation in graphene oxide nanofluids. *Appl. Therm. Eng.* **2017**, *114*, 961–968.

66. Iranmanesh, S.; Ong, H.C.; Ang, B.C.; Sadeghinezhad, E.; Esmaeilzadeh, A.; Mehrali, M. Thermal performance enhancement of an evacuated tube solar collector using graphene nanoplatelets nanofluid. *J. Clean. Prod.* **2017**, *162*, 121–129.

67. Fan, D.; Li, Q.; Chen, W.; Zeng, J. Graphene nanofluids containing core-shell nanoparticles with plasmon resonance effect enhanced solar energy absorption. *Sol. Energy* **2017**, *158*, 1–8.

68. Seong, H.; Kim, G.; Jeon, J.; Jeong, H.; Noh, J.; Kim, Y.; Kim, H.; Huh, S. Experimental Study on Characteristics of Grinded Graphene Nanofluids with Surfactants. *Materials (Basel).* **2018**, *11*, 950.

69. Mahbubul, I.M.; Chong, T.H.; Khaleduzzaman, S.S.; Shahrul, I.M.; Saidur, R.; Long, B.D.; Amalina, M.A. Effect of Ultrasonication Duration on Colloidal Structure and Viscosity of Alumina–Water Nanofluid. *Ind. Eng. Chem. Res.* **2014**, *53*, 6677–6684.

70. Georgakilas, V.; Vrettos, K.; Katomeri, K.; Kouloumpis, A.; Dimos, K.; Gournis, D.; Zboril, R. Highly dispersible disk-like graphene nanoflakes. *Nanoscale* **2015**, *7*, 15059–15064.

71. Yau, H.C.; Bayazit, M.K.; Steinke, J.H.G.; Shaffer, M.S.P. Sonochemical degradation of N-methylpyrrolidone and its influence on single walled carbon nanotube dispersion. *Chem. Commun.* **2015**, *51*, 16621–16624.

72. Xia, G.; Jiang, H.; Liu, R.; Zhai, Y. Effects of surfactant on the stability and thermal conductivity of Al2O3/de-ionized water nanofluids. *Int. J. Therm. Sci.* **2014**, *84*, 118–124.

73. Mahmudul Haque, A.K.M.; Kwon, S.; Kim, J.; Noh, J.; Huh, S.; Chung, H.; Jeong, H. An experimental study on thermal characteristics of nanofluid with graphene and multi-wall carbon nanotubes. *J. Cent. South Univ.* **2015**, *22*, 3202–3210.

74. Xuan, Y.; Li, Q.; Tie, P. The effect of surfactants on heat transfer feature of nanofluids. *Exp. Therm. Fluid Sci.* **2013**, *46*, 259–262.

75. Tavares, J.; Coulombe, S. Dual plasma synthesis and characterization of a stable copper–ethylene glycol nanofluid. *Powder Technol.* **2011**, *210*, 132–142.

76. Zhang, Y.Y.; Pei, Q.X.; He, X.Q.; Mai, Y.-W. A molecular dynamics simulation study on thermal conductivity of functionalized bilayer graphene sheet. *Chem. Phys. Lett.* **2015**, *622*, 104–108.

77. Tesfai, W.; Singh, P.; Shatilla, Y.; Iqbal, M.Z.; Abdala, A.A. Rheology and microstructure of dilute graphene oxide suspension. *J. Nanoparticle Res.* **2013**, *15*, 1989.

78. Turgut, A.; Tavman, I.; Chirtoc, M.; Schuchmann, H.P.; Sauter, C.; Tavman, S. Thermal Conductivity and Viscosity Measurements of Water-Based TiO_2 Nanofluids. *Int. J. Thermophys.* **2009**, *30*, 1213–1226.

79. Loh, K.P.; Bao, Q.; Ang, P.K.; Yang, J. The chemistry of graphene. *J. Mater. Chem.* **2010**, *20*, 2277.

80. Hermann, H.; Schubert, T.; Gruner, W.; Mattern, N. Structure and chemical reactivity of ball-milled graphite. *Nanostructured Mater.* **1997**, *8*, 215–229.

81. Cahill, D.G. Thermal conductivity measurement from 30 to 750 K: The 3ω method. *Rev. Sci. Instrum.* **1990**, *61*, 802–808.

82. Cahill, D.G. Erratum: “Thermal conductivity measurement from 30 to 750 K: The 3ω method” [Rev. Sci. Instrum. 61 , 802 (1990)]. *Rev. Sci. Instrum.* **2002**, *73*, 3701–3701.

83. Chen, F.; Shulman, J.; Xue, Y.; Chu, C.W.; Nolas, G.S. Thermal conductivity measurement under hydrostatic pressure using the 3ω method. *Rev. Sci. Instrum.* **2004**, *75*, 4578–4584.

84. Oh, D.-W.; Jain, A.; Eaton, J.K.; Goodson, K.E.; Lee, J.S. Thermal conductivity measurement and sedimentation detection of aluminum oxide nanofluids by using the 3ω method. *Int. J. Heat Fluid Flow* **2008**, *29*, 1456–1461.

85. Lubner, S.D.; Choi, J.; Wehmeyer, G.; Waag, B.; Mishra, V.; Natesan, H.; Bischof, J.C.; Dames, C. Reusable bi-directional 3 ω sensor to measure thermal conductivity of 100-μ m thick biological tissues. *Rev. Sci. Instrum.* **2015**, *86*.

86. Viswanath, D.S.; Bhagwant Rao, M. Thermal conductivity of liquids and its temperature dependence. *J. Phys. D. Appl. Phys.* **1970**, *3*, 1444–1450.

87. Kole, M.; Dey, T.K. Investigation of thermal conductivity, viscosity, and electrical conductivity of graphene based nanofluids. *J. Appl. Phys.* **2013**, *113*, 084307.

88. Mehrali, M.; Sadeghinezhad, E.; Tahan Latibari, S.; Mehrali, M.; Togun, H.; Zubir, M.N.M.; Kazi, S.N.; Metselaar, H.S.C. Preparation, characterization, viscosity, and thermal conductivity of nitrogen-doped graphene aqueous nanofluids. *J. Mater. Sci.* **2014**, *49*, 7156–7171.

89. Patil, M.; Seo, J.-H.; Kang, S.-J.; Lee, M.-Y. Review on Synthesis, Thermo-Physical Property, and Heat Transfer Mechanism of Nanofluids. *Energies* **2016**, *9*, 840.

90. Sekrani, G.; Poncet, S. Ethylene- and Propylene-Glycol Based Nanofluids: A Litterature Review on Their Thermophysical Properties and Thermal Performances. *Appl. Sci.* **2018**, *8*, 2311.

91. Vallejo, J.P.; Żyła, G.; Fernández-Seara, J.; Lugo, L. Rheological behaviour of functionalized graphene nanoplatelet nanofluids based on water and propylene glycol:water mixtures. *Int. Commun. Heat Mass Transf.* **2018**, *99*, 43–53.

92. Vallejo, J.; Żyła, G.; Fernández-Seara, J.; Lugo, L. Influence of Six Carbon-Based Nanomaterials on the Rheological Properties of Nanofluids. *Nanomaterials* **2019**, *9*, 146.

93. Venkata Chalapathi, V.; Venkata Ramiah, K. Normal vibrations of N, N-dimethylformamide and N, N-dimethylacetamide. *Proc. Indian Acad. Sci. - Sect. A* **1968**, *68*, 109–122.

94. Rozpłoch, F.; Patyk, J.; Stankowski, J. Graphenes Bonding Forces in Graphite. *Acta Phys. Pol. A* **2007**, *112*, 557–562.

95. Kemnitz, C.R.; Loewen, M.J. “Amide Resonance” Correlates with a Breadth of C−N Rotation Barriers. *J. Am. Chem. Soc.* **2007**, *129*, 2521–2528.

96. Adams, W.A.; Kruus, P.; Patraboy, T.J. The system sulfur dioxide – N -methyl-2-pyrrolidinone. *Can. J. Chem.* **1983**, *61*, 37–44.

97. Basma, N.S.; Headen, T.F.; Shaffer, M.S.P.; Skipper, N.T.; Howard, C.A. Local Structure and Polar Order in Liquid N -Methyl-2-pyrrolidone (NMP). *J. Phys. Chem. B* **2018**, *122*, 8963–8971.

98. Dil, J.G. Brillouin scattering in condensed matter. *Reports Prog. Phys.* **1982**, *45*, 285–334.

99. Benedek, G.; Greytak, T. Brillouin scattering in liquids. *Proc. IEEE* **1965**, *53*, 1623–1629.

100. Yogi, T.; Sakai, K.; Takagi, K. Light beating spectroscopy of Brillouin scattering in gases and solids. *J. Appl. Phys.* **2006**, *100*, 023505.

101. Bohidar, H.; Jossang, T.; Feder, J. A Brillouin scattering study of sound velocity in single-component liquids up to 800 bar. *J. Phys. D. Appl. Phys.* **1988**, *21*, S53–S55.

102. Nemoto, S. Measurement of the refractive index of liquid using laser beam displacement. *Appl. Opt.* **1992**, *31*, 6690.

103. Aminabhavi, T.M.; Gopalakrishna, B. Density, Viscosity, Refractive Index, and Speed of Sound in Aqueous Mixtures of N,N-Dimethylformamide, Dimethyl Sulfoxide, N,N-Dimethylacetamide, Acetonitrile, Ethylene Glycol, Diethylene Glycol, 1,4-Dioxane, Tetrahydrofuran, 2-Methoxyethanol, and 2-Ethox. *J. Chem. Eng. Data* **1995**, *40*, 856–861.

104. Akıner, T.; Mason, J.K.; Ertürk, H. Nanolayering around and thermal resistivity of the

water-hexagonal boron nitride interface. *J. Chem. Phys.* **2017**, *147*, 044709.

105. Prasher, R.; Phelan, P.E.; Bhattacharya, P. Effect of Aggregation Kinetics on the Thermal Conductivity of Nanoscale Colloidal Solutions (Nanofluid). *Nano Lett.* **2006**, *6*, 1529–1534.

106. Keblinski, P.; Thomin, J. Hydrodynamic field around a Brownian particle. *Phys. Rev. E* **2006**, *73*, 010502.

107. Le Brun, C. Molten salts and nuclear energy production. *J. Nucl. Mater.* **2007**, *360*, 1–5.

108. Fernández, A.G.; Ushak, S.; Galleguillos, H.; Pérez, F.J. Development of new molten salts with LiNO3 and Ca(NO3)2 for energy storage in CSP plants. *Appl. Energy* **2014**, *119*, 131–140.

109. Nunes, V.M.B.; Lourenço, M.J.V.; Santos, F.J.V.; Nieto de Castro, C.A. Molten alkali carbonates as alternative engineering fluids for high temperature applications. *Appl. Energy* **2019**, *242*, 1626–1633.

110. Papaelias, M.; Cheng, L.; Kogia, M.; Mohimi, A.; Kappatos, V.; Selcuk, C.; Constantinou, L.; Muñoz, C.Q.G.; Marquez, F.P.G.; Gan, T.H. Inspection and Structural Health Monitoring techniques for Concentrated Solar Power plants. *Renew. Energy* **2016**, *85*, 1178–1191.

111. International Atomic Energy Agency (IAEA) *Challenges Related to the Use of Liquid Metal and Molten Salt Coolants in Advanced Reactors. Report of the collaborative project cool of the international project on innovative nuclear reactors and fuel cycles (INPRO)*; Vienna, 2013;

112. Lin, C.; Chi, Y.; Jin, Y.; Song, H. Experimental Study on Molten Salt Oxidation of High Salt Content Pharmaceutical Residue. *Procedia Environ. Sci.* **2016**, *31*, 335–344.

113. Galek, V.; Stoklasa, J.; Hadrava, J.; Hrbek, J.; Bezdicka, P.; Sedlárová, I. The Behavior of Corundum Ceramic in Molten Salt. *J. Nucl. Eng. Radiat. Sci.* **2019**, *5*, 030905.

114. Yao, Z.; Li, J.; Zhao, X. Molten salt oxidation: A versatile and promising technology for the destruction of organic-containing wastes. *Chemosphere* **2011**, *84*, 1167–1174.

115. Fray, D.J. Emerging molten salt technologies for metals production. *JOM* **2001**, *53*, 27–31.

116. Korenko, M. Interfacial Tension between Aluminum and Cryolite Alumina Melts. *J. Chem. Eng. Data* **2008**, *53*, 794–797.

117. Park Thermal International Corporation *A guide to the safe use of molten salt baths*; Georgetown, ON, Canada, 1996;

118. MacPherson, H.G. The Molten Salt Reactor Adventure. *Nucl. Sci. Eng.* **1985**, *90*, 374–380.

119. He, Z.; Tang, H.; Zhang, C.; Gao, Y.; Xia, H.; Zhou, X. The Compatibility of Nuclear Graphite With Molten Salt in the Molten Salt Reactor. In Proceedings of the Volume 2: Plant Systems, Structures, Components, and Materials; Risk Assessments and Management; ASME, 2018; p. V002T03A026.

120. Janz, G.J.; Krebs, U.; Siegenthaler, H.F.; Tomkins, R.P.T. Molten Salts: Volume 3 Nitrates, Nitrites, and Mixtures: Electrical Conductance, Density, Viscosity, and Surface Tension Data. *J. Phys. Chem. Ref. Data* **1972**, *1*, 581–746.

121. Wu, Y.-T.; Li, Y.; Ren, N.; Zhi, R.-P.; Ma, C.-F. Experimental study on the thermal stability of a new molten salt with low melting point for thermal energy storage applications. *Sol. Energy Mater. Sol. Cells* **2018**, *176*, 181–189.

122. Eastman, J.A.; Choi, U.S.; Li, S.; Thompson, L.J.; Lee, S. Enhanced Thermal Conductivity through the Development of Nanofluids. *MRS Proc.* **1996**, *457*, 3.

123. Shin, D.; Banerjee, D. Enhancement of specific heat capacity of high-temperature silica-nanofluids synthesized in alkali chloride salt eutectics for solar thermal-energy storage applications. *Int. J. Heat Mass Transf.* **2011**, *54*, 1064–1070.

124. Liu, M.; Severino, J.; Bruno, F.; Majewski, P. Experimental investigation of specific heat capacity improvement of a binary nitrate salt by addition of nanoparticles/microparticles. *J. Energy Storage* **2019**, *22*, 137–143.

125. Sang, L.; Liu, T. The enhanced specific heat capacity of ternary carbonates nanofluids with different nanoparticles. *Sol. Energy Mater. Sol. Cells* **2017**, *169*, 297–303.

126. Dunlop, T.O.; Jarvis, D.J.; Voice, W.E.; Sullivan, J.H. Stabilization of molten salt materials using metal chlorides for solar thermal storage. *Sci. Rep.* **2018**, *8*, 8190.

127. Villada, C.; Bonk, A.; Bauer, T.; Bolívar, F. High-temperature stability of nitrate/nitrite molten salt mixtures under different atmospheres. *Appl. Energy* **2018**, *226*, 107–115.

128. Fereres, S.; Prieto, C.; Giménez-Gavarrell, P.; Rodríguez, A.; Sánchez-Jiménez, P.E.; Pérez-Maqueda, L.A. Molten carbonate salts for advanced solar thermal energy power plants: Cover gas effect on fluid thermal stability. *Sol. Energy Mater. Sol. Cells* **2018**, *188*, 119–126.

129. Olivares, R.I.; Edwards, W. LiNO3-NaNO3-KNO3 salt for thermal energy storage: Thermal stability evaluation in different atmospheres. *Thermochim. Acta* **2013**, *560*, 34–42.

130. Raade, J.W.; Padowitz, D. Development of Molten Salt Heat Transfer Fluid With Low Melting Point and High Thermal Stability. *J. Sol. Energy Eng.* **2011**, *133*, 031013.

131. Mantha, D.; Wang, T.; Reddy, R.G. Thermodynamic modeling of eutectic point in the LiNO3–NaNO3–KNO3–NaNO2 quaternary system. *Sol. Energy Mater. Sol. Cells* **2013**, *118*, 18–21.

132. Ren, N.; Wu, Y.; Ma, C.; Sang, L. Preparation and thermal properties of quaternary

mixed nitrate with low melting point. *Sol. Energy Mater. Sol. Cells* **2014**, *127*, 6–13.

133. Bradshaw, R.W.; Cordaro, J.G.; Siegel, N.P. Molten Nitrate Salt Development for Thermal Energy Storage in Parabolic Trough Solar Power Systems. In Proceedings of the ASME 2009 3rd International Conference on Energy Sustainability, Volume 2; ASME, 2009; pp. 615–624.

134. van Uitert, L.G.; Grodkiewicz, W.H. Nitrate glasses. *Mater. Res. Bull.* **1971**, *6*, 283–291.

135. Furukawa, T.; Brawer, S.A.; White, W.B. Raman spectroscopic study of nitrate glasses. *J. Chem. Phys.* **1978**, *69*, 2639.

136. Zhang, P.; Cheng, J.; Jin, Y.; An, X. Evaluation of thermal physical properties of molten nitrate salts with low melting temperature. *Sol. Energy Mater. Sol. Cells* **2018**, *176*, 36–41.

137. Rhodes, E.; Smith, W.E.; Ubbelohde, A.R. Melting and crystal structure: association in nitrate melts. *Proc. R. Soc. London. Ser. A. Math. Phys. Sci.* **1965**, *285*, 263–274.

138. Angell, C.A.; Helphrey, D.B. Corresponding states and the glass transition for alkali metal nitrates. *J. Phys. Chem.* **1971**, *75*, 2306–2312.

139. Angell, C.A.; Wong, J.; Edgell, W.F. Far-Infrared Spectra of Inorganic Nitrate and Chloride Glasses, Liquids, and Crystals: Complex Ions or Optical Phonons? *J. Chem. Phys.* **1969**, *51*, 4519–4530.

140. Cleaver, B.; Rhodes, E.; Ubbelohde, A.R. Studies of phase transformations in nitrates and nitrites I. Changes in ultra-violet absorption spectra on melting. *Proc. R. Soc. London. Ser. A. Math. Phys. Sci.* **1963**, *276*, 437–452.

141. Janz, G.J.; James, D.W. Raman Spectra and Ionic Interactions in Molten Nitrates. *J. Chem. Phys.* **1961**, *35*, 739–745.

142. Serrano-López, R.; Fradera, J.; Cuesta-López, S. Molten salts database for energy applications. *Chem. Eng. Process. Process Intensif.* **2013**, *73*, 87–102.

143. Ren, N.; Wu, Y.T.; Ma, C.F.; Sang, L.X. Preparation and thermal properties of quaternary mixed nitrate with low melting point. *Sol. Energy Mater. Sol. Cells* **2014**, *127*, 6–13.

144. Coastal Chemical Co., L.L.C. HITEC ® Heat Transfer Salt. Technical Data Guide. **2009**.

145. Sohel Murshed, S.M.; Nieto de Castro, C.A. A critical review of traditional and emerging techniques and fluids for electronics cooling. *Renew. Sustain. Energy Rev.* **2017**, *78*, 821–833.